

**Quantum transport in strongly interacting, ultracold  
Fermi gases in box potentials**

by

Parth Patel

B.S., University of California, Riverside (2014)

Submitted to the Department of Physics  
in partial fulfillment of the requirements for the degree of  
Doctor of Philosophy in Physics

at the

MASSACHUSETTS INSTITUTE OF TECHNOLOGY

June 2022

© Massachusetts Institute of Technology 2022. All rights reserved.

Author .....  
Department of Physics  
February 8, 2022

Certified by .....  
Martin W. Zwierlein  
Thomas A. Frank (1977) Professor of Physics  
Thesis Supervisor

Accepted by .....  
Deepto Chakrabarty  
Associate Department Head of Physics



# Quantum transport in strongly interacting, ultracold Fermi gases in box potentials

by

Parth Patel

Submitted to the Department of Physics  
on February 8, 2022, in partial fulfillment of the  
requirements for the degree of  
Doctor of Philosophy in Physics

## Abstract

Transport of strongly interacting fermions is crucial for systems as varied as high- $T_c$  superconductors, twisted bi-layer graphene, nuclear fission, and neutron stars. In this thesis, I will describe the experiments we performed to measure the transport properties of a strongly-interacting atomic Fermi gas. This system features interactions as strong as allowed by quantum mechanics and features one of the highest pairing strength, with a superfluid transition temperature on the order of the Fermi temperature. Moreover, it is also scale-invariant, making its properties directly relevant for systems with many order of magnitude higher densities. We trap these atoms in a uniform box potential made from repulsive laser light, the key experimental advancement that makes the transport experiment presented here possible. Here, we observe a very low, universal, Heisenberg-uncertainty limited diffusion of both sound and heat by studying the propagation of sound waves and conduction of heat in a uniform gas. Similar to a growing number of high- $T_c$  superconductors, we observe anomalous transport properties, like the viscosity and thermal conductivity, that cannot be explained by a Fermi-liquid theory. We show the temperature dependence of all non-zero transport properties, which constitutes a complete characterization of transport phenomena in the spin-balanced, strongly-interacting Fermi gas. Our findings inform theories of fermion transport, with relevance for hydrodynamic flow of electrons, neutrons, and quarks.

Thesis Supervisor: Martin W. Zwierlein  
Title: Thomas A. Frank (1977) Professor of Physics

*To my family and teachers*

## Acknowledgments

My time at MIT has been full of many ups and a few downs. I could not have gone through it without the support from many wonderful people. Here, I would like to briefly think them.

First and foremost, I would like to sincerely thank my research advisor, Martin Zwierlein, for teaching me to be a better physicist. I have learned a great deal from him throughout the past years, including atomic physics, the physics of strongly-interacting fermions, and, even the nitty-gritty details of making and running an ultracold atoms experiment. His excitement about physics has been a constant source of inspiration for me and I've always appreciated him for sharing his latest findings with us. I have always been amazed at his skills to solve complex problems, both regarding many-body physics and annoying issues in the lab. I will always cherish the countless spontaneous meetings we have had on the hallway and at *Area 4* while getting a coffee.

The work presented here was a big team effort, and would not have been possible without a wonderful team. I am indebted to Tarik Yefsah, Julian Struck, and Richard Fletcher, the three wonderful post-docs, and Biswaroop Mukherjee and Zhenjie Yan, the two wonderful graduate students, without whom this work would have been impossible. The charming conversations I had with Tarik and Mark Ku while visiting Martin's group were one of the reasons I decided to join *BEC 1*. I joined this group with a limited knowledge about optics and ultracold atoms, but, thanks to Tarik and Julian, I was able to quickly fill in those gaps and learn the ways around *BEC 1*. Tarik's *cowboy* style and Julian's attention to details were the perfect combination to quickly try new things out and, if they work, make a second version that's rock solid. Julian's persistence to upgrade the ages old optics in the lab took us from tweaking the MOT twice a day to twice a month, and eventually saved us months of accumulated time. His detailed understanding of the underlying physics and inner workings of the experiment lead us to three wonderful studies on the properties of Fermi gases.

I could not have asked for better lab mates than Biswaroop and Zhenjie. After Tarik left, Biswaroop took charge of his *cowboy* style. I was always amazed at the speed at which Biswaroop can learn new things and turn them into reality. Biswaroop quickly became a big brother to me, always encouraging me to make healthier choices and guiding me to have a better lab schedule. Zhenjie and I joined Martin's group at the same time and learned the machine together. I am always amazed at his ability to solve problems both in physics courses and in lab, and appreciate his stubbornness to question everything, which has saved us many factors of 2's and  $\pi$ 's over the years. I vividly remember spending many nights together with everyone to see the first signs of the homogeneous Fermi gas and propagation of sound waves.

The addition of Richard Fletcher, Cedric Wilson and Airlia Shaffer to the team was a very welcoming one. Richard brought with him fresh new ideas and focus to the lab. I am always amazed at his ability to reduce complex problems to their basics and find a very elegant solution. Cedric and Airlia brought with them a whole new level of energy and excitement. Their dedication and hard work turned *Fermi 3* into a reality in a very short period of time. I will always cherish the memories we made while setting up the new experiment listening to Major Lazer.

The recent addition of Eric Wolf, Huan Bui, and Ruixiao Yao gave me big hopes for the future all over again. Even if it was brief, working with Eric and Huan in *BEC 1* was a pure joy and made me wish that they had joined lab sooner.

I want to thank the many teachers from whom I've learned over the years. In particular, Wolfgang Ketterle for teaching me AMO physics, both through his classes and online lectures. They were truly instrumental in my understanding of AMO experiments and I often find myself referring back to them. I want to thank my academic advisor Joe Checkelsky for guiding me to success and many life advises. I also want to thank my thesis committee members Wolfgang Ketterle and Daniel Harlow for their advice and feedback.

In addition, I want to thank the many current and former members of Martin's group and many members of the CUA community, including Yiqi, Carsten, Enrique, Zoe, Boris, Alex, Tom, Botond, Jared, Jasmine, Carter, Matt, Lawrence, Melih,

Jia, Julie, Hyungmok, Jesse, Niki, Will, Ivana, Furkan, Timur, Colin, Cody, Hao, Alan, Zach, Sebastian, Huanqian, Peter, Elmer, Mark, Lev, and many more. Their willingness to help in the moments of great need (like when the vacuum breaks!), for let me borrow (um... sometimes permanently) optics and electronics, discussing new physics and techniques are truly appreciated. I have created countless lifelong memories with them, including the daily lunches, dinners at the student center, beach and hiking trips, camping in Acadia, playing video games. Additionally, without the constant background support from the Al, Bill, Joanna, Paula, Cathy, and Sydney, getting through my time here would have been much more difficult. This community truly felt like a one big family.

Without the constant background support from many of my family members and lifelong friends, getting through the downs would have been nearly impossible. My uncle and aunt, Dilip and Kumud, provided me a home and raised me like their own son during the first few critical years in the US. My cousin and his wife, Umang and Miloni, provided me with a home away from home and filled in the role of an older brother and sister during my years at MIT. I want to thank some of my closest friends Alina, Bruce, Courtaney, Luka, Cesar, and Ram for their unknowing support. Special thanks goes to Alina for introducing me to the field of experimental AMO, encouraging me to apply to MIT, and always pushing me to go beyond my comfort zone, and to Bruce for always being there regardless of the hardship or the situation.

Finally, I would like to thank my family, especially my parents, Bharat and Bhavna, and sisters Himani and Punam. Without their constant support and words of encouragement, none of this would have been possible. The innocence and curiosity of the newest and smallest members of my family, Himarsh, Tirth, Maherash, and Saanvi, provides me with a renewed hope and constant source of inspiration.



# Contents

<b>1</b>	<b>Introduction</b>	<b>17</b>
1.1	Thesis outline . . . . .	26
<b>2</b>	<b>Strongly interacting Fermi systems</b>	<b>29</b>
2.1	Ideal fermions . . . . .	30
2.2	Strongly interacting fermions . . . . .	34
2.3	Transport phenomena . . . . .	39
2.3.1	Hydrodynamics . . . . .	41
2.3.2	Attenuation of sound waves . . . . .	44
2.3.3	Attenuation of temperature gradients . . . . .	46
<b>3</b>	<b>Homogeneous unitary Fermi gas of <math>{}^6\text{Li}</math> atoms</b>	<b>49</b>
3.1	Uniform box potentials . . . . .	50
3.1.1	Cylindrical box potential . . . . .	51
3.1.2	Loading and alignment . . . . .	54
3.1.3	Characterization . . . . .	56
3.2	Thermometry . . . . .	58
3.3	Imaging ${}^6\text{Li}$ . . . . .	62
3.3.1	Atomic structure of ${}^6\text{Li}$ at high magnetic fields . . . . .	63
3.3.2	Near resonant light-atoms interactions . . . . .	65
3.3.3	Absorption imaging with Doppler correction . . . . .	67
3.3.4	Phase contrast imaging . . . . .	72

<b>4 Sound waves, measuring the coupled transport of momentum and heat</b>	<b>79</b>
4.1 Mysterious resonances while heating the gas . . . . .	79
4.2 Traveling sound wave and its dispersion relation . . . . .	82
4.2.1 Creating and imaging sound waves . . . . .	82
4.2.2 Dispersion relation . . . . .	84
4.3 Sound diffusivity from the resonant modes . . . . .	86
4.3.1 Steady state response . . . . .	87
4.3.2 Imaging the resonant box modes, the sonogram, and $\chi_n$ . . . . .	88
4.3.3 Speed of sound . . . . .	90
4.3.4 Attenuation of sound in the hydrodynamic and collisionless regime	92
4.3.5 Sound diffusivity . . . . .	94
<b>5 Transport Properties of a Strongly Interacting Fermi Gas</b>	<b>99</b>
5.1 Measuring the Thermal Diffusivity . . . . .	100
5.1.1 Local heater . . . . .	100
5.1.2 Temporal Evolution of heat . . . . .	103
5.1.3 Thermal Diffusivity . . . . .	104
5.2 Viscosity and Thermal Conductivity . . . . .	106
<b>6 Summary and Outlook</b>	<b>113</b>
<b>A New apparatus to study ultracold atoms under rapid rotation</b>	<b>119</b>
A.1 Zeeman slower . . . . .	119
A.2 Time-averaged orbiting potential . . . . .	122
<b>B Homogeneous Atomic Fermi Gases</b>	<b>127</b>
<b>C Spectral Response and Contact of the Unitary Fermi Gas</b>	<b>137</b>
<b>D Boiling a Unitary Fermi Liquid</b>	<b>147</b>
<b>E Universal sound diffusion in a strongly interacting Fermi gas</b>	<b>159</b>

F Geometric squeezing into the lowest Landau level	177
G Crystallization of bosonic quantum Hall states in a rotating quantum gas	205



# List of Figures

1-1	Neutron star equation of state . . . . .	19
1-2	Comparison of superfluid critical temperature . . . . .	20
1-3	Viscosity of liquid- <sup>3</sup> He and liquid- <sup>4</sup> He . . . . .	21
2-1	Fermi-Dirac distribution . . . . .	31
2-2	Ideal Fermi gas equation of state . . . . .	33
2-3	Feshbach resonances in <sup>6</sup> Li . . . . .	37
2-4	Experimentally measured equation of state of the unitary Fermi gas .	39
2-5	Density response function . . . . .	45
3-1	Homogeneous Fermi gas in the optical box trap . . . . .	52
3-2	Optical setup for cylinder-shaped trap . . . . .	53
3-3	Characterizing wall steepness . . . . .	56
3-4	Characterizing potential uniformity . . . . .	57
3-5	Isoenergetic expansion for box thermometry . . . . .	60
3-6	Useful transitions in <sup>6</sup> Li . . . . .	64
3-7	Doppler correction for absorption imaging . . . . .	70
3-8	Verification of the lookup table . . . . .	71
3-9	High density imaging . . . . .	72
4-1	Signature of resonant sound modes of the box. . . . .	80
4-2	Properties of sound from resonant heating . . . . .	81
4-3	Creating sound waves . . . . .	82
4-4	Imaging sound waves . . . . .	83

4-5	The dispersion and attenuation rate of traveling sound waves . . . . .	85
4-6	Resonant modes of the cylindrical box . . . . .	89
4-7	Density response function $\chi_n$ . . . . .	90
4-8	Scale invariant speed of sound . . . . .	91
4-9	Sound attenuation rate in the hydrodynamic and collisionless regimes	93
4-10	Temperature dependence of the sound diffusivity . . . . .	94
4-11	Sound diffusivity of liquid helium . . . . .	96
5-1	Local heater . . . . .	101
5-2	Time evolution of temperature perturbations . . . . .	103
5-3	Decay rate of temperature gradient and thermal diffusivity . . . . .	104
5-4	Thermal diffusivity measured from the Fick's law of diffusion . . . . .	106
5-5	Transport properties of the spin-balanced, unitary Fermi gas . . . . .	108
5-6	Prandtl number . . . . .	110
A-1	Schematics for the Zeeman slower . . . . .	125

# List of Tables

A.1 Zeeman slower . . . . .	121
-----------------------------	-----



# Chapter 1

## Introduction

Quantum mechanics is perhaps the most successful theory ever produced. Its application to single or few particle systems produces results that have been verified by experiments with extreme precision. However, the complexity in this theory grows many-fold when inter-particle interactions are added or when a system of many particles is considered. The problem is even more intractable for strongly-interacting fermions. First, strong-interactions often lead to strong-correlations, which invalidate any theoretical approach based on a perturbative expansion starting from a non-interacting system, and second, Fermi statistics lead to a so-called ‘sign problem’ which plagues computational efforts. Theoretical calculations of both equilibrium and non-equilibrium properties based on first-principles are often not possible, and instead, they rely on approximate methods based on a heuristic approach. Here, experimental determination of physical properties is of crucial importance since they inform and validate theoretical models.

We strive to experimentally study these strongly-interacting fermionic systems using an analog quantum simulator made from ultracold atoms [20]. The experimental realization of Bose-Einstein condensation (BEC) in dilute atomic gases of  $^{87}\text{Rb}$  by Eric Cornell and Carl Wieman at JILA [4] and of  $^{23}\text{Na}$  by Wolfgang Ketterle at MIT [44] in 1995 opened the door to a wide range of new novel experiments [93, 21, 147]. A few years later, dilute gases of fermionic atoms were cooled to quantum degeneracy using the BEC as a refrigerant [94, 45, 184, 165, 89, 74, 67, 153]. Over the years, physicists

have figured out a wide range of experimental techniques to simulate, among many others, crystalline structure using optical lattices [24, 37, 122], strong interactions using Feshbach resonances [39], an-isotropic interactions using polar molecules [155, 193, 196], long-range interactions using Rydberg atoms [115, 16, 73], quantum hall physics using artificial gauge fields [64, 112, 59, 65] or rotating traps [202, 183, 8], low-dimensional systems using tight optical traps. These quantum systems also offer a very high degree of both control and access to almost all physical aspects like temperature, density, disorder, interactions, trapping potentials, etc., making them an ideal system for quantum simulators [21, 30, 71, 20, 192, 160]. Additionally, different components of some complicated system, like disorder or strong-interactions, can be individually turned on or off, and complexities can slowly be added, to systematically investigate the properties of the underlying system. These are truly dream systems for experimental and theoretical physicists alike.

A resonantly interacting ultracold sample of fermionic atoms, often known as the *unitary* Fermi gas, can be made using Feshbach resonances, where inter-spin interactions are as strong as allowed by quantum mechanics [203, 97, 11]. This system features interactions with a range that is much smaller than all other length scales, making it possible to confidently replace the complicated inter-atomic potential with a simplified zero-range contact interaction. The Hamiltonian of this system is then exactly known, a statement that cannot always be made about most real-world systems. In absence of any interaction related length scale, it is described by the two remaining length scales, corresponding to the density and the temperature of the gas. Here, all thermodynamic and transport properties are described by universal functions of ratio of the two remaining length scales, often written as the ratio of the temperature to the Fermi temperature  $T/T_F$ . In other words, this is scale-invariant system, whose properties can directly be compared to systems with many orders of magnitude different densities. With its properties independent of all microscopic details like the interaction range, density or even the type of particles, the unitary Fermi gas provides a unique testbed to study strongly interacting Fermi systems in general.

For example, it was recently proposed to use the unitary Fermi gas as a simu-

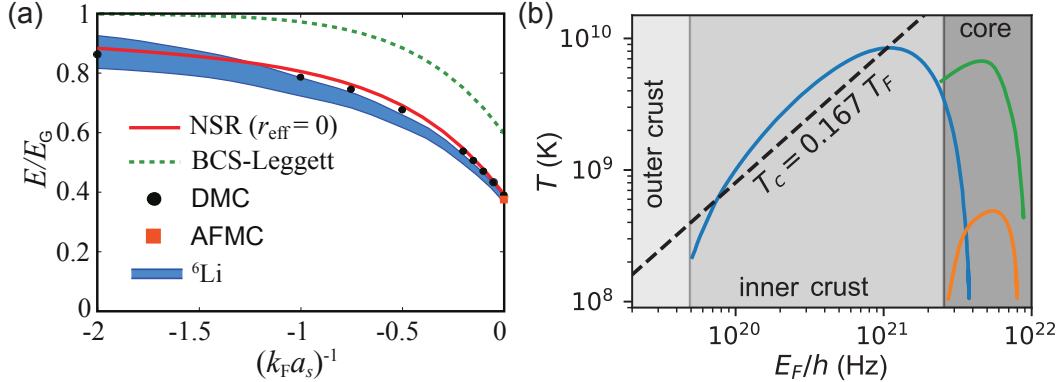


**Figure 1-1: Neutron star equation of state.** (a) Reproduced from [185]. The predicted equation of state for the neutron matter in the crust of a neutron star [185] is shown in red line. It was calculated using the properties of an ultracold atomic Fermi gas [83], shown in blue shaded region. (b) The superfluid transition temperatures predicted for a neutron star [5] and measured in a strongly-interacting unitary Fermi gas [103] are shown. Here, blue, orange, and green lines correspond to neutron-single, neutron-triplet, and proton-singlet pairing, respectively, while the black dashed line corresponds to the unitary Fermi gas. A similarity between these two systems exists because they both feature strong  $s$ -wave interactions with a scattering length that is much larger than interparticle spacing.

lator for the study of neutron-star equation of state, specifically in its ‘low-density’ crust [185]. With a radius of only about 10 km, but the mass of an entire sun, a neutron star is quite possibly the densest object in the universe [167]. Just a few meter below the surface lies a sea of neutrons, which are expected to be in a superfluid phase, and thought to be responsible for cooling the neutron star [138] and producing glitches in its rotation [35]. This is an exotic system with a superfluid transition temperature predicted at  $10^{10}$  K [5], but, it is not experimentally accessible. However, a connection between the unitary Fermi gas and neutron matter is possible because they both feature similar  $s$ -wave interactions with a scattering length that is much larger than the inter-particle spacing. The scale-invariance of the unitary Fermi gas makes it possible to use it as a simulator for the neutron matter at more than 18 orders of magnitude higher densities. Fig. 1-1 (a) shows the equation of state predicted for the neutron star (red line) using the Fermi gas’s properties and a comparison between their superfluid transition temperatures in (b).

The strong interactions in the unitary Fermi gas leads to a superfluid phase [202]

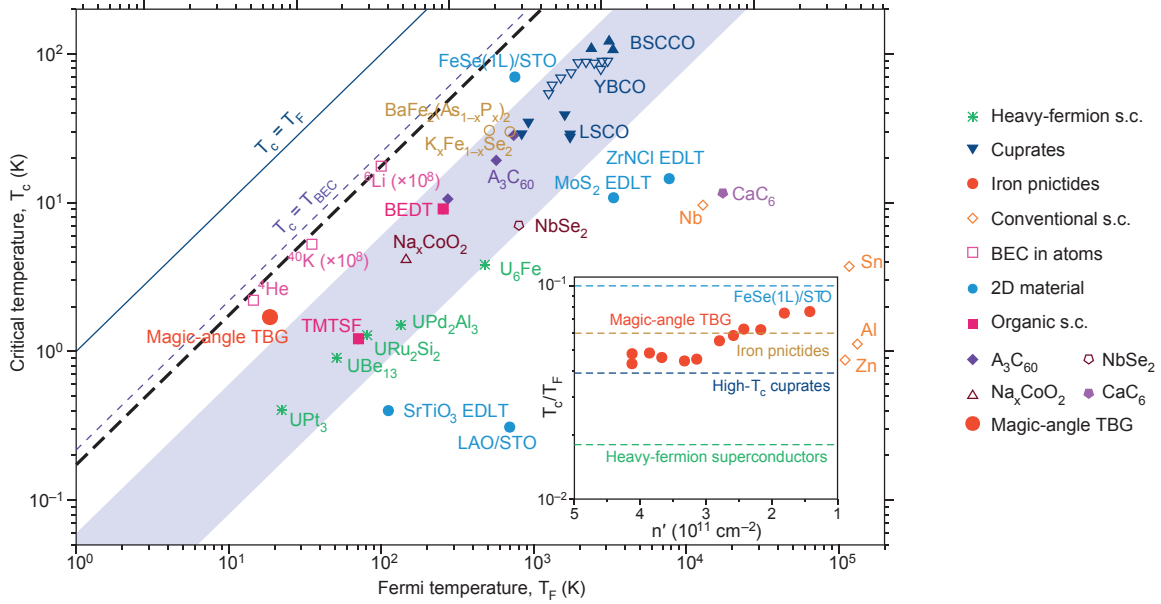


Figure 1-2: **Comparison of superfluid critical temperature.** Reproduced from [32]. The critical temperature  $T_c$  for superfluidity/superconductivity is shown for various materials as a function of their Fermi temperature  $T_F$ . Notably, the scale-invariant unitary Fermi gas, with one of the highest  $T_c/T_F = 0.167$  [103], is shown in black dashed line, the magic-angle twisted bi-layer graphene is shown in red circle, and a collection of high- $T_c$  cuprate superconductors lie in the blue-shaded region.

with one of the highest relative pairing-gap of any known fermionic system and a superfluid transition temperature  $T_c = 0.167(13) T_F$  [103] on the order of the Fermi temperature  $T_F$ . In contrast, most conventional BCS superconductors, for example Zn and Nb, feature orders of magnitude lower transition temperature  $T_c \sim 10^{-5} T_F$ . Other systems that have come the closest to the unitary Fermi gas are ‘unconventional’ superconductors, for example cuprate, heavy-fermion, and organic superconductors, with  $T_c = 0.01 - 0.05 T_F$ , and, more recently, the magic-angle twisted bi-layer graphene [32], with  $T_c \approx 0.08 T_F$ . If an electronic system, with its high  $T_F \sim 10^4$  K, were engineered to interact resonantly similar to the Fermi gas, then it would feature a superconductor transition temperature  $T_c \approx 1600$  K much higher than the room-temperature, achieving a long-standing goal in modern physics.

There are some features that are common among all of these ‘unconventional’ high- $T_c$  superconductors. First, they display an anomalous linear-in-temperature resistivity [79, 111] and other transport properties [149, 190, 126]. However, this can-

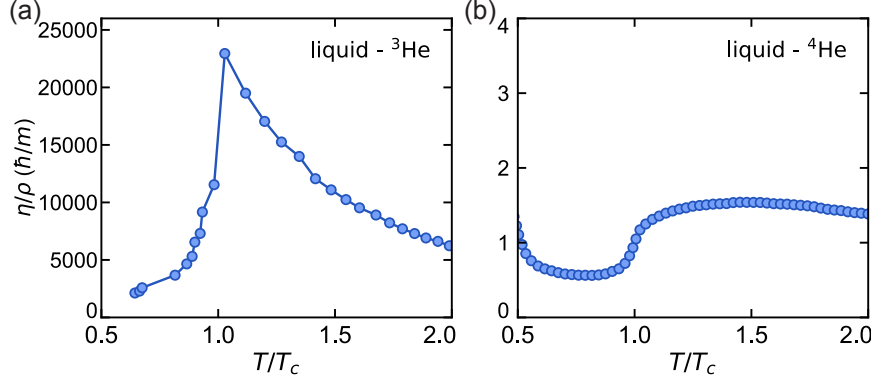


Figure 1-3: **Viscosity of liquid- $^3\text{He}$  and liquid- $^4\text{He}$ .** Measured kinematic viscosity  $\eta/\rho$  of (a) liquid- $^3\text{He}$  [76] and (b) liquid- $^4\text{He}$  [46] near the superfluid transition temperature are shown in units of  $\hbar/m$ , where  $m$  is the mass of  $^3\text{He}$  and  $^4\text{He}$  atom respectively.

not be explained by the Fermi-liquid theory [79], a description of interacting fermions based on perturbative expansion about the ideal Fermi gas, applicable to most metals at low temperatures, hinting that electrons in these systems are strongly-interacting and strongly-correlated. The origin of this behavior is still an open question, but new theories based on quantum critical fluctuations [51, 43] and incoherent transport [77] might offer an explanation. And second, their superconductivity is thought to originate from strong electron correlations instead of the weak electron-phonon coupling [60, 198], making the unitary Fermi gas, with its quantum limited interactions, an ideal platform to investigate strongly correlated quantum matter.

Liquid- $^3\text{He}$  and liquid- $^4\text{He}$  are two other quantum fluids whose equilibrium and transport properties are well studied [14, 17, 189, 119], and may shed some light on transport properties of quantum matter. In particular, let's consider their viscosity, shown in Fig. 1-3, in units of  $\hbar/m$ , where  $m$  is the mass of either  $^3\text{He}$  or  $^4\text{He}$  atom. The viscosity of the fermionic  $^3\text{He}$  in its normal phase is well described the Fermi-liquid theory, seen as  $\eta \propto 1/T^2$  divergence at  $T/T_c > 1$ . The applicability of the Fermi-liquid suggests that the normal phase of  $^3\text{He}$  is well understood by weakly-interacting, long-lived, quasi-particles. Upon transitioning to a superfluid state,  $\eta$  suddenly falls by more than a factor of 10, and saturates to values  $\sim 2000 \hbar/m$ . In contrast, the viscosity of the strongly-interacting, bosonic  $^4\text{He}$  is already very low  $\sim \hbar/m$  in its

normal phase and drops by less than a factor of 2 upon crossing to a superfluid state. Notably, it does not feature any divergent behavior near  $T_c$  nor in its normal phase. Apriori, it is not clear whether the transport properties of a strongly-interacting, fermionic, gas of atoms, electrons, or neutrons should resemble that of a quantum liquid, and if so, whether it corresponds more closely to the strongly interacting, but bosonic, liquid  $^4\text{He}$  or to the fermionic, but weakly interacting, liquid  $^3\text{He}$ .

While the field of strongly-interacting Fermi gases is vast, here we focus on their transport properties with hopes of answering a few basic questions.

1. what are the transport properties of a spin-balanced, resonantly interacting Fermi gas? While their equilibrium properties have been fully characterized by measuring the equation of state [133, 103], their transport properties are largely unknown, partly due to the lack of uniform samples [3].
2. is it possible to describe the transport properties of this system using well-defined quasi-particles? This question is more for theorists, but the experimental measurements presented here could serve as a benchmark. One possibility is a pseudo-gap phase where fermion pairs exist without long range order [87, 151].
3. do new theories developed to explain the anomalous transport properties of unconventional superconductors, like quantum critical transport and incoherent transport, also apply to the strongly-interacting Fermi gas?
4. are there common features in the transport properties of all strongly interacting quantum matter?, hinting at the possibility of describing them all with a universal theory.

**Overview of transport properties and ways to measure them.** Transport physics aims to describe the out-of-equilibrium dynamics of a system. If perturbations are small enough and interactions are large enough to maintain a local thermal equilibrium, then transport physics is conveniently described by hydrodynamics. At its heart lies conservation laws. For one-component gas or liquid, these are the conservation of mass, momentum, and energy. Combined with the thermodynamic relations, these conservation laws describe the dynamics of any physical quantity, like

local density, current, or temperature, after an arbitrary perturbation of the system. Additionally, internal friction damps the flow of momentum and heat, leading to two transport phenomena; viscous flow and heat conduction. The flow of heat from regions of higher to lower temperatures is quantified by the thermal conductivity  $\kappa$ . Momentum, being a vector quantity, damps due to shear forces, quantified by the shear viscosity  $\eta$ , or due to compression, quantified by the bulk viscosity  $\zeta$ . These three transport properties constitute a complete characterization of transport phenomena in one-component systems. In two-component systems, an imbalance in the concentration of two components leads to an irreversible flow of particles, quantified by a diffusion constant. For example, the transport of spin concentrations after some spin-imbalance in a spin-1/2 Fermi gas is quantified by the spin diffusivity [173, 28, 100]. However, if the two spin concentrations are kept equal, spin transport does not play a role in the dynamics of the gas.

Determination of these transport properties from first principles for strongly-interacting quantum matter is a very difficult task. For classical systems like the ideal gas, kinetic theory provides the tools necessary to compute transport properties, but it requires the gas to be composed of particles that freely travel through the system, except during perfectly elastic collisions. Here, all transport properties are given by some characteristic relaxation time and average velocity of the particles. For example,  $\eta = \rho v^2 \tau_\eta$  and  $\kappa = \rho c_P v^2 \tau_\kappa$ , where  $\rho$  is the mass density and  $c_P$  is the specific heat at constant pressure of the system. A similar approach is possible for interacting quantum systems, but only if the excitations of the system can be well-described by weakly-interacting and long-lived quasi-particles [13]. For example, both the equilibrium and transport properties of most metals and liquid Helium are very well described by the Fermi liquid theory. It is based on the assumption that an interacting Fermi gas behaves similarly to a non-interacting gas, but with particles replaced by long-lived quasi-particles with renormalized properties like mass. In contrast, typical excitations in the strongly-interacting Fermi gas have a mean-free-path as short as inter-particle spacing with a mean-lifetime much shorter than their inverse-energy. Apriori, it is unclear if the same perturbative Fermi-liquid theory

will hold in the strongly-interacting regime, and, if not, is it possible to describe the system using other quasi-particles or a completely new approach is required.

Experimental determination of transport properties often entail measuring the response of a system to some external perturbation. Perhaps the simplest example is conduction of heat. Heating one side of a sample creates a gradient in its temperature and forces heat to flow. This flow of heat is directly proportional to the thermal conductivity. Therefore, a measurement of the flow of heat provides a direct access to  $\kappa$ . Similarly, the measurements of the local momentum of a fluid confined between two parallel plates, one of which is forced to move tangentially, gives a direct access to the shear viscosity. However, physical limitation often make it impossible to make such a direct measurement or create such an idealistic perturbation. Fortunately, time evolution after a perturbation in any of the system's properties is determined by a combination of the same fundamental transport phenomena, often referred to as the diffusion constants.

Consider, for example, sound waves. They are ubiquitous in nature; from ripples in a pond to waving of a flag and phonons in a crustal. They are easy to create since any perturbation in the density of a fluid inevitably results in sound waves. Along with the density, sound waves are also accompanied by oscillations in both the local momentum and temperature, which are attenuated by the viscous flow and heat conduction. The specific combination of the transport properties responsible for sound attenuation is known as the sound diffusivity  $D_s = \frac{4\eta}{3\rho} + \frac{\zeta}{\rho} + (\gamma - 1)\frac{\kappa}{\rho c_P}$ , where  $\gamma = \frac{c_P}{c_V}$  is the ratio of specific heats of the fluid. Therefore, by studying the attenuation of sound, we can measure the coupled transport of momentum and heat.

Note that, in general, three independent measurements involving the transport properties  $\eta$ ,  $\zeta$ , and  $\kappa$  are necessary to uniquely determine their values. However, in scale invariant systems like the unitary Fermi gas, the bulk viscosity is identically zero. This follows from the fact that the entropy of a scale invariant system does not change under a uniform expansion. Here, a second, independent measurement of transport is enough to characterize transport phenomena. Consider a temperature perturbation, which, unlike sound waves, attenuate only because of the irreversible

flow of heat, quantified by the thermal diffusivity  $D_T = \frac{\kappa}{\rho c_P}$ . Determination of both  $D_s$  and  $D_T$  constitute a complete characterization of transport phenomena in spin-balanced unitary Fermi gases.

A crucial tool required to make these measurements is an access to a uniform sample. This might sound like a trivial request for most condensed matter physicists, but ultracold atomic gases have historically been trapped using magnetic fields or at the focal point of an attractive laser beam. Both of these methods create a sample whose density varies across space. The propagation of sound is completely different in such inhomogeneous samples, where the speed of sound itself varies across space. Here, instead of traveling plane waves, one observes collective oscillations, with properties that are very different from typical sound waves. Moreover, the varying density implies that atoms at different locations in the trap experience different points in the phase space. It is even possible for the atoms near the center of the trap to be in a superfluid phase, while the atoms near the edges are normal. This makes it difficult to extract the properties of a homogeneous system from trap averaged measurements.

Nevertheless, experiments have measured some trap averaged transport properties using inhomogeneous samples of the unitary Fermi gas. From the dynamics of a controllably imprinted spin-imbalance, the diffusive transport spin concentrations was observed enabling the experimental determination of the corresponding spin diffusivity [173, 174, 100, 10]. Here, a Heisenberg-uncertainty limited diffusivity was observed where  $D \gtrsim \hbar/m$  is given only by the reduced Planck's constant and particle mass. Apart from the harmonically trapped gas, experiments have used terminal configurations, where two separate reservoirs containing ultracold fermionic atoms are linked with a small 2D or 1D channels. Here, the transport of heat [26], particles [27, 176], and spin [101, 109] were measured. A comparison between the transport of particles and heat through a very small 1D channel suggests a breakdown of the Wiedman-Franz law [86] in the unitary Fermi gas. From collective oscillations [186, 121], hydrodynamic damping rates were observed [98, 97, 181, 72]. From the hydrodynamic free-expansion of trapped Fermi gases [136], the trap-averaged shear viscosity was measured [31, 50]. While it is possible to extract the viscosity of a homogeneous

system from their trap averaged values, see for example [90, 22], it requires a very careful treatment of the dilute corona [3]. Another approach is to selectively probe the nearly homogeneous center of harmonically trapped gases. Here, experiments have excited sound waves using focused-beam Bragg-spectroscopy and measured the density response function [82, 104].

In this thesis, for the first time, we directly trap an ultracold gas of fermionic atoms inside a box, a technique first pioneered by Z. Hadzibabic for bosonic atoms [63]. The box is made from repulsive laser beams that keep the atoms trapped inside, where they experience zero external potential. This creates a homogeneous, constant-density sample of ultracold atoms ideal for transport experiments. We have developed several techniques to locally excite sound waves and inject heat to measure the transport properties of this system.

## 1.1 Thesis outline

In chapter 2, we begin by describing the physics background needed to understand the experiments presented in this thesis. We review the equilibrium properties of both the non-interacting and strongly-interacting Fermi gases. The experimentally measured equation of state of the unitary Fermi gas is provided, which enables us to interchange thermodynamic state variables, useful for converting the measured temperature into pressure, heat capacity, etc. With regard to transport physics, we derive the hydrodynamic equations from conservation laws, specifically for a one-component, or spin-balanced, fluid. We provide two applications of these equations, one for the propagation and attenuation of sound, and other for attenuation of temperature perturbations.

In chapter 3, we provide the experimental tools necessary to create and probe a homogeneous Fermi gas. We describe how to create, load, align, and characterize the uniform box potential. Several methods developed to measure the temperature of a homogeneous gas are then given. Extracting quantitative information from images of a very dense clouds of a light atoms like  ${}^6\text{Li}$  turned out to be tricky as well. We find

the Doppler correction for the usual absorption imaging and describe phase contrast imaging for  ${}^6\text{Li}$  at high magnetic fields.

Chapter 4 presents the study of sound which attenuate through a coupled transport of momentum and heat. We begin by describing a little mystery that lead us to sound waves. From traveling waves of sound, we measure a remarkably linear dispersion, and from resonant sound modes, we measure the density response function. We demonstrate the scale invariance of the unitary Fermi gas and demonstrate the applicability of hydrodynamics using the speed and attenuation of sound. And, finally, we provide the measurements of the sound diffusivity.

Chapter 5 presents the study of heat transport followed by the determination of both transport properties. We have created a temperature gradient by locally injecting heat into the system. The subsequent time evolution allows us to measure the thermal diffusivity. By combining the sound and thermal diffusivities, we uniquely determine both the shear viscosity and the thermal conductivity, painting a complete picture of transport properties of the strongly-interacting unitary Fermi gas. We compare these results to other quantum systems.

Appendix A presents the schematics for the Zeeman slower and the magnetic TOP trap used to rotate quasi-two dimensional gases of  ${}^{23}\text{Na}$  and  ${}^6\text{Li}$ .

The remaining appendices present the publications relevant to this thesis, including the first realization of the homogeneous atomic Fermi gas [130] (presented in Ch. 3), measurements of the spectral response and contact of unitary Fermi gas [128] (presented in B. Mukherjee's thesis [127]), measurements of the Fermi Polaron in highly spin-imbalanced gases [195] (presented in Z. Yan's thesis [194]), observation of sound and measurements of the sound diffusivity [141] (presented in Ch. 4). We have also included results from the new apparatus, first on geometric squeezing a BEC into lowest Landau level through rotation [54] and second on the spontaneous crystallization of a BEC near the lowest Landau level [129].



# Chapter 2

## Strongly interacting Fermi systems

This chapter presents the physics background needed to understand the experiments presented in the rest of this thesis. Our goal is to better understand the transport properties of strongly interacting Fermi systems. We begin by reviewing the ideal Fermi gases, including their anti-symmetric exchange statistics and thermodynamic properties. Quantum scattering theory, in particular the *s*-wave scattering prominent at ultracold temperatures, provides a description for interacting particles, and scattering resonances set a quantum limit for the strongest possible interactions. These are realized in the experiment using a magnetic Feshbach resonance to produce the strongly-interacting unitary Fermi gas. This is a scale-invariant system similar to the ideal Fermi gas, making its properties relevant to other fermionic quantum systems. Its equilibrium properties are compared to that of non-interacting Fermi gas, and the experimentally measured equation of state is presented.

Transport physics describes the response of a system to external perturbations. Its results are summarized by a set of hydrodynamic equations presented here. They relate perturbations in various physical quantities, for example the local density, temperature, velocity, etc., and are quantified by a set of transport properties like the viscosity and thermal conductivity. We provide a general solution to hydrodynamic equation in the limit of small amplitude perturbations, and provide two specific examples. First, we find the attenuation of sound, a propagating density wave supported by the hydrodynamic equations, determined by the coupled transport of momentum

and heat, and, second, we solve the time evolution after an arbitrary temperature perturbation determined by the transport of heat.

## 2.1 Ideal fermions

**Quantum statistics of identical particles.** Every fundamental particle, for example an electron, is identical to all other particles of the same type. This basic idea has a profound consequence in physics. Consider an ensemble of these identical particles described by a many-particle wavefunction  $\Psi(r_1, r_2, \dots, r_i, \dots)$ . Exchanging any two, for example  $i \leftrightarrow j$ , must produce the same physical state, requiring  $|\Psi(r_j, r_i)|^2 = |\Psi(r_i, r_j)|^2$ . This leads to two possibilities,

$$\Psi(r_j, r_i) = +\Psi(r_i, r_j), \quad (2.1a)$$

$$\text{or } \Psi(r_j, r_i) = -\Psi(r_i, r_j), \quad (2.1b)$$

corresponding to a symmetric (+) or an anti-symmetric (-) exchange. All particles in three dimensions must correspond to one of these two categories. In 1940, Wolfgang Pauli proved [142], based on postulates of relativity and quantum mechanics, that bosonic particles have an integer spin and must follow the Bose-Einstein statistics while fermionic particles have a half-integer spin and must follow the exclusion principle. Suppose that two fermions are in the same quantum state  $|n\rangle$  with a wavefunction  $\Psi(r_1, r_2) = \Psi(n, n)$ . Exchange symmetry of eq. 2.1b requires  $\Psi(n, n) = -\Psi(n, n)$ , which is only possible if  $\Psi(n, n)$  is identically zero, implying that two fermions cannot occupy the same quantum state. This is Pauli's exclusion principle. It plays a dominant role in fermionic systems, makes the periodic table of elements possible, and stabilizes the neutron star against its immense gravity.

**Thermodynamic properties of ideal Fermi gases.** Before we introduce interactions between particles, it is educational to understand the thermodynamic properties of an ensemble of non-interacting fermions in a box. At zero temperature,  $N$  fermions

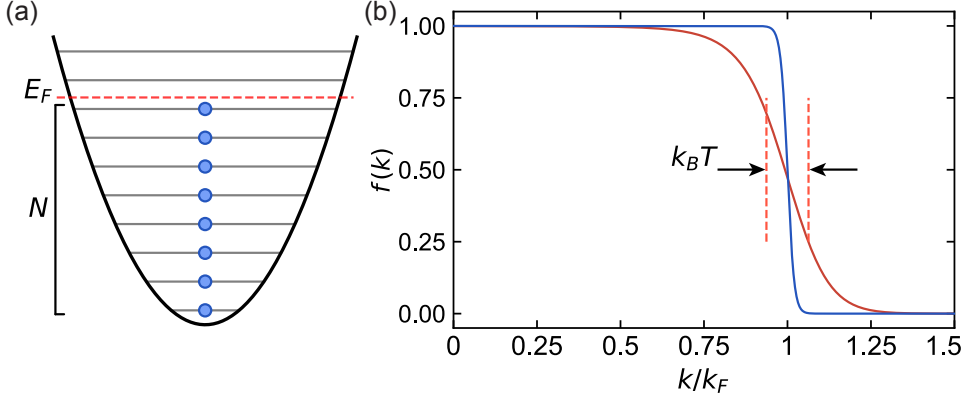


Figure 2-1: **Fermi-Dirac distribution.** (a) A cartoon depicting Fermi-Dirac distribution. Each state is occupied by at most one fermion. At zero temperature,  $N$  fermions occupy the  $N$  lowest quantum state. The highest occupied state has an energy  $E_F$ , the Fermi energy. (b) Fermi-Dirac distribution is shown at  $T = 0.02 T_F$  (blue) and  $T = 0.13 T_F$  (red). A sharp Fermi surface is visible in blue, while a Fermi surface broadened by  $\sim k_B T$  is visible in red.

in box of length  $L$  and volume  $V = L^3$  occupy the  $N$  lowest eigenstates of the system, namely the momentum eigenstates  $|\mathbf{k}\rangle$ , with each state having at most one fermion. This forms a ‘Fermi sea’ with a Fermi surface located at the highest occupied state with momentum  $\hbar k_F$ , the Fermi momentum, and energy  $E_F = \frac{\hbar^2 k_F^2}{2m}$ , the Fermi energy, see Fig. 2-1 (a). We find the Fermi momentum by equating the total number of states below  $k_F$  to the number of particles  $N$ ,

$$N = \sum_{\mathbf{k}=0}^{k_F} 1 = \int_0^{k_F} \frac{d^3 \mathbf{k}}{(2\pi/L)^3} = \frac{V}{(2\pi)^3} \int_0^{k_F} dk \ 4\pi k^2 = \frac{V k_F^3}{6\pi^2}, \quad (2.2)$$

resulting in

$$k_F = (6\pi^2 n)^{1/3}, \quad E_F = \frac{\hbar^2 (6\pi^2 n)^{2/3}}{2m}, \quad (2.3)$$

where  $n = N/V$  is the number density of fermions. If the Fermi gas is composed of an equal mixture of two spins, each having  $N_\uparrow = N_\downarrow = N$  atoms, with total atom number  $N_t = 2N$  and total density  $n_t = 2n$ , then the Fermi momentum is  $k_F = (6\pi^2 n)^{1/3} = (3\pi^2 n_t)^{1/3}$ . The momentum distribution is exactly  $f(k) = 1$  below the Fermi surface, at  $k \leq k_F$ , and  $f(k) = 0$  elsewhere.

The qualitative effects of finite temperature is to excite some fermions close to

the Fermi surface, within  $\sim k_B T$  of  $E_F$ , from below the Fermi surface to above, effectively softening the sharp Fermi surface as shown in Fig. 2-1 (b). The exact probability distribution is easily computed in the grand canonical ensemble, where one finds a grand partition function  $\mathcal{Q}$ ,

$$\ln \mathcal{Q} = \sum_{\mathbf{k}} \ln \left[ 1 + e^{\frac{\mu - \epsilon_k}{k_B T}} \right], \quad (2.4)$$

where  $\mu$  is the chemical potential and  $\epsilon_k = \frac{\hbar^2 k^2}{2m}$  is the energy of a state  $|k\rangle$ . Eq. 2.4 is derived in most statistical mechanics textbooks, see for example [92]. All thermodynamic quantities are easily calculated from various combinations of  $\mathcal{Q}$ . For example, the exact probability of occupying a state  $|k\rangle$  is

$$f(\mathbf{k}) = -\frac{\partial \ln \mathcal{Q}}{\partial (\epsilon_k / (k_B T))} = \frac{1}{e^{(\epsilon_k - \mu) / (k_B T)} + 1}, \quad (2.5)$$

also known as the Fermi-Dirac distribution, shown in Fig. 2-1(b). Note that  $\mu$  coincides with the Fermi energy at zero temperature. Number density, energy density, and pressure are given below,

$$n = \frac{N}{V} = \frac{\sum 1 \cdot f(\mathbf{k})}{V} = -\frac{1}{\lambda^3} \text{Li}_{3/2} \left( -e^{\frac{\mu}{k_B T}} \right), \quad (2.6a)$$

$$\epsilon = \frac{E}{V} = \frac{\sum \epsilon_k f(\mathbf{k})}{V} = -\frac{3}{2} \frac{k_B T}{\lambda^3} \text{Li}_{5/2} \left( -e^{\frac{\mu}{k_B T}} \right) = \frac{3}{2} P, \quad (2.6b)$$

$$P = \frac{k_B T}{V} \ln \mathcal{Q} = -\frac{k_B T}{\lambda^3} \text{Li}_{5/2} \left( -e^{\frac{\mu}{k_B T}} \right) = \frac{2}{3} \epsilon, \quad (2.6c)$$

where we have used the thermal wavelength  $\lambda = \sqrt{\frac{2\pi\hbar^2}{mk_B T}}$ , replaced the  $\sum_{\mathbf{k}} = \left(\frac{L}{2\pi}\right)^3 \int d^3\mathbf{k}$  and used polylogarithm of order  $m$ ,  $\text{Li}_m$ , defined as  $-\text{Li}_m(-z) \equiv f_m(z) = \frac{1}{(m-1)!} \int_0^\infty dx \frac{x^{m-1}}{z^{-1}e^x + 1}$ .

**Scale invariance of the ideal Fermi gas.** Another important characteristic of the ideal Fermi gas is its scale-invariance, which will become even more relevant when discussing the strongly-interacting Fermi gas. Let's consider a general Hamiltonian  $H = \frac{p^2}{2m} + V_{\text{int}}$  representing a system of particles with arbitrary interparticle interac-

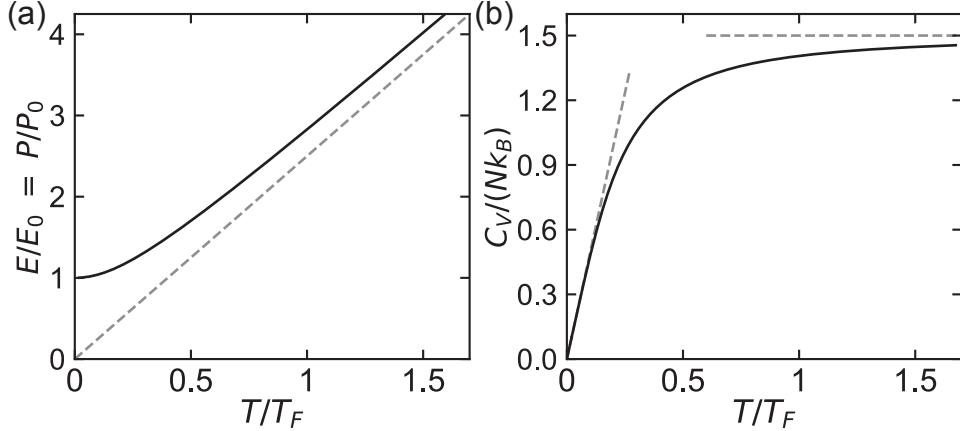


Figure 2-2: **Ideal Fermi gas equation of state.** (a) The total energy is shown as a universal function  $E/E_0 = f_E(T/T_F)$ , independent of the scale, i.e. the density, of the gas, and  $E/E_0 = P/P_0$  follows from  $E = \frac{3}{2}PV$ . Here,  $E_0 = \frac{3}{5}NE_F$  is the total energy and  $P_0 = \frac{2}{5}nE_F$  is the pressure of an ideal Fermi gas at zero temperature. For reference, the energy of a classical ideal gas  $E = \frac{3}{2}Nk_B T \rightarrow E/E_0 = \frac{5}{2}T/T_F$  is shown in black dashed line. (b) The heat capacity at constant volume is shown as a universal function  $C_V/(Nk_B) = f_{C_V}(T/T_F)$ . For reference, its value in the limit of zero temperature,  $C_V \rightarrow \frac{\pi^2}{2}T/T_F$  and its value for a classical gas  $C_V = \frac{3}{2}Nk_B$  are shown in black dashed line.

tions  $V_{\text{int}}$ . Upon rescaling of space by a factor  $\xi$ , such that  $r \rightarrow \xi r$  and  $p \propto \frac{d}{dr} \rightarrow \frac{1}{\xi}p$ , the kinetic energy  $\frac{p^2}{2m} \rightarrow \frac{1}{\xi^2} \frac{p^2}{2m}$  while the scaling of interaction term depends on its specific form. If  $V_{\text{int}} \not\propto \frac{1}{\xi^2}V_{\text{int}}$ , then the energy, and other thermodynamic properties, of the system depends on the specific scale of the system, and cannot be determined from its value at different scales. In contrast, if  $V_{\text{int}} \rightarrow \frac{1}{\xi^2}V_{\text{int}}$ , then  $H \rightarrow \frac{1}{\xi^2}H$ , the system energy  $E \rightarrow \frac{1}{\xi^2}E$ , and all other properties of the system can be found by simple rescaling. Meaning that, measurement of thermodynamic properties at a specific density are enough to completely characterize the system and their value at any other densities are found by simple rescalings. Here, it is convenient to write the thermodynamic quantities as dimension-full constant times a universal function that only depends on dimensionless ratios of different length-scales of the system. Some examples of systems with scale-invariance include the classical ideal gas and ideal Fermi gas where  $V_{\text{int}} = 0$ , and any system with  $V_{\text{int}} \propto 1/r^2 \rightarrow \frac{1}{\xi^2}V_{\text{int}}$ .

Let's consider the specific example of ideal Fermi gas. The only two length scales present in this system, the interparticle spacing  $l \sim n^{-1/3} \propto T_F^{-1/2}$  ( $T_F \equiv E_F/k_B$ ) and

the thermal wavelength  $\lambda = \sqrt{\frac{2\pi\hbar^2}{mk_B T}} \propto T^{-1/2}$ , are set by the density and temperature respectively. Therefore, all thermodynamic properties can be written as universal functions of the ratio  $l/\lambda$ , or more conveniently the ratio  $T/T_F$ , where  $T$  and  $T_F$  are set by the temperature and density respectively. For example, instead of defining the energy  $E = f(T)$ , with some function  $f$  that depends on the specific density of the gas, it is more useful to provide  $\frac{E}{E_0} = f_E\left(\frac{T}{T_F}\right)$ , where  $E_0$  is a dimension-full constant, typically the energy of the Fermi gas at zero temperature, and the function  $f_E$  is a universal function valid at all scales of the system, i.e., at all temperatures and densities. The dimensionless functions for the energy (or equivalently the pressure) and heat capacity are shown in Fig. 2-2.

To demonstrate the power of scale-invariance, let's consider the isotropic speed of sound  $c$ . In an arbitrary system,  $c$  is given by the equation

$$mc^2 = \frac{\partial P}{\partial n}\Big|_S = \frac{V^2}{N} \frac{\partial^2 E}{\partial V^2}\Big|_S, \quad (2.7)$$

where  $P = -\frac{\partial E}{\partial V}\Big|_S$  is the pressure. In scale-invariant systems, this derivative can be calculated purely based on scaling arguments. We already saw that  $E \rightarrow \frac{1}{\xi^2}E$  under a dilation of space, requiring  $E \propto L^{-2} \propto V^{-2/3}$  for a system with a characteristic size  $L = V^{1/3}$ . Therefore,  $\frac{\partial E}{\partial V} = -\frac{2}{3}\frac{E}{V} \propto V^{-5/3}$  and  $\frac{\partial^2 E}{\partial V^2} = \frac{10}{9}\frac{E}{V^2}$ , and

$$mc^2 = \frac{10}{9} \frac{E}{N}. \quad (2.8)$$

This is a universal relation, applicable for *all* scale-invariant systems, independent of their equation of state, temperature, or even their phase.

## 2.2 Strongly interacting fermions

While the ideal Fermi gas displays some non-classical behavior, like the Fermi surface and quantum pressure, interactions are required to realize exotic features and phases of matter like superfluidity [9], strange-metals [116], and fractional quantum hall states [182]. In this section, we describe the interactions experienced by neutral

ultracold atoms, and describe the experimental tool used to tune its strength. This produces a strongly-interacting Fermi gas with a collision cross-section as high as allowed by quantum mechanics [39]. We discuss the properties of this strongly interacting gas based on its scale-invariance, and provide the experimentally determined equation of state, fully characterizing its equilibrium properties.

**Quantum scattering theory.** We begin with a quick review of quantum scattering theory, a framework to describe all interactions in quantum mechanics. Detailed derivation can be found in most quantum mechanics texts, see for example [69, 159]. Interactions between particles can be described in terms of scattering events, where one particle is a stationary target for the other. The moving particle is assumed to be freely propagating towards the target, with a momentum  $\hbar k$  and a wavefunction  $\propto e^{ikz}$ . Suppose that two particles interact with an arbitrary conservative potential  $V(\mathbf{r})$ , where  $\mathbf{r}$  is the relative distance. The incoming particles interact with this potential in some complicated way, however, in the far field, away from the effective range of this potential, they are again free with the same kinetic energy as before. The effects of the potential is to scatter more or less particles in different directions with different phase shifts, summarized by the scattering amplitude  $f(\theta, \phi)$  and the outgoing spherical wavefunction  $f(\theta, \phi)e^{ikr}/r$ . Therefore, the differential cross-section  $d\sigma$  to scatter particles in some solid angle  $d\Omega$  is given by this scattering amplitude as  $d\sigma = |f(\theta, \phi)|^2 d\Omega$ .

In the case of a spherically symmetric interparticle potential,  $V(\mathbf{r}) \rightarrow V(r)$ , angular momentum is conserved, and it is best to solve for  $f$  using partial wave analysis. Here, both the incoming and outgoing wavefunction are separable and re-written as  $\sum_l R_l(r)Y_l^0(\theta, \phi)$ , where the spherical harmonics  $Y_l^m(\theta, \phi)$  account for the angular dependence while the radial wavefunction  $R(r) = u(r)/r$  satisfies the radial Schrödinger equation  $-\frac{\hbar^2}{2m} \frac{d^2u}{dr^2} + \left(V(r) + \frac{\hbar^2}{2m} \frac{l(l+1)}{r^2}\right)u = Eu$ . Conservation of angular momentum implies that the amplitude of  $l^{\text{th}}$  partial wave remain the same before and after scattering and all that can happen is a relative phase shift,  $\delta_l$  between the incoming and outgoing wavefunctions. Intuitively,  $l^{\text{th}}$  partial waves comes in, interacts with the potential, and comes back out with the same amplitude, but with a different phase.

The set of  $\delta_l$  completely determine the scattering properties, and their values depend on the details of the interaction potential  $V(r)$ . For example, the total collision cross-section is

$$\sigma = \frac{4\pi}{k^2} \sum_{l=0}^{\infty} (2l+1) \sin^2(\delta_l). \quad (2.9)$$

Another useful quantity related to the phase shift for the  $s$ -partial wave ( $l = 0$ ) is the scattering length  $a \approx -\tan(\delta_0)/k$ . It measures the effective range of the potential and is often used to quantify the strength of interactions.

**Scattering resonances in ultracold gases.** Neutral atoms interact with each other through the Van der Waals force at long range and experience a hardcore repulsion at short range. In general, characterizing these interactions would require many partial waves and values of many  $\delta_l$ 's. However, at ultracold temperatures, the kinetic energy of particles is much lower than the energies required to overcome the centrifugal barrier  $\frac{\hbar^2}{2m} \frac{l(l+1)}{r^2}$ , therefore, only the lowest energy  $s$ -wave scattering is present, significantly simplifying the interactions. At the  $s$ -wave scattering resonance, where  $\delta_0 \rightarrow \pi/2$  and  $a \rightarrow \infty$ , the atoms interact with the strongest possible interactions with a collision cross-section  $\sigma = 4\pi/k^2$ . For more details, see [39, 15].

In the case of fermionic atoms like  ${}^6\text{Li}$ , even the  $s$ -wave scattering is forbidden between identical particles owing to the Pauli-exclusion principle. In fact, a spin-polarized ultracold gas of fermionic atoms is perhaps the best realization of an ideal, non-interacting gas across all of physics. Mixture of two or more internal states of a fermionic atom are necessary for them to interact, where their interactions are again described by  $s$ -wave scattering.

While the exact inter-spin interaction potential  $V_{\text{int}}$  has a complicated form, hard core repulsion plus a weak Van der Waals attraction, its effects are completely determined by a single parameter, the  $s$ -wave scattering length, at ultracold temperatures. Meaning that, any other potential that produces the same scattering length is indistinguishable from the exact interaction potential. The most commonly used pseudopotential is the Fermi pseudopotential [84]  $V_{\text{int}}(\mathbf{r}) = \frac{4\pi\hbar^2 a}{m} \delta^3(\mathbf{r}) \frac{\partial}{\partial r} r$ , where  $\mathbf{r}$  is the relative position between two atoms,  $a$  is the  $s$ -wave scattering length, and

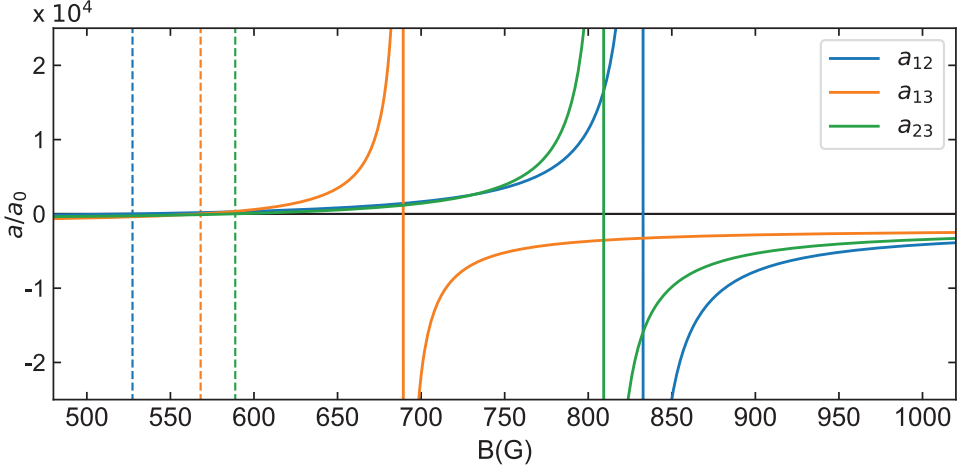


Figure 2-3: **Feshbach resonances in  ${}^6\text{Li}$ .** The  $s$ -wave scattering length between the three lowest hyperfine states,  $|1\rangle$ ,  $|2\rangle$ , and  $|3\rangle$ , of  ${}^6\text{Li}$  are shown. The  $a_{12}$ ,  $a_{13}$ , and  $a_{23}$  feature Feshbach resonances (solid vertical lines) at 832.18 G, 809.76 G, and 689.68 G, respectively, feature zero-crossings (i.e. zero interactions, dashed vertical lines) at 527.3 G, 568.1 G, and 588.8 G, respectively. The background scattering lengths at zero magnetic field are  $\approx -1 a_0$ ,  $-820 a_0$ , and  $24 a_0$ , respectively.

features a zero-range contact interaction. Now, the Hamiltonian

$$H = \sum_i \frac{p_i^2}{2m} + \sum_{i < j} \frac{4\pi\hbar^2 a}{m} \delta^3(\mathbf{r}_{ij}) \frac{\partial}{\partial r_{ij}} r_{ij} \quad (2.10)$$

of the strongly interacting Fermi gas is completely known; a statement which cannot always be said for many real-world systems.

**Feshbach resonance.** Under normal conditions, ultracold alkali atoms interact with a scattering length  $a \sim 100 a_0$ , where  $a_0$  is the Bohr radius. While this is strong enough for sympathetic cooling or studying weakly interacting Bose-Einstein condensates, we desire to study the strongly-interacting Fermi gases where the scattering length is much larger than all other length scales of the system. Luckily, ultracold alkali atoms also feature Feshbach resonances, which allows the interparticle interactions to be changed with an external bias magnetic field. Essentially, the external magnetic field changes the difference in energies between a molecular bound state and two colliding atoms, owing to their differential magnetic moment. When the molecular state is brought in resonance, the atoms experience a resonant scattering where

the phase shift  $\delta \rightarrow \pi/2$  and the scattering length  $a \rightarrow \infty$  diverges. Close to this resonance, the scattering length is given by  $a = a_{\text{bg}}(1 - \Delta B/(B - B_0))$ , parametrized by the background scattering length  $a_{\text{bg}}$ , the width  $\Delta B$  and the center  $B_0$  of the resonance. For more details, see [39].

Fermionic  ${}^6\text{Li}$  features several broad Feshbach resonances that are easily accessible in our experiments shown in Fig. 2-3. The ground state manifold of  ${}^6\text{Li}$  has six states, labeled  $|1\rangle$ ,  $|2\rangle$ , etc. We typically work with a mixture of states  $|1\rangle$  and  $|3\rangle$  which feature a resonance at 689.68 G, or with a mixture of states  $|1\rangle$  and  $|2\rangle$ , featuring a resonance at 832.18 G [166, 200]. This produces a two spin mixture of ultracold Fermi gas with inter-spin interactions as strong as allowed by quantum mechanics, often called the unitary Fermi gas.

**Properties of the strongly-interacting, unitary Fermi gas.** While the properties of an ideal Fermi gas can easily be calculated, solving for the properties of a strongly-interacting Fermi gas is an extremely hard problem. However, the unitary Fermi gas is a unique system. Similar to the non-interacting Fermi gas, it also features scale-invariance, where upon a rescaling of space by  $r \rightarrow \xi r$ , the Hamiltonian shown in eq. 2.10 scales as  $H \rightarrow \frac{1}{\xi^2}H$ . This scale-invariance can rigorously be proved using a wavefunction of the form  $\psi \propto 1/a - 1/r_{ij}$  and Wigner-Bethe-Peierls boundary condition, see for example [34, 201, 135].

At the scattering resonance the only interactions related length scale diverges  $a \rightarrow \infty$ , meaning that the properties of this system cannot explicitly depend on  $a$ . Here, similar to the non-interacting Fermi gas, all thermodynamic and transport properties must be given by universal functions of the ratio of the two remaining length scales, corresponding to the density  $n$  and temperature  $T$ . It is often convenient to use the ratio  $T/T_F$  where  $k_B T_F = E_F = \frac{\hbar^2(6\pi^2 n)^{2/3}}{2m}$  to write these universal functions. At zero temperature, the situation simplifies significantly, where all properties must be proportional to a dimension full constant involving the density, with a universal prefactor. For example, the energy of the gas must be  $E = \xi^3 N E_F \equiv \xi E_0$ , where we have used the energy  $E_0$  of a non-interacting Fermi gas as the dimension full

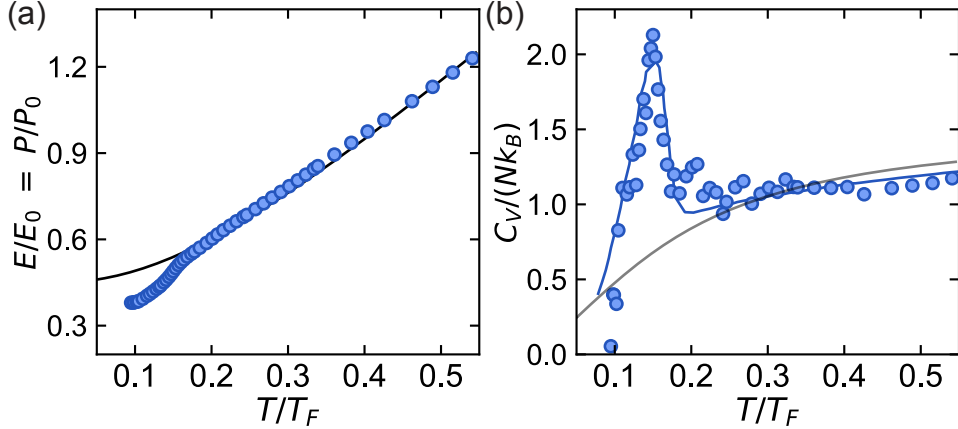


**Figure 2-4: Experimentally measured equation of state of the unitary Fermi gas.** The measured energy equation of state (a) and the entropy equation of state (b) are reproduced here from [103]. Similar to the ideal Fermi gas, the unitary Fermi gas is also scale-invariant, making it possible to show these equations of state as dimensionless functions of  $T/T_F$ . The energy of the unitary gas near  $0.25 \lesssim T/T_F \lesssim 1$  is well approximated by the ideal gas energy, but shifted by  $\xi_n - 1$  (black line), where  $\xi_n \approx 0.45$ , because of interactions. The heat capacity features the iconic  $\lambda$ -shape near the superfluid phase transition at  $T_c = 167(13)$   $T_F$ . The heat capacity of an ideal Fermi gas is shown in black line.

constant, with a universal constant  $\xi^1$  known as the Bertsch parameter [78]. The value of this universal constant was experimentally measured  $\xi = 0.376(4)$  [103]. At finite temperatures, this prefactor becomes a universal function of the ratio  $T/T_F$ , with energy  $E = f_E(T/T_F) E_0$ . Other thermodynamic properties are also given by similar functions, for example the entropy  $S = f_S(T/T_F) Nk_B$ , the chemical potential  $\mu = f_\mu(T/T_F) E_F$ , the heat capacity  $C_V = f_{C_V}(T/T_F) Nk_B$ , etc. These equations of state were measured by [103], reproduced here in Fig. 2-4. They are very powerful, completely characterizing all thermodynamic properties of the unitary Fermi gas, and are used through out this thesis to interchange thermodynamic state variables.

## 2.3 Transport phenomena

In this sections, we provide a review of transport physics relevant to measurements presented in this thesis. Transport physics concerns with the out-of-equilibrium dy-

---

<sup>1</sup>Please note that the Bertsch parameter  $\xi$  is not related to the previously used symbol  $\xi$  to demonstrate scale invariance.

namics of physical systems. At first, predicting the time evolution of a system after an arbitrary perturbation seems like a daunting task, however, if the system is only slightly perturbed from a state of equilibrium, then the subsequent dynamics are beautifully described by hydrodynamics reviewed below. For detailed description see books [170, 107, 108] and seminal papers [81, 96, 91].

In one-component fluids, there are only two types of transport phenomena, the viscous flow and heat conduction. They are described by a set of hydrodynamic equations (reviewed below) and quantified by three transport properties. The viscosity measures the resistance of a fluid resulting from gradients in local velocity. There are two types of gradients: shear gradients, for example  $dv_x/dy$ , are damped by the shear viscosity  $\eta$ , while compression gradients, for example  $dv_x/dx$ , are damped by the bulk viscosity  $\zeta$ . The irreversible flow of heat is quantified by the thermal conductivity  $\kappa$ , responsible for removing gradients in local temperature. A determination of all three of these transport properties constitute a complete characterization of transport phenomena of a system<sup>2</sup>.

Their measurements typically require measuring the response of a system after some perturbation. For example, an ideal measurement of the thermal conductivity would be to create a gradient in the temperature and measure the subsequent flow of heat; the proportionality constant between the two is defined as the thermal conductivity. However, such idealistic measurements are not always possible due to physical limitations, and one needs to rely on indirect measurements. In general, the time evolution after a perturbation in arbitrary quantity can be computed using the set of hydrodynamic equations and transport properties, and often feature a decay rate  $\Gamma = Dk^2$  with a characteristic wavevector squared dependence and a diffusion constant  $D$  that depends on some combinations of the three transport properties.

We first derive the hydrodynamic equations from conservation laws, followed by its application in two specific cases. We calculate the dynamics after a perturbation in, first, the local density, and second, the local temperature of the gas. Later, in

---

<sup>2</sup>We are only considering perturbations that are small in amplitude such that hydrodynamics is applicable.

Chapters 4 and 5, we experimentally create these perturbations, demonstrate the applicability of hydrodynamics, and measure the relevant transport properties.

### 2.3.1 Hydrodynamics

Let's consider perturbations that are small in amplitude and slowly varying over space and time (long wavelength and small frequency). If the interparticle interactions are sufficiently large to locally maintain thermal equilibrium, subsequent time evolution is beautifully described by hydrodynamics.

At its heart lies conservation laws; particularly the conservation of mass, momentum, and energy for one-component fluids and gases. They all take the form of continuity equations. Consider, for example, a general conserved quantity  $q$ . Conservation of  $q$  requires  $\partial\rho/\partial t + \nabla \cdot \mathbf{j} = 0$  since any change in its volume density  $\rho = q/V$  must flow through some surface accounted by gradient of its flux density  $\mathbf{j} = \rho\mathbf{v}$ . If the quantity  $q$  is being created or destroyed at a rate  $Q$ , then

$$\frac{\partial\rho}{\partial t} + \nabla \cdot \mathbf{j} = Q. \quad (2.11)$$

The unitary Fermi gas is a prototypical strongly interacting fluid with mean free path as small as the interparticle spacing. In its normal regime, it is convenient to write the conservation laws for mass density  $\rho$ , momentum current density  $j = \rho\mathbf{v}$ , and entropy density  $s = S/V$ , instead of energy. If we only consider changes in one dimension, say along  $z$ , then the three conservation laws for  $\rho$ ,  $j$ , and  $s$  are

$$\frac{\partial\rho}{\partial t} + \frac{\partial j}{\partial z} = 0, \quad (2.12a)$$

$$\frac{\partial j}{\partial t} + \frac{\partial P}{\partial z} = 0, \quad (2.12b)$$

$$\frac{\partial s}{\partial t} + \frac{\partial(sv)}{\partial z} = 0, \quad (2.12c)$$

where flux density corresponding to  $j$  is the pressure  $P$ . Note that we are only considering the normal phase of the unitary Fermi gas here. In the superfluid phase, gradient of the phase of the emergent macroscopic wavefunction  $\Psi e^{i\Phi}$  is also conserved, leading

to a conservation law for the superfluid velocity  $\mathbf{v}_s = (\hbar/m)\nabla\Phi$ .

While mass is never destroyed in our system, momentum and entropy may change due to dissipation. Non-zero shear viscosity  $\eta$ , bulk viscosity  $\zeta$ , and thermal conductivity  $\kappa$  will damp momentum current and increase entropy. Note that the unitary Fermi gas is a scale-invariant system where the bulk viscosity is identically zero [175, 52, 57], we therefore do not include it in the equations below. Furthermore, any changes in the external potential  $U$  can also generate momentum current. Note that one can also increase the entropy by directly injecting heat at a rate  $\frac{\partial S}{\partial t} = \frac{1}{T}\frac{\partial Q}{\partial t}$ , however, for the sake of simplicity, we omit adding this term here and directly calculate the response of a system to heat using the definition of  $\kappa$  in section 2.3.3.

Including these effects, the conservation laws are

$$\frac{\partial\rho}{\partial t} + \frac{\partial j}{\partial z} = 0, \quad (2.13a)$$

$$\frac{\partial j}{\partial t} + \frac{\partial P}{\partial z} = \frac{4\eta}{3\rho}\frac{\partial^2 j}{\partial z^2} - \rho\frac{\partial U}{\partial z}, \quad (2.13b)$$

$$\frac{\partial s}{\partial t} + \frac{\partial(sv)}{\partial z} = \frac{\kappa}{T}\frac{\partial^2 T}{\partial z^2}. \quad (2.13c)$$

In principle, we can stop here. This set of equations, plus thermodynamic relations, are complete. Using them, we can calculate the time evolution in density, current, temperature, entropy, etc. after an arbitrary perturbation. However, it is often convenient to analyze arbitrary perturbations using Fourier analysis, therefore, we try to find plane wave solutions next.

**Plane wave solution.** We consider plane wave perturbations of form  $\rho = \rho_0 + \delta\rho e^{ikz-i\omega t}$  for all quantities. Using eqs. 2.13, our goal is to find relations between physical quantities and find the dispersion relation  $\omega(k)$ .

Inserting the plane wave assumption into the hydrodynamic equations 2.13, we

get

$$-i\omega \delta\rho + ik \delta j = 0 \implies u \delta\rho - \delta j = 0, \quad (2.14a)$$

$$-i\omega \delta j + ik \delta P = -\frac{4}{3} \frac{\eta}{\rho} k^2 \delta j - ik \rho \delta U \implies u \delta j - \delta P + ik \frac{4}{3} \frac{\eta}{\rho} \delta j = \rho \delta U, \quad (2.14b)$$

$$-i\omega \delta(\sigma\rho) + ik \sigma \delta j = -\frac{\kappa}{T} k^2 \delta T \implies u \rho \delta\sigma + u \sigma \delta\rho - \sigma \delta j + ik \frac{\kappa}{T} \delta T = 0, \quad (2.14c)$$

where we have used  $j = \rho v$  to replace  $\delta v = \delta j/\rho$  in favor of  $\delta j$ , used the definition for phase velocity  $u = \omega/k$ , and replaced the entropy density  $s = \sigma\rho$  in favor of entropy per total mass  $\sigma = S/(mN)$ . So far, we have five unknowns<sup>3</sup>,  $\delta\rho$ ,  $\delta\sigma$ ,  $\delta j$ ,  $\delta P$ , and  $\delta T$  and only three equations. However, since local thermal equilibrium is always maintained, we can use thermodynamics to relate  $\delta P$  and  $\delta T$  to  $\delta\rho$  and  $\delta\sigma$ .

$$\delta P = \left. \frac{\partial P}{\partial \rho} \right|_{\sigma} \delta\rho + \left. \frac{\partial P}{\partial \sigma} \right|_{\rho} \delta\sigma = \frac{1}{\rho \kappa_S} \delta\rho - \frac{\rho}{\alpha_S} \delta\sigma, \quad (2.15a)$$

$$\delta T = \left. \frac{\partial T}{\partial \rho} \right|_{\sigma} \delta\rho + \left. \frac{\partial T}{\partial \sigma} \right|_{\rho} \delta\sigma = -\frac{1}{\rho \alpha_S} \delta\rho + \frac{T}{c_V} \delta\sigma, \quad (2.15b)$$

where  $\kappa_S$  is the isentropic compressibility,  $\alpha_S$  is thermal expansivity at constant entropy, and  $c_V$  is the specific heat at constant volume. We now have five equations (eqs. 2.14 and 2.15) with five unknowns to fully solve for all quantities and the dispersion relation.

Here, we only highlight the results relevant for this thesis. For a complete derivation see work by P. Hohenberg, P. Martin, and L. Kadanoff [91, 81]. Since the system responds to an external perturbation  $\delta U$ , it is best to find the density and entropy response functions  $\chi_{\rho\rho}$  and  $\chi_{\sigma\rho}$  defined as

$$\delta\rho = -\chi_{\rho\rho} \delta U, \quad (2.16a)$$

$$\delta\sigma = -\chi_{\sigma\rho} \delta U, \quad (2.16b)$$

---

<sup>3</sup>Note that  $\delta U$  is an external input and not an unknown.

with

$$\chi_{\rho\rho}(\omega, k) = \frac{\rho}{m} k^2 \frac{-\omega - ik^2 \gamma D_T}{(\omega^2 - c^2 k^2 + iD_s k^2 \omega)(\omega + iD_T k^2)}, \quad (2.17a)$$

$$\chi_{\sigma\rho}(\omega, k) = \frac{\alpha_S}{m \rho \kappa_S} k^2 \frac{-ik^2 (\gamma - 1) D_T}{(\omega^2 - c^2 k^2 + iD_s k^2 \omega)(\omega + iD_T k^2)}, \quad (2.17b)$$

where  $\gamma = c_P/c_V$ , and the isentropic speed of sound  $c$ , thermal diffusivity  $D_T$ , and sound diffusivity  $D_s$  are given by

$$c = \sqrt{\frac{1}{\rho \kappa_S}}, \quad (2.18a)$$

$$D_T = \frac{\kappa}{\rho c_P}, \quad (2.18b)$$

$$\begin{aligned} D_s &= \frac{4}{3} \frac{\eta}{\rho} + (\gamma - 1) \frac{\kappa}{\rho c_P}, \\ &= \frac{4}{3} \frac{\eta}{\rho} + \frac{4}{15} \frac{\kappa T}{P}. \end{aligned} \quad (2.18c)$$

The last simplification in  $D_s$  is possible because of the scale invariance of the unitary Fermi gas.

These response functions allow for an oscillating sound mode given by the pole  $\omega^2 = c^2 k^2 - i\omega D_s k^2$ , discussed in the next section. The density response function is shown in Fig. 2-5 using typical experimental values at  $T = 0.5 T_F$ . Here, the pole corresponding to the sound waves appears as a peak at  $\omega = ck$  with a width  $\Gamma = D_s k^2$ , while the broad peak located at zero frequency with a width  $\Gamma = 2D_T k^2$  corresponds to the slow diffusion of heat.

### 2.3.2 Attenuation of sound waves

Sound waves are traveling perturbations in the local density. They are easy to create since any perturbation in the external potential will inevitably result in sound waves, and, on ultracold gases, where the primary source of information is absorption images, they are equally easy to observe, making them an ideal experimental tool to study the transport.

In hydrodynamics, sound appears as a pole in the density response function, lo-

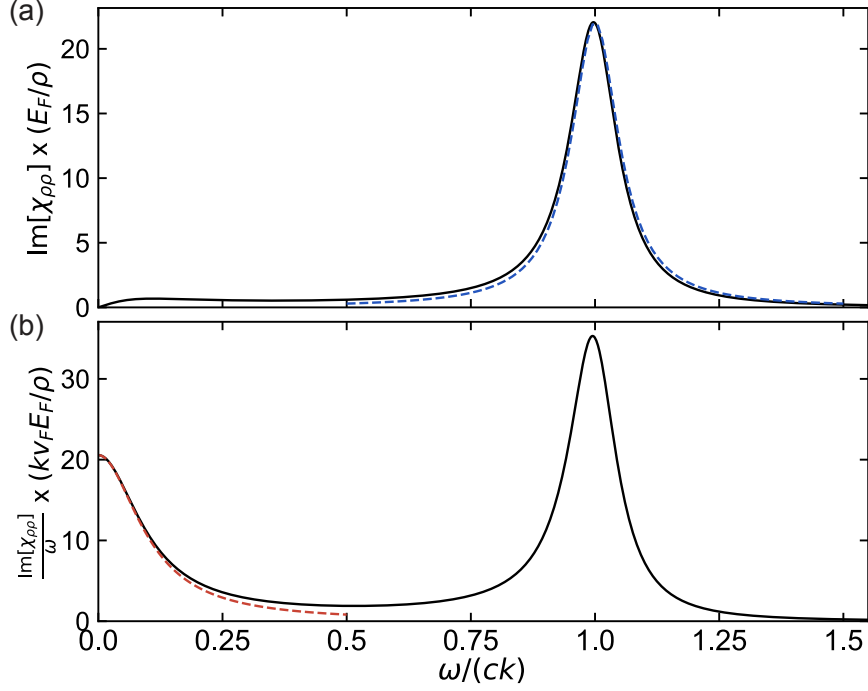


Figure 2-5: **Density response function  $\chi_{\rho\rho}$ .** The imaginary part of the density response function (a)  $\text{Im}[\chi(\omega, k)]$  and (b)  $\text{Im}[\chi(\omega, k)]/\omega$  are shown at a fixed value of  $k$  and as a function of  $\omega$  using the thermodynamic and transport properties of the unitary Fermi gas at  $T = 0.5 T_F$ . The peak in (a) at the sound resonance condition  $\omega = ck$  is well approximated by a Lorentzian function with a full-width at half-maximum of  $\Gamma = D_s k^2$ , shown in blue dashed line. (b)  $\text{Im}[\chi(\omega, k)]/\omega$  is useful when computing the response of a system to a step-function perturbation in the potential. Here, the density responds at two different time scales; the fast response is again characterized by sound waves, the peak near  $\omega = ck$ , while the slow relaxation of the density coming from the diffusion of heat is seen as a peak at zero frequency. It is well approximated by a Lorentzian function with a  $\Gamma = 2D_T k^2$ , shown in red dashed line.

cated at  $\omega^2 = c^2 k^2 - i\omega D_s k^2$ . Solving for  $\omega$ , we find

$$\omega = \sqrt{(ck)^2 - (\Gamma/2)^2} - i\Gamma/2 \equiv \omega' - i\Gamma/2, \quad (2.19)$$

where  $\Gamma = D_s k^2$  is the decay rate of sound. Here, the density evolves in time as

$$\delta\rho \propto e^{-i\omega t} = e^{-i\omega' t} e^{-\Gamma t/2}. \quad (2.20)$$

This is identical to a classical harmonic oscillator, including the modified oscillation

frequency  $\omega'$  and decay of the sound amplitude at a rate  $\Gamma/2$ . Similarly, the evolution of the density in space is  $\delta\rho \propto e^{ikz} = e^{i\omega' z/c} e^{-\Gamma t/(2c)}$ . This pole appears as a Lorentzian peak in  $\chi_{\rho\rho}$  with full-width at half-maximum width of  $\Gamma$ . We have observed sound waves and determined  $\Gamma$  using all three of these methods shown in chapter 4.

As postulated at the beginning of this chapter, perturbation in an arbitrary quantity decays at a rate  $\Gamma = Dk^2$  with the diffusion constant given by some combination of the transport properties. Since sound waves contain oscillations in both the local velocity and temperature, they decay with a rate  $\Gamma = D_s k^2$  and a diffusion constant  $D_s = \frac{4\eta}{3\rho} + (\gamma - 1)\frac{\kappa}{\rho c_P}$  containing both  $\eta$  and  $\kappa$ . Using sound waves, we measure the coupled transport of momentum and heat.

### 2.3.3 Attenuation of temperature gradients

Notice that sound waves alone are not enough to uniquely determine both non-zero transport properties. We need another, independent, measurement to decouple  $\eta$  and  $\kappa$  from  $D_s$ . Here, we describe the attenuation of temperature perturbations carried out by transport of heat.

The flow of heat from regions of higher to lower temperatures is governed by the Fourier's law, the defining equation for the thermal conductivity,

$$\mathbf{q} = -\kappa \nabla T, \quad (2.21)$$

where  $\mathbf{q}$  is the heat current density (or heat flux). This flow of heat is often difficult to measure directly, however, we can convert it to changes in local temperature. First, the conservation of energy,  $\frac{\partial u}{\partial t} + \nabla \cdot \mathbf{q} = 0$ , relates the heat current to the energy density  $u$ , and second, the specific heat at constant pressure  $c_P$  relates the change in energy density to the temperature,  $du = \rho c_P dT$ . Taking a gradient of the Fourier's law,  $\nabla \cdot \mathbf{q} = -\frac{\partial u}{\partial t} = -\rho c_P \frac{\partial T}{\partial t} = -\kappa \nabla^2 T$ , we find the heat equation

$$\frac{\partial T}{\partial t} = \frac{\kappa}{\rho c_P} \nabla^2 T \equiv D_T \nabla^2 T, \quad (2.22)$$

where we again find the thermal diffusivity  $D_T = \frac{\kappa}{\rho c_P}$ .

This heat equation describes the time evolution of the local temperature  $T$  after an arbitrary perturbation also in  $T$ . It is most easily analyzed in Fourier space, where a perturbation with wavevector  $k$  decays at a rate  $\Gamma = D_T k^2$ . Notably, it does not allow an oscillating mode, as was seen for sound waves. We again find the characteristic  $k^2$  dependence expected from hydrodynamics. Here, the thermal diffusivity is only given by  $\kappa$  because temperature gradients diffuse because of transport of heat alone.

The measurements of  $D_s$  from attenuation of sound waves and of  $D_T$  from attenuation of temperature gradients constitute a complete characterization of transport properties in the spin-balanced unitary Fermi gas, as long as hydrodynamics is applicable.



# Chapter 3

## Homogeneous unitary Fermi gas of $^6\text{Li}$ atoms

Ultracold atoms experiments have traditionally used optical dipole traps, where the atomic density varies across the trap. This is very unusual when compared to ‘conventional’ systems like liquid helium, superconductors, graphene, etc. At first, the varying density was turned into a unique feature. By considering an inhomogeneous system as an ensemble of many local homogeneous systems, experiments can simultaneously make measurements that span a wide range of phase space [80, 131, 131, 197, 103, 173, 171]. However, for studies of transport properties or critical behavior, such local approaches do not work. For example, the properties of sound waves, which travel through the entire system, are completely different in a harmonically trapped gas, and requires complicated theories and assumptions to extract local measurements [3, 22]. Several experiments have measured local properties by probing a small central region of harmonically trapped gases, for both thermodynamic [47, 157, 33] and transport [104] measurements. However, the best approach is to trap ultracold atoms in a uniform box potential made from repulsive laser light [63, 130].

Advances in the production and implementation of homogeneous box potentials [63, 130] paved the way for new measurement techniques that allowed for the study of transport properties in Fermi gas experiments. This section describes the ‘bread and butter’ behind all of the measurements performed using the homogeneous atomic

Fermi gas. We begin by describing the optical box potential, followed by its alignment procedure and characterization. We then describe various ways used to probe the homogeneous atomic Fermi gas, from absorption and phase-contrast imaging to thermometry and momentum distribution in the box.

An optical box was first pioneered by Z. Hadzibabic at Cambridge for an ultracold Bose gas [63]. This new experimental tool made a wide range of experiments possible, including the measurements of thermodynamic properties of the weakly-interacting Bose-Einstein condensate [164, 66], quench-dynamics through a phase transition [134], strongly-interacting Bose gas [48, 113, 49], quantum depletion [114], transport properties [61], and sound waves [40]. J. Dalibard at ENS trapped an ultracold Bose gas in a 2D uniform box [187], where they have also observed sound propagation [188] and interesting far-from-equilibrium dynamics resulting from scale-invariance [158]. Soon after our first realization of homogeneous atomic Fermi gases [130] presented here, H. Moritz at University of Hamburg realized a homogeneous Fermi gas in 2D [85], where they've studied the sound propagation [23], Josephson oscillations [118], and superfluidity [172] in 2D Fermi gases and single particle excitation spectrum [18] in 3D Fermi gases. Very recently, J. E. Thomas at North Carolina State University also realized a 3D homogeneous Fermi gas [7] and used it to study the hydrodynamic linear response [7] and relaxation [191].

### 3.1 Uniform box potentials

**Producing ultracold atomic Fermi gases.** The first step in creating homogeneous Fermi gases is to create an ultracold gas of  ${}^6\text{Li}$  atoms. Here, we only give a brief overview of the steps involved in creating an ultracold gas, for more details see previous thesis cited below or the book [125]. This work was performed in a dual-species  ${}^{23}\text{Na}$ - ${}^6\text{Li}$  experiment, referred to as ‘BEC1’ at MIT. At first, BEC1 was designed to only produce ultracold gases of bosonic  ${}^{23}\text{Na}$ , described in the thesis of A. Chikkatur [38] and D. Stamper-Kurn [177]. Fermionic  ${}^6\text{Li}$  was later added in the early 2000’s to study ultracold Fermi gases. The atoms begin their journey in the oven

(described in C. Stan [178]), where solid rocks of  $^{23}\text{Na}$  and  $^6\text{Li}$  are heated to  $\sim 400^\circ\text{C}$ . The resulting atomic vapors are guided in a straight line through the Zeeman slower, where they are slowed from  $\sim 600$  m/s all the way down to  $\sim 10$  m/s, and loaded into the magneto-optical trap (MOT) with a dark spot [95]. After a few seconds of loading, we turn the MOT off, pump the both atoms into their magnetically trappable stretched states, and move them to a magnetic trap made using cloverleaf coils. Here,  $^6\text{Li}$  atoms are sympathetically cooled to quantum degeneracy with  $^{23}\text{Na}$  atoms using evaporative cooling. In absence of  $^6\text{Li}$  atoms, we generate Bose-Einstein condensate of about 10 million  $^{23}\text{Na}$  atoms, which is enough to cool about 20 million  $^6\text{Li}$  atoms to quantum degeneracy. For more details see PhD thesis of Z. Hadzibabic [75] and M. W. Zwierlein [204]. The remaining ultracold  $^6\text{Li}$  atoms are transferred into an optical dipole trap, at the focus point of a 1064 nm laser beam, where their internal state can now be manipulated. A microwave Landau-Zener sweep transfers the atoms from the stretched state  $|6\rangle = |F = 3/2, m_F = 3/2\rangle$  to the ground state  $|1\rangle = 1/2, 1/2$ . The bias magnetic field is now increased to  $\sim 500$  G where the three lowest states display weak inter-spin interactions. We now convert some of the state  $|1\rangle$  atoms into  $|3\rangle$  using a pair of radio-frequency sweeps, clean the leftover atoms in  $|2\rangle$ , and finally increase the bias magnetic field to  $\approx 690$  G where states  $|1\rangle$  and  $|3\rangle$  resonantly interact. Here, another quick evaporation is performed by reducing the intensity of the optical dipole trap to cool the spin mixture all the way to superfluidity. For more details see PhD thesis of M. Ku [102].

This strongly-interacting, degenerate, inhomogeneous, atomic Fermi gas is now transferred into a cylindrical box described in the next section.

### 3.1.1 Cylindrical box potential

A box potential is conceptually not any more difficult than the standard optical dipole trap. It is based on dipole forces [55, 70]; an atom with a resonance frequency  $\omega_0$  is attracted to any light with a frequency lower than  $\omega_0$  and is repulsed by any light with a frequency higher than  $\omega_0$ .  $^6\text{Li}$  has a  $\omega_0 \approx 2\pi c/(671 \text{ nm})$ , meaning that the readily available high-power 1064 nm infrared (532 nm green) laser is an ideal source

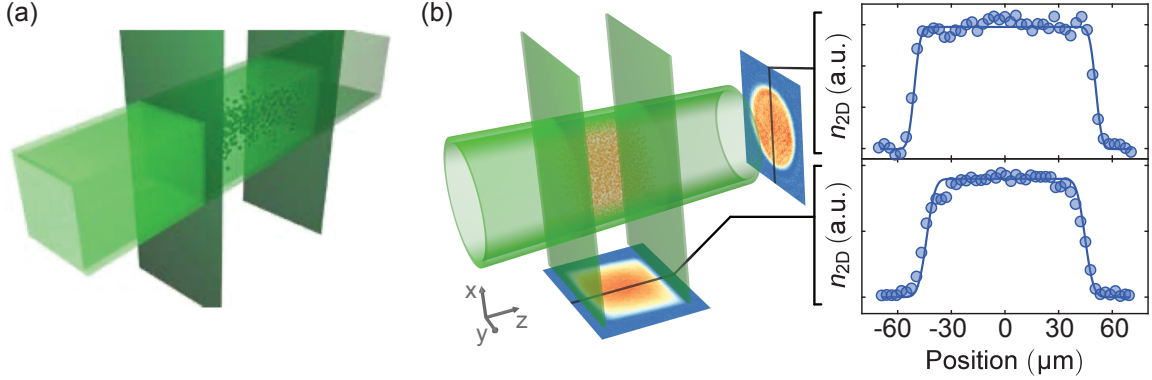


Figure 3-1: **Homogeneous Fermi gas in the optical box trap.** Optical box traps are made from a set of repulsive laser beams, typically a green 532 nm laser. (a) A square box is created from 6 intersecting sheets of laser light. (b) A cylindrical box is created by intersecting a ring-shaped beam with 2 sheets of laser light. Absorption images taken along two different axis of the box show homogeneous density profiles.

for attractive (repulsive) potential. In order to create an attractive optical dipole trap, one simply needs to focus an infrared laser beam onto the atoms. The laser intensity is highest at its focal point, attracting the atoms towards it, and falls off with a Gaussian profile, creating an approximately harmonic, attractive trap along all three directions.

Creating a uniform box potential using laser beams is similar in concept to the dipole trap, but requires tailoring specific intensity profiles. While creating a uniform box potential from the attractive infrared laser light is possible, there are two major downsides. First, in order to create a uniform potential for the atoms, the intensity of the laser beam must be uniform in space as well. This cannot be easily done using standard optical elements and requires tools like digital mirror devices (DMD) or spatial light modulators (SLM). Even if this was easily possible, the second issue is that atoms spend most of their time in presence of high-intensity laser beams, where the background scattering with photons could heat up the ultracold gas.

A much better solution is to create a box potential using the repulsive green laser beam. The idea behind it is the same as a cardboard box, where the walls keep the contents inside. The cardboard box can be mimicked for the atoms by replacing the 6 sizes of a cardboard box with 6 sheets of light; 4 traveling along one direction forming

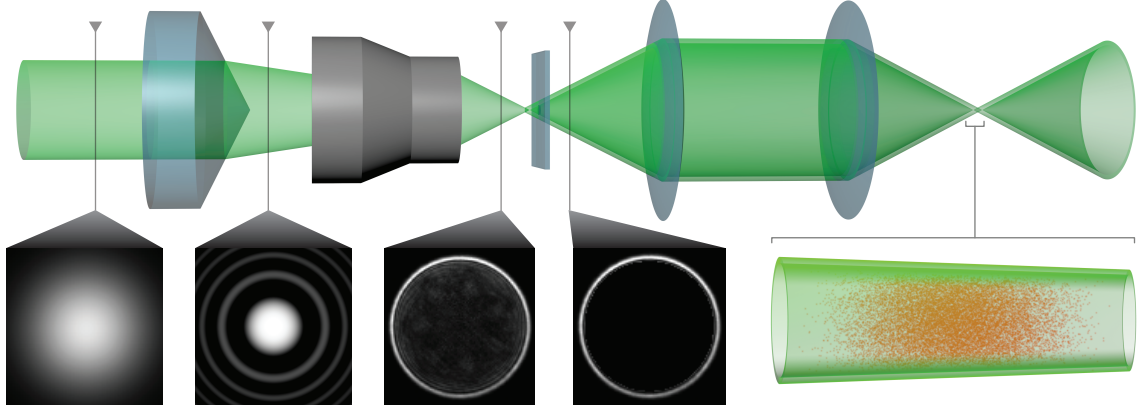


Figure 3-2: **Optical setup for cylinder-shaped trap.** From left to right: A Gaussian beam propagates through an axicon resulting in a Bessel beam in the near field. Subsequently the Bessel beam is focused through a microscope objective. In the focal plane, the resulting intensity pattern is a ring with Gaussian rim. A matched circular opaque mask is used to block out residual light in the center of the ring. Finally the mask is projected through an imaging system onto the atoms, creating the cylinder-shaped trap for the atoms. A small variation of cylinder radius is unavoidable when using a single axicon [62].

a square-shaped tube, and other 2 traveling in a perpendicular direction, serving as endcaps, i.e. closing the top and bottom of a box, see Fig. 3-1(a). Another, optically simpler, configuration is a cylindrical box shown in Fig. 3-1(b). It is composed of only three laser beams; a cylindrical tube trapping the atoms radially, and two sheets of light serving as endcaps. Note that atoms spend most of their time away from the high-power green laser beams and only interact with it for a short amount of time while reflecting off of the walls. This is ideal for two reasons; first it reduces the background scattering and the associated heating, and second any imperfections in the optical potential does not directly effect the homogeneity of the contained gas.

We have implemented the cylindrical box in the experiment because of its relative simplicity. All three beams are generated by passing Gaussian laser beams through off-the-shelf optical elements. A sheet of light is constructed by squeezing a Gaussian beam along one direction using a pair of elliptical lenses by about a factor of 8. A ring of light, while it may seem complicated at first, is constructed by passing a Gaussian beam through an ‘axicon’ [123, 120], an off-the-shelf optical element with a conical surface, which creates a Bessel intensity profile in the near-field and a ring-shaped

intensity profile in the far-field. In the experiment, this is achieved by stacking (1) a fiber out-coupler delivering a green Gaussian beam, (2) a pellicle beam-sampler for intensity stabilization, (3) an axicon, and (4) a microscope objective to convert the near-field Bessel- into far field ring-shaped intensity profile, into a single lens tube assembly, see Fig. 3-2.

Directly imaging these ring and elliptical beams onto the atoms would work, but produce a potential with relatively soft edges. It is better to shine these beams onto a mask first, a circular one for the ring beam and a rectangular one for the two endcaps, with roughly the same dimension, and image this mask onto the atoms. This way the edge sharpness of the potential at the atoms is only limited by the optical resolution of the imaging optics and independent of the width of the ring and elliptical beams. In principle, one could avoid the beam shaping completely and directly shine a Gaussian laser beam on these masks, however this method would waste too much power, for example the circular mask would eat away most of the light located at the center of a Gaussian beam, and create a box wall with uneven height, making the beam shaping a crucial first step.

The diameter of the ring is  $\approx 120 \mu\text{m}$  while the separation between two endcap beams is easily changeable. For the data presented in this thesis, we worked with a separation of  $\approx 100 \mu\text{m}$ . We will comment on our reasons behind picking these values in the next section.

It is crucial to detune the light frequency of any intersecting beams if the same coherent light source is used. This ensures that the final potential is void of any interference pattern and avoids Bragg diffraction which could significantly heat up the atoms. In our case, we make sure to use opposite orders of the 80 MHz AOM used for intensity stabilization of the ring and endcap beams.

### 3.1.2 Loading and alignment

Atoms are transferred from the optical dipole trap to box with the aid of an additional crossed dipole beam (using the same 1064 nm laser). In our setup, the ring beam is co-propagating with the optical dipole trap, and the endcap beams are co-propagating

with the cross dipole beam. To transfer the atoms, one simply needs to increase the intensity of both dipole beams until atoms squeeze into a region smaller than the size of the box, then turn the box potential on, and dipole beams off. However, we do not have enough power in the dipole beams to simultaneously squeeze the atoms along both radial and axial directions, so, instead, we transfer the atoms in several steps. First, the intensity of the dipole beam is increased until the radial size of the atoms is smaller than the diameter of the ring beam,  $\approx 120 \mu\text{m}$ . Second, the intensity of the ring beam is increased and the optical dipole beam is subsequently turned down and off. At this point, the atoms are radially held by the ring potential. Now similar two steps are performed with the crossed dipole beam and the endcap beams to completely transfer the atoms to the box. Note that all changes in the intensity are made adiabatically to avoid heating the gas.

One of the reason for picking a  $120 \mu\text{m}$  diameter and  $100 \mu\text{m}$  length is apparent here. It would be difficult to load atoms into a much smaller box, while a much larger box might dilute the atomic density. Suppose we could load the atoms into a smaller box and we desired higher atomic densities. Even then, it might be a bad idea to reduce the size of the box by too much, because the ratio of the effective volume occupied the the edges to the volume of the box itself increases significantly as the box size is reduced. This, in turn, makes a larger fraction of the gas inhomogeneous, defeating the purpose of making a uniform box potential. The experimental measurement of the fraction of atoms that experience a uniform density is shown in the next section.

Apart from aligning the optical dipole beams with the green beams, one needs to cancel the gravity. This can easily be done using a magnetic field gradient where the gravitation force  $mg$  is compensated by the magnetic force  $\mu_B g_i m_i B'$ , where  $B'$  is the gradient in the magnetic field,  $\mu_B$  is the Bohr magneton, and  $\mu_B g_i m_i$  is the magnetic moment of a particular atomic state. At low magnetic fields, it becomes difficult to exactly cancel the gravity for multiple atomic states simultaneously because they often have different magnetic moments. However, at  $\approx 690 \text{ G}$ , the Zeeman structure of  ${}^6\text{Li}$  atom is in the high-field regime, where magnetic moment for the three lowest states

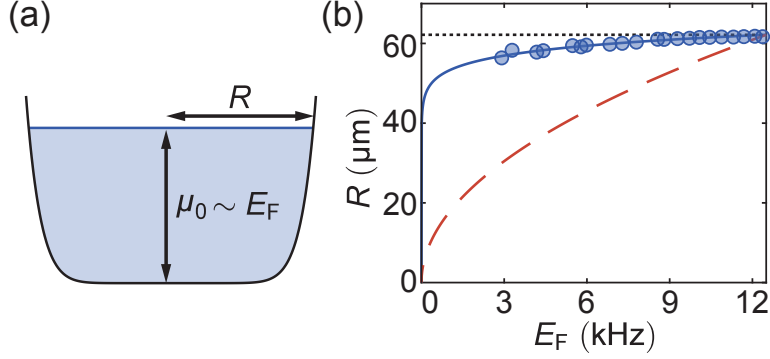


Figure 3-3: **Characterizing wall steepness.** (a) A cartoon depicting the dependence of the radius  $R$  of a cloud with its Fermi energy  $E_F$  in an imperfect box. The box potential is modeled as a high order polynomial  $V(r) \sim (r/r_0)^l$ . (b) Radius of the cloud as a function of the Fermi energy. The dotted black and dashed red lines correspond to a perfect box potential and a harmonic potential, respectively, and are scaled to converge at the highest  $E_F$ . The blue solid line corresponds to a power law potential  $V \sim r^{16}$ .

is approximately the same,  $g_i m_i \approx 1$  with deviations much smaller than a percent. In the experiment, we use the gradient present in a saddle potential produced by the magnetic fields. We align the atoms to its center until the effects of gravity visually disappear.

The saddle potential also produces a residual trapping along the axial direction of  $\approx 2\pi \cdot 23.4$  Hz, and an anti-trapping along the radial direction of  $\approx 2\pi \cdot 16.5$  Hz. The radial anti-trapping is canceled using by using the attractive optical dipole beam (very small intensities are required). We have left the axial trapping on since it only amount to a maximum of  $\frac{1}{2}m(2\pi \cdot 23.4 \text{ Hz})^2(50 \mu\text{m})^2 \approx 2\pi \cdot 400$  Hz at the edges of the box at  $\pm 50 \mu\text{m}$ , which is only  $\approx 4\%$  of the Fermi energy. In fact, a combination of this axial trapping and ring potential creates a hybrid trap, having two homogeneous and one harmonic axes, convenient to study thermodynamic properties.

### 3.1.3 Characterization

We measure two important quantities to characterize the homogeneity of the box, first measures the steepness of the wall and second measures the uniformity of the potential.

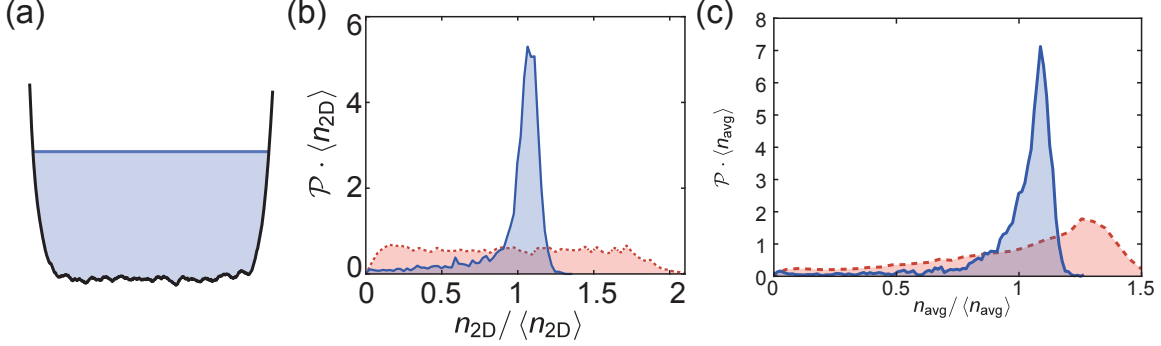


Figure 3-4: **Characterizing potential uniformity.** (a) A box potential with noise is shown, which could result in inhomogeneous density. Measurements presented in Fig. 3-3 are not sensitive to this noise, but, a probability distribution  $\mathcal{P}(n)$  that measures the fraction of atoms at a particular density  $n$  will show the inhomogeneity as a broad peak. (b) Measured radial probability density  $\mathcal{P}(n_{2D})$  for the column integrated density  $n_{2D}$ , averaging about 20 in-trap images. The blue solid and red dashed lines correspond to the uniform and Gaussian traps, respectively. Absorption images are taken along the symmetry axis (z-axis according to Fig. 3-1) of the box. (c) Similar data as in (b), but with absorption images taken along an orthogonal radial (x-axis) of the box. Here, the red solid lines correspond to the hybrid trap, where two axes are homogeneous while the third axis is harmonic.

**Wall steepness.** To measure the steepness of the walls of the box, we measure the effective radius of the cloud  $R$  as a function of its Fermi energy  $E_F$ . In a perfectly sharp box, the cloud radius  $R$  should be independent of  $E_F$  and any deviations must come from soft edges of the box. The measured  $R$  is shown in Fig. 3-3.

To quantify the edge sharpness, we model the trapping potential as  $V(r) \propto (r/r_0)^l$ , where  $r_0$  is the radius of the box. A perfectly sharp box corresponds to  $l \rightarrow \infty$  while a harmonic trap corresponds to  $l = 2$ . At zero temperature, the atoms are filled up to the chemical potential  $\mu_0$  implying  $\mu_0 = V(R) \propto (r/r_0)^l$  and  $R \propto \mu_0^{1/l} \propto E_F^{1/l}$ . A fit to the data suggests  $l = 16(2)$  for the radial direction and  $l = 15(3)$  for the axial direction.

**Uniformity of the potential.** The steepness of the walls doesn't tell us about the inhomogeneity present near the center of the box. Even though we are imaging perfectly dark masks onto the atoms, there is always some amount of light inside the box caused by imperfect optics, limited resolution of the imaging setup, or diffraction and back-reflections. To quantify these, we measure the fraction of atoms that expe-

rience a uniform density, shown in Fig. 3-4 as the probability  $P(n)$  to find an atom at a density  $n$ . In a perfectly homogeneous system, all 100% of the atoms are at the mean density  $n_0$ , seen as a delta function at  $n_0$ . Any small leakage light will make the potential inside the box non-zero, and slightly reduce the atomic density. This is seen as a broadened peak near the mean density. We estimate that about 80% of the atoms experience a density within 20% of  $n_0$ . In contrast, atoms in a harmonic trap feature a uniform  $P(n)$ , meaning that only 20% of the atoms experience a density within 20% of  $n_0$ . The long tails observed at lower densities come from the edges of the box.

## 3.2 Thermometry

In a typical ultracold experiment, temperature of the gas is measured by turning all trapping potentials off and letting the gas expand in free space. After some time-of-flight (tof)  $\tau$ , the position of the atoms reveal their initial velocity given by  $r(\tau) = r_0 + v\tau$ . If the  $\tau$  is large enough such that  $v\tau$  is much larger than the initial size of the cloud, then the velocity distribution can be calculated by  $v \approx r/\tau$ . However, this requires a ballistic expansion of the atoms which is not possible in strongly interacting systems like the unitary Fermi gas. Here, instead of a ballistic expansion, the atoms go through hydrodynamic expansion [124], and display features, like the inversion of aspect ratio, that are far from a free expansion.

The usual solution for this problem is to place the strongly interacting gas in a harmonic trap, for example the optical dipole trap, and extract the temperature from the density distribution  $n(z)$  or  $n(U)$  where, for a harmonic trap,  $U \propto r^2$ . If the equation of state of the system is known, then one can directly fit the  $n(U)$  and extract a temperature. Even if the equation of state is not known, it is possible to get the global temperature from the tails of  $n(z)$ . Sufficiently far into the tails, in the region where the local chemical potential is larger than its global value, the density should be well approximated by the non-interacting equation of state, namely the Boltzmann distribution, where  $n(U) \propto e^{-U/(k_B T)}$ . However, this method doesn't

work in our case either. In a box, all atoms are at the same density, and there are no tails.

We've found several methods to determine the temperature of a strongly-interacting uniform gas described below. First, the shot noise in the atom numbers is related to the temperature of the gas [68]. One can calculate the atom shot noise from a single image by assuming a homogeneous gas, or from repeated images of identically prepared clouds. While feasible, we did not explore this route in details.

**Adiabatic transfer from the box to a harmonic trap.** One thing was clear from the beginning: the inhomogeneous density of a harmonic trap is ideal for thermometry. We adiabatically transferred atoms from the box to the optical dipole trap. This was accomplished with the aid of two attractive, crossed dipole beams, which would allow us to squeeze the atoms into a region smaller than the size of the box. Once in a harmonic trap, we can easily measure the temperature and the Fermi energy of the harmonically trapped gas, convert it to entropy using the equation of state, and, finally, estimate the temperature in the box by assuming the same entropy and an independently measured Fermi energy in the box. To our surprise, this method worked. We moved the cloud back-and-forth between the box and harmonic trap up to five times, and found the entropy to remain unchanged after subtracting the increase in entropy due to typical background heating. However, it requires precise alignment of the crossed dipole beams with the center of the box. Furthermore, we lacked the laser power for the crossed dipole beam to completely squeeze the atoms when working with typical Fermi energies of  $\approx h \cdot 10$  kHz.

**Isoenergetic expansion from the box to a harmonic trap.** An alternate solution is to forgo adiabatic transfer in favor of an isoenergetic one. Since the walls of the box potential are sharp, there is minimal potential energy stored in the gas. Therefore, suddenly releasing the atoms from the box into a hybrid trap does not change the total energy of the system. Here the hybrid trap refers to the combination of green ring light providing the radial confinement and a magnetic harmonic trap providing the axial confinement. Going from the box to the hybrid trap only requires turning the two endcap beams off. Once in the hybrid trap, we can easily measure

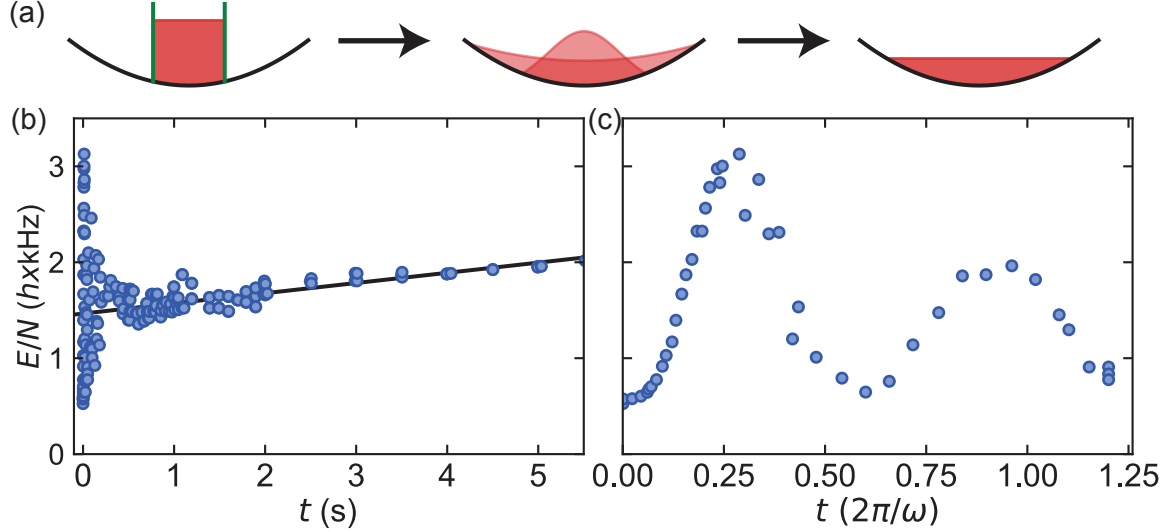


**Figure 3-5: Isoenergetic expansion for box thermometry.** (a) Atoms are released from the box trap into a harmonic trap by suddenly removing the endcaps. Atoms move around in the harmonic trap, eventually reaching a thermal equilibrium. After some evolution time, the energy of the gas is measured  $E/N = 2m\omega^2 \langle z^2 \rangle$  from the second moment  $\langle z^2 \rangle$  of the density  $n(z)$ , where  $\omega \approx 2\pi \cdot 23$  Hz is the frequency of the harmonic trap. The complete time evolution is shown in (a), while the first period is shown in (b). The background heating rate in the harmonic trap is calculated by fitting the data after 1.5 seconds, shown in black line, which yields a heating rate of  $\approx h \cdot 0.1$  kHz/s.

the total energy of the gas using equipartition theorem described below. Assuming an isoenergetic expansion, we can calculate the temperature in the box using the equation of state and an independent measurement of the Fermi energy in the box. This is ideal compared to the adiabatic transfer, because it is independent of any alignments, and only relies on the walls of the box being sharp. This is the primary method we have used to measure the temperature of the gas for the data presented in this thesis. A sample of the complete time evolution is shown in Fig. 3-5. We releasing the atoms in to the hybrid trap, we wait  $\approx 1.5$  seconds before measuring the energy, which is found to sufficient to reach thermal equilibrium, see Fig. 3-5(b). From the measured  $E/N$ , we subtract  $\approx h \cdot 0.1$  kHz/s  $\times 1.5$  s to account for the background heating, which is calibrated from data shown in Fig. 3-5(b). In principle, the pressure of the Fermi gas can be calculated from the early time expansion shown in Fig. 3-5(c), however we did not investigate this in details.

The walls of the box are of course not perfectly sharp. There is a small amount of potential energy that gets lost when suddenly removing the walls of the box. We experimentally investigate the effects of this by first removing only one of the endcaps. Here, one half of the cloud is in a harmonic trap while the other half is still in the box. We measure the energy from the harmonic side, and then remove the second endcap to let the atoms expand into the hybrid trap. Here, we re-measure the total energy and compare it to the first measurement. If the potential energy stored in the endcaps were significant, then the energy of the fully expanded gas would be lower than partially expanded gas. In contrast, we find the two energies to agree with each other, within the shot-after-shot fluctuations, leading us to conclude that internal energy, the sum of kinetic and interaction energy, far outweighs the small amount of potential energy.

### Total energy in the hybrid trap.

The total energy  $E$  of a gas trapped in an external potential  $U(\mathbf{r})$  is the sum of its internal energy density  $\epsilon(\mathbf{r})$  and potential energy,

$$E = \int d^3\mathbf{r} [\epsilon(\mathbf{r}) + n(\mathbf{r})U(\mathbf{r})], \quad (3.1)$$

where  $n(\mathbf{r})$  is the number density. First, in a hybrid trap with  $x$  and  $y$  directions homogeneous, and a cross-sectional area  $A$ , the integral simplifies to

$$E = A \int dz [\epsilon(z) + n(z)U(z)]. \quad (3.2)$$

While we can measure the atomic density and calibrate the trapping potential, it is typically not possible to measure the internal energy. However, for the scale invariant unitary Fermi gas,  $\epsilon = \frac{3}{2}P$ . Furthermore, the condition of mechanical equilibrium requires  $\nabla P = -n\nabla U$ , which, for a harmonic trap  $U(z) \propto z^2$ , implies  $\frac{dP}{dz} = -n\frac{dU}{dz} =$

$-2n\frac{U(z)}{z}$ . Let's first calculate the total internal energy  $E_{\text{int}}$

$$\begin{aligned} E_{\text{int}} &= A \int dz \epsilon(z) = \frac{3A}{2} \int dz P(z), \\ &= 3A \int dz n(z)U(z), \end{aligned} \quad (3.3)$$

where we have used integration by parts in the last step. The total energy is then

$$\begin{aligned} E &= A \int dz [\epsilon(z) + n(z)U(z)] = A \int dz [3n(z)U(z) + n(z)U(z)], \\ &= 4A \int dz n(z)U(z) = 4N \langle U \rangle, \end{aligned} \quad (3.4)$$

where we have used the definition for mean potential energy

$$\langle U \rangle = \frac{\int d^3\mathbf{r} n(\mathbf{r})U(\mathbf{r})}{\int d^3\mathbf{r} n(\mathbf{r})} = \frac{A \int dz n(z)U(z)}{N}. \quad (3.5)$$

Surprisingly, we find that the total energy of the unitary gas in a hybrid trap is simply 4 times its potential energy. This is similar to the equipartition theorem, which states that the energy is equally distributed among all degrees of freedom that appear quadratically in the Hamiltonian. Assuming a potential  $U(z) = \frac{1}{2}m\omega^2 z^2$ , we can rewrite eq. 3.4 using the second moment of the density

$$\langle z^2 \rangle = \frac{\int d^3\mathbf{r} n(\mathbf{r})z^2}{\int d^3\mathbf{r} n(\mathbf{r})} = \frac{A \int dz n(z)z^2}{N}, \quad (3.6)$$

$$E/N = 4 \langle U \rangle = 2m\omega^2 \langle z^2 \rangle. \quad (3.7)$$

With the measurements of the atomic density and a calibration of the trapping potential, the total energy is simply proportional to the second moment of the density.

### 3.3 Imaging ${}^6\text{Li}$

Imaging is the primary way we collect information about the state of the atoms. Typically, these images only reveal the atomic density; however, by clever preparations,

like time-of-flight and radio frequency spectroscopy, we can measure anything from the momentum distribution and condensate fraction to sound waves.

In this section, we start by reviewing the atomic structure of  ${}^6\text{Li}$ , particularly at high magnetic field, followed by reviewing the properties of near resonant light-atom interaction that make both absorption and phase contrast imaging possible. Imaging lighter atoms, such as  ${}^6\text{Li}$ , posses additional challenges because they can get Doppler shifted by more than a linewidth during absorption imaging. We discuss these subtleties and their solutions for absorption imaging of  ${}^6\text{Li}$ . While absorption imaging is broadly used, it has limitations when imaging very dense clouds ( $od \gg 1$ ). To overcome this we have implemented phase contrast imaging, where the phase shift, rather than the absorption caused by atom-light interactions, is measured. With this technique, it is possible to maximize the measurement sensitivity at a desired density or directly measure the spin imbalance.

### 3.3.1 Atomic structure of ${}^6\text{Li}$ at high magnetic fields

We want to review the atomic structure of  ${}^6\text{Li}$  relevant for atom cooling, trapping, and imaging.

**General structure.** For  ${}^6\text{Li}$  atoms, the outer shell electron with spin  $S = 1/2$ , nucleus with total nuclear spin  $I = 1$ , and their bound state with principal quantum number  $n$  and orbital angular momentum  $L$  determine the good quantum numbers and the state of the atom. So, 7 quantum numbers are needed to completely define the state of the atoms, including  $n, S, I, L$ , and projection of three angular momenta,  $m_S, m_I$ , and  $m_L$ . For simplicity, we will omit  $n = 2, S = 1/2$ , and  $I = 1$  when writing atomic states, since their value is fixed at ultracold temperatures. A general state of the atom can then be defined by specifying  $|L, m_L, m_S, m_I\rangle$ . However, the spin-orbit interactions couple  $L \cdot S$  to form  $J = L + S$  (fine structure), and electron-nucleus interactions couple  $J \cdot I$  to form the total angular momentum of the atom  $F = J + I$  (hyperfine structure). In absence of any external fields, the energy eigenstates of the atoms are therefore defined by  $|L, J, F, m_F\rangle$ , where we have replaced  $m_L, m_S, m_I$  in favor of their sum  $J, F, m_F$ .

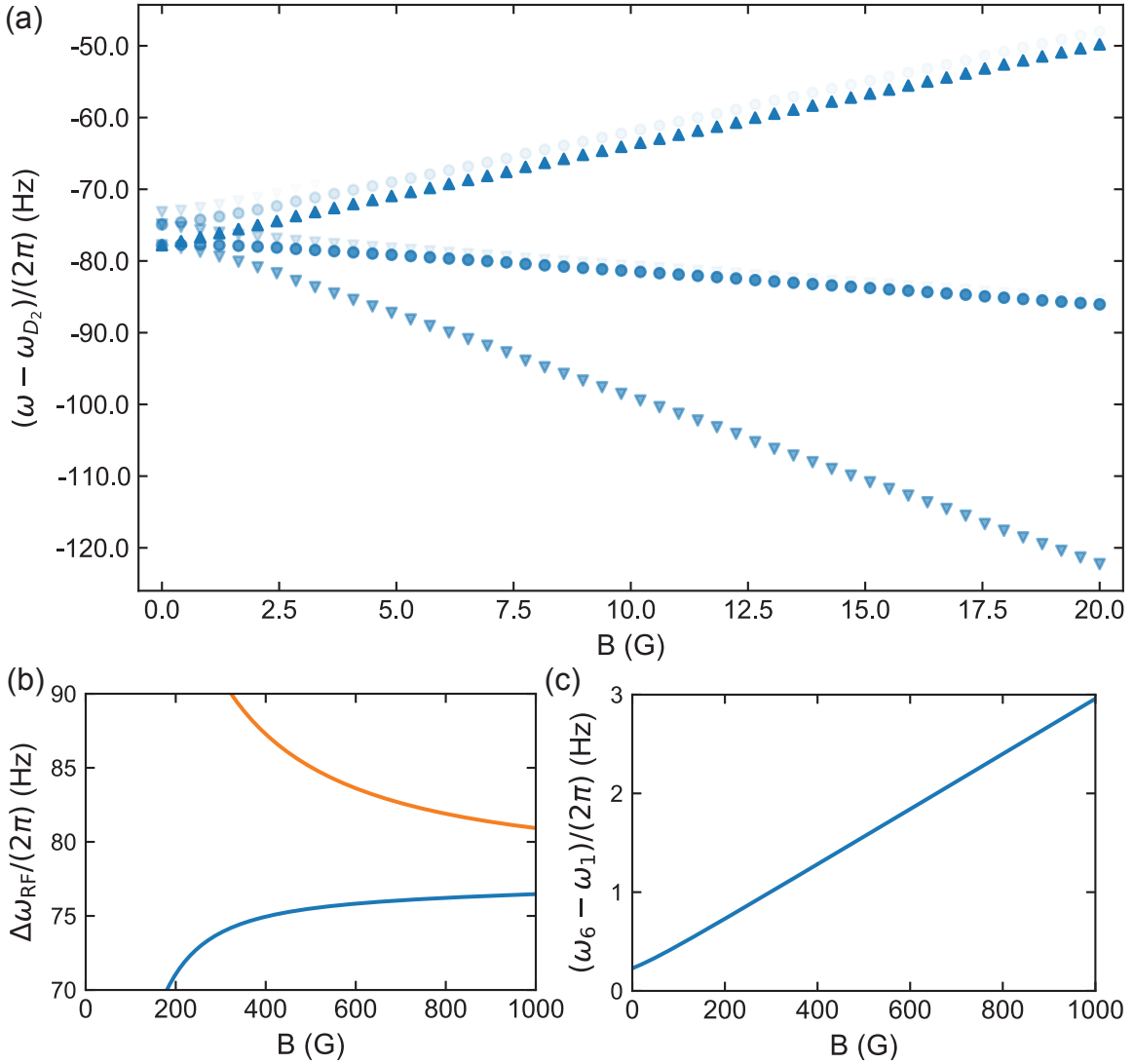


**Figure 3-6: Useful transitions in  ${}^6\text{Li}$ .** (a) Transitions for optical pumping. All transition connecting  $|6\rangle$  and any excited state in the  $D_2$ -manifold are shown. The shapes (up arrow, circle, down arrow) refers to the polarization of light required ( $\sigma^+$ ,  $\pi$ ,  $\sigma^-$ ). The brightness of the point indicate the coupling strength for that transition. Add  $2\pi \cdot 305.66$  Hz, the detuning between the  $D_2$  line and main laser lock in *Fermi 3* lab, from these values to find the detuning specifically for the lab. (b) Frequency required for the RF-transitions, blue line for  $|1\rangle \rightarrow |2\rangle$  and orange line for  $|2\rangle \rightarrow |3\rangle$ , are shown. (c) Frequency required for the MW-transition  $|6\rangle \rightarrow |1\rangle$  is shown.

**Zeeman structure.** External magnetic field, for example  $\mathbf{B} = B\hat{\mathbf{z}}$ , couple to the magnetic moment  $\boldsymbol{\mu}$  of the atom and induce a magnetic dipole moment with energy

$$H_B = -\boldsymbol{\mu} \cdot \mathbf{B} = \left( \mu_B \frac{g_L \mathbf{L} + g_S \mathbf{S} + g_I \mathbf{I}}{\hbar} \right) \cdot \mathbf{B}, \quad (3.8)$$

where  $\mu_B = e\hbar/(2m_e)$  is the Bohr magneton (in SI units),  $e$  is the elementary charge,  $m_e$  is electron mass, and  $g$ 's are  $g$ -factors corresponding to different angular momenta. Notice that  $H_B$  is easily diagonalized in  $|L, m_L, m_S, m_I\rangle$  basis while the energy eigenstates of the atoms are defined using the total angular momentum in  $|L, J, F, m_F\rangle$  basis. When the strength of the magnetic field is lower than that of the hyperfine structure,  $H_B$  can be treated perturbatively to find the Zeeman energy shift  $E_Z = \mu_B g_F m_F B$  of energy eigenstates, where  $g_F$  comes from the sum  $g_L \mathbf{L} + g_S \mathbf{S} + g_I \mathbf{I}$  [55]. However, as the strength of the magnetic field increases beyond hyperfine splitting,  $F$  stops being a good quantum number in favor of  $|L, J, m_J, m_I\rangle$  basis, where the energy shifts are  $\approx \mu_B g_J m_J B$ . At even stronger magnetic field, beyond fine structure splitting,  $J$  stops being a good quantum number in favor of  $|L, m_L, m_S, m_I\rangle$  basis, where the energy shifts are  $\approx \mu_B (g_L m_L + g_S m_S) B$ .

Exact determination of energies require diagonalizing the full Hamiltonian, including fine- and hyperfine structure terms, and the Zeeman term  $H_B$ . Some of the useful transitions for optical pumping and state preparation are shown in Fig. 3-6.

### 3.3.2 Near resonant light-atoms interactions

As light travels through a piece of semi-transparent glass, two things happen: the phase velocity of light gets reduced and a fraction of light gets scattered or absorbed. The same thing happens when near-resonant light travels through a gas of atoms. Both of these effects are quantified by the real and imaginary parts of the index of refraction<sup>1</sup>,  $\mathcal{N} = 1 + \mathcal{N}' + i\mathcal{N}''$ . Inside the cloud, the electric field of the light evolves

---

<sup>1</sup>To avoid confusion with the atomic number density  $n$ , we are using the symbol  $\mathcal{N}$  for index of refraction.

with a modified wavevector  $k = \omega/v = \mathcal{N}\omega/c$  as

$$E(z) = E_0 e^{ikz} = E_0 e^{i(\omega/c)z} e^{i\mathcal{N}'(\omega/c)z} e^{-\mathcal{N}''(\omega/c)z}. \quad (3.9)$$

Here,  $e^{i\mathcal{N}'(\omega/c)z}$  accounts for the additional phase shift resulting from the modified velocity and  $e^{-\mathcal{N}''(\omega/c)z}$  accounts for the reduction in electric field amplitude resulting from absorption or scattering. These two effects serve as the basis for phase contrast and absorption imaging described in sections below. However, for them to be useful for imaging, we first need to explicitly show their density dependence.

In general, for any linear dielectric material, the index of refraction is

$$\mathcal{N} = c/v = \frac{\sqrt{1/\epsilon_0\mu_0}}{\sqrt{1/\epsilon\mu}} \approx \sqrt{\epsilon/\epsilon_0} = \sqrt{1 + \chi_e} = \sqrt{1 + n\alpha} \approx 1 + \frac{n\alpha}{2}, \quad (3.10)$$

$$\mathcal{N}' \approx \frac{n\text{Re}[\alpha]}{2}, \quad \mathcal{N}'' \approx \frac{n\text{Im}[\alpha]}{2}, \quad (3.11)$$

where  $v$  ( $c$ ) is speed of light in the dielectric material (in free space),  $\epsilon$  ( $\epsilon_0$ ) is electric permittivity (in free space),  $\mu$  ( $\mu_0$ ) is magnetic permeability (in free space),  $\chi_e$  is electric susceptibility,  $n$  is atomic number density, and  $\alpha$  is the polarizability. Here, we are assuming that the material is non-magnetic,  $\mu/\mu_0 \approx 1$ , and atomic density is small enough<sup>2</sup> such that  $n\alpha \ll 1$ .

Incident electric field of the laser induces a dipole moment,  $\mathbf{d} = \alpha\mathbf{E}$ , with a proportionality constant  $\alpha$ , the electric polarizability. The exact solution for  $\alpha$  involves solving a Hamiltonian for the atom + quantum radiation + laser field system. Quantum radiation includes all modes of electromagnetic waves and is responsible for the decay of the excited state. The laser field is treated classically since it contains macroscopic number of photons in a single mode. The solution to this Hamiltonian is known as the optical Bloch equations, see [42] pgs. 604-606 or chapter V for derivation. For a dilute ensemble of two level atoms, polarizability is

$$\alpha = \frac{2c}{\omega}\sigma \left( -\frac{\delta}{\Gamma} + i\frac{1}{2} \right), \quad (3.12)$$

---

<sup>2</sup>This condition may be violated for clouds with very high density.

with absorption cross-section

$$\sigma = \frac{\sigma_0}{1 + (2\delta/\Gamma)^2 + I/I_{\text{sat}}}, \quad (3.13)$$

where  $\omega$  is laser frequency,  $\omega_0$  is atomic resonance frequency,  $\delta = \omega_0 - \omega$  is laser detuning,  $\Gamma$  is atomic linewidth,  $I_{\text{sat}} = (\hbar\omega_0^3\Gamma)/(12\pi c^2)$  is saturation intensity,  $\sigma_0 = 6\pi c^2/\omega_0^2$  is the maximum absorption cross-section. Another useful quantity is the photon scattering rate

$$\gamma = \frac{\Gamma}{2} \frac{I/I_{\text{sat}}}{1 + (2\delta/\Gamma)^2 + I/I_{\text{sat}}}. \quad (3.14)$$

The electric field then evolves as

$$E(z) = E_0 e^{i(\omega/c)z} e^{-in\sigma(\delta/\Gamma)z} e^{-n\sigma z/2}. \quad (3.15)$$

After travelling through a uniform ensemble of atoms of length  $L$ , the laser light acquires an additional phase shift of  $-n\sigma L\delta/\Gamma$  and its amplitude reduces to  $E_0 e^{-n\sigma L/2}$  (or intensity to  $I_0 e^{-n\sigma L} \sim |E|^2$ ). In a general, non-uniform sample, it is possible for  $n$ ,  $\sigma$ , and  $\delta$  to be a function of  $z$ . In this case, column integrated values are used, where the additional phase shift  $\Delta\phi$  and final intensity  $I_f$  are found by solving

$$\Delta\phi = - \int dz n\sigma\delta/\Gamma \quad (3.16a)$$

$$I_f = I_0 e^{-\int dz n\sigma} \quad \text{or} \quad \frac{dI}{I} = -n\sigma dz. \quad (3.16b)$$

These two effects are now explicitly density dependent and serve as the basis for phase contrast and absorption imaging.

### 3.3.3 Absorption imaging with Doppler correction

Absorption imaging works by measuring the fraction of light scattered by an atomic cloud and converting it into atomic density using eqs. 3.16. We shine resonant ( $\delta = 0$ ) light,  $I_0(x, y)$ , at an atomic cloud with number density  $n(x, y, z)$  and image the transmitted light,  $I_f(x, y)$ , on a camera. Light scattered by the atoms appear as

missing light (or a shadow) on the camera and is proportional to the density of atoms. Below, we will look at solutions to eq. 3.16b in different regimes.

**Low intensity imaging: Beer-Lambert law.** In this simple scenario, we assume  $I \ll I_{\text{sat}}$  and  $\delta = 0$ , resulting in  $\sigma \approx \sigma_0$ . With this, the exponential in eq. 3.16b simplifies to  $-\sigma_0 \int dz n$ , and we can easily solve for the column density

$$n_{2d}(x, y) = \int dz n(x, y, z) = -\frac{1}{\sigma_0} \ln \frac{I_f}{I_0}. \quad (3.17)$$

Since only the ratio of intensities appear, we don't need to calibrate the counts on the camera ( $N_f$  and  $N_0$ ) to absolute intensity, and  $I_A/I_0 = N_A/N_0$ . The usefulness of this method lies in the optical density  $od_0(x, y) \equiv n_{2d}\sigma_0 = -\ln N_A/N_0$ , which requires no additional inputs or calibrations to interpret absorption images.

While this regime is simple and widely useful, corrections to it are necessary when higher imaging intensities ( $I \gtrsim I_{\text{sat}}$ ) or optical densities ( $od_0 \gg 1$ ) are necessary.

**High intensity imaging: saturated Beer-Lambert law.** Often, it is necessary to use higher imaging intensities to improve the signal to noise ratio of the camera. If  $I_0 \gtrsim I_{\text{sat}}$ , the absorption cross-section  $\sigma(I, \delta=0) = \sigma_0/(1+I/I_{\text{sat}})$  reduces significantly due to saturation of the excited state population. We can still solve the differential form of eq. 3.16b exactly by utilizing separation of variables.

For simplicity, let's first convert all intensities into a unitless form  $s \equiv I/I_{\text{sat}}$ ,  $s_0 \equiv I_0/I_{\text{sat}}$  and  $s_f \equiv I_f/I_{\text{sat}}$ , then solve the differential equation using separation of variables.

$$\begin{aligned} \frac{ds}{s} &= -n\sigma_0 \frac{1}{1+s} dz, \\ \int_{s_0}^{s_f} ds \frac{1+s}{s} &= - \int_0^L dz n\sigma_0, \\ \ln \frac{s_f}{s_0} + (s_f - s_0) &= -n_{2d}\sigma_0, \\ n_{2d} &= -\frac{1}{\sigma_0} \left( \ln \frac{I_f}{I_0} + \frac{I_f - I_0}{I_{\text{sat}}} \right). \end{aligned} \quad (3.18)$$

While eq. 3.18 is not much more complicated than the Beer-Lambert law, there is one

important distinction: using it requires absolute calibration of the imaging intensity. This can be done in two ways. First, we can directly convert the electron counts reported by the camera to an intensity if camera's gain and efficiency are calibrated, losses along the imaging path are known, and magnification of the imaging system is calibrated. Alternatively, we can directly measure the saturation count  $N_{sat} \propto I_{sat}$  by scanning the imaging intensity and measuring the observed *od* on identically prepared clouds.

**Including the Doppler shift crucial for lighter atoms.** Let's first see how much of a problem Doppler shift would pose under typical imaging conditions. Each scattered photon with momentum  $\hbar k_L$  increases the atom's momentum by the same amount and velocity by  $v = \hbar k_L/m$ ; which, in turn, Doppler shifts the imaging light by  $\delta_D = k_L v = \hbar k_L^2/m$ . For  ${}^6\text{Li}$ , the Doppler shift per photon is  $\delta_D \approx 2\pi 0.15\text{MHz} \approx \frac{1}{40}\Gamma$ , where  $\Gamma \approx 2\pi 6\text{MHz}$  is the natural linewidth of the excited state. At  $I \approx 1I_{sat}$ , a resonant atom would absorb photons at a rate  $\frac{\Gamma}{2} \frac{I/I_{sat}}{1+I/I_{sat}} = \frac{\Gamma}{4} \approx 9 \text{ photons}/\mu\text{s}$ . During a typical  $10 \mu\text{s}$  imaging pulse, this would amount to 90 scattered photons or  $\approx 2.3\Gamma$  of Doppler shift! Under these conditions, it is absolutely necessary to account for the Doppler shift. For the same imaging conditions,  ${}^{23}\text{Na}$ , the next heavier alkali, would be detuned by approximately  $m_{{}^6\text{Li}}/m_{{}^{23}\text{Na}} \approx 0.26$  times less, i.e.,  $\approx 0.6\Gamma$ .

A typical solution to this problem is to change the imaging frequency during the imaging pulse such that atoms are perfectly on resonance with the light. However, such a scheme only works for either 2D gases or when atomic densities are low ( $od_0 \ll 1$ ). In a dense 3D gas, atoms closer to the beam absorb a larger fraction of the light compared to atoms away from the beam. This causes the Doppler shift to vary across the cloud, hence, changing the imaging frequency doesn't completely solve the problem.

Instead, we include this Doppler shift in eq. 3.16b and exactly solve the resulting coupled differential equations shown below. Atoms absorb or scatter photons at a rate  $\gamma$  and experience an average force  $F = m dv/dt = \gamma \times \hbar k_L$ . This results in an increase in velocity  $v$ , which in turn increases the detuning to  $\delta = kv$ . The two

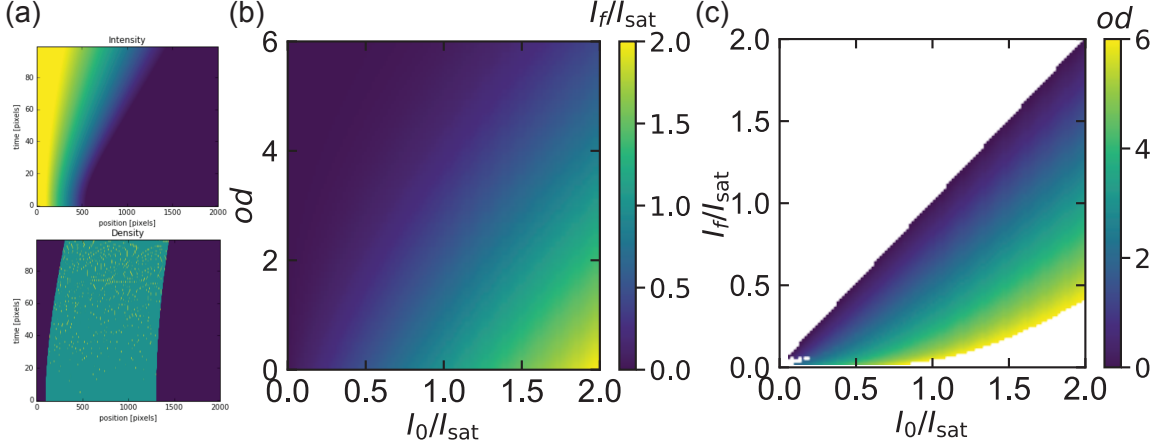


**Figure 3-7: Doppler correction for absorption imaging.** We solve the coupled differential equation 3.20 for varying combinations of initial intensity  $s_0 = I_0/I_{\text{sat}}$  and  $od$  to find  $s_f - I_f/I_{\text{sat}}$ . (a) Typical solution for the reduced intensity  $s(z, t)$  and atomic density  $n(z, t)$  are shown for 10  $\mu\text{s}$  of imaging time. Towards the end, atoms are Doppler shifted by more than a linewidth, resulting in a larger transmission. (b) The results of many solutions are summarized as  $s_f(s_0, od)$ . (c) From these results, we form a lookup table,  $od(s_0, s_f)$  shown here, to easily calculate the optical density from the measured initial and final imaging intensities.

coupled differential equations for reduced intensity  $s \equiv I/I_{\text{sat}}$  and velocity  $v$  are

$$\frac{ds}{s} = -n \frac{\sigma_0}{1 + (2kv/\Gamma)^2 + s} dz, \quad (3.19a)$$

$$\frac{\partial v}{\partial t} = \frac{\Gamma \hbar k_L}{2m} \frac{s}{1 + (2kv/\Gamma)^2 + s}. \quad (3.19b)$$

It is convenient to rewrite these equations using the reduced velocity  $u \equiv 2kv/\Gamma$  and Doppler shift per photon  $\delta_D \equiv \hbar k_L^2/m$ ,

$$\frac{\partial s}{\partial z} = -n\sigma_0 \frac{s}{1 + s + u^2}, \quad (3.20a)$$

$$\frac{\partial u}{\partial t} = \delta_D \frac{s}{1 + s + u^2}. \quad (3.20b)$$

Unfortunately, it is not possible to solve these equations analytically; however, we numerically solve them for different initial imaging intensities  $I_0$  and optical densities  $od \equiv n\sigma_0$  to generate a ‘lookup table’ shown in Fig. 3-7(b). Using it, we create a function which translates the measured intensities  $I_0$  and  $I_f$  to optical density  $n\sigma_0$ ,

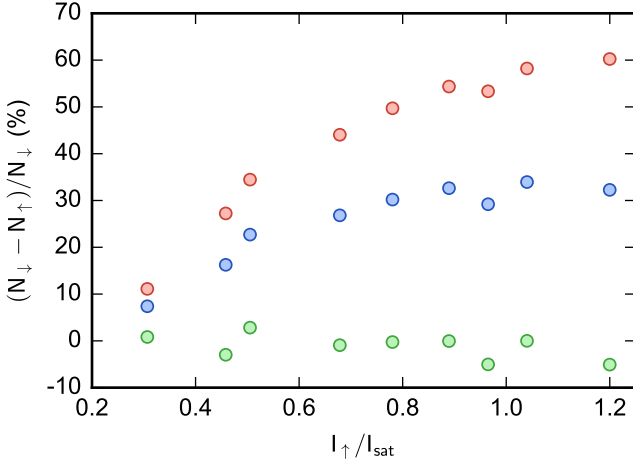


Figure 3-8: **Verification of the lookup table.** Apparent atom count for the spin up component ( $N_{\uparrow}$ ) measured at different imaging intensities ( $I_{\uparrow}$ ). A reference atom count ( $N_{\downarrow}$ ) is obtained by subsequently imaging a second spin component at a fixed imaging intensity ( $I_{\downarrow} = 0.23 I_{\text{sat}}$ ). Red circles, blue circles, and green circles are obtained using Beer-Lambert, saturated Beer-Lambert, and Doppler Beer-Lambert, respectively. Spin balanced clouds are used for these measurements.

shown in Fig. 3-7(c). Fig. 3-8 compares observed density using these three methods. It is absolutely necessary to include these corrections if quantitative atom numbers are needed.

**Issues at higher densities, re-absorption of scattered photons.** We often found discrepancies between the expected atom numbers (for example from the equation of state) and the measured atom numbers, even after including the effects of high intensity and Doppler shift. Furthermore, the discrepancies seemed to be larger for high density clouds. To quantify this effect, we make two measurements of the atom numbers of an identically prepared clouds, first in-situ and second after a 5 ms time-of-flight (tof). The atomic density in the tof images is at least a factor of 5 lower than in-situ, where we expect the high intensity and Doppler shift corrected ‘lookup table’ to work. Fig. 3-9 shows these two measurements for a range of different atomic densities up to  $\approx 1.2 \mu\text{m}^{-3}$ . It is clear from this data that the ‘lookup table’ only works well for densities  $\lesssim 0.2 \mu\text{m}^{-3}$ . At a density of  $\approx 1.0 \mu\text{m}^{-3}$ , insitu measurements are about 66% lower than ones from tof, meaning that the insitu densities need to be multiplied by a factor of  $\approx 1.5$  to get the true atomic densities. The density depen-

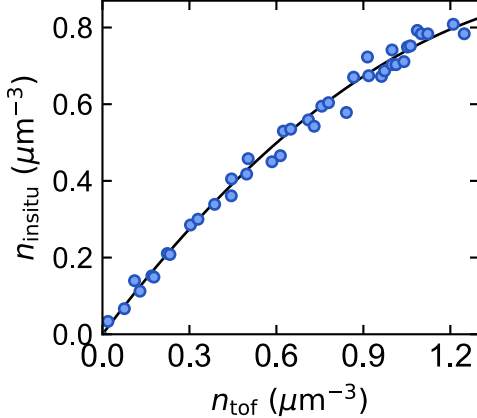


Figure 3-9: **High density imaging.** Atom numbers in the box are measured in two different ways, first in-situ (y-axis) and second, after a 5 ms time-of-flight (x-axis). These numbers are calculated using the lookup table, and converted into a density using the volume of the box. A non-linear dependence is observed, suggesting presence of effects that are not accounted by the lookup table. We fit the data with a polynomial of order 2 (black line).

dence of this multiplicative factor makes the situation even worse for measurements that require a change in density, for example  $\frac{dn}{dz}$ . An insitu measurement of  $\frac{dn}{dz}$  would need to be multiplied by a factor of  $\approx 2.5$  in order to get the true slope of the density.

Our best guess for the cause of this effect is the so far ignored re-absorption of an already scattered photon. We expect re-absorption to be more significant at higher densities, consistent with our measurements. Including these effects through equations similar to 3.19 or even simulating this system is a difficult task because the scattered light propagates in all directions. Instead, we fit the data shown in Fig. ?? with a polynomial  $n_{\text{insitu}} = 1.0 n + a_2 n^2$ , where  $n_{\text{insitu}}$  is the density observed insitu and  $n = n_{\text{tof}}$  is the true density as measured after a 5 ms tof, yielding  $a_2 = -0.29(2)$ . We convert insitu densities to true densities using this equation whenever necessary.

For measurements that require the most accurate atom numbers, phase contrast imaging described in the next section is ideal.

### 3.3.4 Phase contrast imaging

Phase contrast imaging (or polarization rotation imaging) works by measuring the atom induced phase shift of the transmitted light and converting it into atomic density

using eqs. 3.16. Here, we utilize off-resonant  $\delta \gtrsim \Gamma$  imaging light to enhance the atom induced phase shift  $\propto \delta/\Gamma$  and to minimize absorption.

Since CCD cameras only measure the intensity of light, we first need to convert the phase information into intensity. Simplest approach would be to construct an interferometer by splitting the imaging light in two, one goes around and other goes through the atoms, and merging them before the camera. Any phase shift induced by the atoms will be mapped onto the intensity because of interference.

Instead of two separate beams, we form the two arms of the interferometer with two orthogonal polarizations of a single imaging beam, ensuring that only one of which is in resonance with the atomic transition. Note that this is not always possible to do. Often, the second polarization still connects to another atomic transition, making this approach challenging. For  ${}^6\text{Li}$  at high magnetic fields, and imaging perpendicular to the quantization axis, it is possible. Here, only one of the polarization gets a phase shift, while the other serves as a reference. Interference between the two polarizations can be performed using a circular polarizer as shown below.

*Jones calculus* provides a convenient way to manipulate polarization of any laser field where polarization is a length 2 column vector and operators like waveplates and polarizers are  $2 \times 2$  matrices. Suppose that the laser is traveling along  $z$ -direction; linear polarizations along  $x$  and  $y$  are  $|H\rangle = \begin{pmatrix} 1 \\ 0 \end{pmatrix}$  and  $|V\rangle = \begin{pmatrix} 0 \\ 1 \end{pmatrix}$ , respectively, diagonal ( $+45^\circ$ ) and anti-diagonal ( $-45^\circ$ ) polarization from  $x$ -axis are  $|D\rangle = \frac{1}{\sqrt{2}} \begin{pmatrix} 1 \\ 1 \end{pmatrix}$  and  $|A\rangle = \frac{1}{\sqrt{2}} \begin{pmatrix} 1 \\ -1 \end{pmatrix}$ , and finally, right- and left-circular polarizations are  $|R\rangle = \frac{1}{\sqrt{2}} \begin{pmatrix} 1 \\ i \end{pmatrix}$  and  $|L\rangle = \frac{1}{\sqrt{2}} \begin{pmatrix} 1 \\ -i \end{pmatrix}$ .

We use an imaging beam with a diagonal polarization  $|D\rangle$ , where the atoms only interact with the  $|H\rangle$  component while  $|V\rangle$  serves as a reference. The atoms can impart a phase shift and reduce the light amplitude quantified by eqs. 3.16a and b. It is convenient to define the intensity and detuning dependent optical depth,

$$od \equiv \int dz n\sigma = \int dz \frac{n\sigma_0}{1 + (2\delta/\Gamma)^2 + I/I_{\text{sat}}} \approx \frac{od_0}{1 + (2\delta/\Gamma)^2 + I/I_{\text{sat}}}. \quad (3.21)$$

Here, the last step is only possible for  $\delta/\Gamma \gtrsim 1$ , where absorption of photons is

suppressed and  $\delta$ ,  $I$  can safely be assumed to be independent of  $z$ . In terms of this  $od$ , the phase shift and absorption simplify to

$$\Delta\phi = -\frac{\delta}{\Gamma} \int dz n\sigma = -\frac{\delta}{\Gamma} od, \quad (3.22a)$$

$$a \equiv \frac{E_f}{E_0} = e^{-\frac{1}{2} \int dz n\sigma} = e^{-od/2}. \quad (3.22b)$$

The action of the atoms can then be accounted by an operator

$$A \equiv \begin{pmatrix} a e^{i\Delta\phi} & 0 \\ 0 & 1 \end{pmatrix} = \begin{pmatrix} e^{-\frac{od}{2}} e^{-i\frac{\delta}{\Gamma} od} & 0 \\ 0 & 1 \end{pmatrix}. \quad (3.23)$$

Using a right circular polarizer,  $\text{RCP} = \frac{1}{2} \begin{pmatrix} 1 & i \\ -i & 1 \end{pmatrix}$ , we can interfere the two  $|H\rangle$  and  $|V\rangle$  polarizations. Putting it all together, the initial polarization state  $|D\rangle$  transforms to  $\text{RCP} \cdot A \cdot |D\rangle$  at the camera, which measures an intensity

$$I_f = I_0 |\text{RCP} \cdot A \cdot |D\rangle|^2. \quad (3.24)$$

**Large detuning limit.** It is fruitful to first consider a simple situation where  $\delta/\Gamma \gg 1$  such that the absorption is negligible and phase shift is non-zero, ideally close to 1. This is only possible for large  $od_0 \gg 1$  by picking  $\delta/\Gamma \approx od_0$ ; here,  $od \approx \frac{od_0}{(\delta/\Gamma)^2} \rightarrow \frac{1}{od_0} \ll 1$  ensures that the absorption is negligible while the phase shift  $\frac{\delta}{\Gamma} od \approx \frac{od_0}{\delta/\Gamma} \rightarrow 1$ . The action of the atoms then simplifies to  $A \approx \begin{pmatrix} \exp[i\Delta\phi] & 0 \\ 0 & 1 \end{pmatrix}$  and camera measures an intensity

$$I_f = \frac{I_0}{2} \left[ 1 - \sin \left( \frac{\delta}{\Gamma} od \right) \right]. \quad (3.25)$$

After removing the background intensity  $I_0/2$ , the signal  $\sin \left( \frac{\delta}{\Gamma} od \right) \approx \frac{\delta}{\Gamma} od + \mathcal{O}(od^2)$  is linearly proportional to the atomic density. Moreover, we can maximize the signal to noise ratio at a desired  $od$  by simply changing the detuning. In contrast, the signal in absorption imaging,  $e^{-od} \approx 1 - od + \mathcal{O}(od^2)$  is always *only* sensitive at low  $od \lesssim 1$ .

Analyzing these images is straightforward. Using eq. 3.25, laser detuning  $\delta =$

$\omega_0 - \omega$ , and measured  $I_f, I_0$ , we can calculate the  $od = \frac{\Gamma}{\delta} \sin^{-1}(1 - 2I_f/I_0)$  and

$$od_0 = \frac{1}{\delta/\Gamma} \left( 1 + \left( \frac{2\delta}{\Gamma} \right)^2 + \frac{I_0}{I_{\text{sat}}} \right) \sin^{-1} \left( 1 - \frac{2I_f}{I_0} \right). \quad (3.26)$$

**Exact solution.** Including the absorption effects can also be done analytically. According to eq. 3.24, the intensity at the camera is

$$I_f = \frac{I_0}{2} \left[ \left( \frac{1}{2} + \frac{e^{-od}}{2} \right) - e^{-od/2} \sin \left( \frac{\delta}{\Gamma} od \right) \right]. \quad (3.27)$$

The signal  $2I_f/I_0 \propto \frac{od}{2} + \frac{\delta}{\Gamma} od + \mathcal{O}(od^2)$  is still linearly proportional to the density with the freedom of maximizing sensitivity at a particular  $od$ . Unlike the large detuning limit (eq. 3.26), we cannot analytically solve for  $od$  here, however, it is efficiently done with a numerical solver.

**Considering experimental imperfections.** The main challenge with phase contrast imaging is ensuring that none of the optical elements on the imaging path are birefringent. For example, dielectric mirrors add a differential phase shift to the horizontal and vertical polarizations of the reflected beam. This could produce a signal that is indistinguishable from atoms. It is crucial to properly correct these imperfections for an accurate measurement of the atomic density.

One part of the solution is to use optical elements with minimal birefringence such as metallic mirrors. In a typical experiment, it may not be possible to completely remove all birefringent optical elements. However, we can characterize the total differential phase shift in absence of atoms and remove it from the imaging beam by replacing the last RCP with with a quarter waveplate (QWP) plus a linear polarizer (LP).

$$\text{QWP}(\theta) = e^{-i\pi/4} \begin{pmatrix} \cos^2 \theta + i \sin^2 \theta & (1-i) \sin \theta \cos \theta \\ (1-i) \sin \theta \cos \theta & \sin^2 \theta + i \cos^2 \theta \end{pmatrix}, \quad (3.28a)$$

$$\text{LP}(\theta) = \begin{pmatrix} \cos^2 \theta & \sin \theta \cos \theta \\ \sin \theta \cos \theta & \sin^2 \theta \end{pmatrix}. \quad (3.28b)$$

First, note that replacing RCP in eq. 3.24 with  $\text{LP}(\theta = 0) \cdot \text{QWP}(\theta = -\pi/4)$  produces the same  $I_f$ . Suppose the combined effect of all optics is to add a differential phase shift  $\epsilon$  captured by the operator  $S = \begin{pmatrix} \exp(i\epsilon) & 0 \\ 0 & 1 \end{pmatrix}$ . This unwanted phase can be removed with  $\text{LP}(\theta = \epsilon/2) \cdot \text{QWP}(\theta = -\pi/4)$ . Here, the quarter waveplate converts the diagonal polarization with both the unwanted ( $\epsilon$ ) and atoms induced ( $\phi$ ) phase shift (polarization state  $A \cdot S \cdot |D\rangle$ ) into a linear polarization at an angle  $-(\frac{\phi}{2} + \frac{\epsilon}{2} + \frac{\pi}{4})$  from the x-axis. Changing the angle of the linear polarizer to  $\text{LP}(\theta = \epsilon/2)$  both removes the effects of  $S$  while ensuring that the atoms induced phase shift gets converted to an intensity signal identical to eq. 3.24 and eq. 3.27.

**Imaging two spin states.** Typically, we want to simultaneously image two atomic states. Luckily, for Lithium at 690 Gauss, the desired states  $|\uparrow\rangle = |1\rangle$  and  $|\downarrow\rangle = |3\rangle$  are detuned by  $\approx 120$  MHz, much larger than the laser linewidth and  $\Gamma$ . This makes it possible to quickly change the imaging frequency and take two consecutive images,  $A$  and  $B$ . For absorption imaging, each image is decoupled from the other and shows the signal from a single atomic state. In contrast, for phase contrast imaging, things are a little more complicated. We would still need to take two images, and change the imaging frequency in between, however, each image would contain a signal coming from both atomic states. These two images need to be analyzed together to independently calculate the atomic density of both states.

Let's label all atoms related quantities with  $\uparrow/\downarrow$  ( $n_\uparrow$ ,  $n_\downarrow$ ,  $od_0^\uparrow$ , etc.), all image related quantities with  $A/B$  ( $\omega_A$ ,  $I_0^B$ ,  $I_f^A$ , etc.), and quantities that depend on both atoms and images with their combination ( $\delta_\uparrow^A = \omega_0^\uparrow - \omega_A$ ,  $od_\downarrow^A = \int dz n_\downarrow \sigma_0 / (1 + (2\delta_\downarrow^A / \Gamma)^2 + I_0^A / I_{\text{sat}}) \approx od_0^\downarrow / (1 + (2\delta_\downarrow^A / \Gamma)^2 + I_0^A / I_{\text{sat}})$ ,  $od_\downarrow^B$ , etc.). These images measure the response from both atomic states with individual phase shift and attenuation given by eqs. 3.22a and b. The total phase shift and attenuation for the two images are

$$\phi_A = -\frac{\delta_\uparrow^A}{\Gamma} od_\uparrow^A - \frac{\delta_\downarrow^A}{\Gamma} od_\downarrow^A, \quad a_A = e^{-od_\uparrow^A/2} e^{-od_\downarrow^A/2}, \quad (3.29a)$$

$$\phi_B = -\frac{\delta_\uparrow^B}{\Gamma} od_\uparrow^B - \frac{\delta_\downarrow^B}{\Gamma} od_\downarrow^B, \quad a_B = e^{-od_\uparrow^B/2} e^{-od_\downarrow^B/2}, \quad (3.29b)$$

and intensities at the camera are

$$I_f^A = \frac{I_0^A}{2} \left[ \left( \frac{1}{2} + \frac{a_A^2}{2} \right) - a_A \sin(\phi_A) \right], \quad (3.30a)$$

$$I_f^B = \frac{I_0^B}{2} \left[ \left( \frac{1}{2} + \frac{a_B^2}{2} \right) - a_B \sin(\phi_B) \right]. \quad (3.30b)$$

Even though there are a lot of variables, only two are unknown,  $od_0^\uparrow$  and  $od_0^\downarrow$  (or, alternatively,  $n_\uparrow$  and  $n_\downarrow$ ). With the two measured intensities, we can solve the system of equations to find the two densities. While it is not possible to analytically solve these equations, it is efficiently done with a numerical solver.



# Chapter 4

## Sound waves, measuring the coupled transport of momentum and heat

The study of non-equilibrium physics is typically closely linked to the study of sound waves. They are ubiquitous in nature from ripples in a pond, waving of a flag to phonons in a crystal. They are the first things that show up when a system is perturbed and their properties dictate the low-energy excitations of materials.

Our goal is to study the non-equilibrium, transport properties of strongly interacting Fermi gases using sound waves. We will first discuss how to create and observe sound waves, followed by measuring its fundamental property, the linear dispersion. The attenuation of sound provides a direct route to measure transport properties of this system. We study this attenuation rates' dependence on sound frequency and gas temperature. At low frequencies, the attenuation of sound is governed by hydrodynamics, where we measure the sound diffusivity.

But first, I want to tell the story of how we came across sound waves.

### 4.1 Mysterious resonances while heating the gas

Among countless other topics, non-equilibrium transport physics was always on top of our list of things to study in the box. However, we didn't have a set path to tackle this problem. So, after creating and characterizing the box, we began to explore equi-

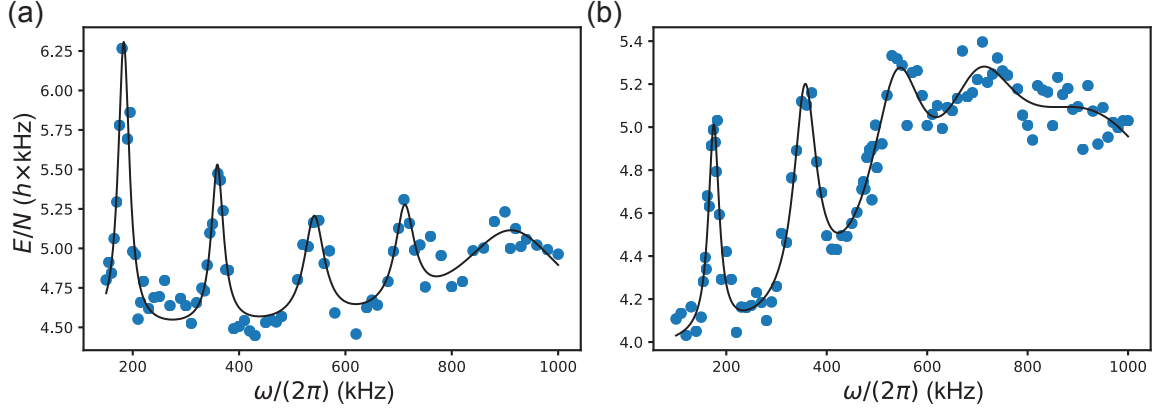


Figure 4-1: **Signature of resonant sound modes of the box.** The intensity of the endcaps of a cylindrical box is modulated at a drive frequency  $\omega$  for 150 cycles. This induces density waves in the Fermi gas, which travel through the box, reflect off of the box walls, and eventually dissipate into heat. The final internal energy per particle  $E/N$  is shown for a Fermi gas in both the superfluid phase **(a)** and in the normal phase **(b)**. This data is fit (black line) with a sum of five Lorentzian functions with independent widths and centers.

librium physics, specifically thermodynamics and radio-frequency spectroscopy. This required producing homogeneous gases with temperatures ranging from the deeply degenerate limit  $T/T_F \lesssim 0.1$  to high-temperatures  $T/T_F \gg 1$ . However, our box loading procedure always produced deeply degenerate clouds, and getting hotter gases required some way to inject heat into the system. We employed the simplest approach; modulating the intensity of one of the trapping light for a variable amount of time. This would create density ripples (i.e. sound waves) which would decay and convert input energy into heat. On a particular day and at a particular modulation frequency (typically 1 kHz), we could reliably and reproducibly heat the Fermi gas. However, from day to day, especially if the box size had changed due to mask alignment, we found the same modulation to result in different final temperatures. At first, we just ignored this, thinking it must be just one of those days! Until, we became curious enough and decided to closely inspect the heating rate as a function of the modulation frequency shown in Fig. 4-1.

To our surprise, we found several resonances in the heating rates. While we knew that we were injecting sound waves, seeing these resonances made it clear to us that these sound waves were reflecting off of the walls and interfering with themselves to

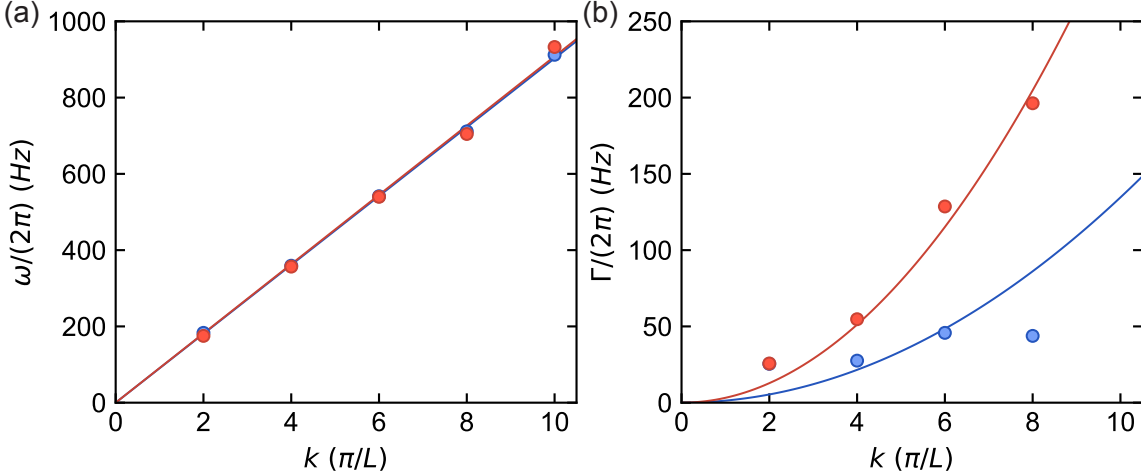


Figure 4-2: **Properties of sound from resonant heating.** The Lorentzian fits shown in Fig. 4-1 give access to the resonance frequency (a) and attenuation rates (b) of five resonant modes of the box. Blue data are for a Fermi gas in the superfluid phase while red data are in the normal phase. The dispersion relation is fit with a linear function  $\omega = ck$  which yields a speed of sound  $c = 18.1(1)$  mm/s and  $18.2(2)$  mm/s for the two datasets. The attenuation rates are fit with a quadratic function,  $\Gamma = D_s k^2$  which yields a sound diffusivity  $D_s = 0.8(2)$   $\hbar/m$  (below  $T_c$ ) and  $1.9(1)$   $\hbar/m$  (above  $T_c$ ).

create standing waves of sound. The distinct resonances were coming from different harmonic modes, or resonant modes, of the box. They are evenly spaced and feature a linear dispersion shown in Fig. 4-2 (a), a telltale sign of sound waves. The widths of these resonances gave us direct access to the attenuation rate of sound shown in Fig. 4-2 (b). While we cannot definitively claim, at this point, that we see the characteristic  $\Gamma = D_s k^2 \propto k^2$  scaling expected from hydrodynamics, we nonetheless estimate a sound diffusivity  $D_s \approx 1 \hbar/m$  below  $T_c$  and  $\approx 2 \hbar/m$  above  $T_c$ . Even though this method provides us a quantitative tool to study the transport of sound, we quickly abandoned it after seeing the potential of in-situ observations of sound waves presented in the rest of this chapter.

This little mystery opened the door to several projects in our lab, starting with the sound waves presented in this chapter, heat transport presented in the next chapter and second sound presented in Z. Yan’s thesis [194].

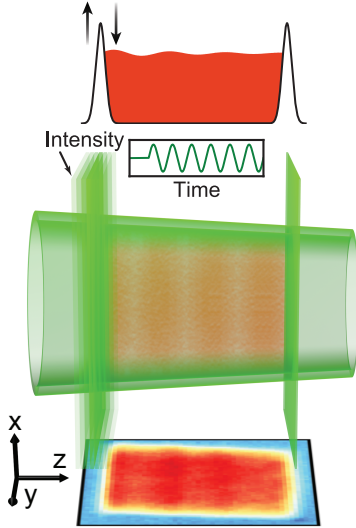


Figure 4-3: **Creating sound waves.** Sound is excited by sinusoidally modulating the intensity of the left endcap wall. The endcap potential's sharpness is  $\approx 3 \mu\text{m}$ . Therefore, increasing its intensity imparts an inward force on atoms closest to the walls and causes a local increase in gas density. This perturbation subsequently propagates through the box.

## 4.2 Traveling sound wave and its dispersion relation

### 4.2.1 Creating and imaging sound waves

Creating sound waves is probably the easiest thing one can do; any perturbation in the external potential will inevitably result in sound waves. Here, changes in external potential (de)compresses the density, which in turn travel as a wave and eventually decay to reach thermal equilibrium.

We create sound waves using the same principle; by modulating the intensity of one or both of the endcap beams, as shown in Fig. 4-3. Note that if the endcap beams were to produce an infinitely sharp trapping potential, modulating its intensity wouldn't cause a change in density. However, the sharpness of the edge of the endcap beam is limited by the optical resolution  $\approx 3 \mu\text{m}$ . This produces a trapping potential with an edge that can be approximated by an error function of a width  $\approx 3\mu\text{m}$ . With this finite width, increasing the intensity of the endcap beams does push the atoms inwards, creating a density perturbation.

In a non-interacting gas, this density perturbation would slowly disappear (wash

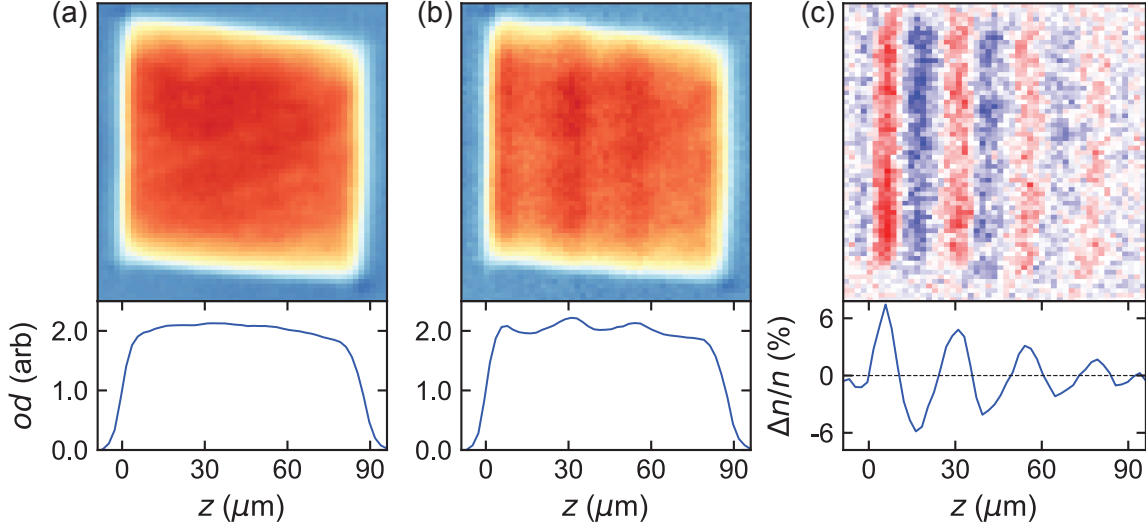


Figure 4-4: **Imaging sound waves.** Absorption images without (a) and with (b) intensity modulation, along with their difference (c) are shown. Optical densities averaged over the homogeneous axis are shown in the bottom panel of (a) and (b), while their difference, normalized by the average density, is shown in the bottom panel of (c). Propagating density perturbation is visible in (b), but it is made clearer by subtracting the background density shown in (c). Here, the intensity of the left endcap beam was modulated at  $2\pi \cdot 600$  Hz for  $\approx 5$  ms before taking an absorption image.

out) as particles travel ballistically throughout the fluid. In contrast, the unitary Fermi gas is a strongly interacting system with mean free path as small as interparticle spacing [15]. Here, particles quickly transfer their momentum to their neighbors, resulting in the imprinted density perturbation to travel as a wave across the box.

These density waves are directly observed in absorption images, see Fig. 4-4 (b), where the bottom panel shows the density integrated over the homogeneous axis of the box. Subtracting the background density taken without any modulation (Fig. 4-4 (a)) makes the density wave clearer, see Fig. 4-4 (c). These images were taken after  $\approx 5$  ms of intensity modulation at  $2\pi \cdot 600$  Hz frequency. Modulating the endcaps of a cylindrical box, as opposed to the cylindrical walls, was ideal because it produced sound waves that travel along the symmetry axis of the cylinder. These sound waves are essentially one dimensional in nature and allows us to integrate the density along the two radial axes of the box, one of which is naturally performed by the absorption imaging along  $x$ -direction, to generate one dimensional traces shown in the bottom

panel of fig. 4-4.

When subtracting the background density or averaging repeated experimental runs, it is crucial to align the box of individual run to each other. This is best performed by fitting the integrated density  $n(z)$  with

$$\frac{n_0}{2} \left( \operatorname{erf} \left( \frac{z - z_L}{\sqrt{2}\sigma_L} \right) + \operatorname{erf} \left( -\frac{z + z_R}{\sqrt{2}\sigma_R} \right) \right) + \text{polynomial}, \quad (4.1)$$

where  $n_0, z_L, \sigma_L, z_R, \sigma_R$  are fit parameters, and a slice  $n(y, z \approx 0)$  of the box taken along the center of the box with  $n_0 - n_0((y - y_0)/R)^2$ , where  $n_0, y_0, R$  are fit parameters. The polynomial part of  $n(z)$  is there to account for either the slight inhomogeneity in the box or density oscillation resulting from sound waves. For sound waves with wavelength  $\gtrsim L$  or for densities without any modulation, a simple 2<sup>nd</sup> order polynomial is optimal. The center of the box fluctuates by  $\approx 3 \mu\text{m}$  with a drift of up to  $8 \mu\text{m}$  over a period of an hour.

### 4.2.2 Dispersion relation

The dispersion relates the frequency  $\omega$  of an excitation to its spacial wavenumber  $k$ . The characteristic dependence of  $\omega$  on  $k$  determines the nature of excitations; for example, free particle excitations feature a quadratic dispersion while phonons, or sound waves, display a linear dependence. Here, the dispersion relation is best measured using traveling waves void of any interference effects. We create them at a particular frequency by modulating the intensity of one of the endcap beams for a time long enough such that sound waves reach the other side of the box but not reflect off of it. Taking an absorption image reveals the traveling waves in position domain, shown in the inset of fig. 4-5 (a) at  $\omega = 2\pi \cdot 600$  and  $850 \text{ Hz}$ . We fit a decaying sinusoidal

$$a_0 e^{-\alpha z} \sin \left( \sqrt{k^2 - \alpha^2} z - \phi \right) \quad (4.2)$$

to find the corresponding wavenumbers  $k = 2\pi/(25.9(3) \mu\text{m})$  and  $2\pi/(18.8(2) \mu\text{m})$ . In addition to  $k$ ,  $a_0$ ,  $\phi$ , and  $\alpha$  are fit parameters for the amplitude, phase, and decay

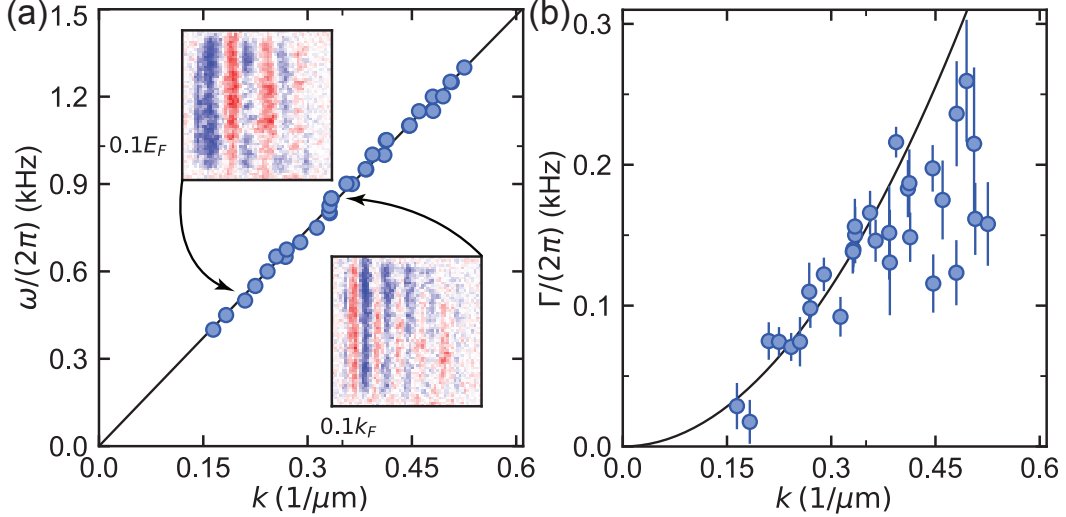


**Figure 4-5: The dispersion and attenuation rate of traveling sound waves.** Sound waves are produced at a frequency  $\omega$  and the corresponding wavenumber  $k$  (shown in (a)) and attenuation rate  $\Gamma$  (shown in (b)) are measured from a sinusoidal fit to the density waves shown in inset of (a). The insets display sound waves observed at  $\omega = 2\pi \cdot 600$  Hz and 850 Hz. The fitted slope (black line in (a)) provides the speed of sound, while a quadratic fit (black line in b) provides the sound diffusivity. Statistical errors are shown in both (a) and (b), however they are smaller than the point size for (a).

constant of sound waves. The decay constant enables us to measure the attenuation rate of sound  $\Gamma = 2c\alpha$ , which should display a  $\propto k^2$  scaling in the hydrodynamic regime. The  $\sqrt{k^2 - \alpha^2}$  term accounts for the effective wavenumber in heavily damped sound waves present at  $\omega \gtrsim 2\pi \cdot 1000$  Hz. For under-damped sound,  $\alpha \ll k$ , resulting in  $\sin(\sqrt{k^2 - \alpha^2}z - \phi) \approx \sin(kz - \phi)$

The dispersion relation  $\omega(k)$  is shown in fig. 4-5 (a) for frequencies  $2\pi \cdot 400 - 1300$  Hz corresponding to  $0.04 - 0.13 E_F$ . It is linear within our measurement errors in the explored region, allowing us to measure the speed of sound  $c = 15.6(1)$  mm/s from its slope. At wavelengths approaching the interparticle spacing, and thus at momenta approaching the Fermi momentum  $k \approx k_F$ , deviations from linear dispersion are expected for the unitary Fermi gas [105]. The lowest order expansion of the dispersion is

$$\omega = ck \left[ 1 + \frac{\gamma}{8} \left( \frac{\hbar k}{mc} \right)^2 \right]. \quad (4.3)$$

A fit to the data yields an upper bound for  $|\gamma| \leq 0.88$ , consistent with theoretical prediction of  $\gamma \approx +0.08$  [105]. Measurements of the dispersion relation close to the Fermi momentum are required to better estimate the sign and strength of this concavity.

The attenuation of sound is already apparent in traveling waves shown in Figs. 4-4 and Fig. 4-5. By fitting  $n(z)$  with the decaying sinusoidal, we also measure the sound attenuation rate  $\Gamma = 2c\alpha$ , shown in Fig. 4-5 (b). While these fits give excellent results for the wavenumber, they are very finicky in determining attenuation rates, especially for highly damped sound at higher frequencies. We nevertheless determine a sound diffusivity using a robust fit  $\Gamma = D_s k^2$  with an arctan loss function shown in Fig. 4-5 (b). For a Fermi gas at  $\approx 0.1 T_F$ , we find a  $D_s \approx 0.8(3) \hbar/m$ .

While traveling waves enable us to measure the attenuation rate of sound, for a precision measurement, we turn to resonant modes described in the next section.

### 4.3 Sound diffusivity from the resonant modes

If we continue to modulate the intensity for a time longer than  $L/c$ , sound waves would reflect off of the second endcap and interfere with itself, eventually reaching some steady state oscillations. If the wavelength of sound wave is close to  $2L/j$  (or frequency close to  $\omega_j = j\omega_0 = jck_0 = jc\frac{\pi}{L}$ ), for any integer  $j$ , then the reflected waves constructively interfere to produce large amplitude resonant modes, while away from it, destructive interference will lead to complete or partial cancellation of sound waves. This is similar to sound waves produced by musical instruments like a flute, where the column of air amplifies sound at a specific resonance frequency and its multiples, i.e. harmonics, determined by the length of the flute and speed of sound in air. We will first calculate the exact steady state response of the system using the density response function and then describe our methods to measure it.

### 4.3.1 Steady state response

A classical damped driven harmonic oscillator with a resonance frequency  $\omega_0$  and damping rate  $\Gamma$  responds to an external sinusoidal potential  $\sim \sin(\omega t)$  at exactly the drive frequency  $\omega$ , but with an amplitude  $A$  and phase shift  $\phi$  that are determined by the detuning  $\omega - \omega_0$ . The amplitude  $A(\omega)$  features a Lorentzian peak centered at  $\omega_0$  while the phase shift goes from 0 to  $\pi$  across the resonance, with  $\phi = \pi/2$  at  $\omega_0$ . The unitary Fermi gas in a box potential responds similarly to a collection of classical oscillators, with  $j^{\text{th}}$  oscillator having a resonance frequency  $\omega_j = j\pi c/L$  and decay rate  $\Gamma_j$ .

We quantitatively find the steady state solution using the density response function  $\chi_n$ . It relates the perturbation in fluid's density to the external potential,  $\delta n(k, \omega) = \chi_n(k, \omega) \delta V(k, \omega)$ , see eq. 2.17a. We can find the density response to an arbitrary external potential with Fourier components  $\delta V(k', \omega') = \int dz e^{-ik'z} \int dt e^{-i\omega't} \delta V(z, t)$  by solving

$$\begin{aligned}\delta n(z, t) &= \int \frac{dk'}{2\pi} e^{ik'z} \int \frac{d\omega'}{2\pi} e^{i\omega't} \chi_n(k', \omega') \delta V(k', \omega'), \\ &= \sum_{k_j=j\frac{\pi}{L}} \cos(k_j z) \int \frac{d\omega'}{2\pi} e^{i\omega't} \chi_n(k_j, \omega') \delta V(k_j, \omega'),\end{aligned}\quad (4.4)$$

where the last step assumes a box with endcaps located at  $z = 0$  and  $L$ . If the endcaps were located at  $z = -L/2$  and  $z = L/2$ , the  $\cos(k_j z)$  would need to be replaced by  $\sin(k_j z)$  for odd  $j$ 's.

We sinusoidally modulate the intensity of an endcap beam using a  $\delta V(t) \sim \sin(\omega t)$  drive. A sine, as opposed to cosine, drive avoids sudden jumps in the potential when the drive is first turned on. Its Fourier amplitude is  $\delta V(\omega') \sim \int dt e^{-i\omega't} \sin(\omega t) = i\pi(\delta(\omega' + \omega) - \delta(\omega' - \omega))$ , where  $\delta(\omega) \equiv \frac{1}{2\pi} \int dt e^{i\omega t}$  is the Dirac delta function. Unlike in the experiment, here we are assuming the drive to be on at all times in order to find the steady state solution. If the transient part was also desired, we would multiply the drive by a Heaviside step function.

The spatial Fourier amplitude of the drive is determined by the shape of the

modulating potential, i.e. the endcap potential,  $V(z)$ . The endcap beams are well modeled by a Gaussian error function with an edge sharpness of  $\sim 3\mu\text{m}$ , resulting in a Fourier amplitude with a Gaussian shape of width  $\approx \pi/(3\mu\text{m})$ . For  $k \ll \pi/(3\mu\text{m})$ , it is safe to assume  $\delta V(k) \sim V_0$  to be uniform. Plugging the drive

$$\delta V(z, t) = V(z) \sin(\omega t), \quad (4.5a)$$

$$\delta V(k', \omega') = i\pi V(k') (\delta(\omega' + \omega) - \delta(\omega' - \omega)), \quad (4.5b)$$

into eq. 4.4, we find the density response

$$\delta n(k_j, t) = V(k_j) (-\sin(\omega t) \operatorname{Re}[\chi_n(k_j, \omega)] + \cos(\omega t) \operatorname{Im}[\chi_n(k_j, \omega)]), \quad (4.6a)$$

$$\delta n(z, t) = \sum_{k_j=j\pi/L} \delta n(k_j, t) \cos(k_j z). \quad (4.6b)$$

In general, the system responds at a range of  $k_j$  for any particular  $\omega$ , however,  $\chi_n$  is strongly peaked at the sound resonance  $k_j = \omega/c$ . Consequently, if  $\omega/c$  is away from any  $k_j$ 's, the response will be very small. These are precisely the resonant modes of the box potential. Furthermore, the in- and out-of-phase amplitudes of the response are given by  $V_0(k_j) \operatorname{Re}[\chi_n(k_j, \omega)]$  and  $V_0(k_j) \operatorname{Im}[\chi_n(k_j, \omega)]$ , which can easily be measured by imaging the density when either  $\cos(\omega t) = 0$  or  $\sin(\omega t) = 0$ , respectively.

### 4.3.2 Imaging the resonant box modes, the sonogram, and $\chi_n$

Resonant modes are best observed in frequency and position domain by measuring the density after a steady state is reached at varying drive frequencies. Notice that in the steady state, the density oscillates at  $\omega$ , meaning that at different times during the drive cycle, we would observe different amplitudes of the sound wave. However, it is not necessary to measure the density response at all times; only two independent variables, the amplitude and phase shift of the response, or, equivalently, the real and imaginary parts of  $\chi_n$ , completely characterize the response. Furthermore, the density at  $t = N \frac{2\pi}{\omega}$  and  $t = (N + 1/4) \frac{2\pi}{\omega}$ , for any integer  $N$ , is proportional to  $\operatorname{Im}[\chi_n]$  and  $\operatorname{Re}[\chi_n]$  respectively, providing us a direct route to measure  $\chi_n$ .

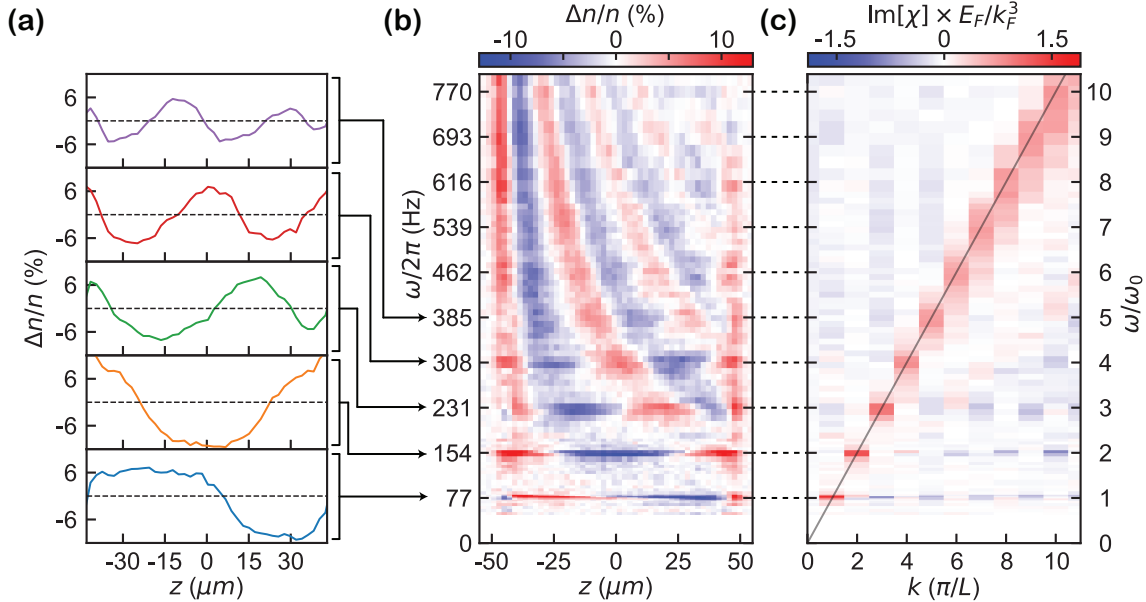


Figure 4-6: **Resonant modes of the cylindrical box.** The steady-state density response of the gas is obtained by modulating the endcap wall at a frequency  $\omega$  for 30 cycles of the drive. Standing waves of the sound corresponding to the resonant modes in the box are observed at frequencies  $\omega_j = j\pi c/L \approx 2\pi \cdot 77 \text{ Hz}$  (where  $j$  is any positive integer), the first five of which are shown in (a). The full sonogram is shown in (b). Here, each row of pixels corresponds to a particular realization of the experiment at a given frequency. (c) The spatial Fourier transport directly yields the density response  $\text{Im}[\chi_n(k, \omega)]$ . It reveals well-defined resonance peaks exhibiting both the linear dispersion of sound (shown in black line) and increasing widths if frequency at higher wave numbers, corresponding to increased rates of sound attenuation.

We image the density after 30 complete cycles at  $t = 30 \frac{2\pi}{\omega}$  of a  $\sin(\omega t)$  drive. This time was experimentally confirmed to be long enough to reach a steady state at all frequencies explored. These measurements are summarized in Fig. 4-6 for a unitary Fermi gas at  $T/T_F \approx 0.1$  in a box of length  $L \approx 95 \mu\text{m}$ . Each row of fig. 4-6 (b) shows the fractional density modulation at a particular drive frequency,  $\delta n(z, \omega)/n$ . This is the ‘sonogram’ of the unitary Fermi gas in a cylindrical box. Here, discrete resonant modes of the box are easily visible, the first five of which are shown in fig. 4-6 (a). A spatial Fourier transform extracts the response  $\delta n(k_j, \omega)/n$  at a particular  $k_j$ , enabling us to find the density response function  $\text{Im}[\chi_n(k_j, \omega)] = \delta n(k_j, \omega)/V(k_j)$  shown in Fig. 4-6 (c) and again in Fig. 4-7.

Each resonant mode of the box with a wavenumber  $k_j$  features a peak in  $\text{Im}[\chi_n](\omega)$

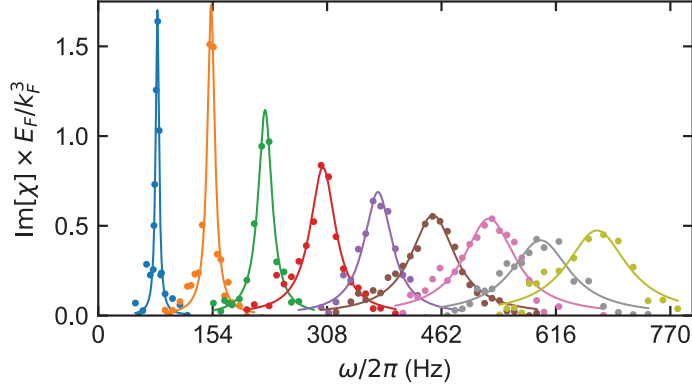


Figure 4-7: **Density response function  $\chi_n$ .** The imaginary part of the density response function at each resonant mode wave number  $k_j$  is obtained from a spatial Fourier transform of the steady-state response. It displays a well-defined peak in frequency, whose full-width at half-maximum yields the mode damping rate  $\Gamma$ . This is obtained from a Lorentzian fit, shown by solid lines.

(see Fig. 4-7) at  $\omega_j = ck_j$  with a full width at half maximum  $\Gamma_j$ , enabling us to measure the dispersion, speed, and attenuation rates of sound. We fit a Lorentzian

$$a_0 \frac{(\Gamma_j/2)^2}{(\omega - \omega_j)^2 + (\Gamma_j/2)^2} \quad (4.7)$$

to each of the resonant modes to find the speed  $c = \omega_j/k_j$  from the center and sound attenuation rate  $\Gamma_j$  from the width of the peaks. The sound attenuation rate can be seen to increase with  $k$ , revealed in both a broadened frequency response as well as a reduced peak height. This spectroscopic method of measuring  $\Gamma$  produces much higher quality data than traveling waves or heating rate shown before. From the speed of sound, we test the universality of the unitary Fermi gas, and from the attenuation rates, we test the applicability of Hydrodynamics and measure the sound diffusivity.

### 4.3.3 Speed of sound

The precise determination of the speed of sound enable us to test the scale invariance of the unitary Fermi gas. In general, the speed of sound in a particular system depends on its specific equation of state; however, for all non-relativistic, scale-invariant systems in three dimensions, a universal relation emerges,  $mc^2 = \frac{10}{9} \frac{E}{N}$ , relating the

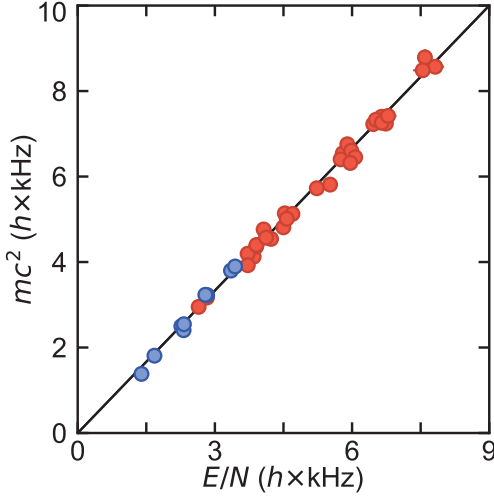


Figure 4-8: **Scale invariant speed of sound.** Measurement of the universal relation between the speed of sound and the energy-per-particle  $E/N$ . The speed of sound is measured from the peak of the second resonant mode of the box while the energy is measured from an isoenergetic expansion of the homogeneous gas from the box to a harmonic potential. The black solid line shows the predicted linear dependence for any nonrelativistic scale-invariant system in three dimensions:  $mc^2 = \frac{10}{9}E/N$ . Data are shown for both the normal (red) and the superfluid (blue) phase.

speed of isentropic sound  $c$  to system's energy per particle  $E/N$  as described below.

For any system, the speed of isentropic sound is given by

$$mc^2 = \left. \frac{\partial P}{\partial n} \right|_S = \left. \frac{V^2}{N} \frac{\partial^2 E}{\partial V^2} \right|_S, \quad (4.8)$$

where  $m$  is particle mass,  $N$  is number of particles,  $n = N/V$  is number density,  $V$  is system volume,  $S$  is entropy,  $E$  is total internal energy, and  $P = -\left. \frac{\partial E}{\partial V} \right|_S$  is pressure. Let's consider a non-relativistic scale-invariant system. Under dilation of space by a factor  $\lambda$ , its position  $x \rightarrow \lambda x$ , momentum  $p \rightarrow p/\lambda$  and energy  $E \rightarrow E/\lambda^2$ . Such a scaling for the energy is only possible if  $E \propto L^{-2} \propto V^{-2/3}$ , where  $L = V^{1/3}$  is the size of the system, resulting in  $\frac{\partial E}{\partial V} = -\frac{2}{3}\frac{E}{V} \propto V^{-5/3}$  and  $\frac{\partial^2 E}{\partial V^2} = \frac{10}{9}\frac{E}{V^2}$ . This yields the universal relation

$$mc^2 = \frac{10}{9} \frac{E}{N}, \quad (4.9)$$

independent of the equation of state, temperature, or even the phase of the system.

In fig. 4-8, we show the measured  $mc^2$  as a function of the gas energy per particle

$E/N$ . The speed of sound is calculated from the peak of the lowest symmetric resonant mode ( $j = 2$ ) of the box and  $E/N$  is measured from an isoenergetic expansion of the gas from the box into a harmonic trap (described in sec. 3.2). In both the superfluid (blue circles) and normal (red circles) phases, and for varying temperatures and Fermi energies, the scale invariant prediction (black line) captures our data well with no free parameters. With this verification, speed of sound provides us a convenient tool to measure the energy and therefore the temperature of the gas using the equation of state.

#### 4.3.4 Attenuation of sound in the hydrodynamic and collisionless regime

The qualitative dependence of the sound attenuation rate  $\Gamma$  on its wavenumber  $k$  is intricately dependent on the underlying interactions between phonons and other thermal excitations in the fluid and reveals the nature of transport. A classic example is hydrodynamic damping of sound where  $\Gamma \propto k^2$  with proportionality constant being the sound diffusivity  $D_s$ . Here, sound oscillations are assumed to be slow enough to maintain local thermal equilibrium. This is the case when the sound frequency is small compared to scattering rates of thermally excited phonons  $\Gamma_{t,\text{ph}}$  and other quasi-particles. Once the frequency of sound waves  $\omega = ck \gtrsim \Gamma_{t,\text{ph}}$ , hydrodynamic damping becomes invalid and sound waves enter a ‘collisionless’ regime. Here, the qualitative scaling of  $\Gamma(k)$  depends on the specific form of interactions between phonons and other thermal excitations, and on the concavity of the dispersion relation [106].

In Fig. 4-9, we show  $\Gamma(k)$  at various gas temperatures in both linear and log scale. Here,  $\Gamma$  is the measured full-width at half-maximum of the Lorentzian peaks located at each of the resonant modes, see Fig. 4-7. In the normal phase, for  $T > T_C \approx 0.17 T_F$ , we find a quadratic scaling  $\Gamma \propto k^2$  for the range of wavenumbers explored,  $k \lesssim 0.3 mc/\hbar \approx 0.1 k_F$ , validating hydrodynamic transport. In contrast, at  $T \approx 0.1 T_F$ , we observe a departure from the quadratic scaling for wavenumbers  $k \gtrsim 0.15 mc/\hbar$ , indicating a departure from the purely hydrodynamic transport at

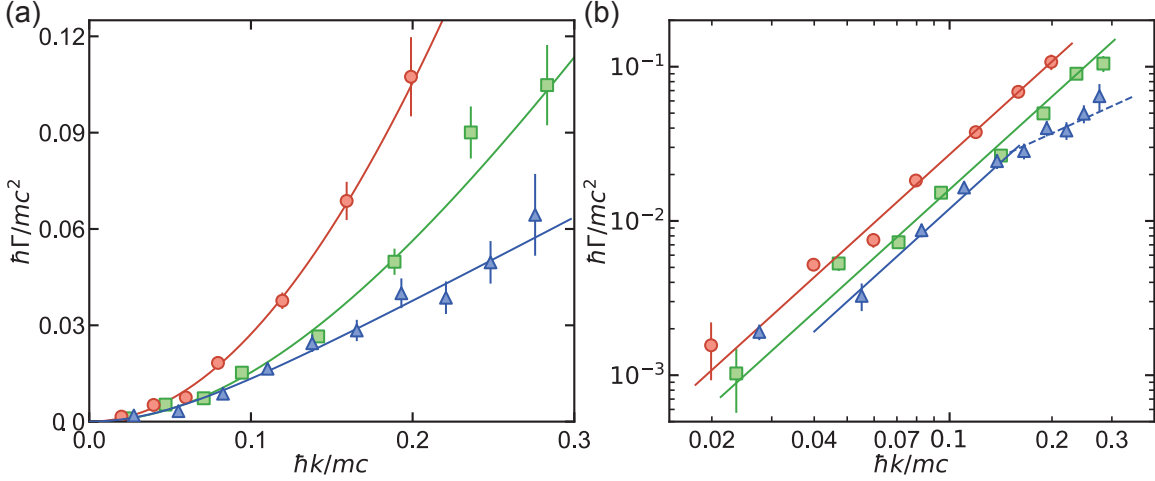


**Figure 4-9: Sound attenuation rate in the hydrodynamic and collisionless regimes.** Sound attenuation rate  $\Gamma(k)$  for gas temperatures  $T/T_F = 0.36(5)$  (red circles),  $T/T_F = 0.21(3)$  (green squares), and  $T/T_F = 0.13(2)$  (blue triangles) are shown in both a linear scale (a) and in log-log scale (b). For all temperatures,  $\Gamma(k)$  displays a quadratic scaling at low momenta characteristic of diffusive damping and predicted by hydrodynamics. This is clearly seen in log-log space, where  $\Gamma \propto k^2$  (solid lines in (b)) at low momenta. For our coldest samples, as  $k$  increases, we observe a deviation from this behavior. Here, we observe  $\Gamma \propto k$  (blue dashed line in (b)) expected from collisionless damping [106]. At all temperatures and wavenumbers, our data are well captured by the model of [144] (solid lines in (a)), which connects the hydrodynamic and collisionless regimes by including the finite relaxation rate of the fluid. Error bars represent  $1\sigma$  statistical uncertainty.

higher wavenumbers.

In the collisionless regime, non-linearities arising from the kinetic energy carried by sound waves and the density dependence of the speed of sound lead to phonon-phonon scattering and decay of sound. To lowest order, three-phonon collisions are considered where the injected phonon either combines with a thermal phonon (Landau process,  $\Gamma \propto k$  [144, 106]) or decays into two thermal phonons (Beliaev process,  $\Gamma \propto k^5$  [106]). For  $k \ll k_B T/\hbar c$ , or equivalently  $k \ll 0.6 mc/\hbar$  at  $T = 0.1 T_F$ , Landau damping process is prominent, consistent with the measured  $\Gamma(k)$  shown in Fig. 4-9. The crossover from the hydrodynamic to collisionless regime is smooth and well characterized by  $\Gamma(k) = D_s k^2 f(ck/\Gamma_{t.ph})$  with  $f(x) = \tan^{-1}(x)/x$  [144]. A fit (solid lines in (a)) yields a  $\Gamma_{t.ph} \approx 0.027 E_F/\hbar \approx 0.27 k_B T/\hbar$  at  $T \approx 0.1 T_F$ , meaning that sound waves with  $\omega = ck \ll \Gamma_{t.ph} \approx 2\pi \cdot 270$  Hz decay according

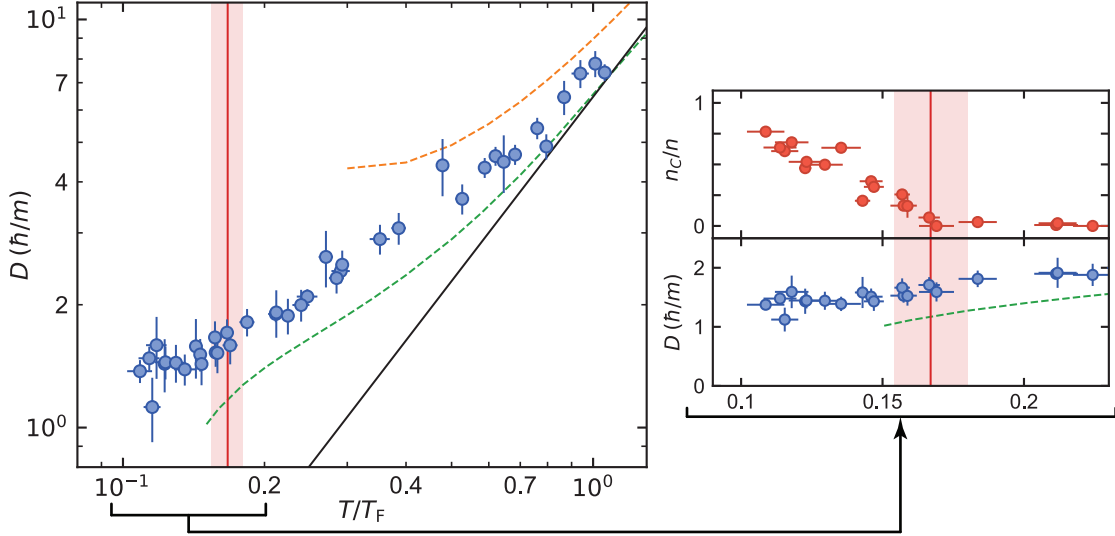


Figure 4-10: **Temperature dependence of the sound diffusivity.** For temperatures comparable to the Fermi temperature, the sound diffusivity ( $D$ , normalized by  $\hbar/m$ ; blue circles) approaches the expected high temperature scaling of  $T^{3/2}$  (solid black line). As the temperature is lowered,  $D$  decreases monotonically and attains a quantum-limited value close to  $\hbar/m$ . Below the superfluid transition (vertical red line, from [103]),  $D$  is observed to be almost independent of temperature and condensate fraction ( $n_C/n$ , red circles in inset). From the transition temperature ( $n_C/n = 0$ ) to the coldest temperatures ( $n_C/n \sim 0.8$ ), the changes in  $D$  are within the standard error of the measurements. Theoretical predictions for  $D$ : the dashed orange line is from the sound attenuation length calculated in the framework of kinetic theory [25] and the dashed green line is from a calculation of shear viscosity [52] assuming a Prandtl number of  $2/3$ . Bars denote statistical error arising from the uncertainty in  $\Gamma$ . Additionally, the dominant systematic uncertainty in  $D$  is an error of 13% arising from the non-zero width of the endcaps.

to hydrodynamics. At higher temperatures,  $T \gtrsim 0.17 T_F$ , the fit yields a  $\Gamma_{t,\text{ph}}$  much higher than the frequency of the highest measured resonant mode of the box, implying that the sound waves are always well described by hydrodynamics.

### 4.3.5 Sound diffusivity

In Fig. 4-10, we show the sound diffusivity as a function of temperature, where both the  $D_s$  and  $T$  are measured from the lowest symmetric resonant mode of the box ( $j = 2$ ). The peak frequency of the resonance is converted into the temperature using  $c = \omega_j/k_j$ ,  $E/N = \frac{9}{10}mc^2$  and the equation of state  $\frac{T}{T_F} \left( \frac{E/N}{E_F} \right)$  (see Fig. 2-4

and [103]), while the width of the resonance is converted into the sound diffusivity using  $D_s = \Gamma_j/k_j^2$ . The lowest symmetric mode is ideal for this measurement because it is void of imperfections plaguing the fundamental mode while having a frequency that is at least  $< 0.5 \Gamma_{t,\text{ph}}$ . Below, we will analyze this data, from the high temperature regime to the superfluid phase.

While it is difficult to theoretically calculate transport properties, like the sound diffusivity, for a strongly interacting system, we can gain insight by considering its value at limiting temperatures or in simpler systems. The basis for these calculations is kinetic theory which yields an estimate  $D \approx lv$  where  $l = 1/(n\sigma)$  and  $v$  are the mean free path and average velocity of (quasi-) particles responsible for transport with a number density  $n$  and collision cross-section  $\sigma$  [108, 170].

At very high temperatures  $T \gg T_F$ , the unitary Fermi gas is predicted to be composed of well-defined quasi-particles [15, 201]. Here, the thermal wavelength  $\lambda = \sqrt{\frac{2\pi\hbar^2}{mk_B T}}$  sets the scale of both  $l \sim \frac{1}{n\lambda^2}$  and  $v \sim \frac{\hbar}{m\lambda}$ , resulting in a  $D \sim lv \propto 1/\lambda^3 \propto T^{3/2}$ . The solid black line in Fig. 4-10 shows this scaling quantitatively,  $D = 6.46 \frac{\hbar}{m} \left(\frac{T}{T_F}\right)^{3/2}$ , with the prefactor calculated using the high-temperature values for  $\eta$ ,  $\kappa$ , and equation of state [103]. It begins to capture our data well without any free parameters at temperatures beyond  $T_F$ . However, as the gas cools and enters the degenerate limit, this simple model underestimates the measured sound diffusivity. In this regime, the existence of the Fermi surface suppresses scattering which in turn reduces the scattering cross-section and increases the sound diffusivity, consistent with our observations.

The nature of the unitary Fermi gas in the deeply degenerate normal phase ( $0.17 T_F < T \ll T_F$ ) is still unclear [56, 51, 156, 132, 154]. Typically the normal phase of degenerate Fermi gases, like  ${}^3\text{He}$ , is described by the Fermi liquid theory, where the velocity of the quasi-particles is restricted to  $v \sim v_F$  because of the Fermi surface and scattering cross-section is heavily suppressed at low temperatures because of Pauli blocking with  $\sigma \propto T^2$ . It predicts a diverging diffusivity  $D \propto 1/T^2$  observed in  ${}^3\text{He}$  [76], and most metals [99]. In contrast, we find the sound diffusivity to monotonically decrease all the way into the superfluid phase, suggesting that the Fermi

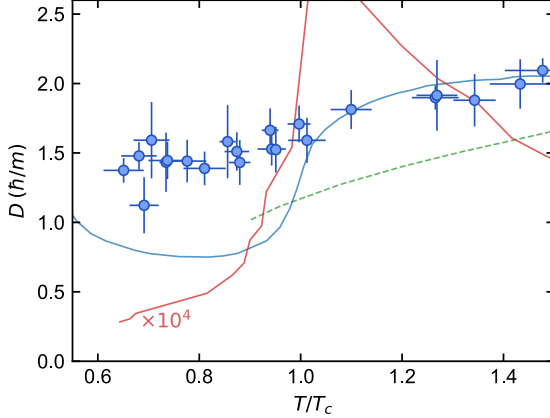


Figure 4-11: **Sound diffusivity of liquid helium.** The measured sound diffusivity of the unitary Fermi gas (blue circles), along with the previously measured sound diffusivity of the liquid-<sup>3</sup>He [76] (red line, rescaled by a factor of  $10^4$ ) and liquid-<sup>4</sup>He [46] (blue line) are shown as a function of  $T/T_c$ . Here  $T_c$  and  $m$  are the critical temperature and mass of the corresponding system. Sound diffusivity of the unitary Fermi gas closely follows that of liquid-<sup>4</sup>He.

liquid description is not adequate to model the normal phase of the unitary Fermi gas. In this regime, a pseudo-gap phase is also predicted to exist, where the existence of pre-formed pairs could alter transport properties [88, 199]. Furthermore, the scale invariance of the unitary gas leads to a quantum critical point at  $\mu = 0$ ,  $T = 0$ , separating the zero-density superfluid phase from zero-density normal phase at zero temperature [51, 56]. Above this point lies a finite-density quantum critical regime  $T \sim 0.4 T_F$ , where the presence of critical fluctuations lead to a universal Planckian scaling for the decay and scattering rates  $\propto T$ . This is consistent with the linear in  $T$  resistivity measured in ‘strange metals’ [111]. Here, we do not directly measure the scattering rates and cannot comment on the applicability of this theory for the unitary Fermi gas.

Upon crossing the superfluid transition temperature, we do not observe any sudden change in  $D_s$ . This is further demonstrated in Fig. 4-10 (b), where we find the  $D_s$  to remain approximately constant as the temperature is reduced, despite a rise in the pair condensate fraction. This is in contrast to the liquid <sup>3</sup>He, where the sound diffusivity features a steep drop from  $\sim 50,000 \text{ } \hbar/\text{m}$  to  $\sim 5000 \text{ } \hbar/\text{m}$  [76]. In the superfluid phase, as the temperature is further reduced, the sound diffusivity remains approximately

constant. Despite being a Fermi-liquid in the normal phase, the superfluid phase of the weakly interacting liquid  $^3\text{He}$  features a sound diffusivity that is similar to one observed here. Such a behavior in the superfluid phase can qualitatively be understood by realizing that the viscosity arises entirely from the normal component, yielding  $D \sim \frac{n_n}{n} lv$  where  $l = \frac{1}{n_n \sigma}$  is the mean free path of a typical excitation with density  $n_n$ . Note that the strongly temperature dependent normal fraction  $n_n$  cancels and  $D \sim v/(n\sigma)$ . At the temperatures studied here, the normal component is composed almost entirely of broken pairs [15] formed close to the Fermi surface with  $v \sim v_F = \hbar k_F/m$ . In absence of a Fermi surface, these quasiparticles would have a cross-section  $\sigma \sim k_F^{-2}$ , however, in the presence of a Fermi surface broadened by the pairing gap  $\Delta$ , Pauli blocking reduces the cross-section to  $\sigma \sim k_F^{-2}(\Delta/E_F)^2$ , yielding a  $D \sim \left(\frac{E_F}{\Delta}\right)^2 \frac{\hbar}{m}$ . The strongly interacting unitary Fermi gas features a pairing gap as large as the Fermi energy,  $\Delta \approx 0.4E_F$  [82, 163], yielding  $D \sim \hbar/m$ . In contrast, the weakly interacting liquid- $^3\text{He}$ , features a small pairing gap,  $\Delta \sim 10^{-3}E_F$  [189], leading to a much high diffusivity,  $D \sim 5000 \hbar/m$  [53, 137].

In general, diffusivity varies by many orders of magnitude across different liquids and gases, however, the Heisenberg uncertainty principle,  $\Delta x \Delta p \approx lmv \gtrsim \hbar$ , may impose a universal limit on *all* strongly interacting quantum fluids. Here, the mean free path becomes as small as interparticle spacing, requiring the average velocity  $v \sim \hbar/(ml)$  and diffusivity  $D \sim \hbar/m$  to take on Heisenberg-limited values, independent of the scale of the system. Such values are observed in systems at many length scales, from the unitary Fermi gas [173, 10, 117] and liquid Helium [46] to quark-gluon plasma [162, 3, 180]. Here, we also observe a Heisenberg-limited value for the sound diffusivity with  $D_s \approx 1.3 \hbar/m$  close to  $T \approx 0.1 T_F$ .

Sound waves are composed of perturbations in both momentum and heat; therefore, the measurements of  $D_s$  presented here constrains the values of  $\kappa$  and  $\eta$  according to  $D_s = 4\eta/(3\rho) + 4\kappa T/(15P)$ . Another independent measurement is required to uniquely calculate both transport properties. In the next chapter, we describe our measurement of the thermal diffusivity and independent determination of  $\eta$  and  $\kappa$ .



# Chapter 5

## Transport Properties of a Strongly Interacting Fermi Gas

While particle number, total momentum, and total energy are conserved in all microscopic collisions in fluids, internal friction leads viscous flow and heat conduction, the only two irreversible transport phenomena present in one-component (or spin-balanced) fluids. If perturbations are sufficiently small, and interaction are sufficiently large, to maintain local thermal equilibrium, then these transport phenomena are described by a set of hydrodynamic equations (eqs. 2.13) and quantified by the shear viscosity  $\eta$ , bulk-viscosity  $\zeta$ , and thermal conductivity  $\kappa$ . With the knowledge of these transport properties, time evolution after an arbitrary perturbation in density, momentum, or heat can be calculated. While measurements of the sound diffusivity (sec. 4.3.5) constrained the values of  $\kappa$ ,  $\eta$ , and  $\zeta$ , it is our goal here to make other independent measurements to uniquely determine each of the transport properties and fully characterize the transport phenomena of a spin-balanced unitary Fermi gas.

This chapter present the study of heat conduction in the normal phase of the unitary Fermi gas, accomplished by measuring the relaxation of a controllably imprinted temperature gradient (sec. 5.1). The study of heat conduction and sound diffusion (ch. 4.3), combined with the equation of state of the spin-balanced unitary Fermi gas (ch. 2.2, [103]), provide a complete picture of transport phenomena in this system. We present all non-zero transport properties in sec. 5.2 and compare them

with transport properties of other strongly interacting quantum systems like, liquid helium and high-T<sub>c</sub> superconductors.

## 5.1 Measuring the Thermal Diffusivity

The time evolution after an arbitrary temperature perturbation is described by the heat equation  $\frac{\partial T}{\partial t} = D_T \nabla^2 T$  (see eq. 2.22) and quantified by the thermal diffusivity  $D_T$ . For example, the amplitude of a spatially sinusoidal temperature perturbation  $\sim \sin(kz)$  relaxes exponentially in time  $\sim e^{-\Gamma t}$  with a decay rate  $\Gamma = D_T k^2$ . In a box trap, the heat equation is optimally analyzed in the Fourier space, where the  $j^{\text{th}}$  spatial Fourier component of an arbitrary temperature perturbation decays in time at a rate  $\Gamma_j = D_T k_j^2$ , where  $k_j = j \frac{\pi}{L}$ . A direct measurement of the thermal diffusivity only requires two things: the ability to locally and non-uniformly inject heat into the system and a way to measure the subsequent time evolution of the local temperature. We utilize high-frequency sound waves with a very low quality factor to locally inject heat into the system and infer the local change in temperature from the accompanying change in density given by the thermal expansivity.

### 5.1.1 Local heater

We imprint a temperature gradient across the sample by locally heating one side of the gas. This is accomplished by selectively injecting sound waves with a quality factor  $\sim 1$  on one side of the box which quickly dissipate into heat.

Sound waves with a wavenumber  $k = \omega/c$  attenuate at a rate give by  $\Gamma = D_s k^2 = D_s \omega^2/c^2$  and have a quality factor  $Q = \omega/\Gamma = c^2/(D_s \omega)$ , see Ch. 4. A unitary Fermi gas with a Fermi energy  $E_F \approx \hbar \cdot 10$  kHz at a temperature  $T \approx 0.2 - 1.0$   $T_F$  has a speed of sound  $c \approx 16 - 30$  mm/s and sound diffusivity  $D_s \approx 2 - 8$   $\hbar/\text{m}$ . Sound waves with a wavenumber  $k \approx 2\pi/(10 \mu\text{m})$  in this gas have a resonance frequency  $\omega \approx 2\pi \cdot 1500 - 3000$  Hz and a quality factor  $Q \approx 0.5 - 1.2$ , indicating that they decay within one to two oscillations and dissipate into heat.

To locally create these high-frequency sound waves, we imprint a blue-detuned

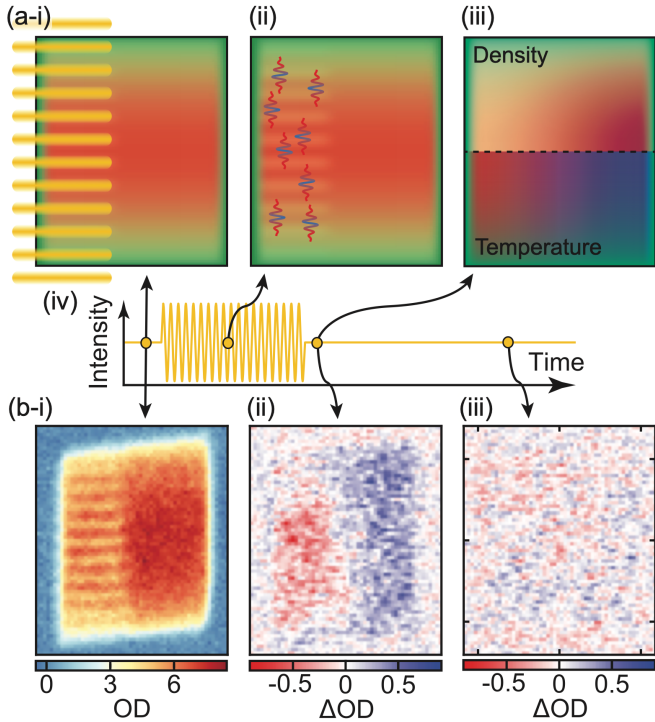


**Figure 5-1: Local heater.** **(a)** Fermionic  ${}^6\text{Li}$  atoms are trapped in a three-dimensional cylindrical box made from green laser beams. A perspective seen along the axial direction is shown here. (i) A fraction of the box is illuminated by an optical lattice formed from blue-detuned 589 nm laser with a spacial period  $\approx 10 \mu\text{m}$ . The lattice intensity is modulated at frequencies ranging from  $2\pi \cdot 1500 - 3000 \text{ Hz}$  for a short amount of time (iv) to excite sound waves (ii) with a quality factor  $\lesssim 1$ . These sound waves dissipate into heat within one to two oscillations (ii), causing the local temperature of the gas to rise (iii). Increase in the local temperature is accompanied by a proportional decrease in the local density (iii) according to the thermal expansivity of the gas. **(b)** (i) Atomic optical depth (OD) (serving as the background OD) in presence of the cylindrical box potential and the 589 nm optical lattice. For demonstration purposes, we have used a much higher intensity of the optical lattice in (i) than the rest of the experiments. The background subtracted optical depth right after injecting the heat (ii) and after 100 ms of equilibration time (iii) are shown.

optical lattice with a wavelength  $\approx 10 \mu\text{m}$  on one half of the box (Fig. 5-1 (a-i)). Its intensity is first turned on adiabatically to avoid sloshing the density, and then sinusoidally modulated with a frequency that closely matches the resonance frequency  $ck$ , typically between  $2\pi \cdot 1500 - 3000 \text{ Hz}$  (Fig. 5-1 (a-iv)). The modulation is left on for a time that is long enough for heat to flow to the other side of the box and is between 30 and 50 ms for data shown here. This predominantly creates a gradient in temperature across the length of the box (Fig. 5-1 (a-iii)), which has Fourier amplitude that is largest for the lowest mode with  $k = \pi/L$ . The amplitude of the intensity modulation is chosen to create a small but measurable perturbation in temperature, typically between 5 to 10% of the gas temperature.

Typically, absorption imaging is not sensitive to the temperature of the gas<sup>1</sup>, making it difficult to measure the temperature gradient. However, we exploit the coupling between changes in the local temperature and density arising from the non-zero thermal expansivity at constant pressure,  $\alpha = \frac{1}{V} \left( \frac{\partial V}{\partial T} \right)_P$ . For example, at  $T \approx 0.5T_F$  and  $E_F \approx h \cdot 10 \text{ kHz}$ , a temperature perturbation of  $\sim 7\%$  results in a density perturbation of  $\sim 5\%$ . Fig. 5-1 (b) shows the measured change in density accompanying the imprinted temperature gradient, where a local increase in temperature manifests as a local density depletion. This density perturbation decays over  $\sim 100 \text{ ms}$ , indicating a relaxation towards thermal equilibrium (Fig. 5-1 (b-iii)).

Our local temperature probe developed to study the second sound (a wave in temperature or entropy rather than the usual density) [194] would be ideal to study the thermal diffusion as well. There, a radio-frequency (rf) pulse mapped the local temperature of the gas into the density of a third spin state. This mapping relied on a strong dependence of the rate of rf transfer on the local temperature of the gas. For the unitary Fermi gas, the rf response has a peak with a center and a width that strongly varies with the gas temperature, but only for  $T \lesssim 0.4T_F$ , resulting in an rf transfer rate that is approximately linearly dependent on the gas temperature [128]. At higher temperatures, the peak has a center that is approximately constant at the bare atomic

---

<sup>1</sup>At ultracold temperatures, the thermal Doppler shift is much smaller than the linewidth of the imaging transition.

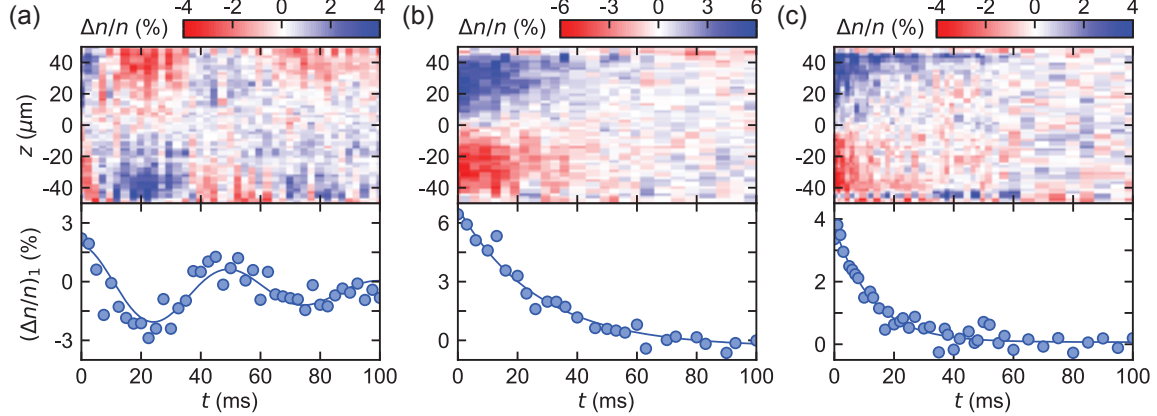


**Figure 5-2: Time evolution of temperature perturbations.** Data is shown for a Fermi gas in the superfluid phase at  $0.1 T_F$  (a) and in normal phase at  $0.25 T_F$  (b) and at  $0.69 T_F$  (c). Top row shows the time evolution of density perturbations averaged over the homogeneous axis of the box and the bottom row shows the amplitude of the first spatial mode of these density perturbations with  $k = \pi/L$ . In the superfluid phase, oscillations in the temperature gradients are observed. In contrast, temperature gradients are observed to decay exponentially in the normal phase.

resonance and a width that is only weakly dependent on the temperature, resulting in a weak dependence of the rf transfer rate on the gas temperature. Therefore, for the range of temperature studied here,  $0.2 T_F \lesssim T \lesssim 1.0 T_F$ , the density probe is more useful than the rf probe.

### 5.1.2 Temporal Evolution of heat

Fig. 5-2 shows the measured time evolution of the temperature gradient both below and above the superfluid transition temperature. Here, we wait a variable time after heating the gas before taking an absorption image. We subtract a background image taken without any temperature perturbation from these images and average the fractional change in density over the homogeneous axis. The resulting  $\Delta n/n$  is shown as a function of evolution time in the top row of Fig. 5-2. We quantify the gradient in the temperature using the amplitude of the first spatial Fourier mode  $(\Delta n/n)_1$  with  $k_1 = 1 \pi/L$ , shown in the bottom row of Fig. 5-2.

The qualitative behavior is strikingly different above and below the superfluid transition. In the superfluid phase, at  $T \approx 0.1 T_F$ , we find the temperature perturba-

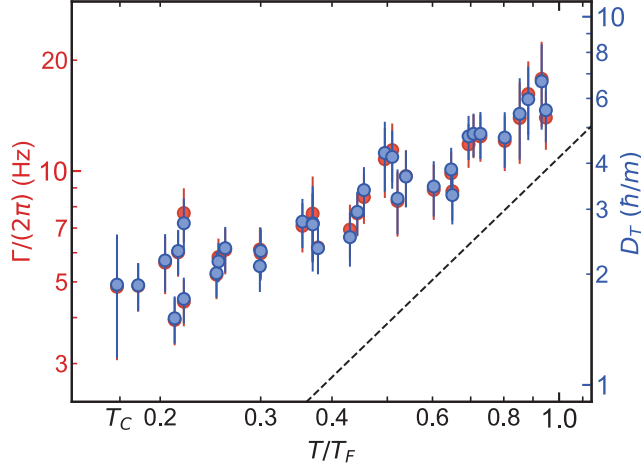


Figure 5-3: **Decay rate of temperature gradient and thermal diffusivity.** The decay rate  $\Gamma$  (red circles, left y-axis) of the first spatial mode with  $k = \pi/L$  is shown for temperatures ranging from the critical temperature  $T_c \approx 0.17 T_F$  to  $\approx 1.0 T_F$ . The extracted thermal diffusivity  $D_T = \Gamma/k^2$  (blue circles, normalized by  $\hbar/m$ , right y-axis) for the same temperature range is also shown. The small differences in  $\Gamma$  and  $D_T$  are from small variations in the length of the box. Near the Fermi temperature, the measured  $D_T$  begins to approach the high temperature prediction [29, 52] (black dashed line).

tion to oscillate in time (Fig. 5-2 (a)), indicating that the injected heat travels like as a wave in this fluid. This heat wave is known as the second sound [], a unique feature originating from the out-of-phase oscillation between the superfluid- and normal-components of the fluid. In the normal phase, the temperature perturbation decays exponentially in time, indicating that the injected heat diffuses from the hotter to colder region of the fluid similar to the flow of heat in air or in metals. The decay rate of the temperature perturbation is seen to increase with the gas temperature when comparing Fig. 5-2 (b) at  $\approx 0.25 T_F$  with Fig. 5-2 (c) at  $\approx 0.69 T_F$ .

### 5.1.3 Thermal Diffusivity

The observation of diffusion of heat permits us calculate the thermal diffusivity  $D_T = \Gamma_j/k_j^2$  from any Fourier component of the temperature perturbation with a decay rate  $\Gamma_j$  and spatial wavenumber  $k_j$ . We use the lowest ( $j = 1$ ) Fourier component since our local heater predominantly creates a temperature perturbation resembling it with a  $k \equiv k_1 = \pi/L$ . We measure  $\Gamma \equiv \Gamma_1$  by fitting the time evolution of  $(\Delta n/n)_1$  with

an exponential function  $\sim e^{-\Gamma t}$ , shown in Fig. 5-2 (b, c). The thermal diffusivity  $D_T$  is shown in Fig. 5-3 as a dual axis to emphasize that  $D_T$  immediately follows from  $\Gamma$ . The small differences between  $\Gamma$  and  $D_T$  arise from small variations in the effective length of the box.

Notice that the determination of  $D_T$  from the decay rate  $\Gamma$  also requires a precise determination of the length  $L$  of the box. While there is no ambiguity in the length of a perfect box, here we have a box with soft edges whose length depends on a particular definition. Typically, we define the length to be the distance between two points where the density is 50% of its mean value. However, it is apriori not clear if the same definition should be used when calculating  $D_T = \Gamma/k^2 \propto L^2$ . The systematic error in  $L$  arising from this uncertainty can be approximated as the total thickness of both edges of the box and is approximately  $\delta L \approx 10 \mu\text{m}$  or  $\delta L/L \approx 0.1$ , resulting in a systematic uncertainty  $\delta D_T/D_T \approx 0.2$ .

We can reduce these systematic uncertainties by independently measuring the thermal diffusivity using techniques that do not require the length of the box. For example, the flow of heat arising from a temperature imbalance also results in a flow of particles as described below. The flow of heat is conveniently described by the Fourier's law  $\mathbf{q} = -\kappa \nabla T$ , where  $\mathbf{q}$  is the heat current density (see eq. 2.21). The non-zero thermal expansivity  $\alpha$  of the gas converts the temperature gradient into a density gradient according to  $dT = \frac{-1}{n\alpha} dn$ , while the heat current gives rise to a particle current according to  $\frac{1}{\rho c_P} \mathbf{q} = \frac{-1}{n\alpha} \mathbf{j}$ . Here, we have used the conservation of energy density  $u$ ,  $\frac{\partial u}{\partial t} + \nabla \cdot \mathbf{q} = 0$ , conservation of particle number,  $\frac{\partial n}{\partial t} + \nabla \cdot \mathbf{j} = 0$ , thermal expansivity  $\alpha = \frac{1}{V} \frac{\partial V}{\partial T}|_P = \frac{-1}{n} \frac{\partial n}{\partial T}|_P$ , and specific heat  $c_P = \frac{1}{\rho} \frac{du}{dT}$ . The resulting particle current is  $\mathbf{j} = -D_T \nabla n$ , also known as the Fick's law of diffusion.

Determining the thermal diffusivity using Fick's law of diffusion only requires the gradient in density and current at some location in the box and is independent of the length of the box. We measure both of these quantities from the time evolution of heat shown in Fig. 5-2. While Fick's law is satisfied at all locations in the box, we specifically measure  $j$  and  $dn/dz$  at the center of the box where their amplitude is the largest. The current is calculated from the change of number imbalance between

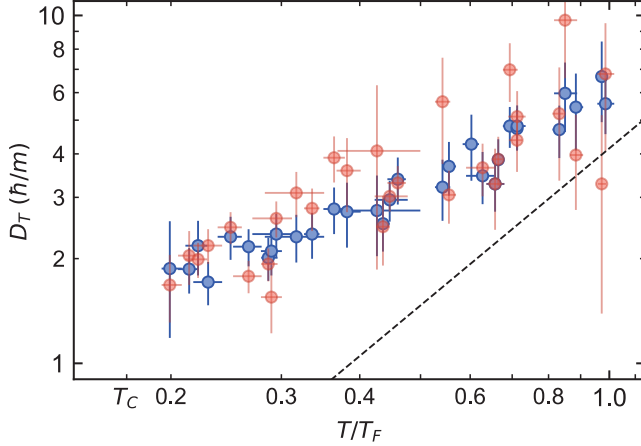


Figure 5-4: **Thermal diffusivity measured from the Fick’s law of diffusion.** Comparison between the thermal diffusivity measured using the heat equation (blue circles, from Fig. 5-3) and using the Fick’s law of diffusion (red circles).

the left ( $N_L$ ) and right ( $N_R$ ) half of the box (measuring the flow of atoms through an imaginary boundary at  $z = 0$ )  $j = \frac{1}{A} \frac{d}{dt} \frac{N_R - N_L}{2}$ . The gradient in density is measured by fitting a polynomial to  $n(z)$  in a small region around  $z = 0$ . The  $D_T = -j/(dn/dz)$  is shown in Fig. 5-4. While this method of determining  $D_T$  produces larger statistical errors, it can be compared with the previous method to limit the systematic errors in the length of the box. Such a comparison suggests that the length of the box relevant for thermal transport is the distance between two points where the density falls to  $\approx 90\%$  of its mean value. Data shown in Fig. 5-3 use this definition of the length.

## 5.2 Viscosity and Thermal Conductivity

For any normal one-component (or spin-balanced) fluid, there are only two transport phenomena; viscous flow and heat conduction corresponding to the conservation of momentum and energy, respectively [170, 108]. They are characterized by three underlying hydrodynamic transport parameters, the thermal conductivity  $\kappa$ , the shear viscosity  $\eta$ , and the bulk viscosity  $\zeta$ . Therefore, a complete characterization of transport phenomena in fluids would typically require three independent measurements. However, in any scale invariant system, such that the internal energy  $E \rightarrow E/\xi^2$  under a spatial rescaling  $r \rightarrow \xi r$ , the ratio  $T/T_F$ , and thus  $S/Nk_B$ , is preserved under

symmetric rescaling of space. This means that a uniform dialation or contraction of the fluid does not change entropy, and the bulk viscosity  $\zeta$  is identically zero at all temperatures [175]. Therefore, measurements of sound attenuation and heat diffusion are sufficient to uniquely determine shear viscosity and thermal conductivity in the normal phase of the unitary Fermi gas.

Note that diffusion of particles does not correspond to a proper transport phenomena in one-component fluids because transport of particles is related to the free movement of the center of mass of the system [170, 108]. Instead, transport of particles is already accounted in heat conduction and in viscous flow. In two-component fluids, such as the spin-balanced Fermi gas considered here, an imbalance in spin concentration leads to a diffusion of particle until equilibrium is reached. This does correspond to a new transport phenomena, the irreversible flow of concentrations, described by the spin diffusivity studied in unitary Fermi gases trapped in a harmonic potential [28, 173, 100, 10, 117].

In Fig. 5-5, we show the extracted values of  $\kappa$  and  $\eta$  as a function of gas temperature. The thermal conductivity is directly proportional to the thermal diffusivity (eq. 2.22),  $\kappa = \rho c_P D_T$ , where we have used the previously measured specific heat [103] shown in Fig. 2-4. Since sound waves attenuate due to gradients in both temperature and momentum, the sound diffusivity  $D_s = \frac{4\eta}{3\rho} + \frac{4\kappa T}{15P}$  (eq. 2.18, [141]) contains contributions from both  $\eta$  and  $\kappa$ . Determining  $\eta = \frac{3\rho}{4} \left( D_s - \frac{4\kappa T}{15P} \right)$  is then straightforward using  $D_s$ ,  $\kappa$ , and the pressure from the equation of state [103] shown in Fig. 2-4. To gain a better understanding, we will consider values of these transport properties in different regimes and systems, starting with the high temperature  $T \gg T_F$  regime.

Kinetic theory is perhaps the simplest model that can describe transport phenomena. It assumes that the particles in a gas move ballistically with minimal interactions and constantly collide with each other like hard spheres (elastic collisions). In interacting systems, kinetic theory is only applicable if the excitations of the system can effectively be described by an ensemble of long-lived quasi-particles [161]. At high temperatures, atoms in the unitary Fermi gas have an energy  $\sim k_B T$  and a scattering rate  $\Gamma \sim n\sigma v \propto 1/\sqrt{T}$  (or lifetime  $\sim 1/\Gamma$ ), where  $\sigma \propto 1/T$  is the unitarity-

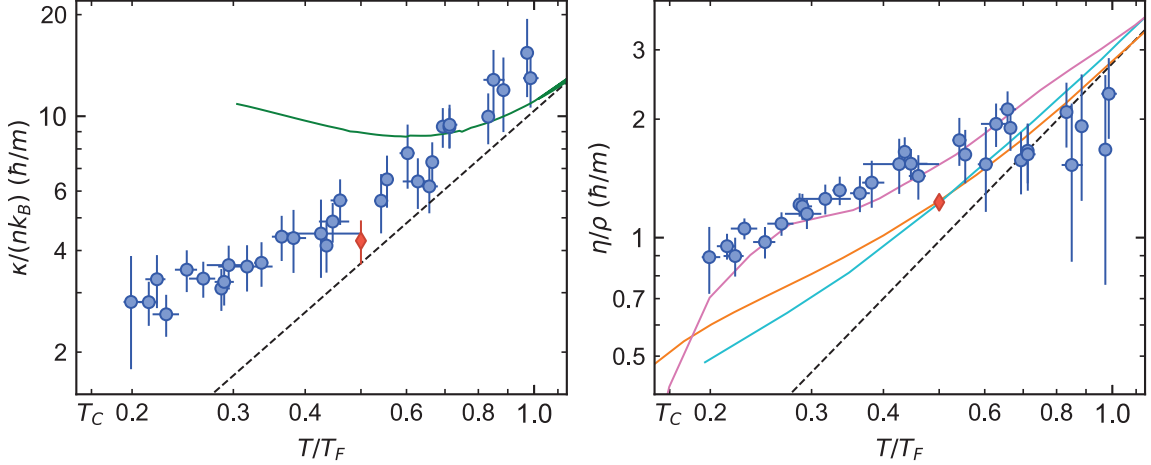


**Figure 5-5: Transport properties of the spin-balanced, unitary Fermi gas.** By combining our measurements of thermal- and sound diffusivities [141], and the equation of state [103], we calculate the thermal conductivity  $\kappa$  and shear viscosity  $\eta$ . Temperature dependence of **(a)**  $\kappa$  divided by the number density  $n$  and Boltzmann's constant  $k_B$  (blue circles, normalized by  $\hbar/m$ ) and **(b)**  $\eta$  divided by the mass density  $\rho = nm$  (blue circles, normalized by  $\hbar/m$ ) are shown. Both transport properties approach the expected high temperature scaling of  $T^{3/2}$  (dashed black line [25]) close to  $T_F$ . In the normal phase of the degenerate regime  $T_c < T \ll T_F$ , we do not observe any divergence expected from the Fermi liquid theory [2, 13], instead, as the temperature is lowered, both transport properties monotonically decrease and attain a Heisenberg limited value close to  $\hbar/m$ . Previous measurements of  $\kappa$  in a uniform box (red diamond [7]) and of  $\eta$  in harmonic trap (pink line [90], cyan line [22]), as well as theoretical predictions for  $\eta$  (orange line [52]) and for  $\kappa$  (green line [56]) are shown.

limited collision cross-section and  $v \propto \sqrt{T}$  is the thermal velocity. Since the ratio  $\frac{\hbar\Gamma}{k_B T} \propto T^{-3/2} \rightarrow 0$  at very high temperatures, atoms in the gas constitute well-defined quasi-particles and the kinetic theory description is applicable xxx. In this theory,  $\eta \simeq \rho\tau_\eta v^2$  and  $\kappa \simeq c_P \rho\tau_\kappa v^2$  are determined by the typical quasiparticle velocity  $v \propto \sqrt{T}$  and the mean-free-time of momentum and energy changing collisions  $\tau_\eta$  and  $\tau_\kappa \sim 1/(n\sigma v) \propto \sqrt{T}$ , yielding a scaling  $\eta \propto T^{3/2}$  and  $\kappa \propto T^{3/2}$ . An exact calculation using the Boltzmann equation yields  $\kappa/(nk_B) = 10.38(\hbar/m)(T/T_F)^{3/2}$  [25] and  $\eta/\rho = 2.77(\hbar/m)(T/T_F)^{3/2}$  [29, 52], shown in black dashed line in Fig. 5-5, which captures our measurements well without any free parameters.

As the gas cools and becomes degenerate  $T \sim T_F$ , Pauli blocking and the emerging Fermi surface begins to play an important role. While the quasi-particle description

may not hold at these temperatures, we can continue to use the kinetic theory equations to estimate the effects of Pauli blocking on transport properties. In this regime, we expect both the mean velocity and mean-free-time to be larger than their high temperature scaling because Pauli blocking limits the mean velocity to the Fermi velocity and reduces the phase space available for momentum and energy exchanging collisions. Since  $\eta, \kappa \propto \tau v^2$ , we expect their values to be higher than the high temperature predictions, consistent with our observations at  $T \lesssim 1.0 T_F$ .

The normal phase of a typical fermionic system in the deeply degenerate limit  $T \ll T_F$  is often described by the Fermi liquid theory [13, 2]. A Fermi liquid contains quasiparticles whose mean velocity  $v \approx v_F$  is saturated at the Fermi velocity and scattering rate  $\Gamma \propto T^2$  displays a paradigmatic quadratic scaling with temperature. It shares a lot of thermodynamic properties with the non-interacting Fermi gas, but with a modified mass  $m^*$ , for example a temperature dependent heat capacity  $C \propto T/T_F$ , where  $T_F = \frac{\hbar^2 k_F^2}{2m^*}$ . Its transport properties are calculated using kinetic theory, which predicts diverging shear viscosity  $\eta \sim \rho v^2/\Gamma \propto 1/T^2$  and thermal conductivity  $\kappa \sim c_P \rho v^2/\Gamma \propto 1/T$ , observed in liquid helium 3 [76, 189]. However, we do not observe these diverging transport properties, instead, both  $\eta/\rho$  and  $\kappa/(nk_B)$  monotonically decrease and attain values  $\sim \hbar/m$ .

We can gain valuable insight about transport processes from the ratios of different transport properties. For example, the Wiedemann-Franz law states that the ratio of the thermal- ( $\kappa$ ) to electrical conductivity ( $\sigma$ ) in all metals remains proportional to the temperature,  $\kappa/\sigma = LT$ , with a proportionality constant  $L$ , the Lorentz number, that is independent of temperature and same in all metals [6, 99]. This follows from the fact that in metals, the same sea of mobile electrons are responsible for transport of both energy and charge. Most metals close to room temperatures display this behavior with approximately the same  $L \approx \frac{\pi^2 k_B^2}{3e^2}$ . Any deviations from this law typically indicates a change in the underlying microscopic transport processes. For example, spin-charge separation in quasi-one-dimensional materials lead to a violation of this law with  $L$  reaching values orders of magnitude higher at degenerate temperatures [190]. In metallic vanadium dioxide nanobeams, the electronic contribution to the thermal

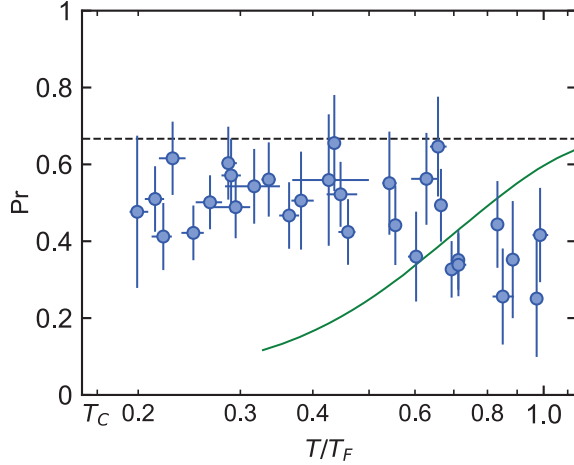


Figure 5-6: **Prandtl number.** The Prandtl number  $\text{Pr} = c_P \eta / \kappa$  calculated from transport properties shown in Fig. 5-5. While  $\eta$  and  $\kappa$  deviate from their high-temperature and Fermi-liquid predictions at low-temperatures, their ratio  $\text{Pr}$  remains close to its high-temperature value  $2/3$  [25, 56]. A theoretical prediction is shown, green line [56].

conductivity is observed to be much smaller than expected [110], indicating that in presence of strong interactions charge and heat might propagate independently. The breakdown Wiedemann-Franz law was also observed in two reservoirs of the unitary Fermi gas connected via very small one-dimensional channel [86], where they measured a Lorentz number about factor of 10 smaller than expected.

In typical gases, the same underlying particles transport both momentum and heat, resulting in the ratio  $c_P \eta / \kappa \equiv \text{Pr}$ , known as the Prandtl number, to remain approximately constant. Most gases feature a Prandtl number close to  $2/3$  [170] while its value in viscous liquids, like glycerol, can be orders of magnitude higher. The extracted values of  $\text{Pr}$  are shown in Fig. 5-6. Even though the two transport properties deviate significantly from both the high-temperature and Fermi-liquid predictions, their ratio, the Prandtl number  $\text{Pr} = c_P \eta / \kappa$ , remains approximately constant and close to its high temperature value of  $2/3$ . This indicates that even though the strongly interacting Fermi gas isn't described by well defined quasi-particles, the transport of both momentum and heat is carried out by the same underlying mechanism. A similar behavior is observed in the pseudogap phase of high-temperature cuprate superconductors [126]. There, the electrical conductivity displays a  $1/T$  de-

pendence instead of  $1/T^2$  expected from the Fermi liquid theory, indicating absence of quasi-particles, however, the ratio of electrical to thermal conductivity follows the classical Wiedemann-Franz law, indicating that the same underlying mechanism transports both charge and heat. It is unclear if similar behavior can be expected for all strongly interacting quantum systems.



# Chapter 6

## Summary and Outlook

In previous chapters, we have described two experiments performed on the spin-balanced, strongly-interacting, homogeneous Fermi gas to completely characterize its transport properties in the small-amplitude and low-frequency limit where linear-hydrodynamics is applicable. First, the coupled transport of momentum and heat was measured from the properties of sound waves. A precise measurement the speed of sound made it possible to test the scale-invariance of the unitary Fermi gas. The attenuation rate of sound waves displayed the characteristic  $\propto k^2$  scaling expected from hydrodynamics, from which we measured the sound diffusivity  $D_s$ . Second, the transport of heat was independently measured from the thermal evolution of temperature perturbations. They were observed to decay exponentially in time, indicating the diffusion of heat expected from hydrodynamics. Their decay rate enabled us to measure the thermal diffusivity  $D_T$ . And last, by combining the measurements of  $D_s$  and  $D_T$ , we calculated the two non-zero transport properties of this system, the shear viscosity  $\eta$  and the thermal conductivity  $\kappa$ .

Their values at high-temperatures  $T \gg T_F$  can be understood from kinetic theory where the relevant quasi-particles are the resonantly interacting fermions. However, as the temperature is reduced, Pauli blocking and the emerging Fermi surface begins to play an important role and the underlying transport theory becomes less and less clear. The degenerate regime of typical fermionic systems are well described by the Fermi-liquid theory, which assumes long-lived quasi-particle excitations near the

Fermi surface. However, here, strong-interactions lead to strong-correlations, placing a doubt on the applicability of theories based on quasi-particles. We do not observe diverging  $\eta \propto 1/T^2$  and  $\kappa \propto 1/T$  expected from the Fermi-liquid theory, instead, they monotonically decrease and attain values  $\propto \hbar/m$ . These measurements provide a benchmark for transport properties of strongly-interacting Fermi systems and inform theories.

We had began this thesis with a goal to measure the transport properties of the strongly-interacting Fermi gas and posed a few basic questions in the introduction. We would like to address them here.

1. *What are the transport properties of a spin-balanced, resonantly interacting Fermi gas?*

I would claim that we have successfully measured them, summarized above. The realization of a homogeneous unitary Fermi gas trapped in a uniform box potential was crucial for this task.

2. *Is it possible to describe the transport properties of this system using well-defined quasi-particles?*

I had indicated in the introduction that this question is more for theorists, but the experimental measurements presented here could serve as a benchmark. One thing is clear from the data presented here; the Fermi-liquid theory, based on quasi-particles near the Fermi surface, without any modification, is not adequate to describe the normal phase of the unitary Fermi gas. In contrast, a forced normal state at  $T < T_c$ , made stable by spin-imbalance, was previously observed to be described by a Fermi-liquid theory [132]. This question deserves further investigation described in the outlooks. Another possibility is the existence of a pseudo-gap phase where pair-excitations could exist without long range order [87, 151, 199].

3. *Do theories developed to explain the anomalous transport properties of unconventional superconductors, like quantum critical transport and incoherent transport, also apply to the strongly-interacting Fermi gas?*

These theories are based on the idea that the dissipative timescales in transport processes are universal,  $\tau \sim \hbar/(k_B T)$ , and scale inversely with the temperature. However, we do not directly measure these time scales and cannot comment on their validity without further investigations. A recent theoretical prediction [56] based on quantum critical transport agrees well with the measured  $\kappa$ , but only at  $T \gtrsim 0.5T_F$  and fails at lower temperatures.

4. *Are there common features in the transport properties of all strongly interacting quantum matter?, hinting at the possibility of describing them all with a universal theory.*

Interestingly, yes. For example, we have found the sound diffusivity of the unitary Fermi gas to closely resemble the properties of a strongly-interacting, but bosonic liquid  $^4\text{He}$ , instead of a fermionic, but weakly-interacting liquid  $^3\text{He}$ . Implying that strong-interactions are taking a precedence over the quantum statistics of the particles with regards to their transport properties. Another example is the fact that most strongly interacting quantum systems feature anomalous transport properties that are not described by existence of quasi-particles.

With these measurements, we have demonstrated the power of uniform traps. There is a lot more that we would have liked to do, here are a few examples.

**Transport beyond linear-hydrodynamics.** In this thesis, we have mainly focused on perturbations that are small in amplitude, low in frequency, and low in wavenumber, which are described by linear hydrodynamics. While this is a good start, it is far from a complete characterization of all non-equilibrium properties of this system. We have already seen two signatures of transport that cannot be described by hydrodynamics. First, increasing the amplitude of a sound wave makes it decay at a faster rate, prominently evident at lower temperatures and for the lowest two resonant modes of the box. Here, we observe an spontaneous generation of higher harmonics, observed as non-sinusoidal spatial profiles visible in both position and Fourier space. This could result from the non-linear terms in the energy of a sound wave [1], the

density dependence of the speed of sound [19], or phonon-phonon interactions [106]. The fact that we observe these non-linearity more prominently at lower temperatures, especially  $T \lesssim 0.2 T_F$  and in the superfluid phase, may signal some interesting physics. And second, perturbations with a frequency higher than the relaxation rate of typical thermal excitations featured  $\Gamma \propto k^2$ . Here, transport physics is described by a collisionless transport [186, 106], where interactions between phonons and other thermal excitations need to be considered, and the specific concavity of the dispersion relation may play an important role [105].

**Properties of a spin-imbalanced strongly-interacting Fermi gas.** One of the main motivations for creating a uniform trap was to study the spin-imbalanced Fermi gas. Superfluidity in spin-imbalance systems is an interesting problem. Standard cooper-pairing happens between two atoms of opposite spins and opposite momenta near their common Fermi surface. However, in a spin-imbalanced system, the two Fermi surfaces are located at different energies and pairing between opposite momenta is not possible. This puts the stability of a superfluid in presence of spin-imbalance into question [12, 152, 143, 139], and, at a sufficiently high spin-imbalance, known as the Chandrasekhar-Clogston limit [36, 41, 12], requires superfluidity to breakdown. Below this limit, a superfluid state might be described by pairing between opposite spin atoms with different momenta, i.e., pairs with a finite momentum, known as the Fulde-Ferrell-Larkin-Ovchinnikov (FFLO) state [139, 58, 150]. Here, the superfluid order parameter oscillates in space at the pairing momentum, which might be observed as an oscillation in the spin imbalance. While the FFLO state has been extensively studied, it has yet to be confirmed experimentally in 3D [150]. Apart from the FFLO state, the phase diagram of a spin-imbalanced Fermi gas in general is an interesting topic of study.

Studying spin-imbalanced gases in a harmonic trap is challenging because the minority atoms preferentially accumulate at the center of the trap, creating a nearly spin-balanced Fermi gas, while the access majority atoms live outside, creating a nearly spin-polarized gas. At  $T < T_c$ , this results in a phase separation, where the center is spin-balanced superfluid while the outer shell is a spin-polarized, ideal Fermi

gas [140, 168, 169, 205]. In contrast, spin-imbalanced Fermi gases in an uniform box necessarily have to remain spin-imbalanced, opening the possibility to further investigate the strongly-interacting Fermi gases in presence of spin-imbalance and to look for the FFLO state.

Ultracold atoms experiment provide a highly tunable and accessible system whose Hamiltonian is exactly known, with the ability to precisely control, and even turn off, its complexities. These are ideal systems for the study of strongly-interacting quantum matter. The addition of homogeneous samples opens the door to many new types of experiments that look for new phases of matter and shed light on their properties. I truly believe that we are only at the dawn of understanding many-body quantum physics, with a future powered by unimagined quantum devices.



# Appendix A

## New apparatus to study ultracold atoms under rapid rotation

In this chapter, I want to present some of the tools we have made for a new experiment called *Fermi 3*, with a goal to study two and three dimensional quantum gases under rapid rotation.

### A.1 Zeeman slower

Zeeman slower is the first in a series of tools used to cool atoms down to nano-Kelvin temperatures. It cools atoms from  $\sim 650$  K down to a few mK by repeatedly bouncing resonant photons against an atomic beam. We will begin with the basics of a Zeeman slower followed by its design and construction.

**Basics of a Zeeman slower** The main idea behind a Zeeman slower is to slow an atomic beam using a laser beam traveling in the opposite direction. The main challenge is to keep the laser beam on resonance as the Doppler shift reduces with the atomic velocity. A simple approach is to chirp the laser frequency as the atoms slow [148], however this produces bunches of atoms rather than a continuous stream. In a Zeeman slower, the reducing Doppler shift from slowed atoms is compensated by the Zeeman shift from an increasing magnetic field strength [146]. If  $B(z)$  is chosen such that it exactly compensates the Doppler shift, the atoms experience a constant

decelerating force. This serves as the starting point to designing a Zeeman slower.

We begin by assuming an ideal situation with a constant force  $-\gamma(\hbar k_L \Gamma / 2)$  and deceleration  $a = \gamma \hbar k_L \Gamma / (2m) \equiv \gamma a_{\max}$  (see Sec. 3.3.2 or [55, 42] for details). Here  $\gamma$  is a tuning parameter that multiplies the maximum possible force at saturated intensity. Selecting a smaller value of  $\gamma$  allows for larger imperfections in the magnetic field. Assuming the atoms start with an initial velocity  $v_c$  (the capture velocity of the Zeeman slower) at  $z = 0$ , the equation of motion is  $z(t) = -\gamma a_{\max} t^2 / 2 + v_c t$  and  $v(t) = -\gamma a_{\max} t + v_c$ . The atoms slow from velocity  $v_c$  to close to zero in time  $T = v_c / (\gamma a_{\max})$  and in distance  $L = v_c^2 / (2\gamma a_{\max})$ . Finally, by combining  $z(t)$  and  $v(t)$ , we find the position dependence of the velocity,

$$v(z) = v_c \sqrt{1 - z/L}. \quad (\text{A.1})$$

In a Zeeman slower, the reducing Doppler shift,  $\omega_D = k_L v(z)$ , is exactly compensated with a Zeeman shift,  $\omega_Z(z) = (\mu_B / \hbar) g_{FM} B(z)$ , such that the total detuning  $\omega_D + \omega_Z = \omega_0 - \omega_L$  stays constant and independent of  $z$ . It is typical to perform Zeeman slowing on stretched states where  $g_{FM} = 1$  and to red detune the slower laser by the maximum Doppler shift,  $\omega_0 - \omega_L = k_L v_c$ . With these assumptions, the ideal magnetic field is

$$\begin{aligned} B(z) &= \frac{\omega_0 - \omega_L}{\mu_B / \hbar} - \frac{k_L}{\mu_B / \hbar} v(z), \\ &= B_0 \left( 1 - \sqrt{1 - z/L} \right), \end{aligned} \quad (\text{A.2})$$

where  $B_0 = \hbar k_L v_c / \mu_B$ . Here, the magnetic field steadily increases from 0 to  $B_0$  over the length  $L$  of the slower. This is known as an increasing field Zeeman slower.

There are other types of slower suited for different systems. In a decreasing field Zeeman slower, the magnetic fields start from  $B_0$  and go down to 0. This type of slower is usually ill suited for experiments with a MOT. It requires the slower laser to be near resonant with the MOT, possibly causing undesirable heating. Another example is a spin-flip Zeeman slower. For experiments that require high capture

		value	for $^{23}\text{Na}$ D <sub>2</sub>	Description
constants & atomic properties	$\mu_B$		$\hbar \cdot 1.3996 \text{ MHz/G}$	Bohr magneton
	$m$		$3.8175 \cdot 10^{-26} \text{ kg}$	atomic mass
	$\omega_0$		$2\pi \cdot 508.849 \text{ THz}$	resonance frequency
	$\Gamma$		$2\pi \cdot 9.795 \text{ MHz}$	decay rate
inputs	$v_c$		589 m/s	capture velocity
	$\gamma$		0.417	tuning parameter
useful quantities	$a_{\max}$	$\hbar k_L \Gamma / (2m)$	906533 m/s <sup>2</sup>	max. deceleration
	$L$	$v_c^2 / (2\gamma a_{\max})$	45.9 cm	slower length
	$v(z)$	$v_c \sqrt{1-z/L}$		atoms' velocity
	$\delta\omega$	$-k_L v_c$	- $2\pi \cdot 1.0 \text{ GHz}$	laser detuning
	$\omega_L$	$\omega_0 - k_L v_c$		laser frequency
	$k_L$	$\omega_L/c \approx \omega_0/c$		laser wavenumber
	$B_0$	$\hbar k_L v_c / \mu_B$	714.3 G	max. magnetic field
	$B(z)$	$B_0(1 - \sqrt{1-z/L})$		magnetic field

Table A.1: **Zeeman slower.** Natural constants and atomic properties are from [179]. We have omitted standard error and provided reduced precision here.

velocity, the standard increasing field slower may require too high of magnetic field than desired. In this situation, it is better to use a spin flip slower where the magnetic fields first decrease in magnitude, got to zero and change direction, and then increase in magnitude.

In summary, designing an increasing field Zeeman slower begins by first determining the desired capture velocity  $v_c$  and tuning parameter  $\gamma$ . These, combined with physical properties of the atom, determine everything about the slower as summarized in Table A.1.

**$^{23}\text{Na}$ - $^6\text{Li}$  Zeeman slower.** Now, we will describe the specific design and considerations used for the Fermi 3 Zeeman slower.

Capture velocity  $v_c = 589 \text{ m/s}$ : Ideally, we would like a very high capture velocity to increase the flux of slow atoms. However, this may require unfeasibly high magnetic field, oven temperature, and long slower. For  $\approx 650\text{K}$  oven,  $v_c = 589 \text{ m/s}$  is optimal.

Tuning parameter  $\gamma = 0.417$ : Ideally, we would like  $\gamma \sim 1$  to minimize the length of the slower. However, this requires a very high slower laser intensity and a near-perfect electromagnet. In practice, we can expect a laser intensity  $I \sim I_{\text{sat}}$  (already limiting  $\gamma \lesssim 0.5$ ) and an electromagnet with magnetic field deviations  $\delta B \lesssim \hbar\Gamma/\mu_B$ .

We find  $\gamma \sim 0.4$  to be a good balance between slower length and electromagnet requirements. Specifically, we use  $\gamma = 0.4173$  with slower length of 45.9 cm.

In the new experiment, we use a dual species slower, where both the  $^{23}\text{Na}$  and  $^6\text{Li}$  are slowed in the same slower. This is typically possible between any two atoms if they have somewhat similar capture velocities and deceleration, and they are chemically stable enough to create a dual species oven. It is sufficient to design the slower for the heavier atoms with its lower deceleration,  $^{23}\text{Na}$  in our case.

## A.2 Time-averaged orbiting potential

Magnetic time-averaged orbiting potential (TOP) was first introduced to remove Majorana losses caused by the zero of the magnetic field of a quadrupole magnetic trap [145]. In a TOP trap, the atoms experience an effective harmonic potential. Since this harmonic trap is made from magnetic fields, it is void of many imperfections that typically arise in optical traps. Hence, TOP trap can be tuned to create a remarkably circular and imperfection free harmonic trap useful for studying atoms under rotation.

In this section, we will begin with the basics of a TOP trap and its implementation. We will examine various experimental imperfections and ways to resolve them. Finally, we will describe the alignment procedure and characteristics.

**Experimental implementation** The basic working principle of the TOP trap is summarized. The atoms are subjected to a force whose direction is rapidly rotating in a circle but its magnitude is kept constant. The frequency of this rotation is kept high enough such that the atoms experience a time averaged force. It is easy to see that an atom at the center experiences a net zero force. When an atom moves away from the center, it experiences the inward force for a longer period of time than the outward force, resulting in a net restoring force towards the center. The exact nature and position dependence of this restoring force is described below.

In the experiment, the constant magnitude force is provided by a set of anti-Helmholtz coils producing a gradient in magnetic field  $\{b'x, b'y, -2b'z\}$ . The center of

this magnetic field gradient is moved around in the  $xy$ -plane by two bias coils. The net magnetic field is

$$\mathbf{B}(\mathbf{r}, t) = \begin{pmatrix} b'x \\ b'y \\ -2b'z \end{pmatrix} + \begin{pmatrix} b_0 \cos(\omega_T t) \\ b_0 \sin(\omega_T t) \\ 0 \end{pmatrix}, \quad (\text{A.3})$$

and the potential energy is  $U = -\boldsymbol{\mu}_B \cdot \mathbf{B} = \mu_B g_F (\mathbf{F}/\hbar) \cdot \mathbf{B}$ . At ultracold temperatures, the atoms move slow enough such that their spin adiabatically follows the local magnetic field direction, i.e.  $\hat{\mathbf{F}} \parallel \hat{\mathbf{B}}$ , resulting in  $U = \mu_B g_F m_F |\mathbf{B}|$ . We first find the magnitude of the magnetic field,

$$\begin{aligned} |\mathbf{B}| &= B = \sqrt{b'^2(x^2 + y^2 + 4z^2) + b_0^2 + 2b'b_0(x \cos \omega_T t + y \sin \omega_T t)} \\ &= b_0^2 \sqrt{1 + (x^2 + y^2 + 4z^2)/R^2 + 2(x \cos \omega_T t + y \sin \omega_T t)/R}, \end{aligned}$$

where we have defined the characteristic length  $R = b_0/b'$ . Note that for typical gradient  $b' \sim 100$  g/cm and bias  $b_0 \sim 10$  g, this length  $R \sim 10$  cm is much larger than the typical size of the BEC  $\sim 100$   $\mu\text{m}$ . By substituting  $x_i/R = \tilde{x}_i$  and expanding for small  $\tilde{x}_i \ll 1$ , we get

$$B \approx b_0 \left( 1 + \frac{\tilde{x}^2 + \tilde{y}^2 + 4\tilde{z}^2}{2} + \frac{2\tilde{x} \cos \omega_T t + 2\tilde{y} \sin \omega_T t}{2} - \frac{(2\tilde{x} \cos \omega_T t + 2\tilde{y} \sin \omega_T t)^2}{8} \right) \quad (\text{A.4})$$

Finally, assuming that the atoms are in the stretched state with  $g_F m_F = 1$ , the time-averaged potential experienced by the atoms is

$$\begin{aligned} U_{\text{TOP}}(\mathbf{r}) &= \frac{2\pi}{\omega_T} \int_0^{2\pi/\omega_T} dt \mu_B |\mathbf{B}(\mathbf{r}, t)| \\ &\approx \mu_B b_0 \left( 1 + \frac{\tilde{x}^2 + \tilde{y}^2 + 4\tilde{z}^2}{2} + \frac{0}{2} - \frac{2\tilde{x}^2 + 2\tilde{y}^2}{8} \right) \\ &= \mu_B b_0 + \frac{\mu_B b'^2}{4b_0} (x^2 + y^2 + 8z^2), \end{aligned} \quad (\text{A.5})$$

where we've only kept terms up to  $\mathcal{O}(\tilde{x}_i)^2$ . Comparing Eq. A.5 to a hamronic po-

tential, we find the effective trapping frequency of  $\omega_r = \sqrt{(\mu_B b'^2) / (2mb_0)}$  along the radial  $x$  and  $y$  directions and  $\omega_z = \sqrt{8}\omega_{T_r}$  along the  $z$  direction. The radius of the trap is  $R = b_0/b'$  and the trap depth is  $\mu_B b_0/4$ .

**Experimental imperfections** We discussed the ideal case of the magnetic TOP trap above. There are several things that can be misaligned from this ideal case. First, it is possible that the angle between the two bias coils is not perfectly  $\pi/2$ . This will admix a small fraction of one bias into the other. Second, the bias coils may have different impedances, resulting in a different phase shift and amplitude between the drive voltage and magnetic fields. We will show how these imperfections can be fixed by fine-tuning the amplitude and phase shift of the two drive signals.

Suppose the two drive voltages for bias coils are  $V_1 \cos(\omega_T t)$  and  $V_2 \sin(\omega_T t)$ . This will induce current in two coils,  $I_1 \cos(\omega_T t)$  and  $I_2 \cos(\omega_T t + \phi)$ , where  $\phi$  takes into account the possible phase difference resulting from different impedances. The resulting magnetic fields in the two bias coils are  $B_1 \cos(\omega_T t)\hat{x}$  and  $B_2 \sin(\omega_T t + \phi)(\hat{x} \sin \theta + \hat{y} \cos \theta)$ , where we have allowed the second coil to be off by an angle  $\theta$ .

A perfectly circular TOP trap requires  $B_1/B_2 \rightarrow 1$  and  $\phi, \theta \rightarrow 0$ . Any deviations will result in an elliptical trap. For example, a trap with ellipticity smaller than 1%, i.e.  $\omega_{T_x}/\omega_{T_y} \sim 0.99$ , requires  $B_1/B_2 \sim 0.96$  and  $\phi, \theta \lesssim 2.4$  deg. While the amplitude of the bias magnetic field can be made equal by fine tuning  $V_1$  and  $V_2$ , it is often not possible to fine tune the impedance and angle of the coils. An alternate approach is to compensate for their effect by introducing an additional phase shift  $\beta$  between the two drive voltages,  $V_2 \sin(\omega_T t + \beta)$ . By setting  $\beta = \theta - \phi$ , we can exactly remove these imperfections.

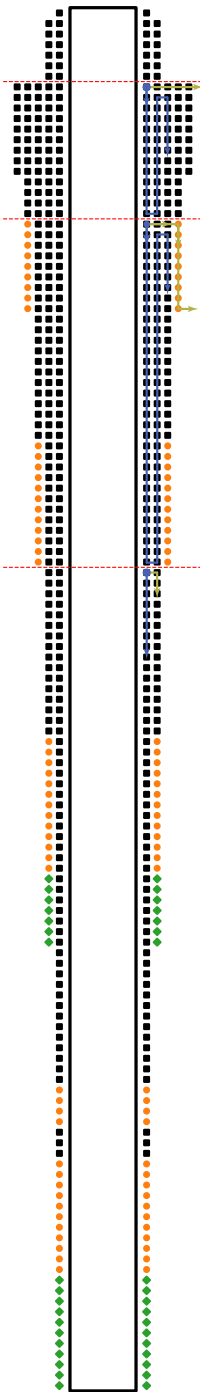


Figure A-1: **Schematics for the Zeeman slower.** Black square, orange circles, and green diamonds correspond to winding with unit density, half density, and a third density, respectively. Red dashed lines separate the four sections of the slower. Blue and yellow lines show the direction of coil winding, where the blue circle marks the starting point.



## Appendix B

### Homogeneous Atomic Fermi Gases

This appendix contains a reprint of Ref. [130]:



## Homogeneous Atomic Fermi Gases

Biswaroop Mukherjee,<sup>1</sup> Zhenjie Yan,<sup>1</sup> Parth B. Patel,<sup>1</sup> Zoran Hadzibabic,<sup>1,2</sup> Tarik Yefsah,<sup>1,3</sup> Julian Struck,<sup>1</sup> and Martin W. Zwierlein<sup>1</sup>

<sup>1</sup>*MIT-Harvard Center for Ultracold Atoms, Research Laboratory of Electronics, and Department of Physics, Massachusetts Institute of Technology, Cambridge, Massachusetts 02139, USA*

<sup>2</sup>*Cavendish Laboratory, University of Cambridge, J. J. Thomson Avenue, Cambridge CB3 0HE, United Kingdom*

<sup>3</sup>*Laboratoire Kastler Brossel, CNRS, ENS-PSL Research University, UPMC-Sorbonne Universités and Collège de France, Paris 75005, France*

(Received 31 October 2016; published 23 March 2017)

We report on the creation of homogeneous Fermi gases of ultracold atoms in a uniform potential. In the momentum distribution of a spin-polarized gas, we observe the emergence of the Fermi surface and the saturated occupation of one particle per momentum state: the striking consequence of Pauli blocking in momentum space for a degenerate gas. Cooling a spin-balanced Fermi gas at unitarity, we create homogeneous superfluids and observe spatially uniform pair condensates. For thermodynamic measurements, we introduce a hybrid potential that is harmonic in one dimension and uniform in the other two. The spatially resolved compressibility reveals the superfluid transition in a spin-balanced Fermi gas, saturation in a fully polarized Fermi gas, and strong attraction in the polaronic regime of a partially polarized Fermi gas.

DOI: 10.1103/PhysRevLett.118.123401

Ninety years ago, Fermi derived the thermodynamics of a gas of particles obeying the Pauli exclusion principle [1]. The Fermi gas quickly became a ubiquitous paradigm in many-body physics; yet even today, Fermi gases in the presence of strong interactions pose severe challenges to our understanding. Ultracold atomic Fermi gases have emerged as a flexible platform for studying such strongly correlated fermionic systems [2–6]. In contrast to traditional solid state systems, quantum gases feature tunable spin polarization, dimensionality, and interaction strength. This enables the separation of quantum statistical effects from interaction-driven effects, and invites the exploration of rich phase diagrams, for example bulk Fermi gases in the BEC-BCS crossover [3–10] and Fermi-Hubbard models in optical lattices [11–20].

So far, Fermi gas experiments have been performed in inhomogeneous traps, where the nonuniform density leads to spatially varying energy and length scales. This poses a fundamental problem for studies of critical phenomena for which the correlation length diverges. Furthermore, in a gas with spatially varying density, a large region of the phase diagram is traversed, potentially obscuring exotic phases that are predicted to occur in a narrow range of parameters. This is most severe for supersolid states, such as the elusive FFLO state [21–23], where the emergent spatial period is well defined only in a homogeneous setting. A natural solution to these problems is the use of uniform potentials, which have recently proved to be advantageous for thermodynamic and coherence measurements with Bose gases [24–27].

Here, we realize homogeneous Fermi gases in a versatile uniform potential. For spin-polarized gases, we observe both the formation of the Fermi surface and the saturation at

one fermion per momentum state, due to Pauli blocking. Spatially uniform pair condensates are observed for spin-balanced gases, offering strong prospects for the exploration of long-range coherence, critical fluctuations, and supersolidity.

In cases where the local density approximation (LDA) is valid, the spatially varying local chemical potential in an inhomogeneous trap can be utilized for thermodynamic [28–31] and spectroscopic [7,32,33] measurements. However, reconstructing the local density from line-of-sight integrated density profiles typically increases noise, while spatially selecting a central region of the gas reduces signal. A potential that is uniform along the line-of-sight is the natural solution. Combining the desirable features of homogeneous and spatially varying potentials, we introduce a hybrid potential that is uniform in two dimensions and harmonic in the third. The line-of-sight integration is now turned into an advantage: instead of averaging over a wide region of the phase diagram, the integration yields a higher signal-to-noise measurement of the local density. Using this geometry, we observe the characteristic saturation of isothermal compressibility in a spin-polarized gas, while a strongly interacting spin-balanced gas features a peak in the compressibility near the superfluid transition [31].

In our experiment, we prepare atoms in the two lowest hyperfine states of  ${}^6\text{Li}$  near a Feshbach resonance, and load them into the uniform potential of the optical box trap depicted in Fig. 1(a), after evaporative precooling in a crossed dipole trap. We typically achieve densities and Fermi energies of up to  $n \approx 10^{12} \text{ cm}^{-3}$  and  $E_F \approx \hbar \times 13 \text{ kHz}$ , corresponding to  $\sim 10^6$  atoms per spin state in the box. The lifetime of the

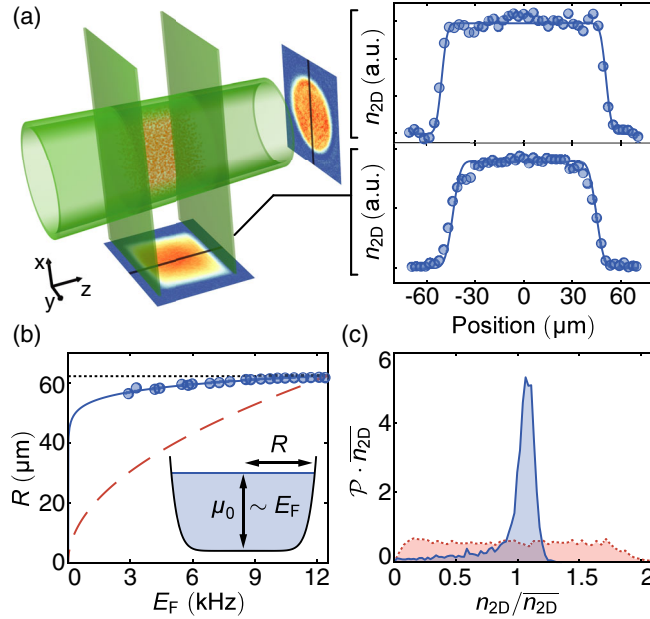


FIG. 1. Homogeneous Fermi gas. (a) Schematic of the box trap and cuts through the column-integrated density profiles along the axial and radial directions. (b) Radius of the cloud as a function of the Fermi energy. The dotted black and dashed red lines correspond to a perfect box potential and a harmonic potential, respectively, and are scaled to converge at the highest  $E_F$ . The blue solid line corresponds to a power law potential  $V(r) \sim r^{16}$ . (c) Measured radial probability density  $P(n_{2D})$  for the column-integrated density  $n_{2D}$ , averaging about 20 in-trap images. The blue solid and red dashed lines correspond to the uniform and Gaussian traps, respectively.

Fermi gas in the box trap is several tens of seconds. The uniform potential is tailored using blue-detuned laser light for the confining walls. The sharp radial trap barrier is provided by a ring beam generated by an axicon [34,35], while two light sheets act as end caps for the axial trapping [36]. Furthermore, the atoms are levitated against gravity by a magnetic saddle potential [3]. The residual radial anticonfining curvature of the magnetic potential is compensated optically, while an axial curvature results in a weak harmonic potential described by a trapping frequency of  $\omega_z = 2\pi \times 23.9$  Hz. This typically results in a variation of the potential along the axial direction that is less than 5% of the Fermi energy. Note that the magnetic moments of the two spin states of  ${}^6\text{Li}$  differ by less than 0.1% at unitarity, resulting in a negligible difference in trapping potentials. We characterize the steepness of the trap walls by measuring the radial extent  $R$  of the cloud as a function of Fermi energy [see Fig. 1(b)]. Modeling the trap walls with a power law potential, we obtain  $V(r) \sim r^{16.2 \pm 1.6}$  [36].

A stringent measure of the homogeneity of the gas is the probability distribution  $P(n)$  for the atomic density  $n$ . Imaging along the  $z$  and  $x$  directions yields the radial and axial probability distribution  $P(n_{2D})$  for the column density  $n_{2D}$  (see Fig. 1(c) and Ref. [36]). The distribution for the

homogeneous gas is sharply peaked near the trap average density  $\bar{n}_{2D}$ . For comparison, we also show  $P(n_{2D})$  for an optical Gaussian trap, which is spread over a large range of densities.

Fermions at low temperatures are characterized by Pauli blocking [1]. Consequences of Pauli blocking have been observed in ultracold gases, for example, in nondegenerate samples, the reduction of collisions in spin-polarized gases below the  $p$ -wave threshold [2,37] and, upon entering degeneracy, Pauli pressure [38,39], reduced collisions [40,41], antibunching in noise correlations [42], and the reduction of density fluctuations [43,44]. In optical lattices under microscopes, Pauli blocking has been observed in real space through observations of band insulating states [16,17,45] and of the Pauli hole in pair correlations [20]. Typically obscured in the time of flight expansion of an inhomogeneous atomic gas, the Fermi surface has been observed by probing only the central region of a harmonically trapped gas [46]. Now, the uniform box potential enables us to directly observe the consequence of Pauli blocking in momentum space for degenerate gases: the Fermi-Dirac momentum distribution, featuring the emergence of a Fermi surface near the Fermi wave vector  $k_F$  and the saturated occupation of momentum states below  $k_F$  to one particle per momentum cell.

To measure the momentum distribution  $f(\mathbf{k})$ , we release a highly spin-imbalanced gas ( $n_\downarrow/n_\uparrow < 0.05$ , where  $n_\uparrow$  and  $n_\downarrow$  are the densities of the majority and minority spin components, respectively) from the uniform potential into the small residual axial harmonic potential (along the  $z$  axis). To ensure the ballistic expansion of the gas, the minority component is optically pumped into a weakly interacting state within 5  $\mu\text{s}$  [36]. After a quarter period of expansion in the harmonic trap, the axial momenta  $k_z$  are mapped into real space via  $z = \hbar k_z / m\omega_z$  [47–50]. In contrast to conventional time of flight measurements, this method is unaffected by the in-trap size of the gas. The measured integrated density profile  $n_{1D}(z) = \int dx dy n(x, y, z)$  reflects the integrated momentum distribution  $f_{1D}(k_z) = (2\pi)^{-2} \int dk_x dk_y f(k_x, k_y, k_z)$  via

$$f_{1D}(k_z) = \frac{2\pi\hbar}{Vm\omega_z} n_{1D}(z). \quad (1)$$

Here,  $V$  is the volume of the uniform trap. Figure 2(a) shows the integrated momentum distribution for different temperatures. Assuming a spherically symmetric momentum distribution,  $f_k \equiv f(\mathbf{k}) = f(k)$ . Noting that  $\int dk_x dk_y f(\sqrt{k_x^2 + k_y^2 + k_z^2}) = \pi \int_{k_z^2}^\infty d(k^2) f(k)$ , the three-dimensional momentum distribution can be obtained from the integrated momentum distribution by differentiation:

$$f_k = -4\pi \frac{df_{1D}(k_z)}{dk_z^2}. \quad (2)$$

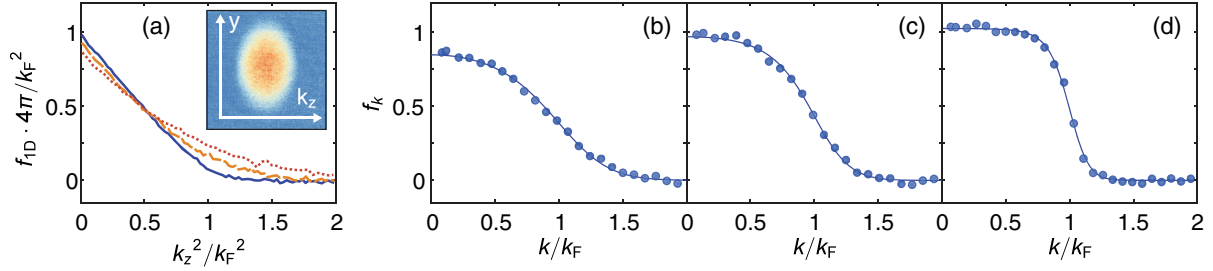


FIG. 2. Momentum distribution of the homogeneous spin-polarized Fermi gas. (a) Doubly integrated momentum distribution  $f_{ID}$  for different temperatures in the uniform trap. In order of decreasing temperature: red dotted line, orange dashed line, and blue solid line. Each line corresponds to averages over seven images. The optical density after momentum space mapping along  $z$  is shown in the inset. (b),(c),(d) Momentum distribution  $f_k = -4\pi df_{ID}/dk^2$ , showing Pauli blocking and Fermi surface formation. Fermi-Dirac fits (solid line) give (b)  $T/T_F = 0.49(2)$ , (c)  $T/T_F = 0.32(1)$ , and (d)  $T/T_F = 0.16(1)$ , with  $k_F$  ranging between  $2.8 \mu\text{m}^{-1}$  and  $3.7 \mu\text{m}^{-1}$ . The estimated systematic error in the measurement of  $f_k$  is 15%.

As the temperature is lowered, the momentum distribution develops a Fermi surface, and we observe a momentum state occupation of 1.04(15) at low momenta [see Figs. 2(b)–2(d)], where the error in  $f_k$  is dominated by the systematic uncertainties in the box volume and the imaging magnification [36]. This is the direct consequence of Pauli blocking and confirms saturation at one fermion per momentum state.

An important motivation for the realization of a homogeneous Fermi gas is the prospect of observing exotic strongly correlated states predicted to exist in narrow parts of the phase diagram, such as the FFLO state [21,22]. In a harmonic trap, such states would be confined to thin isopotential shells of the cloud, making them challenging to observe. We observe pair condensation in a uniformly trapped strongly interacting spin-balanced Fermi gas through a rapid ramp of the magnetic field during time of flight [3,51,52], as shown in Figs. 3(a)–3(c). The pair condensate at the end of the ramp barely expands in time of

flight. As a result, the in-trap homogeneity is reflected in a flat top profile of the condensate [see Fig. 3(f)].

Although a fully uniform potential is ideal for measurements that require translational symmetry, a spatially varying potential can access a large region of the phase diagram in a single experimental run. To harness the advantages of both potentials, we introduce a hybrid geometry that combines the radially uniform cylinder trap with an axially harmonic magnetic trap along the  $z$  direction [see Fig. 4(a)]. As a benchmark for the hybrid trap, we perform a thermodynamic study of both a strongly spin-imbalanced and a spin-balanced unitary gas. Figures 4(c)–4(e) display for both cases the  $y$ -axis averaged local density, temperature, and compressibility. The data shown in Fig. 4 are extracted from an average of just six images per spin component. For comparison, precision measurements of the equation of state at unitarity, performed in conventional harmonic traps, required averaging of over 100 absorption images [31]. The temperature is obtained from fits to the known equations of state of the noninteracting and spin-balanced unitary Fermi gas, respectively. From the local density in the hybrid trap, we determine the normalized isothermal compressibility  $\tilde{\kappa} = \kappa/\kappa_0 = -\partial E_F/\partial U|_T$  for the spin-imbalanced and the spin-balanced gas. Here,  $U$  is the external potential, and  $\kappa_0 = \frac{3}{2}(1/nE_F)$  is the compressibility of the noninteracting Fermi gas at zero temperature [31].

The strongly spin-imbalanced cloud features two distinct regions in the trap. The center of the cloud is a partially polarized region in which  $(n_\uparrow - n_\downarrow)/(n_\uparrow + n_\downarrow) > 0.64$ , well above the Clogston-Chandrasekhar limit of superfluidity [53–55]. Surrounding the center is a fully polarized region, where the compressibility is seen to saturate: the real space consequence of the Pauli blocking in momentum space demonstrated in Fig. 2.

The majority spin component in the partially polarized region is affected by the presence of the minority spin component. We measure the compressibility  $\tilde{\kappa}_\uparrow = -\partial E_{F\uparrow}/\partial U$  in the partially polarized region, and observe an increase compared to the fully polarized gas. This is expected as

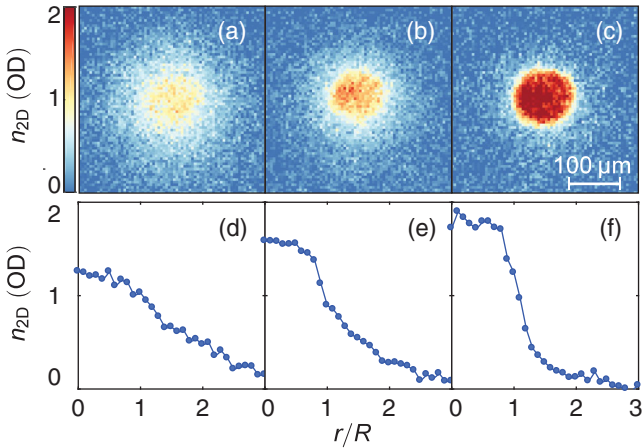


FIG. 3. Pair condensation in the uniform trap. (a), (b), and (c) Absorption images after a rapid ramp of the magnetic field and 10 ms of time of flight. The temperature of the gas is lowered (left to right) by evaporation in the uniform trap. The onset of a bimodal distribution signals the formation of a pair condensate. (d), (e), and (f) show cuts through the images in the top row.

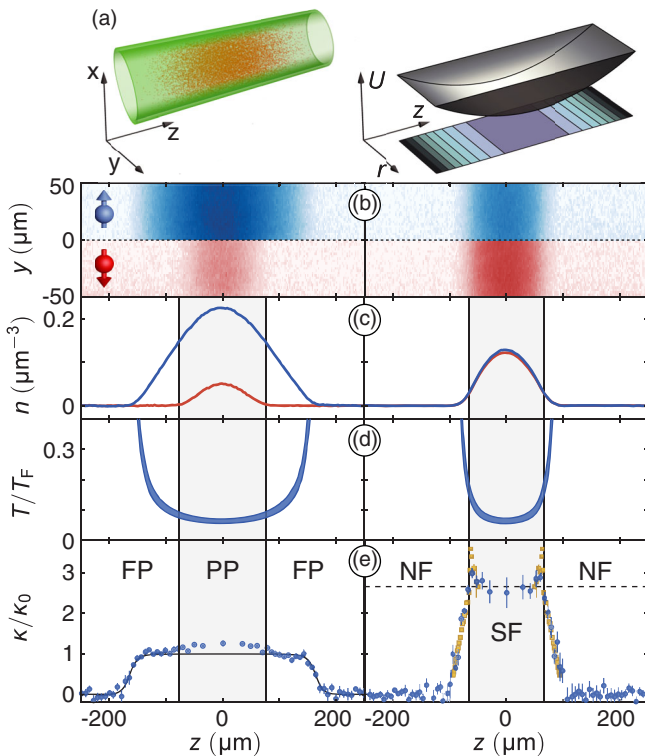


FIG. 4. Unitary Fermi gases in the hybrid trap. (a) Schematic and potential of the trap. The cloud is imaged along an equipotential direction ( $x$  axis). Left panels of (b)–(e) show a spin-imbalanced gas above the Clogston-Chandrasekhar limit, whereas the right side corresponds to a spin-balanced gas. The data are averaged over six images. (b) Local density for both spin components, obtained by dividing the column density by the column length. (c) Average density for each  $x$ - $y$  equipotential slice. The blue (red) line shows the spin-up (-down) component. (d) Spatially resolved temperature of the gas. The blue shaded region represents the error in the temperature determination. (e) Compressibility of the gas. The solid line in the left panel is the compressibility for an ideal Fermi gas. The crossover from the fully polarized (FP) region to the partially polarized (PP) region is accompanied by an increase in  $\tilde{\kappa}$ . The yellow squares in the right panel correspond to a precision measurement of the balanced unitary equation of state in the harmonic trap [31]. The peaks in the compressibility signal the phase transition from normal (N) to superfluid (SF). The horizontal dashed line shows the zero-temperature equation of state  $\kappa/\kappa_0 = 1/\xi$ .

the minority atoms in the center of the trap attract majority atoms and form polarons [7,8]. The effect is indeed predicted by the polaron equation of state [29,30,56]. The observation of this subtle effect highlights the sensitivity of the hybrid potential for thermodynamic measurements.

In the spin-balanced case,  $\kappa/\kappa_0$  is significantly larger than for the ideal Fermi gas due to strong interactions. The two prominent peaks in the reduced compressibility signal the superfluid transition at the two boundary surfaces between the superfluid core and the surrounding normal fluid. Near the center of the trap, the reduced compressibility agrees with the  $T = 0$  equation of state  $\kappa/\kappa_0 = 1/\xi = 2.65(4)$ ,

where  $\xi$  is the Bertsch parameter. The shaded region in the right column of Fig. 4 shows the superfluid part of the gas, where the temperature is below the critical temperature for superfluidity  $T_c = 0.17T_F$  [31].

The realization of uniform Fermi gases promises further insight into phases and states of matter that have eluded observation or quantitative understanding. This includes the observation of the quasiparticle jump [57] in the momentum distribution of a Fermi liquid, critical fluctuations in the BEC-BCS crossover, and long-lived solitons [58]. Of particular interest are spin imbalanced mixtures that have been studied extensively in harmonic traps [29,30,55,59–62], where the trap drives the separation of normal and superfluid phases into a shell structure. This phase separation should occur spontaneously in a uniform spin-imbalanced gas, possibly forming domains of superfluid and eventually ordering into an FFLO state. In addition, the hybrid potential is a valuable tool for precision measurements that rely on an in-trap density variation. For example, spatially resolved rf spectroscopy [32] in the hybrid potential would measure the homogenous response of the system over a large range of normalized temperatures  $T/T_F$  in a single experimental run.

We thank R. Fletcher for a critical reading of the manuscript, and E. A. Cornell and C. Altimiras for helpful discussions. This work was supported by the NSF, the ARO MURI on Atomtronics, AFOSR PECASE and MURI on Exotic Phases, and the David and Lucile Packard Foundation. Z. H. acknowledges support from EPSRC (Grant No. EP/N011759/1).

- [1] E. Fermi, *Rend. Fis. Acc. Lincei* **3**, 145 (1926).
- [2] B. DeMarco and D. S. Jin, *Science* **285**, 1703 (1999).
- [3] *Ultra-cold Fermi Gases, Proceedings of the International School of Physics Enrico Fermi, Course CLXIV, Varenna 2006*, edited by M. Inguscio, W. Ketterle, and C. Salomon (IOS Press, Amsterdam, 2008).
- [4] S. Giorgini, L. P. Pitaevskii, and S. Stringari, *Rev. Mod. Phys.* **80**, 1215 (2008).
- [5] *The BCS-BEC Crossover and the Unitary Fermi Gas*, edited by W. Zwerger, Lecture Notes in Physics Vol. 836 (Springer-Verlag Berlin Heidelberg, Berlin, Heidelberg, 2012).
- [6] M. W. Zwierlein, in *Novel Superfluids* (Oxford University Press, New York, 2014), pp. 269–422.
- [7] A. Schirotzek, C.-H. Wu, A. Sommer, and M. W. Zwierlein, *Phys. Rev. Lett.* **102**, 230402 (2009).
- [8] S. Nascimbène, N. Navon, K. J. Jiang, L. Tarruell, M. Teichmann, J. McKeever, F. Chevy, and C. Salomon, *Phys. Rev. Lett.* **103**, 170402 (2009).
- [9] M. Koschorreck, D. Pertot, E. Vogt, B. Fröhlich, M. Feld, and M. Köhl, *Nature (London)* **485**, 619 (2012).
- [10] C. Kohstall, M. Zaccanti, M. Jag, A. Trenkwalder, P. Massignan, G. M. Bruun, F. Schreck, and R. Grimm, *Nature (London)* **485**, 615 (2012).
- [11] R. Jördens, N. Strohmaier, K. Günter, H. Moritz, and T. Esslinger, *Nature (London)* **455**, 204 (2008).

- [12] U. Schneider, L. Hackermüller, S. Will, T. Best, I. Bloch, T. A. Costi, R. W. Helmes, D. Rasch, and A. Rosch, *Science* **322**, 1520 (2008).
- [13] T. Esslinger, *Annu. Rev. Condens. Matter Phys.* **1**, 129 (2010).
- [14] I. Bloch, J. Dalibard, and S. Nascimbène, *Nat. Phys.* **8**, 267 (2012).
- [15] R. A. Hart, P. M. Duarte, T.-L. Yang, X. Liu, T. Paiva, E. Khatami, R. T. Scalettar, N. Trivedi, D. A. Huse, and R. G. Hulet, *Nature (London)* **519**, 211 (2015).
- [16] D. Greif, M. F. Parsons, A. Mazurenko, C. S. Chiu, S. Blatt, F. Huber, G. Ji, and M. Greiner, *Science* **351**, 953 (2016).
- [17] L. W. Cheuk, M. A. Nichols, K. R. Lawrence, M. Okan, H. Zhang, and M. W. Zwierlein, *Phys. Rev. Lett.* **116**, 235301 (2016).
- [18] M. F. Parsons, A. Mazurenko, C. S. Chiu, G. Ji, D. Greif, and M. Greiner, *Science* **353**, 1253 (2016).
- [19] M. Boll, T. A. Hilker, G. Salomon, A. Omran, J. Nespolo, L. Pollet, I. Bloch, and C. Gross, *Science* **353**, 1257 (2016).
- [20] L. W. Cheuk, M. A. Nichols, K. R. Lawrence, M. Okan, H. Zhang, E. Khatami, N. Trivedi, T. Paiva, M. Rigol, and M. W. Zwierlein, *Science* **353**, 1260 (2016).
- [21] A. J. Larkin and Y. N. Ovchinnikov, *Zh. Eksp. Teor. Fiz.* **47**, 1136 (1964).
- [22] P. Fulde and R. A. Ferrell, *Phys. Rev.* **135**, A550 (1964).
- [23] L. Radzihovsky and D. E. Sheehy, *Rep. Prog. Phys.* **73**, 076501 (2010).
- [24] A. L. Gaunt, T. F. Schmidutz, I. Gotlibovich, R. P. Smith, and Z. Hadzibabic, *Phys. Rev. Lett.* **110**, 200406 (2013).
- [25] T. F. Schmidutz, I. Gotlibovich, A. L. Gaunt, R. P. Smith, N. Navon, and Z. Hadzibabic, *Phys. Rev. Lett.* **112**, 040403 (2014).
- [26] N. Navon, A. L. Gaunt, R. P. Smith, and Z. Hadzibabic, *Science* **347**, 167 (2015).
- [27] L. Chomaz, L. Corman, T. Bienaimé, R. Desbuquois, C. Weitenberg, S. Nascimbène, J. Beugnon, and J. Dalibard, *Nat. Commun.* **6**, 6162 (2015).
- [28] T.-L. Ho and Q. Zhou, *Nat. Phys.* **6**, 131 (2009).
- [29] S. Nascimbène, N. Navon, K. J. Jiang, F. Chevy, and C. Salomon, *Nature (London)* **463**, 1057 (2010).
- [30] N. Navon, S. Nascimbene, F. Chevy, and C. Salomon, *Science* **328**, 729 (2010).
- [31] M. J. H. Ku, A. T. Sommer, L. W. Cheuk, and M. W. Zwierlein, *Science* **335**, 563 (2012).
- [32] Y.-I. Shin, C. H. Schunck, A. Schirotzek, and W. Ketterle, *Phys. Rev. Lett.* **99**, 090403 (2007).
- [33] A. Schirotzek, Y.-I. Shin, C. H. Schunck, and W. Ketterle, *Phys. Rev. Lett.* **101**, 140403 (2008).
- [34] J. H. McLeod, *J. Opt. Soc. Am.* **44**, 592 (1954).
- [35] I. Manek, Y. Ovchinnikov, and R. Grimm, *Opt. Commun.* **147**, 67 (1998).
- [36] See Supplemental Material at <http://link.aps.org/supplemental/10.1103/PhysRevLett.118.123401> for further information on making and characterizing the uniform trap, optical pumping for the momentum-space mapping, and calibrating the absorption imaging.
- [37] R. Thomas, K. O. Roberts, E. Tiesinga, A. C. J. Wade, P. B. Blakie, A. B. Deb, and N. Kjærgaard, *Nat. Commun.* **7**, 12069 (2016).
- [38] A. G. Truscott, K. E. Strecker, W. I. McAlexander, G. B. Partridge, and R. G. Hulet, *Science* **291**, 2570 (2001).
- [39] F. Schreck, L. Khaykovich, K. L. Corwin, G. Ferrari, T. Bourdel, J. Cubizolles, and C. Salomon, *Phys. Rev. Lett.* **87**, 080403 (2001).
- [40] B. DeMarco, S. B. Papp, and D. S. Jin, *Phys. Rev. Lett.* **86**, 5409 (2001).
- [41] A. Sommer, M. Ku, and M. W. Zwierlein, *New J. Phys.* **13**, 055009 (2011).
- [42] T. Rom, T. Best, D. van Oosten, U. Schneider, S. Fölling, B. Paredes, and I. Bloch, *Nature (London)* **444**, 733 (2006).
- [43] T. Müller, B. Zimmermann, J. Meineke, J.-P. Brantut, T. Esslinger, and H. Moritz, *Phys. Rev. Lett.* **105**, 040401 (2010).
- [44] C. Sanner, E. J. Su, A. Keshet, R. Gommers, Y.-I. Shin, W. Huang, and W. Ketterle, *Phys. Rev. Lett.* **105**, 040402 (2010).
- [45] A. Omran, M. Boll, T. A. Hilker, K. Kleinlein, G. Salomon, I. Bloch, and C. Gross, *Phys. Rev. Lett.* **115**, 263001 (2015).
- [46] T. E. Drake, Y. Sagi, R. Paudel, J. T. Stewart, J. P. Gaebler, and D. S. Jin, *Phys. Rev. A* **86**, 031601 (2012).
- [47] I. Shvarchuck, C. Buggle, D. S. Petrov, K. Dieckmann, M. Zielonkovski, M. Kemmann, T. G. Tiecke, W. von Klitzing, G. V. Shlyapnikov, and J. T. M. Walraven, *Phys. Rev. Lett.* **89**, 270404 (2002).
- [48] A. H. van Amerongen, J. J. P. van Es, P. Wicke, K. V. Kheruntsyan, and N. J. van Druten, *Phys. Rev. Lett.* **100**, 090402 (2008).
- [49] S. Tung, G. Lamporesi, D. Lobser, L. Xia, and E. A. Cornell, *Phys. Rev. Lett.* **105**, 230408 (2010).
- [50] P. A. Murthy, D. Kedar, T. Lompe, M. Neidig, M. G. Ries, A. N. Wenz, G. Zürn, and S. Jochim, *Phys. Rev. A* **90**, 043611 (2014).
- [51] C. A. Regal, M. Greiner, and D. S. Jin, *Phys. Rev. Lett.* **92**, 040403 (2004).
- [52] M. W. Zwierlein, C. A. Stan, C. H. Schunck, S. M. F. Raupach, A. J. Kerman, and W. Ketterle, *Phys. Rev. Lett.* **92**, 120403 (2004).
- [53] B. S. Chandrasekhar, *Appl. Phys. Lett.* **1**, 7 (1962).
- [54] A. M. Clogston, *Phys. Rev. Lett.* **9**, 266 (1962).
- [55] M. W. Zwierlein, A. Schirotzek, C. H. Schunck, and W. Ketterle, *Science* **311**, 492 (2006).
- [56] Y.-I. Shin, *Phys. Rev. A* **77**, 041603 (2008).
- [57] G. D. Mahan, *Many-Particle Physics* (Springer, Boston, MA, 2000).
- [58] M. J. H. Ku, B. Mukherjee, T. Yefsah, and M. W. Zwierlein, *Phys. Rev. Lett.* **116**, 045304 (2016).
- [59] G. B. Partridge, W. Li, R. I. Kamar, Y.-A. Liao, and R. G. Hulet, *Science* **311**, 503 (2006).
- [60] Y.-I. Shin, M. W. Zwierlein, C. H. Schunck, A. Schirotzek, and W. Ketterle, *Phys. Rev. Lett.* **97**, 030401 (2006).
- [61] Y.-I. Shin, C. H. Schunck, A. Schirotzek, and W. Ketterle, *Nature (London)* **451**, 689 (2008).
- [62] Y.-A. Liao, A. S. C. Rittner, T. Paprotta, W. Li, G. B. Partridge, R. G. Hulet, S. K. Baur, and E. J. Mueller, *Nature (London)* **467**, 567 (2010).

## Supplemental Material: Homogeneous Atomic Fermi Gases

Biswaroop Mukherjee,<sup>1</sup> Zhenjie Yan,<sup>1</sup> Parth B. Patel,<sup>1</sup>  
Zoran Hadzibabic,<sup>1,2</sup> Tarik Yefsah,<sup>1,3</sup> Julian Struck,<sup>1</sup> and Martin W. Zwierlein<sup>1</sup>

<sup>1</sup>*MIT-Harvard Center for Ultracold Atoms, Research Laboratory of Electronics, and Department of Physics, Massachusetts Institute of Technology, Cambridge, Massachusetts 02139, USA*

<sup>2</sup>*Cavendish Laboratory, University of Cambridge, J. J. Thomson Avenue, Cambridge CB3 0HE, United Kingdom*

<sup>3</sup>*Laboratoire Kastler Brossel, CNRS, ENS-PSL Research University, UPMC-Sorbonne Universités and Collège de France, Paris, France*

### CYLINDER-SHAPED TRAP

For the repulsive optical potential, we use laser light that is blue detuned with respect to the D-lines of  ${}^6\text{Li}$  at 671 nm. The laser source is a multi-mode 10W laser at 532 nm. Figure S1 shows the optical setup that is used to shape the beam into a hollow core cylinder. A collimated gaussian beam propagates through an axicon and a microscope objective, generating a hollow cylindrical beam in the Fourier plane [S2, S3]. An opaque circular silver mask is placed in the focal plane to block the residual light inside the ring and provide a sharper inner edge. The resulting intensity distribution at the focal plane is imaged onto the atoms along the z-axis. This confines the atoms into a cylinder oriented along the axial direction (z-axis).

In addition to the radial cylinder-shaped trap, the uniform trap requires sharp end cap walls that confine the atoms along the axial direction. For the endcaps, we use second 532 nm beam from the same laser source and detuned it by 160 MHz to avoid interference between the beams. The end cap beam is split into two elliptically shaped beams with opposite polarizations, which are fo-

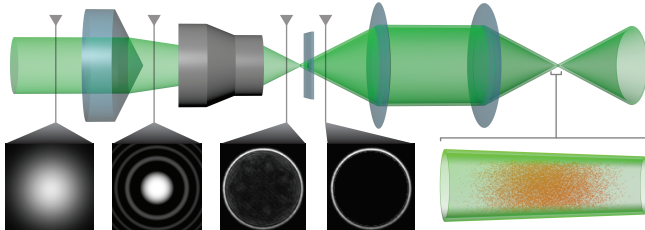


FIG. S1. Optical setup for cylinder-shaped trap. From left to right: A gaussian beam propagates through an axicon resulting in a Bessel beam in the near field. Subsequently the Bessel beam is focused through a microscope objective. In the focal plane, the resulting intensity pattern is a ring with gaussian rim. A matched circular opaque mask is used to block out residual light in the center of the ring. Finally the mask is projected through an imaging system onto the atoms, creating the cylinder-shaped trap for the atoms. A small variation of cylinder radius is unavoidable when using a single axicon [S1].

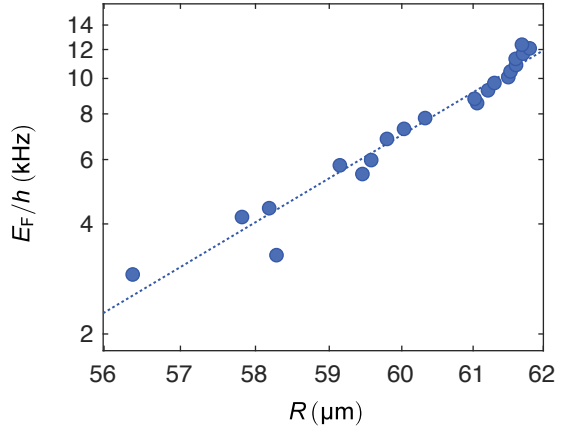


FIG. S2. Determination of the power law exponent of the radial wall potential. Log-log plot of the data shown in Fig. 1(b). The blue dotted line is a linear fit, with a slope of  $m = 16.2 \pm 1.6$  for the power law exponent.

cused onto the edges of a rectangular opaque mask. The intensity distribution at the mask is projected onto the atoms and provides two sharp confining walls.

### TRAP CHARACTERIZATION

#### Radial Trap Wall: Power Law Potential

To describe the radial extent of the gas as a function of the Fermi energy, we model our radial potential with a power law  $U(r) = \alpha r^m$ . Within the local density approximation, the local chemical potential is then determined by  $\mu(r) = \mu_0 - \alpha r^m$ , where  $\mu_0 = \mu(r = 0)$ . The radius measurements have been performed with a spin-balanced superfluid. Assuming  $T = 0$ , the cloud has a well defined Thomas-Fermi radius  $R$ , where the density drops to zero:

$$\mu_0 = \xi E_F = \alpha R^m, \quad (\text{S1})$$

with the Bertsch parameter  $\xi$ . Fitting the data shown in Fig. S2 with a power-law gives  $m = 16.2 \pm 1.6$ .

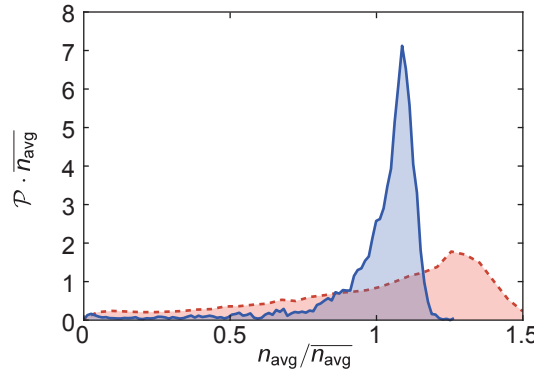


FIG. S3. Axial probability distribution. The blue solid line (red dashed line) shows  $\mathcal{P}(n_{\text{avg}})$  for the uniform (hybrid) trap. Absorption images are taken along x-axis. The line of sight averaged local density  $n_{\text{avg}}$  is calculated assuming a uniform cylindrical trap.

#### Probability Distribution for the Atomic Density

The density distribution  $\mathcal{P}(n)$  describes the probability  $\mathcal{P}(n)dn$  to find an atom at a density between  $n$  and  $n + dn$ , and is normalized to unity. We evaluate the probability distribution from absorption images by binning the measured column integrated density  $n_{2D}$ , and weighting each bin by the number of atoms representing the bin.

To extract information about the axial homogeneity of the gas, we image the atoms along the x-axis. We obtain the line-of-sight averaged local density  $n_{\text{avg}}$  from the column density by dividing by the local column length. Figure S3 shows the probability distribution  $\mathcal{P}(n_{\text{avg}})$  for the line-of-sight averaged density of the uniform and hybrid trap. The axial probability distribution shows a narrow peak similar to the one observed for the radial distribution. The probability distribution for the hybrid trap is broadened due to the harmonic trapping along the z direction.

#### OPTICAL PUMPING OF THE MINORITY ATOMS FOR MOMENTUM-SPACE MAPPING

The measurement of the momentum distribution relies on ballistic expansion of the gas immediately after release from the trap. However, the expansion of the atoms is strongly influenced by a small minority fraction ( $< 5\%$ ) of strongly interacting atoms admixed to ensure the thermalization of the gas. To eliminate the interactions between the two spin states during the expansion, the minority atoms are optically pumped into the hyperfine state  $|m_J = +1/2, m_I = 0\rangle$  that is weakly interacting with the majority cloud. The  $5\ \mu\text{s}$  pumping pulse is applied right before the release of the atoms into the harmonic trap. On average,  $1.5$  photons are required

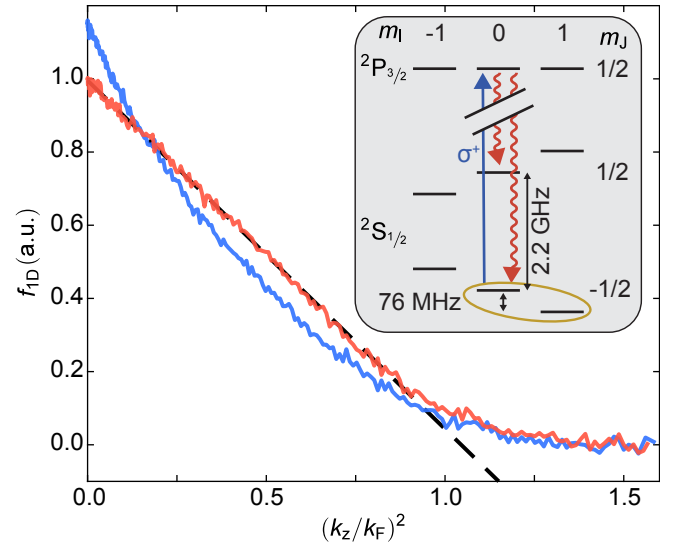


FIG. S4. Influence of the minority atoms on the expansion of the majority cloud. The blue (red) line corresponds to the observed integrated momentum distribution without (with) optical pumping of the minority atoms. The dashed line is a guide to the eye. The inset displays the level scheme for the optical pumping at a magnetic field of  $B = 832\text{G}$ . The yellow ellipse marks the two strongly interacting spin states, where the minority is in  $|m_J = -1/2, m_I = 0\rangle$ . The pumping transition is shown as the blue line and the spontaneous decay channels with red curly lines.

to pump an atom into the weakly interacting hyperfine state. The transitions involved in this pumping scheme are shown in the inset of Fig. S4. Figure S4 shows the integrated momentum distribution of the gas obtained using momentum-space mapping with and without pumping of minority atoms. Note that without the optical pumping of the minority atoms,  $f_{1D}$  is distorted from the triangular shape expected for a low temperature Fermi gas.

#### DENSITY MEASUREMENT WITH ABSORPTION IMAGING

For heavy atoms, such as Rb and Cs, and imaging intensities that are small compared to the saturation intensity ( $I_{\text{sat}}$ ), the column density  $n_{\text{col}} = -(1/\sigma_0) \log(I_f/I_i)$  is determined by the Beer-Lambert law. Here,  $I_i$  and  $I_f$  are the intensities of the imaging beam before and after the atoms, respectively, and  $\sigma_0$  is the absorption cross-section. However, for light atoms such as Li, the Doppler effect plays a dominant role in realistic experimental scenarios, where a low imaging intensity and short exposure time is in conflict with a high signal to noise ratio. For our experiment, depending on the column density of the sample, preferred values for the imaging intensities are  $0.1 - 0.5 I_{\text{sat}}$  at an exposure time of  $4 - 10\ \mu\text{s}$ .

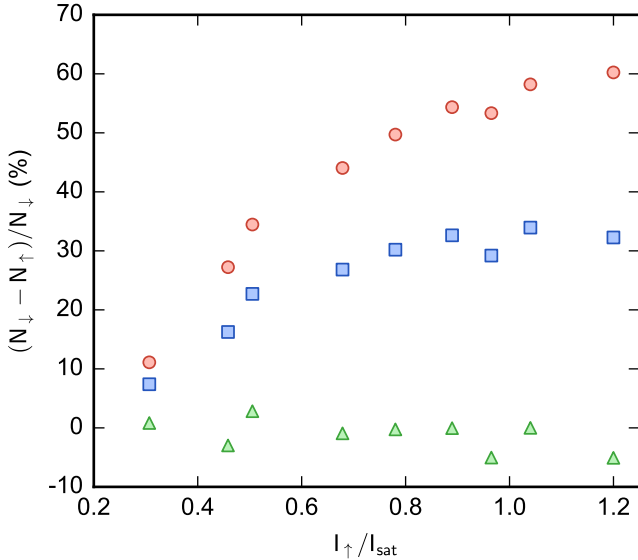


FIG. S5. Apparent atom count for the spin up component ( $N_{\uparrow}$ ) measured at different imaging intensities ( $I_{\uparrow}$ ). A reference atom count ( $N_{\downarrow}$ ) is obtained by subsequently imaging a second spin component at a fixed imaging intensity ( $I_{\downarrow} = 0.23I_{\text{sat}}$ ). Red circles, blue squares, and green triangles are obtained using Beer-Lambert, saturated Beer-Lambert, and Doppler Beer-Lambert, respectively. Spin balanced clouds are used for these measurements.

Under these conditions, each  ${}^6\text{Li}$  atom scatters up to 35 photons. The corresponding photon recoil results in a Doppler shift of up to 6 MHz, which is comparable to the natural linewidth of  ${}^6\text{Li}$ .

In order to account for the Doppler and saturation effects, we numerically solve two coupled differential equations for the local, time-dependent saturation parameter  $s(z, t) = I(z, t)/I_{\text{sat}}$  and velocity  $v(z, t)$ :

$$\frac{\partial s}{\partial z} = -n\sigma_0 \frac{s}{1 + s + (2kv/\Gamma)^2}. \quad (\text{S2a})$$

$$\frac{\partial v}{\partial t} = \frac{\hbar k \Gamma}{2m} \frac{s}{1 + s + (2kv/\Gamma)^2}. \quad (\text{S2b})$$

Here,  $\sigma_0$ ,  $k$ ,  $m$  and  $\Gamma$  are the bare scattering cross-section, photon wave vector, atomic mass and natural linewidth.

In the limit where the Doppler effect is negligible ( $v = 0$ ), the analytical solution of Eq. S2 is  $n_{\text{col}}\sigma_0 = -\log(s_f/s_i) - (s_f - s_i)$ . Here,  $s_i$  and  $s_f$  are reduced imaging intensities before and after the atoms, respectively. This is the modified version of the Beer-Lambert law that includes saturation of the atomic transition. For the general case, we numerically solve Eq. S2 to find the Doppler-corrected relation between  $I_i$  and  $I_f$  (which we call the “Doppler Beer-Lambert” law).

We compare these aforementioned methods by subsequently imaging the two spin states of a spin-balanced gas with a fast SCMOS camera. The first image is taken with fixed saturation intensity of  $s_{\downarrow} = 0.23$  and serves as the density reference. The second absorption image for the other spin component, with a variable  $s_{\uparrow}$ , is obtained 15  $\mu\text{s}$  after the first image. Figure S5 shows the differences in the measured total atom numbers between two spin components for various  $s_{\uparrow}$  calculated using the Beer-Lambert law (red circles), the saturated Beer-Lambert law (blue squares) and Doppler Beer-Lambert (green triangles). For the atom number differences calculated using the Doppler Beer-Lambert law, the mean deviation from the reference density is only 3% compared to 27% and 46% for the saturated Beer-Lambert and the basic Beer-Lambert law, respectively.

- 
- [S1] A. L. Gaunt, *Degenerate Bose Gases : Tuning Interactions & Geometry*, PhD, University of Cambridge (2014).
  - [S2] J. H. McLeod, Journal of the Optical Society of America **44**, 592 (1954).
  - [S3] I. Manek, Y. Ovchinnikov, and R. Grimm, Optics Communications **147**, 67 (1998).



## Appendix C

# Spectral Response and Contact of the Unitary Fermi Gas

This appendix contains a reprint of Ref. [128]:

## Spectral Response and Contact of the Unitary Fermi Gas

Biswaroop Mukherjee,<sup>1</sup> Parth B. Patel,<sup>1</sup> Zhenjie Yan,<sup>1</sup> Richard J. Fletcher,<sup>1</sup>  
Julian Struck,<sup>1,2</sup> and Martin W. Zwierlein<sup>1</sup>

<sup>1</sup>MIT-Harvard Center for Ultracold Atoms, Research Laboratory of Electronics, and Department of Physics,  
Massachusetts Institute of Technology, Cambridge, Massachusetts 02139, USA

<sup>2</sup>Département de Physique, Ecole Normale Supérieure / PSL Research University, CNRS, 24 rue Lhomond, 75005 Paris, France



(Received 21 February 2019; published 23 May 2019)

We measure radio frequency (rf) spectra of the homogeneous unitary Fermi gas at temperatures ranging from the Boltzmann regime through quantum degeneracy and across the superfluid transition. For all temperatures, a single spectral peak is observed. Its position smoothly evolves from the bare atomic resonance in the Boltzmann regime to a frequency corresponding to nearly one Fermi energy at the lowest temperatures. At high temperatures, the peak width reflects the scattering rate of the atoms, while at low temperatures, the width is set by the size of fermion pairs. Above the superfluid transition, and approaching the quantum critical regime, the width increases linearly with temperature, indicating non-Fermi-liquid behavior. From the wings of the rf spectra, we obtain the contact, quantifying the strength of short-range pair correlations. We find that the contact rapidly increases as the gas is cooled below the superfluid transition.

DOI: 10.1103/PhysRevLett.122.203402

Understanding fermion pairing and pair correlations is of central relevance to strongly interacting Fermi systems such as nuclei [1,2], ultracold gases [3–6], liquid  $^3\text{He}$  [7], high temperature superconductors [8], and neutron stars [9]. Strong interactions on the order of the Fermi energy challenge theoretical approaches, especially methods that predict dynamic properties such as transport or the spectral response at finite temperature [10]. Atomic Fermi gases at Feshbach resonances realize a paradigmatic system where the gas becomes as strongly interacting as allowed by unitarity [3–6,11]. Here, the system becomes universal, requiring only two energy scales: the Fermi energy  $E_F$  and thermal energy  $k_B T$ , where  $k_B$  is the Boltzmann constant and  $T$  is the temperature. The corresponding length scales are the interparticle spacing  $\lambda_F = n^{-1/3}$  and the thermal de Broglie wavelength  $\lambda_T = h/\sqrt{2\pi m k_B T}$ , where  $m$  and  $n$  are the mass and number density of the atoms, respectively. When the two energy scales are comparable, the system enters a quantum critical regime separating the high temperature Boltzmann gas from the fermionic superfluid [12]. Quantum criticality is often associated with the absence of quasiparticles [10,12,13], spurring a debate on the applicability of Fermi liquid theory to the degenerate normal fluid below the Fermi temperature  $T_F = E_F/k_B$  but above the superfluid transition temperature  $T_c \approx 0.167T_F$  [14–16]. It has been conjectured that preformed pairs exist above  $T_c$ , up to a pairing temperature  $T^*$  [3,5,11,17–21].

Radio frequency (rf) spectroscopy measures the momentum integrated, occupied spectral function, providing a powerful tool for studying interactions and correlations in Fermi gases [22–27]. Here, a particle is ejected from the

interacting many-body state and transferred into a weakly interacting final state. Shifts in rf spectra indicate attractive or repulsive interactions in the gas. At high temperatures, the width of the rf spectrum reflects the scattering rate in the gas, while at low temperatures, the width has been used to infer the pair size of superfluid fermion pairs [26].

The high frequency tails of the rf spectra are sensitive to the spectral function at high momenta and, therefore, are governed by short range correlations quantified by the contact, which also determines the change of the energy with respect to the interaction strength [28–30]. From the momentum distribution within nuclei [1,2] to the frequency dependence of the shear viscosity in ultracold fermionic superfluids [31,32], the contact is central to Fermi gases dominated by short-range interactions. Since the contact is proposed to be sensitive to the superfluid pairing gap, it could signal a pseudogap regime above  $T_c$  [32–35]. Although the temperature dependence of the contact near  $T_c$  has been the subject of many theoretical predictions, a consensus has not been reached [32,36–38].

Initial studies of unitary Fermi gases using rf spectroscopy were affected by inhomogeneous densities in harmonic traps, yielding doubly peaked spectra that were interpreted as observations of the pairing gap [25,39], and from the influence of interactions in the final state, which caused significantly narrower spectra and smaller shifts than expected [22,39–41]. Measurements of the contact, made using both rf [42,43] and Bragg [44–46] spectroscopy, were also broadened by inhomogeneous potentials. To avoid trap broadening, tomographic techniques have been used to measure local rf spectra, yielding measurements of the superfluid gap [47], the spectral function [17,18], and the

contact [48]. A recent advance has been the creation of uniform box potentials [49–51]. These are ideal for rf spectroscopy and precision measurements of the contact: since the entire cloud is at a constant density, global probes such as rf address all atoms, and benefit from a stronger signal.

In this Letter, we report on rf spectroscopy of the homogeneous unitary Fermi gas in a box potential. A single peak is observed for all temperatures from the superfluid regime into the high temperature Boltzmann gas. The tails of the rf spectra reveal the contact, which shows a rapid rise as the temperature is reduced below  $T_c$ .

We prepare  ${}^6\text{Li}$  atoms in two of the three lowest hyperfine states  $|\downarrow\rangle = |1\rangle$  and  $|\uparrow\rangle = |3\rangle$  at a magnetic field of 690 G, where interspin interactions are resonant. A uniform optical box potential with cylindrical symmetry is loaded with  $N \sim 10^6$  atoms per spin state (with Fermi energies  $E_F \sim h \times 10$  kHz), creating spin-balanced homogeneous gases at temperatures ranging from  $T/T_F = 0.10$  to  $3.0$  [50]. A square rf pulse transfers atoms from state  $|\downarrow\rangle$  into state  $|f\rangle = |2\rangle$ . Final state interactions between atoms in state  $|f\rangle$  and atoms in states  $|\uparrow\rangle$  and  $|\downarrow\rangle$  are small ( $k_F a_f \lesssim 0.2$ , where  $a_f$  is the scattering length characterizing collisions between atoms in the final and initial states, and  $\hbar k_F = \sqrt{2mE_F}$  is the Fermi momentum)

[26]. After the rf pulse, we measure the atom numbers  $N_\downarrow$  and  $N_f$  in the initial and final states. Within linear response, according to Fermi's golden rule,  $N_f$  is proportional to the pulse time  $T_{\text{Pulse}}$ , the square of the single-particle Rabi frequency  $\Omega_R$ , and an energy density of states. Thus, we define a normalized, dimensionless rf spectrum as  $I(\omega) = [N_f(\omega)/N_\downarrow](E_F/\hbar\Omega_R^2 T_{\text{Pulse}})$  [52,57]. Because of the scale invariance of the balanced unitary Fermi gas, this dimensionless function can only depend on  $T/T_F$  and  $\hbar\omega/E_F$ .

For thermometry, we release the cloud from the uniform potential into a harmonic trap along one direction [57]. Since the cloud expands isoenergetically, the resulting spatial profile after thermalization provides the energy per particle, which can be related to the reduced temperature,  $T/T_F$ , using a virial relation and the measured equation of state [14]. To clearly identify the superfluid transition, we measure the pair momentum distribution by a rapid ramp of the magnetic field to the molecular side of the Feshbach resonance before releasing the gas into a harmonic trap for a quarter period [50,52].

Initially, we focus on changes in the line shape for rf frequencies within  $\sim E_F/\hbar$  of the bare (single-particle) resonance [see Fig. 1(a)], and follow the changes in

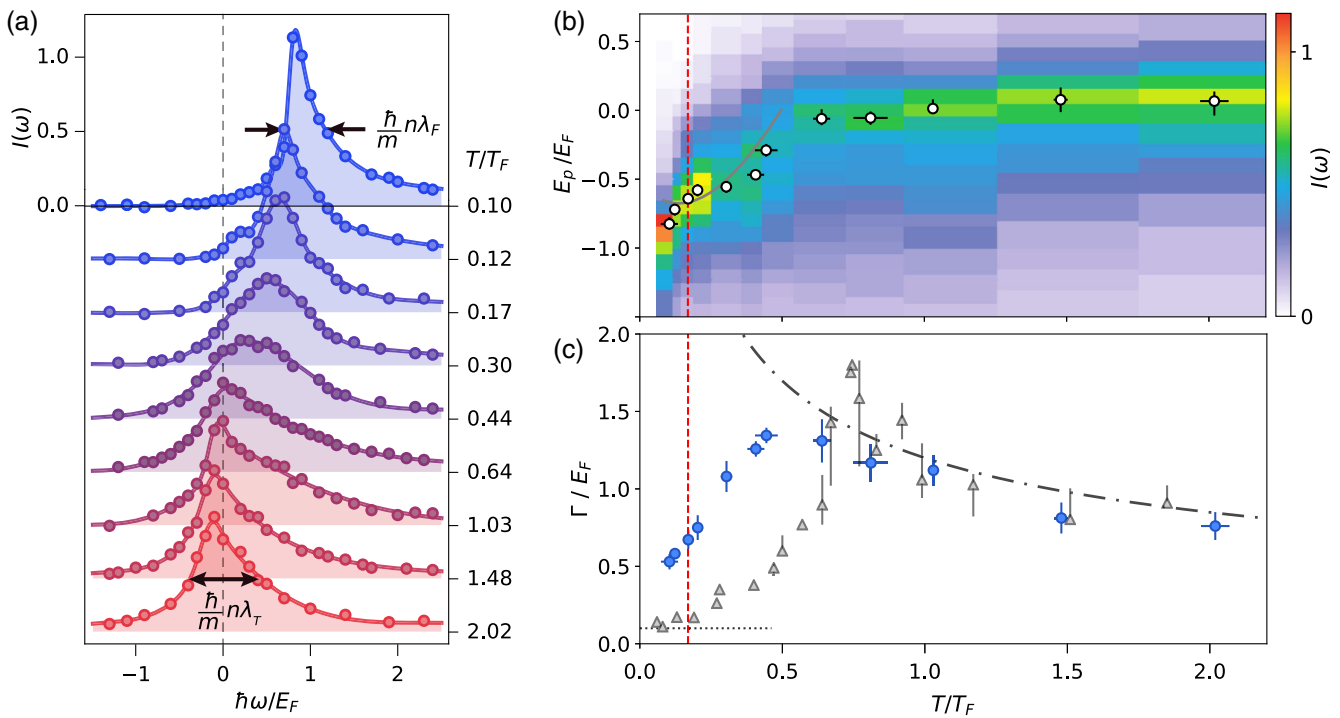


FIG. 1. (a) Thermal evolution of rf spectra. The Rabi frequency is  $\Omega_R = 2\pi \times 0.5$  kHz and the pulse duration is  $T_{\text{Pulse}} = 1$  ms. The solid lines are guides to the eye. (b) Frequency of the peak ( $E_p = -\hbar\omega$ ) of the rf spectra as a function of temperature shown as white dots on an intensity plot of the rf response. The grey solid line is a solution to the Cooper problem at nonzero temperature [52]. (c) The full width at half maximum  $\Gamma$  of the rf peak as a function of  $T/T_F$ . The black dotted-dashed line  $\Gamma/E_F = 1.2\sqrt{T_F/T}$  shows the temperature dependence of the width due to scattering in the high-temperature gas [32,60]. The grey triangles are the corresponding width measurements of a highly spin-imbalanced gas [57]. The horizontal black dotted line represents the Fourier broadening of  $0.1E_F$  [52]. The vertical dashed red line in both (b) and (c) marks the superfluid transition [14].

the peak position  $E_p$  [shown in Fig. 1(b)]. As the hot spin-balanced Fermi gas is cooled below the Fermi temperature, the peak shift decreases from roughly zero for temperatures  $T \gtrsim T_F$ , to  $E_p \approx -0.8E_F$  for temperatures below the superfluid transition temperature [see Fig. 1(b)]. At high temperatures, one might naïvely expect a shift on the order of  $E_p \sim \hbar n \lambda_T / m$  due to unitarity-limited interactions in the gas. However, there exists both an attractive and a repulsive energy branch, which are symmetric about zero at unitarity [58], and when  $T \gg T_F$ , their contributions to the shift cancel [32,59,60]. As to the interpretation of the peak shift at degenerate temperatures, a solution to the Cooper problem in the presence of a  $T > 0$  Fermi sea shows that it is energetically favorable to form pairs when  $T \lesssim 0.5T_F$  [52], and the resulting pair energy agrees qualitatively with the observed shifts [grey line in Fig. 1(b)]. However, it is known that fluctuations suppress the onset of pair condensation and superfluidity to  $0.167(13)T_F$  [5,11,14,61]. In a zero-temperature superfluid, BCS theory would predict a peak shift given by the pair binding energy  $E_B = \Delta^2/2E_F$ , where  $\Delta$  is the pairing gap [3]. Including Hartree terms is found to result in an additional shift of the peak [27,47].

Now, we turn to the widths,  $\Gamma$ , defined as the full width at half maximum of the rf spectra [see Fig. 1(c)]. As the gas is cooled from the Boltzmann regime, the width gradually increases, and attains a maximum of  $\Gamma = 1.35(5)E_F$  near  $T = 0.44(4)T_F$ . For temperatures much higher than  $T_F$ , the system is a Boltzmann gas of atoms scattering with a unitarity limited cross section  $\sigma \sim \lambda_T^2$ . Transport properties and short-range pair correlations are governed by the scattering rate  $\Gamma = n_{\downarrow} \sigma \langle v_{\text{rel}} \rangle \sim \hbar n_{\downarrow} \lambda_T / m$  and a mean-free path  $l = (n_{\downarrow} \sigma)^{-1} \sim (n_{\downarrow} \lambda_T^2)^{-1}$ , where  $n_{\downarrow}$  is the density of atoms in  $|\downarrow\rangle$ , and  $\langle v_{\text{rel}} \rangle \sim \hbar/m\lambda_T$  is the thermally averaged relative velocity. This leads to a width that scales as  $\Gamma \propto 1/\sqrt{T}$ , shown as the dotted-dashed line in Fig. 1(c) [32].

As the cloud is cooled below  $T \approx 0.5T_F$ , the width decreases linearly with temperature to  $\Gamma \sim 0.52E_F/\hbar$  in the coldest gases measured [ $T = 0.10(1)T_F$ ]. For temperatures below  $T_c$ , we expect the gas to consist of pairs of size  $\xi$ . The rf spectrum will be broadened by the distribution of momenta  $\sim \hbar/\xi$  inside each pair, leading to a spread of possible final kinetic energies  $\hbar^2 k^2 / m \sim \hbar^2 / m \xi^2$  and a corresponding spectral width  $\hbar/m\xi^2$ . At unitarity and at  $T = 0$ , the pair size is set by the interparticle spacing  $\lambda_F$  [3,5,26]. Thus, the rf width at low temperatures is  $\Gamma \sim \hbar n \lambda_F / m$ .

For temperatures above  $T_c$ , it has been suggested that the normal fluid can be described as a Fermi liquid [15,62]. This would imply a quadratic relation between the peak width and the temperature [63], as observed in the widths of the rf spectra of Fermi polarons at unitarity [57]. However, the measured width of the spin-balanced Fermi gas changes linearly in temperature, implying non-Fermi

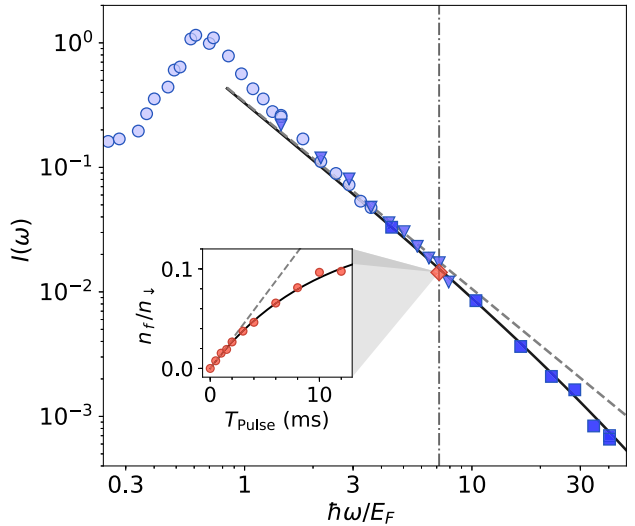


FIG. 2. Rf spectrum at high frequencies. Here, the temperature of the gas is  $T/T_F = 0.10(1)$ , the pulse duration is  $T_{\text{Pulse}} = 1$  ms, and the Rabi frequencies are  $2\pi \times 536$  Hz (light blue circles),  $2\pi \times 1.20$  kHz (medium blue triangles), and  $2\pi \times 3.04$  kHz (dark blue squares). The black solid line shows a fit of Eq. (1) to the data, while the grey dashed line shows the fit neglecting final state interactions. The contact can be directly obtained from the transfer rate at a fixed detuning of 60 kHz ( $\hbar\omega/E_F \sim 7.1$ ) (dotted-dashed vertical line). Inset: we vary the pulse time at this fixed detuning, and extract the initial slope (dashed line) of the exponential saturating fit (solid line). The rf transfer rate obtained from the initial linear slope is shown as the red diamond in the main plot. Here,  $\Omega_R = 2\pi \times 1.18$  kHz.

liquid behavior in the normal fluid. In addition,  $\Gamma > E_F/\hbar$  for  $0.3 \lesssim T/T_F \lesssim 1.2$ , indicating a breakdown of well-defined quasiparticles over a large range of temperatures near the quantum critical regime [10,12,13].

We now consider the rf spectrum at frequencies much larger than  $E_F/\hbar$ , where the rf-coupled high-momentum tails reveal information about the short-range pair correlations between atoms. In a gas with contact interactions, the pair correlation function at short distances is  $\lim_{r \rightarrow 0} \langle n_{\uparrow}(\mathbf{r}_0 + \mathbf{r}/2) n_{\downarrow}(\mathbf{r}_0 - \mathbf{r}/2) \rangle = C/(4\pi r)^2$ . The contact  $C$  connects a number of fundamental relations, independent of the details of the short-range interaction potential [28]. In particular, the contact governs the momentum distribution at large momenta:  $\lim_{k \rightarrow \infty} n(k) = C/k^4$ . For rf spectroscopy, the density of final states scales as  $\sqrt{\omega}$ , and the energy cost to flip a spin at high momenta is  $\lim_{k \rightarrow \infty} \hbar\omega = \hbar^2 k^2 / m$ . Thus, the number of atoms transferred by the rf pulse at high frequencies in linear response is  $\propto C/\omega^{3/2}$  [5,27]. Including final state interactions, the general expression for the rf transfer rate in a gas with unitarity-limited initial state interactions is [64]

$$\lim_{\omega \rightarrow \infty} I(\omega) = \left( \frac{C}{Nk_F} \right) \frac{1}{2\sqrt{2\pi}(1 + \hbar\omega/E_b)} \left( \frac{E_F}{\hbar\omega} \right)^{3/2}, \quad (1)$$

where  $N = N_\uparrow + N_\downarrow$  is the total number of atoms, and the final state molecular binding energy is  $E_b = \hbar^2/m a_f^2 \approx \hbar \times 433 \text{ kHz} \approx 40 E_F$ . Figure 2 shows a typical rf spectrum at  $T/T_F = 0.10$ , with a fit of Eq. (1) to data with detunings  $\hbar\omega > 3E_F$ , using the dimensionless contact  $\tilde{C} = C/Nk_F$  as the only free parameter. At detunings larger than about  $10 E_F$ , the data deviate from a typical  $\omega^{-3/2}$  tail, and are better described by the full expression Eq. (1) including final state interactions. Here, the Rabi frequency was varied across the plot to ensure small transfers near the peak and a high signal-to-noise ratio at detunings up to  $\hbar\omega/E_F = 31$ . The fit of Eq. (1) to the data gives a low-temperature contact of  $\tilde{C} = 3.07(6)$ , consistent with a quantum Monte Carlo result  $\tilde{C} = 2.95(10)$  [65], the Luttinger-Ward (LW) calculation  $\tilde{C} = 3.02$  [27], as well as previous measurements using losses  $\tilde{C} = 3.1(3)$  [66] and Bragg spectroscopy  $\tilde{C} = 3.06(8)$  [46].

For a more efficient measurement of the contact across a range of temperatures, we vary the pulse time at a fixed detuning of 60 kHz ( $\hbar\omega/E_F \gtrsim 6$ ) that is large compared to the Fermi energy and temperature. [52]. Deviations from linear response are observed for transfers as small as 5% (see inset of Fig. 2). We fit the transfers to an exponentially saturating function  $A[1 - \exp(-T_{\text{Pulse}}/\tau)]$ , and find the initial linear slope  $A/\tau$  in order to extract the contact for each temperature using Eq. (1). This ensures that every measurement is taken in the linear response regime.

In Fig. 3(a), we show the temperature dependence of the contact. As the gas is cooled, the contact shows a gradual increase down to the superfluid transition  $T_c$ . Entering the superfluid transition, the contact rapidly rises by approximately 15%. The changes in the contact reveal the temperature dependence of short-range pair correlations in the spin-balanced Fermi gas. At temperatures far above  $T_F$ , the contact reflects the inverse mean free path in the gas  $1/l \sim 1/T$ . At lower temperatures, the behavior of the contact is better described by a third-order virial expansion [see inset of 3(a)] [36]. Near  $T_c$ , predictions of the contact vary considerably. In the quantum critical regime, a leading-order  $1/N$  calculation (equivalent to a Gaussian pair fluctuation or Nozières-Schmitt-Rink method) results in a prediction  $\tilde{C}(\mu = 0, T \approx 0.68T_F) = 2.34$  [10], which is consistent with our measurement of  $\tilde{C}[T = 0.65(4)T_F] = 2.29(13)$ . For temperatures above the superfluid transition, our data agree well with both a bold diagrammatic Monte Carlo calculation [38], and, especially near  $T_c$ , the LW calculation [32]. The contact rises as the temperature is decreased below  $T_c$ , a feature captured by the LW formalism, in which the contact is directly sensitive to pairing:  $\tilde{C} \sim (\Delta/E_F)^2$  [27,33]. While short-range pair correlations do not necessarily signify pairing [35], the rapid rise of the contact below  $T_c$  is strongly indicative of an additional contribution from fermion pairs, as predicted

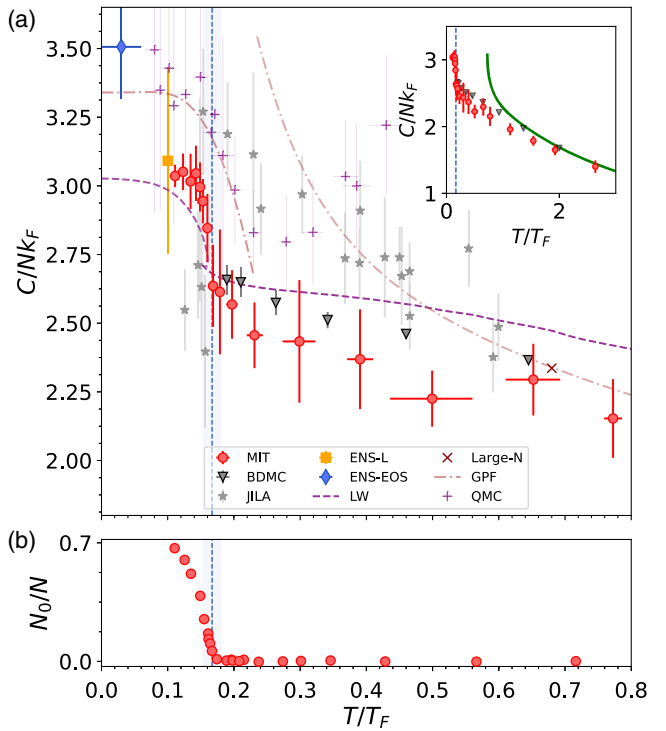


FIG. 3. The dimensionless contact  $C/Nk_F$  (a) and condensate fraction  $N_0/N$  (b) of the unitary Fermi gas as a function of the reduced temperature  $T/T_F$ . Our measurements of the contact (red points) are compared with a number of theoretical estimates: bold-diagrammatic Monte Carlo (BDMC) [38], quantum Monte Carlo (QMC) [37], Luttinger-Ward (LW) [32], large  $N$  [10], and Gaussian pair fluctuations (GPF) [36]. Also shown is the homogeneous contact obtained from the equation of state at the École normale supérieure (ENS-EOS) [62], from loss rate measurements (ENS-L) [66], and from rf spectroscopy by the JILA group [18] across a range of temperatures. The vertical blue dotted lines and light blue shaded vertical regions mark  $T_c/T_F = 0.167(13)$  [14]. The inset of (a) shows the contact over a wider range of temperatures and marks the high-temperature agreement with the third order virial expansion. The error bars account for the statistical uncertainties in the data.

by LW. At temperatures  $T \ll T_c$ , below the reach of our experiment, phonons are likely the only remaining excitations in the unitary Fermi gas, and are expected to contribute to the contact by an amount that scales as  $T^4$  [67].

In conclusion, rf spectroscopy of the homogeneous unitary Fermi gas reveals strong attractive interactions, the non-Fermi-liquid nature of excitations in the gas across the quantum critical regime, and a rapid increase in short-range pair correlations upon entering the superfluid regime. The strong variation with temperature of the position of the spectral peak may serve as a local thermometer in future studies of heat transport in ultracold Fermi gases. Furthermore, these measurements of the contact provide a benchmark for many-body theories of the unitary Fermi gas. The uniform trap enables direct access to homogeneous measurements of thermodynamic quantities,

and increases sensitivity to abrupt changes of those quantities near phase transitions. This could be particularly useful in the limit of high spin imbalance, where the nature of impurities suddenly transitions from Fermi polarons to molecules. [68,69].

We note that measurements of the temperature dependence of the contact were simultaneously performed at Swinburne using Bragg spectroscopy [70]. Their data are in excellent agreement with the present results.

We thank C. J. Vale, F. Werner, and W. Zwerger for helpful discussions. This work was supported by the National Science Foundation (Center for Ultracold Atoms Awards No. PHY-1734011 and No. PHY-1506019), Air Force Office of Scientific Research (FA9550-16-1-0324 and MURI Quantum Phases of Matter FA9550-14-1-0035), Office of Naval Research (N00014-17-1-2257) and the David and Lucile Packard Foundation. J. S. was supported by LabEX ENS-ICFP; ANR-10-LABX-0010/ANR-10-IDEX-0001-02 PSL\*.

- [1] O. Hen *et al.*, *Science* **346**, 614 (2014).
- [2] R. Weiss, B. Bazak, and N. Barnea, *Phys. Rev. Lett.* **114**, 012501 (2015).
- [3] W. Ketterle and M. W. Zwierlein, in “Ultra-Cold Fermi Gases,” *Proceedings of the International School of Physics “Enrico Fermi,” Course CLXIV*, edited by M. Inguscio, W. Ketterle, and C. Salomon (IOS Press, Amsterdam, 2008), pp. 247–422.
- [4] S. Giorgini, L. P. Pitaevskii, and S. Stringari, *Rev. Mod. Phys.* **80**, 1215 (2008).
- [5] W. Zwerger, in “Quantum Matter at Ultralow Temperatures,” *Proceedings of the International School of Physics “Enrico Fermi” Course CLXCI*, edited by M. Inguscio, W. Ketterle, S. Stringari, and G. Roati (IOS Press, Amsterdam, 2016), pp. 63–142.
- [6] M. W. Zwierlein, in *Novel Superfluids* (Oxford University Press, Oxford, 2014), pp. 269–422.
- [7] A. J. Leggett, *Phys. Rev. Lett.* **29**, 1227 (1972).
- [8] P. A. Lee, N. Nagaosa, and X.-G. Wen, *Rev. Mod. Phys.* **78**, 17 (2006).
- [9] G. Baym, C. Pethick, and D. Pines, *Nature (London)* **224**, 673 (1969).
- [10] T. Enss, *Phys. Rev. A* **86**, 013616 (2012).
- [11] M. Randeria and E. Taylor, *Annu. Rev. Condens. Matter Phys.* **5**, 209 (2014).
- [12] P. Nikolic and S. Sachdev, *Phys. Rev. A* **75**, 033608 (2007).
- [13] B. Frank, J. Lang, and W. Zwerger, *J. Exp. Theor. Phys.* **127**, 812 (2018).
- [14] M. J. H. Ku, A. T. Sommer, L. W. Cheuk, and M. W. Zwierlein, *Science* **335**, 563 (2012).
- [15] S. Nascimbène, N. Navon, S. Pilati, F. Chevy, S. Giorgini, A. Georges, and C. Salomon, *Phys. Rev. Lett.* **106**, 215303 (2011).
- [16] I. Z. Rothstein and P. Shrivastava, *Phys. Rev. B* **99**, 035101 (2019).

- [17] J. P. Gaebler, J. T. Stewart, T. E. Drake, D. S. Jin, A. Perali, P. Pieri, and G. C. Strinati, *Nat. Phys.* **6**, 569 (2010).
- [18] Y. Sagi, T. E. Drake, R. Paudel, R. Chapurin, and D. S. Jin, *Phys. Rev. Lett.* **114**, 075301 (2015).
- [19] A. Perali, P. Pieri, G. C. Strinati, and C. Castellani, *Phys. Rev. B* **66**, 024510 (2002).
- [20] H. Hu, X. J. Liu, P. D. Drummond, and H. Dong, *Phys. Rev. Lett.* **104**, 240407 (2010).
- [21] P. Magierski, G. Włazłowski, and A. Bulgac, *Phys. Rev. Lett.* **107**, 145304 (2011).
- [22] S. Gupta, Z. Hadzibabic, M. W. Zwierlein, C. A. Stan, K. Dieckmann, C. H. Schunck, E. G. Van Kempen, B. J. Verhaar, and W. Ketterle, *Science* **300**, 1723 (2003).
- [23] C. A. Regal and D. S. Jin, *Phys. Rev. Lett.* **90**, 230404 (2003).
- [24] C. A. Regal, C. Ticknor, J. L. Bohn, and D. S. Jin, *Nature (London)* **424**, 47 (2003).
- [25] C. Chin, M. Bartenstein, A. Altmeyer, S. Riedl, S. Jochim, J. Denschlag, and R. Grimm, *Science* **305**, 1128 (2004).
- [26] C. H. Schunck, Y.-I. Shin, A. Schirotzek, and W. Ketterle, *Nature (London)* **454**, 739 (2008).
- [27] R. Haussmann, M. Punk, and W. Zwerger, *Phys. Rev. A* **80**, 063612 (2009).
- [28] S. Tan, *Ann. Phys. (Amsterdam)* **323**, 2971 (2008).
- [29] S. Tan, *Ann. Phys. (Amsterdam)* **323**, 2952 (2008).
- [30] S. Tan, *Ann. Phys. (Amsterdam)* **323**, 2987 (2008).
- [31] E. Taylor and M. Randeria, *Phys. Rev. A* **81**, 053610 (2010).
- [32] T. Enss, R. Haussmann, and W. Zwerger, *Ann. Phys. (Amsterdam)* **326**, 770 (2011).
- [33] P. Pieri, A. Perali, and G. C. Strinati, *Nat. Phys.* **5**, 736 (2009).
- [34] F. Palestini, A. Perali, P. Pieri, and G. C. Strinati, *Phys. Rev. A* **82**, 021605(R) (2010).
- [35] E. J. Mueller, *Rep. Prog. Phys.* **80**, 104401 (2017).
- [36] H. Hu, X. J. Liu, and P. D. Drummond, *New J. Phys.* **13**, 035007 (2011).
- [37] O. Goulko and M. Wingate, *Phys. Rev. A* **93**, 053604 (2016).
- [38] R. Rossi, T. Ohgoe, E. Kozik, N. Prokof’ev, B. Svistunov, K. Van Houcke, and F. Werner, *Phys. Rev. Lett.* **121**, 130406 (2018).
- [39] C. H. Schunck, Y. Shin, A. Schirotzek, M. W. Zwierlein, and W. Ketterle, *Science* **316**, 867 (2007).
- [40] G. Baym, C. J. Pethick, Z. Yu, and M. W. Zwierlein, *Phys. Rev. Lett.* **99**, 190407 (2007).
- [41] M. Punk and W. Zwerger, *Phys. Rev. Lett.* **99**, 170404 (2007).
- [42] J. T. Stewart, J. P. Gaebler, T. E. Drake, and D. S. Jin, *Phys. Rev. Lett.* **104**, 235301 (2010).
- [43] C. Shkedrov, Y. Florshaim, G. Ness, A. Gandman, and Y. Sagi, *Phys. Rev. Lett.* **121**, 093402 (2018).
- [44] E. D. Kuhnle, H. Hu, X. J. Liu, P. Dyke, M. Mark, P. D. Drummond, P. Hannaford, and C. J. Vale, *Phys. Rev. Lett.* **105**, 070402 (2010).
- [45] E. D. Kuhnle, S. Hoinka, P. Dyke, H. Hu, P. Hannaford, and C. J. Vale, *Phys. Rev. Lett.* **106**, 170402 (2011).
- [46] S. Hoinka, M. Lingham, K. Fenech, H. Hu, C. J. Vale, J. E. Drut, and S. Gandolfi, *Phys. Rev. Lett.* **110**, 055305 (2013).
- [47] A. Schirotzek, Y.-I. Shin, C. H. Schunck, and W. Ketterle, *Phys. Rev. Lett.* **101**, 140403 (2008).

- [48] Y. Sagi, T. E. Drake, R. Paudel, and D. S. Jin, *Phys. Rev. Lett.* **109**, 220402 (2012).
- [49] A. L. Gaunt, T. F. Schmidutz, I. Gotlibovych, R. P. Smith, and Z. Hadzibabic, *Phys. Rev. Lett.* **110**, 200406 (2013).
- [50] B. Mukherjee, Z. Yan, P. B. Patel, Z. Hadzibabic, T. Yefsah, J. Struck, and M. W. Zwierlein, *Phys. Rev. Lett.* **118**, 123401 (2017).
- [51] K. Hueck, N. Luick, L. Sobirey, J. Siegl, T. Lompe, and H. Moritz, *Phys. Rev. Lett.* **120**, 060402 (2018).
- [52] See Supplemental Material at <http://link.aps.org/supplemental/10.1103/PhysRevLett.122.203402> for further information, which includes Refs. [53–56].
- [53] L. N. Cooper, *Phys. Rev.* **104**, 1189 (1956).
- [54] M. Y. Veillette, D. E. Sheehy, and L. Radzhivsky, *Phys. Rev. A* **75**, 043614 (2007).
- [55] L. Pisani, P. Pieri, and G. C. Strinati, *Phys. Rev. B* **98**, 104507 (2018).
- [56] M. Naraschewski and D. M. Stamper-Kurn, *Phys. Rev. A* **58**, 2423 (1998).
- [57] Z. Yan, P. B. Patel, B. Mukherjee, R. J. Fletcher, J. Struck, and M. W. Zwierlein, *Phys. Rev. Lett.* **122**, 093401 (2019).
- [58] T.-L. Ho and E. J. Mueller, *Phys. Rev. Lett.* **92**, 160404 (2004).
- [59] R. J. Fletcher, R. Lopes, J. Man, N. Navon, R. P. Smith, M. W. Zwierlein, and Z. Hadzibabic, *Science* **355**, 377 (2017).
- [60] M. Sun and X. Leyronas, *Phys. Rev. A* **92**, 053611 (2015).
- [61] P. Nozières and S. Schmitt-Rink, *J. Low Temp. Phys.* **59**, 195 (1985).
- [62] S. Nascimbène, N. Navon, K. J. Jiang, F. Chevy, and C. Salomon, *Nature (London)* **463**, 1057 (2010).
- [63] P. Nozieres and D. Pines, *The Theory of Quantum Liquids, Vol I: Normal Fermi Liquids*, 1st ed. (W.A. Benjamin, New York, 1966).
- [64] E. Braaten, D. Kang, and L. Platter, *Phys. Rev. Lett.* **104**, 223004 (2010).
- [65] J. E. Drut, T. A. Lähde, and T. Ten, *Phys. Rev. Lett.* **106**, 205302 (2011).
- [66] S. Laurent, M. Pierce, M. Delehaye, T. Yefsah, F. Chevy, and C. Salomon, *Phys. Rev. Lett.* **118**, 103403 (2017).
- [67] Z. Yu, G. M. Bruun, and G. Baym, *Phys. Rev. A* **80**, 023615 (2009).
- [68] M. Punk, P. T. Dumitrescu, and W. Zwerger, *Phys. Rev. A* **80**, 053605 (2009).
- [69] A. Schirotzek, C.-H. Wu, A. Sommer, and M. W. Zwierlein, *Phys. Rev. Lett.* **102**, 230402 (2009).
- [70] C. Carcy, S. Hoinka, M. G. Lingham, P. Dyke, C. C. N. Kuhn, H. Hu, and C. J. Vale, preceding Letter, *Phys. Rev. Lett.* **122**, 203401 (2019).

## Supplemental Material: Spectral response and contact of the unitary Fermi gas

Biswaroop Mukherjee,<sup>1</sup> Parth B. Patel,<sup>1</sup> Zhenjie Yan,<sup>1</sup>

Richard J. Fletcher,<sup>1</sup> Julian Struck,<sup>1,2</sup> and Martin W. Zwierlein<sup>1</sup>

<sup>1</sup>MIT-Harvard Center for Ultracold Atoms, Research Laboratory of Electronics, and Department of Physics, Massachusetts Institute of Technology, Cambridge, Massachusetts 02139, USA

<sup>2</sup>Département de Physique, Ecole Normale Supérieure / PSL Research University, CNRS, 24 rue Lhomond, 75005 Paris, France

### DENSITY CALIBRATION IN THE HOMOGENEOUS TRAP

The density of atoms in the homogeneous trap is measured using *in situ* absorption imaging [S1]. The absolute atom numbers are calibrated by loading a spin-imbalanced gas into a hybrid trap that is axially harmonic and radially homogeneous [S2]. In Fig. S1, we plot the 1D density profile given by the integrated profile along the two homogeneous directions and the isothermal compressibility  $\kappa/\kappa_0 = -\partial E_{F\uparrow}/\partial U$  of the majority component, where  $\kappa_0 = \frac{3}{2n_\uparrow E_F}$  is the compressibility of an ideal Fermi gas at density  $n_\uparrow$ . The compressibility in the spin-polarized region provides the calibration of our measurement of density.

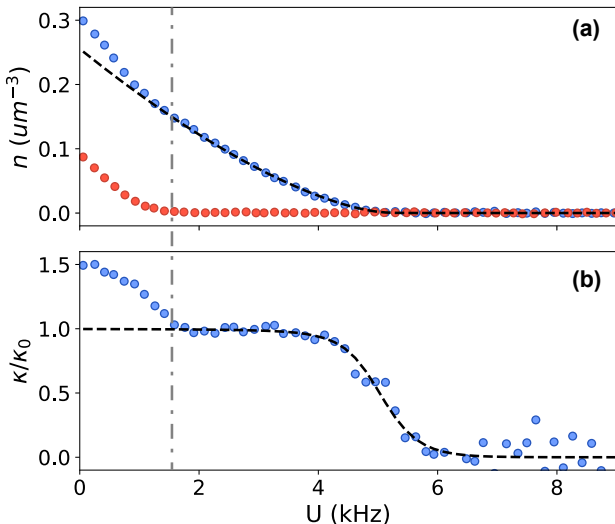


FIG. S1. Density calibration using the spin-imbalanced Fermi gas in the axially harmonic, radially homogeneous trap. Here, the majority Fermi energy is  $E_{F\uparrow}/\hbar = 5.7(1)$  kHz,  $T/T_{F\uparrow} = 0.05(1)$  and the imbalance is  $N_\downarrow/N_\uparrow = 0.18$ . (a) Majority (minority) density profiles in blue (red) data points. The dashed line is a fit to the ideal equation of state for the spin-polarized Fermi gas, restricted to the polarized wings of the cloud (outside the minority component edge, marked with the dot-dashed line). (b) The isothermal compressibility of the majority component as a function of position.

### RF SPECTROSCOPY MEASUREMENTS

For rf spectroscopy measurements, two images are taken within several  $\mu\text{s}$  of each other. The first image records the transferred cloud in state  $|f\rangle = |2\rrangle$ , while the second image allows for counting the number of atoms in the initial state  $|\downarrow\rangle = |1\rangle$ . For measurements of the full spectrum, the pulse time is set to  $T_{\text{Pulse}} = 1$  ms, giving a Fourier-limited spectral resolution of 1 kHz. For measurements of the contact, we select a detuning that is large compared to both the Fermi energy and the temperature of the cloud. This ensures that atoms are transferred from the high-momentum tails, and the transfer rate accurately measures the contact. For detunings between  $\hbar\omega \approx 5E_F$  and  $\hbar\omega \approx 13E_F$ , we verified that the measured value of  $\tilde{C}$  is constant within statistical errors. The Rabi frequencies are adjusted between  $\Omega_R = 2\pi \times 500$  Hz and  $\Omega_R = 2\pi \times 1$  kHz to maintain a high signal to noise ratio.

### COOPER PROBLEM AT FINITE TEMPERATURE

In the Cooper problem [S3] one searches for the binding energy of two opposite-spin fermions on top of the filled Fermi sea. The Fermi sea is treated as “inert”, its only role being to block momentum states that would otherwise be available to the scattering pair. This constraint alone already leads to pairing in three dimensions. Cooper’s solution can be extended to non-zero temperature, in the search of a bound state on top of a finite temperature Fermi gas. A standard approach [S4] yields an equation for the bound state energy  $E_c$  for Cooper pairs:

$$-\frac{m}{4\pi\hbar^2 a} = \int \frac{d^3 p}{(2\pi)^3} \left( \frac{(1 - n_F(\xi_p))^2}{2\xi_p - E_c} - \frac{1}{2\epsilon_p} \right), \quad (\text{S1})$$

where  $n_F(\epsilon) = (1 + \exp(\epsilon/T))^{-1}$  is the Fermi function,  $\xi_p = \frac{p^2}{2m} - \mu$ , and  $\mu$  the chemical potential of the non-interacting Fermi gas at temperature  $T$ . The factor  $(1 - n_F(\xi_p))^2$  represents Pauli blocking of momentum states already occupied in the spin up and the spin down Fermi sea. Without it, there would be no pairing of two

particles, as is well known in three dimensions. This simplest approach to pairing in a Fermi gas predicts a Cooper pair energy at resonance ( $1/a = 0$ ) of  $E_c = -0.61E_F$  at zero temperature, and an onset of pairing ( $E_c < 0$ ) at  $T^*/T_F = 0.41E_F$ . To look for binding in the full many-body framework, one searches for poles of the pair propagator. In the lowest-order T-matrix calculation or equivalently to lowest order in a  $1/N$  expansion [S5, S6] (where  $2N$  is the number of spin components of the Fermi gas), one finds an equation for this pole that is nearly identical to the above:

$$-\frac{m}{4\pi\hbar^2 a} = \int \frac{d^3 p}{(2\pi)^3} \left( \frac{(1 - n_F(\xi_p))^2 - n_F(\xi_p)^2}{2\xi_p - E_c} - \frac{1}{2\epsilon_p} \right). \quad (\text{S2})$$

Compared to the simple Cooper problem, the many-body approach yields an additional contribution to the integral from occupied momentum states  $\propto -n_F(\xi_p)^2$  as fermions within the Fermi sea now also profit from pairing. This does not change the prediction for the  $T = 0$  binding energy  $E_c = -0.61E_F$ , but it yields stronger binding at finite temperature, and predicts an onset of pairing at  $T^*/T_F = 0.5$ . In the main text, we show  $E_c$  from this lowest-order many-body approach. As is well-known, fluctuations reduce the onset of superfluidity to lower  $T_c$ . The next order in the  $1/N$  expansion yields [S5]  $T_c/T_F = 0.14$ , and the self-consistent T-matrix approach [S7] yields  $T_c/T_F = 0.16$ , in agreement with the experimental value  $T_c/T_F = 0.167(13)$  [S8]. However,  $T^*$  is often interpreted as the crossover temperature scale for pair formation [S9], and the region between  $T_c$  and  $T^*$  is the putative “pseudogap” regime. For a recent analysis of pair correlations see [S10].

## CONDENSATE FRACTION

The condensate fraction is measured by performing a momentum space mapping of the pair wavefunction. The atoms are released from the optical box potential into a magnetic harmonic trap with a confining trapping frequency  $\omega_z = 2\pi \times 23$  Hz along the z-direction. Simultaneously, the bias field is rapidly ramped from the Feshbach resonance to a value near a zero crossing of the scattering length, which associates existing fermion pairs into bosonic molecules, and preserves the center of mass momentum. Assuming the resulting molecules are non-interacting, the density profile of the cloud after a quarter-period oscillation in the harmonic trap provides the pair center of mass momentum distribution [S2]. The measured integrated profiles  $n_{1D}(z)$  are functions of the momentum  $k_z = m\omega_z z/\hbar$  along the z direction (see Fig. S2). We fit the wings with the momentum distribution for a thermal gas of non-interacting bosons [S11]:

$$n_{1D}(k_z) = \frac{1}{(2\pi k_B T)^{3/2}} g_{3/2} \left( e^{-|\hbar^2 k_z^2/2m - \mu|/k_B T} \right) \quad (\text{S3})$$

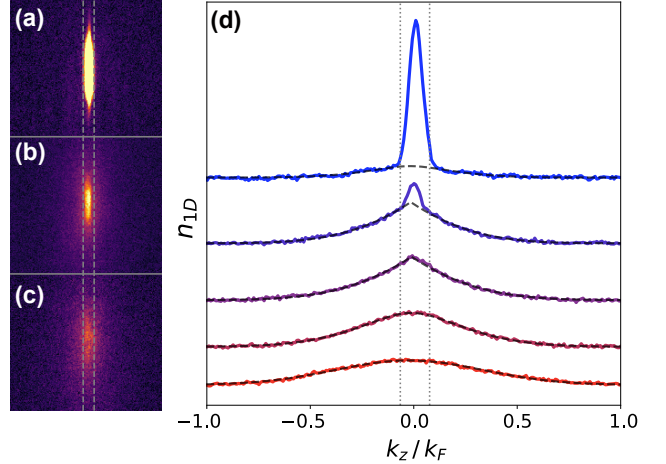


FIG. S2. Momentum space mapping of the box pair wavefunction. (a)-(c) Images of the cloud at  $T/T_F = 0.13$  in (a),  $0.16$  in (b), and  $0.18$  in (c), after a quarter-period release along the horizontal direction. (d) From top to bottom,  $T/T_F = 0.13, 0.16, 0.18, 0.21, 0.43$ . Here,  $n_{1D}$  is the two-axis integrated pair center of mass momentum distribution, and the dashed black lines are polylogarithm fits to the thermal wings. The dashed vertical lines in (a)-(c) and the dotted vertical lines in (d) mark the condensate region excluded from the fit ( $\approx \pm 0.07k_F$ ). Here,  $k_F$  is the Fermi wavevector in the uniform trap.

As the gas is cooled, the profiles display an increased occupation near zero momentum, and at  $T_c$ , a clear condensate peak emerges. We define the condensate fraction  $N_0/N$  as the difference in area between the observed profile and the fit to the thermal wings.

- [S1] Z. Yan, P. B. Patel, B. Mukherjee, R. J. Fletcher, J. Struck, and M. W. Zwierlein, (2018).
- [S2] B. Mukherjee, Z. Yan, P. B. Patel, Z. Hadzibabic, T. Yefsah, J. Struck, and M. W. Zwierlein, Phys. Rev. Lett. **118**, 123401 (2017).
- [S3] L. N. Cooper, Phys. Rev. **104**, 1189 (1956).
- [S4] W. Ketterle and M. W. Zwierlein, *Ultra-cold Fermi Gases, Proceedings of the International School of Physics Enrico Fermi, Course CLXIV, Varenna 2006*, edited by M. Inguscio, W. Ketterle, and C. Salomon (IOS Press, Amsterdam, 2008) pp. 247–422.
- [S5] P. Nikolic and S. Sachdev, Phys. Rev. A **75**, 033608 (2007).
- [S6] M. Y. Veillette, D. E. Sheehy, and L. Radzihovsky, Phys. Rev. A **75**, 043614 (2007).
- [S7] W. Zwerger, *Proceedings of the International School of Physics “Enrico Fermi” - Course 191 “Quantum Matter at Ultralow Temperatures”*, edited by M. Inguscio, W. Ketterle, S. Stringari, and G. Roati (IOS Press, Amsterdam; SIF Bologna, 2016) pp. 63–142.
- [S8] M. J. H. Ku, A. T. Sommer, L. W. Cheuk, and M. W. Zwierlein, Science **335**, 563 (2012).

- [S9] M. Randeria and E. Taylor, Annual Review of Condensed Matter Physics **5**, 209 (2014).
- [S10] L. Pisani, P. Pieri, and G. C. Strinati, Phys. Rev. B **98**, 104507 (2018).
- [S11] M. Naraschewski and D. M. Stamper-Kurn, Phys. Rev. A **58**, 2423 (1998).

## Appendix D

### Boiling a Unitary Fermi Liquid

This appendix contains a reprint of Ref. [195]:

## Boiling a Unitary Fermi Liquid

Zhenjie Yan,<sup>1</sup> Parth B. Patel,<sup>1</sup> Biswaroop Mukherjee,<sup>1</sup> Richard J. Fletcher,<sup>1</sup> Julian Struck,<sup>1,2</sup> and Martin W. Zwierlein<sup>1</sup>

<sup>1</sup>MIT-Harvard Center for Ultracold Atoms, Department of Physics, and Research Laboratory of Electronics, Massachusetts Institute of Technology, Cambridge, Massachusetts 02139, USA

<sup>2</sup>Département de Physique, Ecole Normale Supérieure/PSL Research University, CNRS, 24 rue Lhomond, 75005 Paris, France



(Received 1 November 2018; published 6 March 2019)

We study the thermal evolution of a highly spin-imbalanced, homogeneous Fermi gas with unitarity limited interactions, from a Fermi liquid of polarons at low temperatures to a classical Boltzmann gas at high temperatures. Radio-frequency spectroscopy gives access to the energy, lifetime, and short-range correlations of Fermi polarons at low temperatures  $T$ . In this regime, we observe a characteristic  $T^2$  dependence of the spectral width, corresponding to the quasiparticle decay rate expected for a Fermi liquid. At high  $T$ , the spectral width decreases again towards the scattering rate of the classical, unitary Boltzmann gas,  $\propto T^{-1/2}$ . In the transition region between the quantum degenerate and classical regime, the spectral width attains its maximum, on the scale of the Fermi energy, indicating the breakdown of a quasiparticle description. Density measurements in a harmonic trap directly reveal the majority dressing cloud surrounding the minority spins and yield the compressibility along with the effective mass of Fermi polarons.

DOI: 10.1103/PhysRevLett.122.093401

Landau's Fermi liquid theory provides a quasiparticle description of the low-temperature behavior for a large class of unordered fermionic states of matter, including most normal metals, atomic nuclei, and liquid helium-3 [1]. Strongly interacting Fermi gases with highly imbalanced spin populations have been identified as belonging to the same class [2–14]. The quasiparticles in spin-imbalanced Fermi gases are Fermi polarons: spin impurities dressed by an excess cloud of majority fermions. The stability of quasiparticles in a Fermi liquid is a consequence of the restricted phase space for collisions due to Pauli blocking. With increasing temperature  $T$ , the accessible phase space increases, and the lifetime of quasiparticles shortens, leading to the breakdown of Fermi liquid theory. In this intermediate temperature regime, the gas is neither a Fermi liquid nor a classical Boltzmann gas. For strong interactions, this regime is void of well-defined quasiparticles and controlled by the quantum critical point of the unitary spin-balanced gas at zero chemical potential and temperature [15–17].

Ultracold Fermi gases offer a unique opportunity to study the crossover from a low-temperature Fermi liquid to a classical Boltzmann gas, due to the large accessible temperature range. In spin-imbalanced Fermi gases, the two inequivalent Fermi surfaces provide additional richness. As the temperature is lowered from the classical regime, the Fermi surface of the majority forms first, giving minority spins the quasiparticle character of polarons. At even lower temperatures, the polarons themselves become quantum degenerate and form a Fermi surface.

In this Letter, we access the entire crossover from degenerate polarons to the classical Boltzmann gas through

the quantum critical region. The internal properties of the polaronic quasiparticles are measured via radio-frequency (rf) spectroscopy [10,18–20] on a homogeneous Fermi gas [21,22]. At low temperatures, the peak position and width of the rf spectra reflect energy and decay rate of the polarons. Note that the decay rate of a quasiparticle can be viewed as the rate of momentum relaxation in a transport measurement (see, e.g., [7]). The wings of the rf spectra yield information about the short-range correlations and the contact [23–27], controlling the change in the polaron energy with interaction strength. Further thermodynamic properties of the polaron gas are directly obtained from *in situ* density profiles in the presence of a harmonic potential [6,12,13,28–30], revealing the number of atoms in the majority dressing cloud of a polaron. The compressibility of the impurity gas at low temperature yields the effective mass of Fermi polarons.

For the spectroscopic studies we employ rf *ejection* spectroscopy, where the many-body state is first prepared and then probed by transferring a small fraction of one spin component into a weakly or noninteracting final state. Radio-frequency ejection spectroscopy has been used to, e.g., measure interactions, correlations, pairing phenomena in Fermi gases [31,32], and more specifically, the binding energy of the attractive Fermi polaron at low temperatures [10,19]. A prerequisite for our measurements is a spatially uniform box potential. This avoids the spectral broadening caused by an inhomogeneous density and impurity concentration [21,33]. The three energetically lowest hyperfine states of <sup>6</sup>Li (labeled |1⟩, |2⟩, |3⟩) are utilized to create and probe the strongly interacting spin mixture. The minority

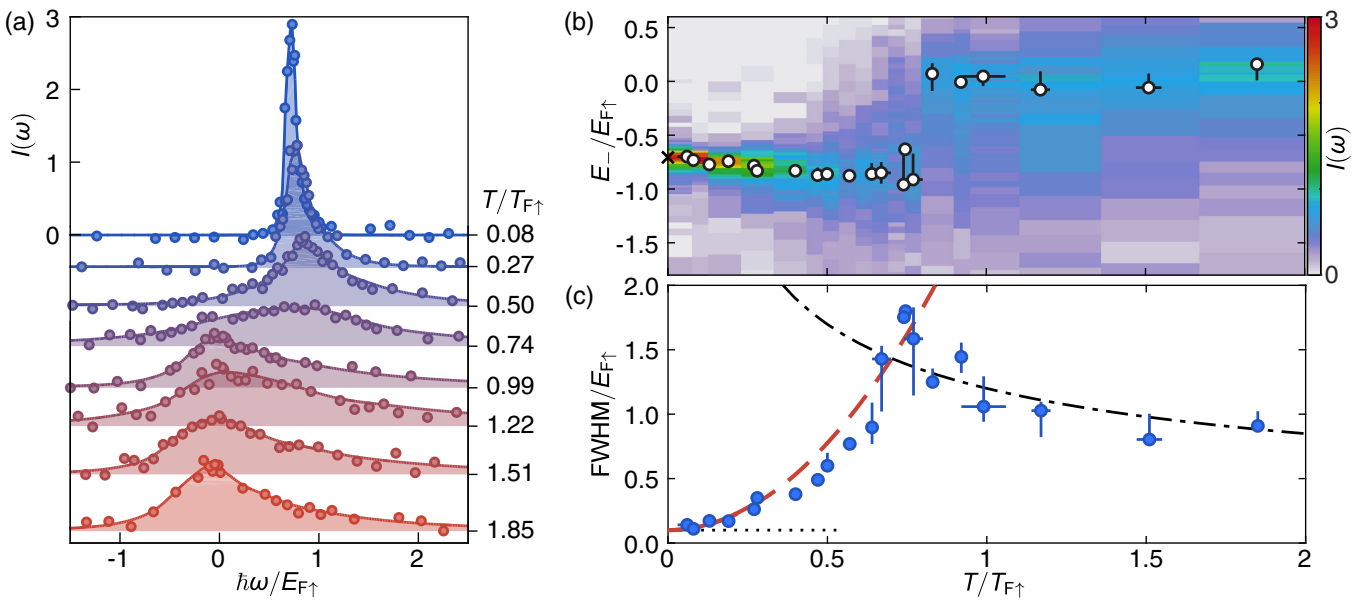


FIG. 1. (a) Thermal evolution of the minority rf spectra. The impurity concentration is  $n_\downarrow/n_\uparrow = 0.10 \pm 0.03$ , the Rabi frequency  $\Omega_R = 2\pi \times 0.5$  kHz, and the pulse duration  $T_{\text{pulse}} = 1$  ms. (b) 2D plot of the minority spectra with maxima highlighted by white points. To reflect the energy of the initial many-body state, the spectra are shown with the inverse frequency  $E_-/E_{F\uparrow}$ , where  $E_- = -\hbar\omega$ . The cross corresponds to the theoretical zero temperature result for the polaron energy, including a correction for final state interactions [3–5,8,38]. (c) FWHM of the rf spectra. (Dotted line) Fourier resolution limit; (dashed red line) single-polaron decay rate  $\Gamma/E_{F\uparrow} = 2.71(T/T_{F\uparrow})^2$  [7], offset by the Fourier limit; (dash-dotted black line) FWHM of the rf spectrum in the high-temperature limit  $\Gamma/E_{F\uparrow} = 1.2\sqrt{T_{F\uparrow}/T}$  [40,41], reflecting the scattering rate in the classical, unitary Boltzmann gas. [For the errors in (b) and (c), see the Supplemental Material [33].]

(impurity) and majority components are prepared in  $|\downarrow\rangle = |1\rangle$  and  $|\uparrow\rangle = |3\rangle$  and transferred via the rf drive into the final state  $|f\rangle = |2\rangle$  [33,37]. All measurements have been performed at a magnetic field of 690 G, where the interactions between minority and majority atoms are unitarity limited. Final state interactions are weakly repulsive with  $k_{F\uparrow}a_{\uparrow f} \lesssim 0.2$  ( $a_{\uparrow f} = 62$  nm). The impurity concentration (minority to majority density ratio  $n_\downarrow/n_\uparrow$ ) is controllably varied between 10% and 30%.

The rf response is linked to the probability that a hole of energy  $E$  and momentum  $\mathbf{p}$  is excited by ejecting a particle from the many-body state, as described by the occupied spectral function  $\mathcal{A}_{-\downarrow}(\mathbf{p}, E)$  [10,32,38,39]. Detecting a free particle of momentum  $\mathbf{p}$  after rf transfer implies a momentum  $\mathbf{p}$  and energy  $E_p = \mathbf{p}^2/2m - \mu_\downarrow - \hbar\omega$  of the leftover hole, where  $\mu_\downarrow$  is the minority chemical potential and  $\hbar\omega$  is the energy of the rf photon with respect to the non-interacting transition. The number of transferred minority atoms  $N_f(\omega)$  is proportional to the momentum integral of the occupied spectral function  $\mathcal{A}_{-\downarrow}(\mathbf{p}, E_p)$ . Fermi liquids feature a spectral function that is sharply peaked around  $\epsilon_0 + \mathbf{p}^2/2m^* - \mu_\downarrow$ , with the effective mass  $m^*$  and dressed energy  $\epsilon_0$  of the quasiparticles. The width of the peak is determined by the quasiparticle decay rate  $\Gamma(p, T)$ . For low temperatures and impurity concentrations, only low-momentum states are populated and the peak position

of the rf spectrum corresponds to the polaron binding energy [10].

Figure 1(a) shows the evolution with temperature of the rf spectra. Here, we have defined the normalized transfer  $I(\omega) = [N_f(\omega)/N_\downarrow](E_{F\uparrow}/\hbar\Omega_R^2 T_{\text{pulse}})$ , with the number of particles in the final (initial) state  $N_f$  ( $N_\downarrow$ ), the pulse duration  $T_{\text{pulse}}$ , and the single particle Rabi frequency  $\Omega_R$ . The term  $\Omega_R^2 T_{\text{pulse}}$  originates from the linear response to the rf pulse. The factor  $E_{F\uparrow}/\hbar$  in  $I$  is owed to the scale invariance of the unitary Fermi gas, which implies that its spectral features, such as the peak position, amplitude, and width directly scale with the Fermi energy [31,32]. The normalized transfer only depends on the dimensionless parameters  $T/T_{F\uparrow}$ ,  $n_\downarrow/n_\uparrow$ , and  $\hbar\omega/E_{F\uparrow}$ , apart from small corrections due to final state interactions and Fourier broadening that break the scale invariance of the system. The energy of the gas is measured by an isoenergetic release from the uniform to a harmonic trap. After thermalization, the in-trap size reveals the energy, from which we obtain the temperature via the equation of state (see Supplemental Material [33]).

In the deeply degenerate limit ( $T/T_{F\uparrow} < 0.1$ ), we observe a sharply defined resonance [Fig. 1(a)] signaling the stable long-lived Fermi polaron [10]. Its width, defined by the full width at half maximum (FWHM), is limited by the Fourier resolution. From the position of the spectral

peak at low temperature [Fig. 1(b)] and correction for weak final state interactions as in [10], we obtain a zero temperature polaron binding energy  $A \equiv \epsilon_0/E_{F\uparrow} = -0.60 \pm 0.05$ , with a linear extrapolation of the peak positions below  $T/T_{F\uparrow} = 0.3$ .

With increasing temperature, the spectral peak initially shifts to higher frequencies and broadens significantly [Figs. 1(b) and 1(c)]. A rise in the polaron binding energy with temperature is expected, given the increased scattering phase space of the majority spins, and is found theoretically [42,43]. However, note that the position of the maximum at finite temperature and impurity concentration is influenced by the density of states, the difference in the effective mass between initial and final state [20], and the thermal population of momentum states. At a temperature near  $T/T_{F\uparrow} \approx 0.75$ , a sharp jump in the position of the global maximum to  $\omega \approx 0$  is observed [Figs. 1(a) and 1(b)] [44]. In this regime, the width of the spectra reaches its maximum [Fig. 1(c)], on the order of the Fermi energy. Beyond this temperature, the position of the maximum remains constant at  $\omega \approx 0$ , as expected theoretically [40,41]. It reflects a merging of attractive and repulsive branches, symmetric about zero on resonance [45], as the temperature exceeds their splitting.

The spectral function of a Fermi liquid is a single Lorentzian peak with a width given by the decay rate of the quasiparticles [1]. The width of the rf spectra is dominated by this decay rate at low temperatures. We observe a quadratic scaling of the width at low temperatures, a hallmark of Fermi liquid theory, in agreement with a theoretical calculation [Fig. 1(c)] [7]. In the quantum critical regime around  $T \approx T_{F\uparrow}$ , the lifetime of the polarons drops below the Fermi time ( $\hbar/E_{F\uparrow}$ ), signaling a breakdown of quasiparticles [15–17]. The decrease in width at temperatures beyond the Fermi temperature is expected for a classical Boltzmann gas with unitarity limited interactions. The thermal scattering rate in the dilute impurity limit is given by  $\Gamma_{\text{th}} = n_\uparrow \sigma_{\text{th}} v_{\text{th}} \sim 1/\sqrt{T}$ , with the thermal velocity  $v_{\text{th}} \sim \sqrt{T}$  and the unitarity limited scattering cross section  $\sigma_{\text{th}} \sim \lambda^2 \sim 1/T$ .

Apart from energies and lifetimes, rf spectra also directly yield the strength of short-range correlations, quantified by contact  $C$  [Fig. 2(a)] [24–27,31,46,47]. The contact is a central quantity in a set of universal relations, linking microscopic properties to thermodynamics, which apply to all many-body systems with contact interactions [23]. It governs the tail of the momentum distribution, short-range pair correlations, and the change in energy with interaction strength [27,31,32]. As the contact is a measure of pair correlations, the tails of the rf spectrum of the minority and majority components are identical. For unitarity limited interactions, the fraction of transferred atoms in the high-frequency limit is given by [27]

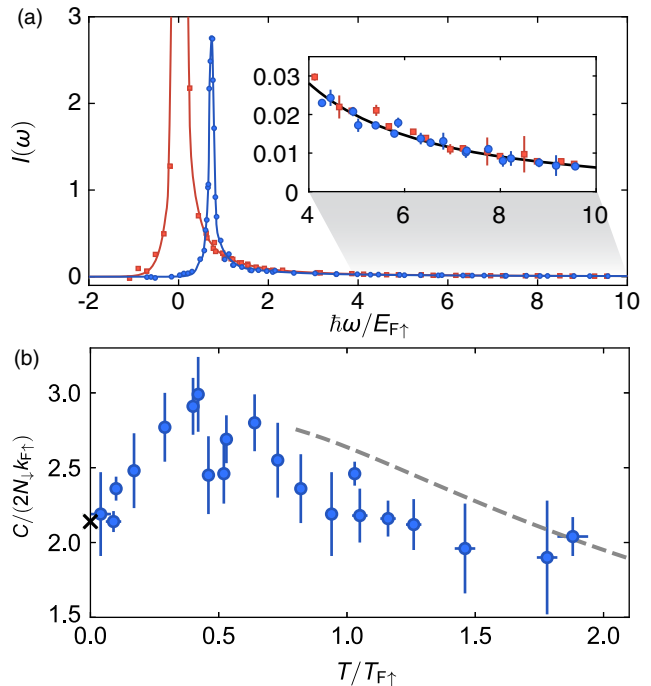


FIG. 2. Contact of the spin-imbalanced Fermi gas. (a) Typical rf spectra of the spin minority (blue circles) and majority (red squares). The impurity concentration is 10%. (Inset) High-frequency tails of the minority and majority spectra together with a fit of Eq. (1). (b) Contact as a function of temperature, obtained by measuring the transferred fraction of atoms as a function of rf pulse duration for frequencies  $\hbar\omega/E_{F\uparrow} > 5.5$  and use of Eq. (1). The gray dashed line shows the third-order viral expansion [48] and the cross shows the result from the Chevy ansatz [3,49].

$$I(\omega) \underset{\omega \rightarrow \infty}{=} \frac{C}{2N_\downarrow k_{F\uparrow}} \frac{1}{2\sqrt{2}\pi(1 + \hbar\omega/E_b)} \left( \frac{E_{F\uparrow}}{\hbar\omega} \right)^{3/2}, \quad (1)$$

where  $E_b = \hbar^2/m a_{\uparrow f}^2 \approx \hbar \times 433$  kHz. The inset of Fig. 2(a) shows the corresponding fit of the tails with Eq. (1), leaving only the contact as a free parameter.

The temperature dependence of the contact displays a nonmonotonic behavior with a maximum located around  $T \approx 0.4T_{F\uparrow}$  [Fig. 2(b)]. The observed initial rise in temperature is partially expected from the increase in scattering phase space and has also been found theoretically in a spin-imbalanced few-body calculation of the contact [50]. In the high-temperature limit, the contact is proportional to the scattering cross section and vanishes as  $1/T$ .

The contact quantifies short-range correlations. However, the polaron is an extended object with pair correlations extending out over distances even beyond the majority interparticle spacing [51]. We thus set out to probe the entire cloud of excess majority atoms surrounding the impurity spin of density  $\Delta n_\uparrow = n_\uparrow(\mu_\uparrow, \mu_\downarrow, T) - n_0(\mu_\uparrow, T)$  by *in situ* density measurements [Fig. 3(a)]. Here,  $n_\uparrow(\mu_\uparrow, \mu_\downarrow, T)$  is the actual measured density of the interacting majority

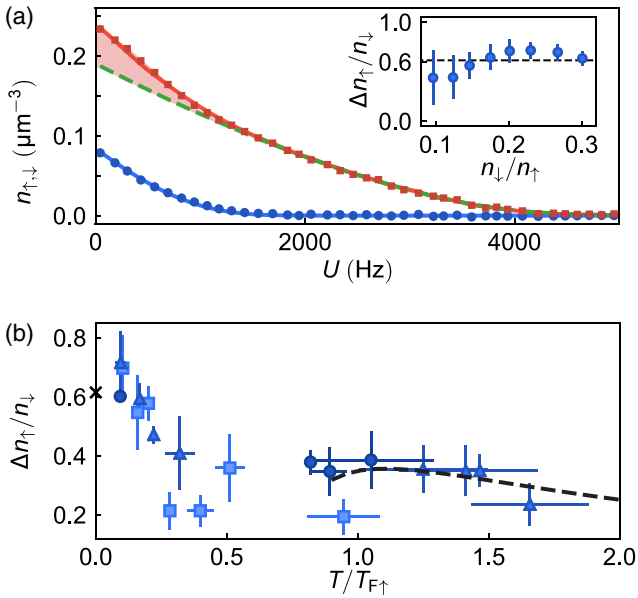


FIG. 3. Observation of the majority excess cloud. (a) Density profiles in a harmonically varying external potential  $U$ . Blue (red) data points indicate the profiles of the minority (majority) spin component. The normalized temperature of the gas is  $T/T_{F\uparrow} = 0.07$  in the trap center ( $U = 0$ ). The green dashed line represents the equation of state of the ideal Fermi gas, the red (blue) solid line is the Fermi liquid ansatz [Eq. (3)] for the majority (minority) component. The red shaded area displays the excess majority density  $\Delta n_{\uparrow}$ . (Inset) Dependence of the excess majority to minority ratio on the impurity concentration. (b) Temperature dependence of the majority excess cloud. Data points show the excess majority density  $\Delta n_{\uparrow}$  for an impurity concentration of  $n_{\downarrow}/n_{\uparrow} = 0.1$  (squares),  $n_{\downarrow}/n_{\uparrow} = 0.2$  (triangles), and  $n_{\downarrow}/n_{\uparrow} = 0.3$  (circles). The cross indicates the low-temperature prediction of the Fermi liquid ansatz  $\Delta n_{\uparrow}/n_{\downarrow} = -A = 0.615$  [8] and the dashed line shows the third-order virial expansion.

component and  $n_0(\mu_{\uparrow}, T)$  corresponds to the density of a noninteracting gas with the same temperature and majority chemical potential. For this measurement, we use a hybrid trapping potential that is harmonic along one direction and uniform along the other two axes [21]. This trapping geometry gives direct access to the density of each spin component as a function of the trapping potential  $U$  [Fig. 3(a)]. Under the local density approximation, the knowledge of  $n_{\uparrow,\downarrow}(U)$  can be used to extract a variety of thermodynamic quantities [12,13,30,33]. The majority chemical potential and temperature are obtained from the low-fugacity wings of the gas. In the case of a partially spin polarized wing, we use the third-order virial expansion [48], whereas for a fully spin polarized wing, we use the ideal equation of state. For the lowest temperatures, the excess majority density per minority atom is  $\Delta n_{\uparrow}/n_{\downarrow} = 0.63(5)$  [Fig. 3(b)]. For increasing temperature, the excess density drops until it reaches the value predicted by the virial expansion for the density.  $\Delta n_{\uparrow}/n_{\downarrow}$  displays no dependency

on the minority concentration within our error up to  $n_{\downarrow}/n_{\uparrow} = 0.3$ .

To elucidate the origin of the excess density from thermodynamics, we model the total pressure of the system as

$$P(\mu_{\uparrow}, \mu_{\downarrow}, T) = P_0(\mu_{\uparrow}, T) + \left(\frac{m^*}{m}\right)^{\frac{3}{2}} P_0(\mu_{\downarrow} - A\mu_{\uparrow}, T). \quad (2)$$

Here,  $P_0(\mu, T)$  is the pressure of the noninteracting Fermi gas. The ansatz describes the total pressure of the system as the sum of the partial pressure of the noninteracting majority component and the partial pressure of an ensemble of polarons with an effective chemical potential of  $\mu_{\downarrow} - A\mu_{\uparrow}$  and an effective mass  $m^*$  [12,13]. It contains weak interactions among the polarons that amount to a few percent of the total energy of the system [52]. From this pressure ansatz, the density can be calculated with the Gibbs-Duhem equation at constant temperature and scattering length ( $dP = n_{\uparrow} d\mu_{\uparrow} + n_{\downarrow} d\mu_{\downarrow}$ ),

$$\begin{aligned} n_{\uparrow}(\mu_{\uparrow}, \mu_{\downarrow}, T) &= n_0(\mu_{\uparrow}, T) - A n_{\downarrow}(\mu_{\uparrow}, \mu_{\downarrow}, T), \\ n_{\downarrow}(\mu_{\uparrow}, \mu_{\downarrow}, T) &= (m^*/m)^{\frac{3}{2}} n_0(\mu_{\downarrow} - A\mu_{\uparrow}, T), \end{aligned} \quad (3)$$

where  $n_0(\mu, T) \equiv \partial P_0 / \partial \mu$  is the density of the noninteracting gas. Each minority is accumulating on average  $|A| = 0.6$  excess majority atoms over the noninteracting limit, in agreement with our measured value [Fig. 3(b)].

Since the Fermi liquid ansatz describes the thermodynamics accurately in the low-temperature regime  $T/T_{F\uparrow} < 0.2$ , we now focus on this temperature regime and utilize the ansatz to determine the effective mass of the polarons from a measurement of the minority compressibility. In analogy to the total compressibility of the gas, the normalized isothermal minority compressibility is defined as  $\tilde{\kappa}_{\downarrow} \equiv -dE_{F\downarrow}/dU_{\text{eff}}$  [30]. Here,  $U_{\text{eff}} = (1 - A)U$  is the effective potential of the minority component generated by the interaction with the majority component [4,11]. Using Eq. (3) for the minority density, one finds

$$\tilde{\kappa}_{\downarrow}(T/T_{F\downarrow}) = \frac{m^* \kappa_0(T, T_{F\downarrow} m^*/m)}{m \kappa_0(0, T_{F\downarrow} m^*/m)}, \quad (4)$$

where  $\kappa_0(T, T_{F\downarrow}) \equiv n_0^{-2} (\partial n_0 / \partial \mu)_T$  is the compressibility of the noninteracting Fermi gas at fixed density. Figure 4 shows the measured isothermal compressibility of the minority component. A fit of Eq. (4) fixing  $A = -0.615$  [8] results in an effective mass of  $m^*/m = 1.25(5)$ , which is in agreement with results obtained from diagrammatic Monte Carlo simulations [8], a variational ansatz [5], and previous low-temperature experiments [11–13]. The saturation of the minority compressibility at low temperatures signals the formation of a degenerate Fermi sea of polarons.

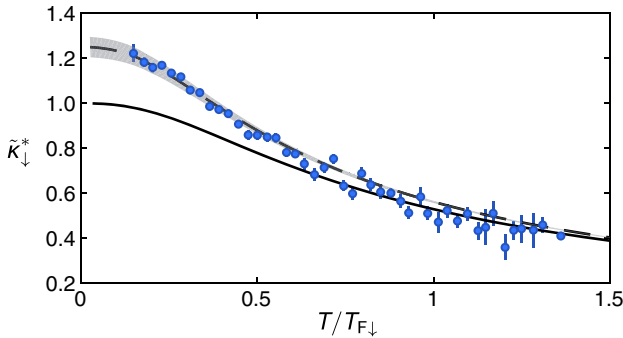


FIG. 4. Isothermal minority compressibility. The solid line is the Fermi liquid ansatz for  $m^*/m = 1$ , while the dashed line corresponds to a fit with an effective mass of  $m^*/m = 1.25(5)$  assuming  $A = -0.615$  [8]. The gray shaded area represents the standard deviation of the fit. For the entire range of temperatures displayed, the majority component is degenerate ( $T/T_{F\uparrow} < 0.2$ ).

In conclusion, we have studied the temperature dependence of a highly spin-imbalanced unitary Fermi gas with rf spectroscopy and in-trap density profiles. When the majority component is degenerate ( $T/T_{F\uparrow} \ll 1$ ), long-lived quasiparticles emerge. In the spirit of Fermi liquid theory, these polarons behave like a weakly interacting Fermi gas forming a sharp Fermi sea for  $T/T_{F\downarrow} \ll 1$ . The weakly interacting character of the quasiparticles is also reflected in the independence of the majority dressing cloud on the impurity concentration. In the opposing high-temperature regime, the gas is accurately described as a classical Boltzmann gas. At intermediate temperatures ( $T \approx T_{F\uparrow}$ ) the quasiparticle description breaks down. The spectral features of the attractive polarons dissolve, merging with excited branches, such as dressed dimerons [8,49,53] and repulsive polarons [18–20,38,53,54].

We thank Richard Schmidt and Felix Werner for helpful discussions. This work was supported by the National Science Foundation (Center for Ultracold Atoms Awards No. PHY-1734011 and No. PHY-1506019), Air Force Office of Scientific Research (FA9550-16-1-0324 and MURI Quantum Phases of Matter FA9550-14-1-0035), Office of Naval Research (N00014-17-1-2257) and the David and Lucile Packard Foundation. J. S. was supported by LabEX ENS-ICFP: ANR-10-LABX-0010/ANR-10-IDEX-0001-02 PSL\*.

- [1] P. Nozières and D. Pines, *The Theory of Quantum Liquids, Vol. I: Normal Fermi Liquids*, 1st ed. (W.A. Benjamin, New York, 1966).
- [2] M. W. Zwierlein, A. Schirotzek, C. H. Schunck, and W. Ketterle, *Science* **311**, 492 (2006).
- [3] F. Chevy, *Phys. Rev. A* **74**, 063628 (2006).
- [4] C. Lobo, A. Recati, S. Giorgini, and S. Stringari, *Phys. Rev. Lett.* **97**, 200403 (2006).
- [5] R. Combescot, A. Recati, C. Lobo, and F. Chevy, *Phys. Rev. Lett.* **98**, 180402 (2007).
- [6] Y.-I. Shin, C. H. Schunck, A. Schirotzek, and W. Ketterle, *Nature (London)* **451**, 689 (2008).
- [7] G. M. Bruun, A. Recati, C. J. Pethick, H. Smith, and S. Stringari, *Phys. Rev. Lett.* **100**, 240406 (2008).
- [8] N. Prokof'ev and B. Svistunov, *Phys. Rev. B* **77**, 020408 (2008).
- [9] M. Veillette, E. G. Moon, A. Lamacraft, L. Radzhovsky, S. Sachdev, and D. E. Sheehy, *Phys. Rev. A* **78**, 033614 (2008).
- [10] A. Schirotzek, C.-H. Wu, A. Sommer, and M. W. Zwierlein, *Phys. Rev. Lett.* **102**, 230402 (2009).
- [11] S. Nascimbène, N. Navon, K. J. Jiang, L. Tarruell, M. Teichmann, J. McKeever, F. Chevy, and C. Salomon, *Phys. Rev. Lett.* **103**, 170402 (2009).
- [12] S. Nascimbène, N. Navon, K. J. Jiang, F. Chevy, and C. Salomon, *Nature (London)* **463**, 1057 (2010).
- [13] N. Navon, S. Nascimbène, F. Chevy, and C. Salomon, *Science* **328**, 729 (2010).
- [14] A. Sommer, M. Ku, and M. W. Zwierlein, *New J. Phys.* **13**, 055009 (2011).
- [15] P. Nikolić and S. Sachdev, *Phys. Rev. A* **75**, 033608 (2007).
- [16] T. Enss, *Phys. Rev. A* **86**, 013616 (2012).
- [17] B. Frank, J. Lang, and W. Zwerger, *ZhETF* **154**, 953 (2018) [*J. Exp. Theor. Phys.* **127**, 812 (2018)].
- [18] C. Kohstall, M. Zaccanti, M. Jag, A. Trenkwalder, P. Massignan, G. M. Bruun, F. Schreck, and R. Grimm, *Nature (London)* **485**, 615 (2012).
- [19] M. Koschorreck, D. Pertot, E. Vogt, B. Fröhlich, M. Feld, and M. Köhl, *Nature (London)* **485**, 619 (2012).
- [20] F. Scazza, G. Valtolina, P. Massignan, A. Recati, A. Amico, A. Burchianti, C. Fort, M. Inguscio, M. Zaccanti, and G. Roati, *Phys. Rev. Lett.* **118**, 083602 (2017).
- [21] B. Mukherjee, Z. Yan, P. B. Patel, Z. Hadzibabic, T. Yefsah, J. Struck, and M. W. Zwierlein, *Phys. Rev. Lett.* **118**, 123401 (2017).
- [22] K. Hueck, N. Luick, L. Sobirey, J. Siegl, T. Lompe, and H. Moritz, *Phys. Rev. Lett.* **120**, 060402 (2018).
- [23] S. Tan, *Ann. Phys. (Amsterdam)* **323**, 2971 (2008).
- [24] G. Baym, C. J. Pethick, Z. Yu, and M. W. Zwierlein, *Phys. Rev. Lett.* **99**, 190407 (2007).
- [25] M. Punk and W. Zwerger, *Phys. Rev. Lett.* **99**, 170404 (2007).
- [26] W. Schneider, V. B. Shenoy, and M. Randeria, *arXiv: 0903.3006*.
- [27] E. Braaten, D. Kang, and L. Platter, *Phys. Rev. Lett.* **104**, 223004 (2010).
- [28] Y.-I. Shin, *Phys. Rev. A* **77**, 041603 (2008).
- [29] M. Horikoshi, S. Nakajima, M. Ueda, and T. Mukaiyama, *Science* **327**, 442 (2010).
- [30] M. J. H. Ku, A. T. Sommer, L. W. Cheuk, and M. W. Zwierlein, *Science* **335**, 563 (2012).
- [31] M. W. Zwierlein, in *Novel Superfluids*, edited by K.-H. Bennemann and J. B. Ketterson, 1st ed. (Oxford University Press, New York, 2014), Vol. 2, Chap. 18, pp. 269–422.
- [32] W. Zwerger, in *Quantum Matter at Ultralow Temperatures, Proceedings of the International School of Physics “Enrico Fermi,” Course CXCI*, edited by M. Inguscio, W. Ketterle,

- S. Stringari, and G. Roati (IOS Press, Amsterdam, 2016), Chap. 2, pp. 63–142.
- [33] See Supplemental Material at <http://link.aps.org/supplemental/10.1103/PhysRevLett.122.093401> for more information regarding the homogeneity of the gas, state preparation, thermometry, and rf spectroscopy, which includes Refs. [34–36].
- [34] J. E. Thomas, J. Kinast, and A. Turlapov, *Phys. Rev. Lett.* **95**, 120402 (2005).
- [35] T. L. Ho, *Phys. Rev. Lett.* **92**, 090402 (2004).
- [36] S. Nascimbène, N. Navon, S. Pilati, F. Chevy, S. Giorgini, A. Georges, and C. Salomon, *Phys. Rev. Lett.* **106**, 215303 (2011).
- [37] C. H. Schunck, Y.-I. Shin, A. Schirotzek, and W. Ketterle, *Nature (London)* **454**, 739 (2008).
- [38] P. Massignan, M. Zaccanti, and G. M. Bruun, *Rep. Prog. Phys.* **77**, 034401 (2014).
- [39] P. Törmä, *Phys. Scr.* **91**, 043006 (2016).
- [40] T. Enss, R. Haussmann, and W. Zwerger, *Ann. Phys. (Amsterdam)* **326**, 770 (2011).
- [41] M. Sun and X. Leyronas, *Phys. Rev. A* **92**, 053611 (2015).
- [42] H. Tajima and S. Uchino, *New J. Phys.* **20**, 073048 (2018).
- [43] B. C. Mulkerin, X.-J. Liu, and H. Hu, [arXiv:1808.07671](https://arxiv.org/abs/1808.07671).
- [44] Recently, a preprint appeared in which the authors, motivated by our work, found similar sudden shifts of the peak rf transfer. See H. Tajima and S. Uchino, [arXiv:1812.05889](https://arxiv.org/abs/1812.05889).
- [45] T. L. Ho and E. J. Mueller, *Phys. Rev. Lett.* **92**, 160404 (2004).
- [46] P. Pieri, A. Perali, and G. C. Strinati, *Nat. Phys.* **5**, 736 (2009).
- [47] J. T. Stewart, J. P. Gaebler, T. E. Drake, and D. S. Jin, *Phys. Rev. Lett.* **104**, 235301 (2010).
- [48] X.-J. Liu and H. Hu, *Phys. Rev. A* **82**, 043626 (2010).
- [49] M. Punk, P. T. Dumitrescu, and W. Zwerger, *Phys. Rev. A* **80**, 053605 (2009).
- [50] Y. Yan and D. Blume, *Phys. Rev. A* **88**, 023616 (2013).
- [51] C. Trefzger and Y. Castin, *Europhys. Lett.* **101**, 30006 (2013).
- [52] C. Mora and F. Chevy, *Phys. Rev. Lett.* **104**, 230402 (2010).
- [53] R. Schmidt and T. Enss, *Phys. Rev. A* **83**, 063620 (2011).
- [54] R. Schmidt, M. Knap, D. A. Ivanov, J.-S. You, M. Cetina, and E. Demler, *Rep. Prog. Phys.* **81**, 024401 (2018).

## Supplemental Material: Boiling a Unitary Fermi Liquid

Zhenjie Yan,<sup>1</sup> Parth B. Patel,<sup>1</sup> Biswaroop Mukherjee,<sup>1</sup> Richard J. Fletcher,<sup>1</sup> Julian Struck,<sup>1,2</sup> and Martin W. Zwierlein<sup>1</sup>

<sup>1</sup>*MIT-Harvard Center for Ultracold Atoms, Research Laboratory of Electronics, and Department of Physics, Massachusetts Institute of Technology, Cambridge, Massachusetts 02139, USA*

<sup>2</sup>*Département de Physique, Ecole Normale Supérieure / PSL Research University, CNRS, 24 rue Lhomond, 75005 Paris, France*

### STATE PREPARATION

The three hyperfine states  $|\downarrow\rangle = |1\rangle$ ,  $|f\rangle = |2\rangle$  and  $|\uparrow\rangle = |3\rangle$  are adiabatically connected to the respective states  $|F = \frac{1}{2}, m_F = \frac{1}{2}\rangle$ ,  $|\frac{1}{2}, -\frac{1}{2}\rangle$  and  $|\frac{3}{2}, -\frac{3}{2}\rangle$  at vanishing magnetic field. As in previous works at MIT [S1], we start from a degenerate and fully spin-polarized gas in state  $|1\rangle$  in an optical dipole trap, and prepare the spin-imbalanced mixture through two consecutive Landau-Zener sweeps at a magnetic field of  $B = 569$  G, where the interactions between all three states are weak. The magnetic field is then ramped up within 1 ms to the  $|1\rangle$ - $|3\rangle$  Feshbach resonance at  $B = 690$  G, where the gas is loaded into the uniform potential and cooled through forced evaporation over 2 seconds [S2].

### UNIFORM CYLINDER TRAP

Uniform trapping potentials offer a crucial advantage for non-local rf spectroscopy. For non-uniform traps, the Fermi energy and the impurity concentration vary spa-

tially, leading to an artificial broadening of the rf spectra.

For the rf measurements we load the gas into a cylinder-shaped uniform optical trap [S2] [Fig.S1 (a) and (b)]. Forced evaporation in this trap leads to temperatures of  $T \simeq 0.05 T_{F\uparrow}$  and majority Fermi energies of  $E_{F\uparrow}/h \sim 10$  kHz. Instead of adjusting the temperature of the gas by evaporation, we introduce an additional heating step by periodically modulating the cylindrical trapping potential by 20% at 1 kHz up to 4.5 s. We have found that this additional step reduces the spread in Fermi energies for different temperatures compared to a control through the evaporation.

We directly probe the variation in impurity concentration in the cloud from in-situ measurements of the cloud profiles [Fig.S1 (c) and (d)]. We find that the ratio of the effective volume of the minority component and the majority component is  $V_\downarrow/V_\uparrow > 0.8$ . More significantly for our purposes, well over 90% of the minority cloud is in a region of constant majority density at all temperatures. The radius  $R_{\uparrow,\downarrow}$  and length  $L_{\uparrow,\downarrow}$  of the gas have been determined by fitting the column integrated density profiles of the minority and majority component. The fitting functions along the radial ( $x$ ) and the axial ( $z$ ) direction are given by:

$$n_{\text{col}}(x) = \bar{n}_{\text{col}} \sqrt{R^2 - x^2}, \quad (\text{S1})$$

$$n_{\text{col}}(z) = \bar{n}_{\text{col}} \left( \text{erf} \left( \frac{L/2 + z}{\sqrt{2}\sigma_1} \right) + \text{erf} \left( \frac{L/2 - z}{\sqrt{2}\sigma_2} \right) \right) / 2. \quad (\text{S2})$$

Here,  $\text{erf}(z)$  denotes the error function and  $\sigma_{1,2}$  the effective widths of the potentials walls along the axial direction.

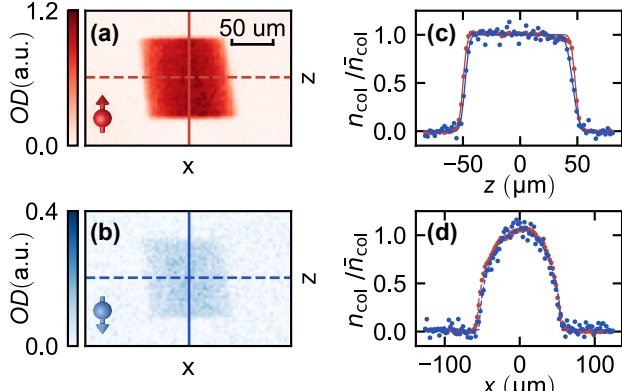


FIG. S1. Spin-imbalanced Fermi gas in the cylinder-shaped optical trap. Here,  $E_{F\uparrow}/h = 10.3 \pm 0.1$  kHz,  $T/T_{F\uparrow} = 0.74 \pm 0.01$  and  $n_\downarrow/n_\uparrow = 0.1$ . *In situ* absorption images of the majority (a) and minority (b) component along the radial direction of the cylinder. The column density along the axial (c) and radial (d) direction. The red (blue) points correspond to the majority (minority) component. The solid lines indicate the fits with Eqs. (S1) and (S2).

### THERMOMETRY OF THE HOMOGENEOUS UNITARY FERMI GAS

Standard thermometry methods for ultracold atoms rely on the low-fugacity tails in non-uniform traps. In addition, for weakly or non-interacting gases the momentum distribution, measured in time-of-flight, can be used to infer the temperature. However, in the case of strongly interacting homogeneous gases none of these methods is

directly applicable. Here we describe our thermometry method to obtain the temperature of the unitary Fermi gas in a uniform trap. First, we determine the energy of the gas in the uniform box potential. This energy then yields the temperature using the equation of state of the imbalanced gas.

### Energy Measurement

The total energy of the homogeneous gas is measured by an isoenergetic expansion into a hybrid cylindrical trap that features a harmonic potential along the axial direction ( $\omega_z = 2\pi \cdot 23$  Hz) and is uniform in the radial direction [S2]. Figure S2 shows the isoenergetic transfer between the two trapping potentials. For the transfer the two endcaps of the cylindrical trap are instantaneously removed and therefore no work is performed on the atoms. Subsequently the gas expands isoenergetically along the axial direction. Note that the underlying harmonic potential along the axial direction is always present, even for the experiments in the uniform trap. However, the potential variation due to the harmonic potential is only a few percent of the Fermi energy [S2]. After the removal of the endcaps we wait for 2 s to equilibrate the gas. The total energy of the gas in the hybrid cylindrical trap can be determined from the *in situ* density profiles using a one-dimensional version of the virial theorem [S3].

The total energy of the system is given by sum of the internal and potential energy

$$E = \int d^3r (\epsilon(r) + n(r) U(r)), \quad (S3)$$

with the internal energy density  $\epsilon(r)$ , the total density  $n(r) = n_{\downarrow}(r) + n_{\uparrow}(r)$  and the potential energy  $U(r)$ . The hybrid trap is uniform along the radial direction and we can express Eq. (S3) with the cylindrical cross-section  $A_{\text{cyl}}$  as

$$E = A_{\text{cyl}} \int dz (\epsilon(z) + n(z) U(z)), \quad (S4)$$

where we have defined  $\epsilon(z) \equiv \epsilon(x = 0, y = 0, z)$ ,  $n(z) \equiv n(x = 0, y = 0, z)$  and  $U(z) \equiv U(x = 0, y = 0, z)$ . For the unitary Fermi gas the internal energy is directly related to the pressure  $\epsilon(z) = 3/2 P(z)$  [S4]. Combined with a partial integration of the first term in Eq. (S4) this leads to

$$E = -\frac{3}{2} A_{\text{cyl}} \int z \frac{\partial P(z)}{\partial z} dz + A_{\text{cyl}} \int n(z) U(z) dz, \quad (S5)$$

where we have assumed that the pressure  $P(z)$  is an even function of  $z$ . With the equation for hydrostatic equilibrium (Gibbs-Duhem equation at constant scattering length and temperature)  $dP = n d\mu$  and the local

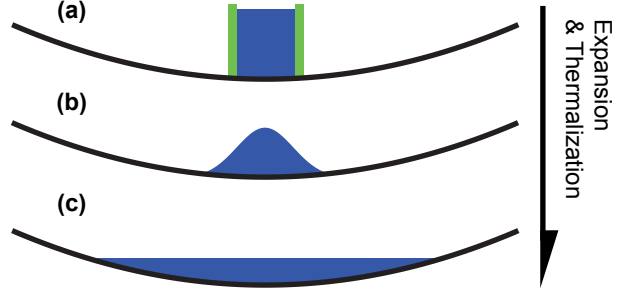


FIG. S2. Isoenergetic expansion from the uniform to harmonic trap. (a) Initially the gas is trapped in a quasi-uniform potential, (b) then the end caps of the trap are instantaneously removed, allowing the gas to expand into a harmonic trapping potential along the axial direction. (c) After a 2 s hold time the gas is in thermal equilibrium and the energy is determined using a one-dimensional virial theorem.

density approximation  $d\mu = -dU$ , we obtain the one-dimensional virial theorem

$$\begin{aligned} E &= \frac{3}{2} A_{\text{cyl}} \int z n(z) \frac{\partial U(z)}{\partial z} dz + A_{\text{cyl}} \int n(z) U(z) dz, \\ &= 2 A_{\text{cyl}} m \omega_z^2 \int n(z) z^2 dz. \end{aligned} \quad (S6)$$

In the second step of Eq. (S6) we have used the explicit expression for the harmonic potential  $U(z) = m \omega_z^2 z^2 / 2$ , with the trapping frequency  $\omega_z$  and mass  $m$ .

### Equation of State of the Spin-Imbalanced Unitary Fermi Gas

The conversion of the total energy into the corresponding temperature requires knowledge of the finite-temperature equation of state of the system. For this purpose, we have measured the finite temperature pressure equation of state of the spin-imbalanced unitary Fermi gas. As mentioned previously, at unitarity pressure and energy are directly related through  $E = 3/2 PV$ , with  $V$  as the volume [S4]. The zero-temperature equation of state of the spin-imbalanced Fermi gas has been measured previously, confirming Fermi-Liquid behaviour beyond the Chandrasekhar-Clogston limit in the normal fluid phase [S5–S9]. We determine the pressure of the gas from *in situ* density profiles in the hybrid trap [S2] and a precise knowledge of the harmonic trapping potential  $U$  along the axial direction of the trap [Fig. S3(a)]. From the equation for hydrostatic equilibrium and the local density approximation follows for the pressure  $P(U) = \int_U^\infty n(U) dU$  [S10] [Fig. S3(b)]. The impurity concentration is varying in this non-uniform trapping potential [Fig. S3(c)]. To fill the three-dimensional parameter space  $P(n, n_{\downarrow}/n_{\uparrow}, T)$ , we measure density profiles for varying initial evaporation parameters. The temperature

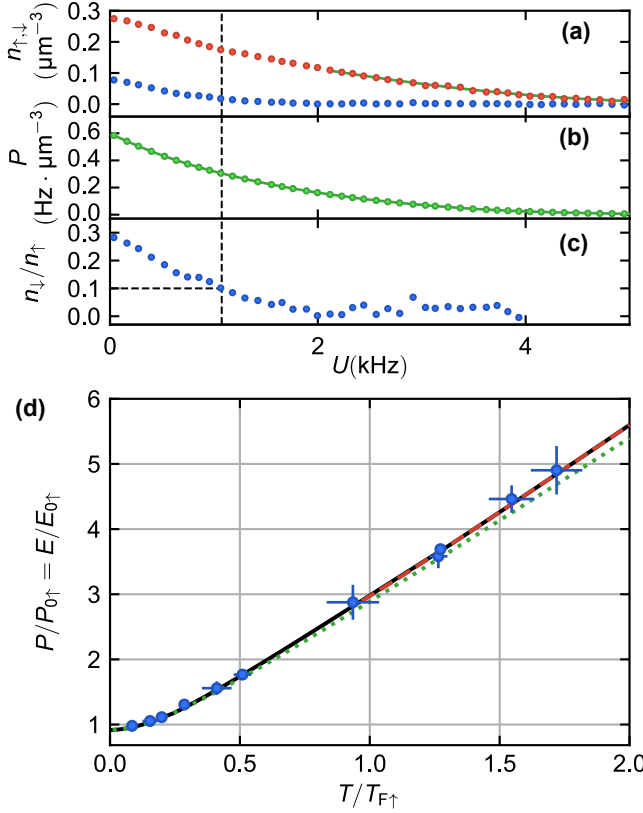


FIG. S3. Pressure of the spin-imbalanced unitary Fermi gas. (a) An example of *in situ* density profiles of the majority (red) and minority (blue) component in the hybrid trap. The temperature of  $T = 31 \pm 2$  nK is determined from a fit of the spin-polarized tail of the majority component with the equation of state of the non-interacting Fermi gas (green solid line). The majority Fermi energy in the center of the trap ( $U = 0$ ) is  $E_{F\uparrow}/h = 5.4 \pm 0.2$  kHz. (b) The local pressure of the gas, obtained from integrating the density profiles. (c) The local minority concentration. The relevant values for a minority concentration of  $n_\downarrow/n_\uparrow = 0.1$  are indicated with the dashed line. (d) The equation of state of the gas at fixed impurity concentration of  $n_\downarrow/n_\uparrow = 0.1$ . Our measurement is compared with the Fermi liquid ansatz (green dotted line) and 3rd order Virial expansion (red dashed line). An interpolation function (black solid line) is used to connect the Fermi liquid ansatz and Virial expansion.

is obtained from third order virial expansion fits [S11] to the low-fugacity tails of the gas or fits with the equation of state of the non-interacting Fermi gas, in case of spin-polarized tails.

Figure S3(d) shows the equation of state at a fixed impurity concentration of  $n_\downarrow/n_\uparrow = 0.1$ . For the unitary Fermi gas, the normalized pressure and energy are identical:  $P/P_{0\uparrow} = E/E_{0\uparrow}$ , with the ground state energy  $E_{0\uparrow} = 3/5 N_\uparrow E_{F\uparrow}$  and pressure  $P_{0\uparrow} = 2/5 n_\uparrow E_{F\uparrow}$  of the majority atoms. At low temperatures, the normalized pressure is in agreement with the Fermi liquid pressure ansatz [Eq. (3)], while at higher temperatures it

is in agreement with the virial expansion. We use an interpolation function that connects the high and low temperature regime to be able to determine the temperature for arbitrary pressure (energy) values [Fig. S3(d)].

## RF SPECTROSCOPY

In this section, we discuss the detection scheme used for rf spectroscopy, the determination of the transfer rate in the linear response regime and the definition of the error bars in Fig. 1 (b) and (c).

### Detection

For the measurement of the normalized transfer  $I(\omega)$ , the atom numbers in all three spin states  $|1\rangle$ ,  $|2\rangle$  and  $|3\rangle$  after the rf pulse need to be determined. For this purpose we have implemented a triple absorption imaging scheme that allows us to detect all three spin components in a single experimental run. The amount of transferred atoms  $N_f$  is determined from an absorption image along the axial direction of the cylinder trap recorded on an EMCCD camera. After 3 ms, the spin components  $|1\rangle$  and  $|3\rangle$  are subsequently imaged along the radial direction of the cylinder trap and recorded on a fast SCMOS camera with a time delay of  $10 \mu\text{s}$  between the two states.

### Linear Response

Linear response is an essential requirement for the applicability of Eqs. (1) and (2), linking the rf spectra to the spectral function and the contact. The linear transfer rate can be determined by measuring the transfer fraction  $N_f/N_\downarrow$  as a function of the rf pulse duration [Fig. S4]. For the contact data we fit the transfer rate with the exponential function  $N_f/N_\downarrow = \Gamma\tau(1 - \exp(-t/\tau))$  to account for saturation effects (time scale  $\tau$ ) and use the initial slope at short times to derive the linear transfer rate  $\Gamma$  [Fig. S4].

### Error Bars in Figure 1

Figure 1 shows the peak position and full width at half maximum (FWHM) at different temperatures. To determine the experimental uncertainty for these observables, we use the standard error of the measured transferred fraction without any rf pulse (see  $T_{\text{Pulse}} = 0$  in Fig. S4). The errors for the peak position and FWHM are then inferred from the frequency range of data points that lie within the standard error of the amplitude of the maximum and half maxima respectively.

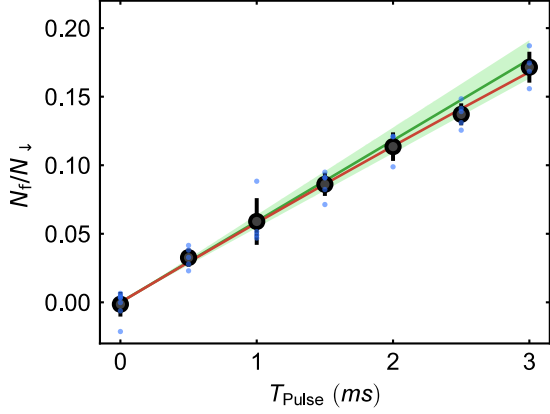


FIG. S4. Time resolved rf response of the minority component. Here, the majority Fermi energy is  $E_{F\uparrow}/h = 9.9 \pm 0.2, the impurity concentration  $n_\downarrow/n_\uparrow = 0.11 \pm 0.02$ , the rf detuning  $\omega = 2\pi \times 60 and the temperature  $T/T_{F\uparrow} = 0.73 \pm 0.02$ . The blue datapoints correspond to the measured rf transfer for several experimental runs and the black circles are the averaged data points. The transferred fraction is fitted with an exponential function (red solid line). The green solid line (shaded area) shows the initial linear slope  $\Gamma$  (standard error) of the fit.$$

- [S1] C. H. Schunck, Y.-I. Shin, A. Schirotzek, and W. Ketterle, *Nature* **454**, 739 (2008).
- [S2] B. Mukherjee, Z. Yan, P. B. Patel, Z. Hadzibabic, T. Yefsah, J. Struck, and M. W. Zwierlein, *Phys. Rev. Lett.* **118**, 123401 (2017).
- [S3] J. E. Thomas, J. Kinast, and A. Turlapov, *Phys. Rev. Lett.* **95**, 120402 (2005).
- [S4] T.-L. Ho, *Phys. Rev. Lett.* **92**, 090402 (2004).
- [S5] Y.-I. Shin, C. H. Schunck, A. Schirotzek, and W. Ketterle, *Nature* **451**, 689 (2008).
- [S6] Y.-I. Shin, *Phys. Rev. A* **77**, 041603 (2008).
- [S7] S. Nascimbène, N. Navon, K. J. Jiang, F. Chevy, and C. Salomon, *Nature* **463**, 1057 (2010).
- [S8] N. Navon, S. Nascimbène, F. Chevy, and C. Salomon, *Science* **328**, 729 (2010).
- [S9] S. Nascimbène, N. Navon, S. Pilati, F. Chevy, S. Giorgini, A. Georges, and C. Salomon, *Phys. Rev. Lett.* **106**, 215303 (2011).
- [S10] M. J. H. Ku, A. T. Sommer, L. W. Cheuk, and M. W. Zwierlein, *Science* **335**, 563 (2012).
- [S11] X.-J. Liu and H. Hu, *Phys. Rev. A* **82**, 043626 (2010).



## Appendix E

### Universal sound diffusion in a strongly interacting Fermi gas

This appendix contains a reprint of Ref. [141]:

## QUANTUM GASES

# Universal sound diffusion in a strongly interacting Fermi gas

Parth B. Patel<sup>1,2,3</sup>, Zhenjie Yan<sup>1,2,3</sup>, Biswaroop Mukherjee<sup>1,2,3</sup>, Richard J. Fletcher<sup>1,2,3</sup>, Julian Struck<sup>1,2,3,4</sup>, Martin W. Zwierlein<sup>1,2,3\*</sup>

Transport of strongly interacting fermions is crucial for the properties of modern materials, nuclear fission, the merging of neutron stars, and the expansion of the early Universe. Here, we observe a universal quantum limit of diffusivity in a homogeneous, strongly interacting atomic Fermi gas by studying sound propagation and its attenuation through the coupled transport of momentum and heat. In the normal state, the sound diffusivity  $D$  monotonically decreases upon lowering the temperature, in contrast to the diverging behavior of weakly interacting Fermi liquids. Below the superfluid transition temperature,  $D$  attains a universal value set by the ratio of Planck's constant and the particle mass. Our findings inform theories of fermion transport, with relevance for hydrodynamic flow of electrons, neutrons, and quarks.

**T**ransport in fermionic quantum matter lies at the heart of phenomena as varied as superconductivity in cuprates (1) and bilayer graphene (2), inspirals of neutron star binaries (3), and perfect fluidity of the early universe (4). For hydrodynamic flow, transport is governed by diffusion, which facilitates the decay of spatial variations in globally conserved quantities—such as momentum, energy, charge, or spin—at a rate set by the corresponding diffusivity. A ubiquitous example is the attenuation of sound in fluids, where the modulation in current density and temperature causes diffusion of momentum and heat, leading to attenuation of sound at a rate set by the sound diffusivity  $D$ . The magnitude and temperature dependence of sound diffusivity reveal many of the characteristic features of the underlying substance.

Kinetic theory yields an estimate of  $D \approx v l$ , where  $v$  is the average velocity of the particles and  $l$  is their mean free path, which can vary over many orders of magnitude across substances. However, for strongly interacting quantum liquids and gases, a certain universality of diffusion coefficients may be expected. Here, the mean free path becomes on the order of the interparticle spacing, and the velocity takes on the Heisenberg-limited value  $v \sim \hbar/m$ , where  $\hbar$  is the reduced Planck's constant and  $m$  is the particle mass. This leads to a limiting value of  $D \sim \hbar/m$ , with a numerical prefactor of order unity determined by the specific microscopic interactions. Such Heisenberg-limited values were observed for the spin diffusivity in a unitary Fermi gas (5–7), as well as the momentum

diffusivity (the shear viscosity) in both the quark-gluon plasma of the early Universe and the unitary Fermi gas (4). Notably, the quantum liquids of bosonic  $^4\text{He}$  and fermionic  $^3\text{He}$  display similar sound diffusivities of  $D \sim \hbar/m$  around 4 K (8, 9). However, upon lowering the temperature into the deeply degenerate regime, these two quantum liquids display markedly different behaviors in the damping of sound. Down to about 1 K, the sound attenuation in  $^4\text{He}$  does not vary strongly with temperature, decreasing only by a factor of two across the superfluid transition, with a minimum of  $D \approx 0.5\hbar/m$  (8, 10). By contrast,  $^3\text{He}$  features a diverging diffusivity ( $\propto 1/T^2$ ), characteristic of a Fermi liquid, growing to  $\sim 50,000\hbar/m$  around 2 mK, followed by a steep drop at the superfluid transition and settling to a value of  $\sim 5000\hbar/m$  (9). A priori, it is unclear whether the temperature dependence of sound attenuation in a strongly interacting, fermionic gas—of atoms, electrons, or neutrons—should resemble that of a quantum liquid, and if so, whether it corresponds more closely to the strongly interacting, but bosonic, liquid  $^4\text{He}$  or to the fermionic, but weakly interacting, liquid  $^3\text{He}$ .

Ultracold atomic Fermi gases at unitarity are a prototypical strongly interacting quantum fluid for transport experiments (11–15). Featuring a mean free path as short as one interparticle spacing, these systems display the most robust form of fermionic superfluidity and near-perfect hydrodynamic flow even in the normal state (16–18). The presence of scale invariance leads to universality in physics properties (13–15, 19–21), including transport (5, 22–24). The universality directly connects this system to a host of other strongly interacting Fermi systems across all energy and length scales from nuclear matter to neutron stars. For the unitary Fermi gas, scale invariance implies that sound diffusivity must remain the same upon changing all length scales by the same

factor. The diffusivity is thus  $\hbar/m$  times a universal function of  $T/T_F$ , where the temperature  $T$  is normalized by the Fermi temperature  $T_F$  that only depends on the particle density  $n$  (25). At nondegenerate temperatures  $T \gg T_F$ , we expect a unitary Boltzmann gas, where the thermal wavelength  $\lambda = \sqrt{2\pi\hbar^2/(mk_B T)}$  ( $k_B$ , Boltzmann constant) sets both the mean free path and the typical velocity of excitations,  $l \sim 1/(n\lambda^2)$  and  $v \sim \hbar/(m\lambda)$ , implying  $D \sim (\hbar/m)(T/T_F)^{3/2}$ . In the quantum critical regime of the unitary gas (26, 27), at  $T \sim T_F$ , the interaction and thermal energies are comparable and even the nature of the equilibrium state is a subject of debate (28, 29). At low temperatures  $T \ll T_F$ , it remains unknown whether the sound diffusivity diverges as  $1/T^2$  (30), as in the Fermi liquid  $^3\text{He}$  (31, 32), and whether any sudden drop in the sound diffusion occurs upon entering the superfluid regime. Calculation of such transport parameters is very difficult; for example, predictions for the shear viscosity vary from zero (33), as suggested by experiments on expanding inhomogeneous gases (22, 24), to infinity if phonon damping dominates (23, 34–36).

Transport experiments on Fermi gases have thus far used harmonic traps (15) or terminal configurations (37, 38) and have been used to probe collective oscillations (39–41), spin transport (5, 7, 42), viscosity (22), conductivity (37), and Josephson oscillations (38). However, obtaining transport coefficients of homogeneous matter from inhomogeneous samples in atom traps requires sophisticated analysis and assumptions on the spatial flow profile (5, 22, 43). With the recent advent of optical box traps (44–47), it is now possible to directly probe the transport properties of homogeneous quantum gases (47–50). The gas is then in the same state throughout, and transport properties are identical across the system.

Measurements of transport properties involve the response of a system to an external drive. In linear response, an applied potential change  $\delta V$  couples to perturbations in the fluid density  $\delta n = -\chi\delta V$  by the density response function  $\chi$ . Sound corresponds to a resonant response, that is, a pole in  $\chi$  at a frequency  $\omega = ck$ , set by the speed of sound  $c$  and wave number  $k$ , in the vicinity of which  $\chi(\omega, k) \sim 1/(\omega^2 - c^2k^2 + i\Gamma\omega)$  (51, 52). Here,  $i$  is the unit imaginary number and  $\Gamma$  is the damping rate of sound, given by  $\Gamma = Dk^2$  (53) for hydrodynamic systems. Measurements of  $\chi$  and  $\Gamma$  thus directly provide the sound diffusivity. Experiments involving liquid helium have used a number of techniques to measure  $\chi$ , from free decay of resonant modes in a cylindrical resonator (8, 9) to Brillouin scattering off of sound waves (54).

In our homogeneous quantum gas, the constant background density enables an ideal realization of a density response measurement

<sup>1</sup>Department of Physics, Massachusetts Institute of Technology, Cambridge, MA 02139, USA. <sup>2</sup>MIT-Harvard Center for Ultracold Atoms, Cambridge, MA 02139, USA. <sup>3</sup>Research Laboratory of Electronics, Massachusetts Institute of Technology, Cambridge, MA 02139, USA. <sup>4</sup>Département de Physique, Ecole Normale Supérieure/PSL Research University, CNRS, 24 rue Lhomond, 75005 Paris, France.

\*Corresponding author. Email: zwierlein@mit.edu

(Fig. 1A). We use an equal two-state mixture of  ${}^6\text{Li}$  atoms with resonant interstate interactions, confined to a cylindrical optical box potential composed of three repulsive laser beams: a hollow cylindrical beam providing the radial confinement (radius 60  $\mu\text{m}$ ) and two sheets of light serving as endcaps (length  $L \sim 100 \mu\text{m}$ ) (45). The number  $N \sim 10^6$  of atoms per spin state yields a Fermi energy of  $E_F = \hbar^2 k_F^2 / (2m) \sim \hbar \times 10 \text{ kHz}$ . To inject sound waves, we sinusoidally modulate the intensity of one endcap beam, which drives the gas at a well-defined frequency  $\omega$ , and a wide range of spatial wave numbers, Fourier limited by the width  $\sim 4 \mu\text{m}$  of the endcap potential's edge (55). At the given driving frequency, the resonant sound response of the gas is dominated by a specific wave number  $k = \omega/c$ , resulting in a traveling wave of sound. An in situ absorption image is taken after an evolution time sufficiently short such that no reflections occur, and the resonant wave number  $k$  is directly measured (Fig. 1B, ii to iv). By repeating this protocol for different drive frequencies, we obtain the dispersion relation  $\omega(k)$  for wave numbers  $k < 0.14k_F$  (Fig. 1C). It is linear within our measurement error, corresponding to a constant speed of sound  $c = \omega/k$  as a function of wave number. We note that at wavelengths approaching the interparticle spacing, and thus at momenta  $\hbar k$  approaching the Fermi momentum ( $k \sim k_F$ ), deviations from linear sound dispersion are expected for the unitary Fermi gas (56).

The precise measurement of the speed of sound allows a sensitive test of scale invariance of the unitary Fermi gas. In general, the speed of isentropic sound propagation  $c$  is directly tied to the equation of state by the hydrodynamic relation  $mc^2 = (\partial P/\partial n)_S = (V^2/N)(\partial^2 E/\partial V^2)|_S$ . Here,  $E$  is the energy,  $S$  is the entropy,  $V$  is the volume, and  $P = -(\partial E/\partial V)|_S$  is the pressure of the gas. A notable property of all nonrelativistic scale invariant systems in three dimensions is that their total energy scales as  $E \propto V^{-2/3}$ ; this follows from the scaling behavior  $E \rightarrow E/\lambda^2$  under dilation of space by a factor  $\lambda$ . This directly yields  $mc^2 = (10/9)E/N$ , independent of temperature or the phase of matter. In Fig. 1D, we show the measured speed of sound as a function of the energy per particle  $E/N$ , obtained from an isoenergetic expansion of the gas from the box into a harmonic trap (57). For both superfluid and normal samples (blue and red, respectively), the scale invariant prediction (solid black line) captures the data well with no free parameters. This demonstrates the universality of the speed of sound and scale invariance in the unitary Fermi gas in the explored window of temperature.

The attenuation of sound is already apparent in the spatial decay of the traveling waves shown in Fig. 1. For a precision measurement

of the sound diffusivity, we now turn to the steady-state response of the system to a continuous drive, which directly reveals the density response function  $\chi$ . The intensity of one of the endcaps is modulated for a sufficiently long time such that the density evolution has reached a steady state. After an integer number of driving cycles, the spatial Fourier transform of the density yields the out-of-phase response of the system, or  $\text{Im}[\chi(\omega, k)]$  (55). This quantity also gives the average power absorbed by the system for a drive at frequency  $\omega$  and spatial frequency  $k$ , and thus directly reveals the poles of  $\chi$  as resonances.

The measurements are summarized in Fig. 2. Each row of pixels in Fig. 2B shows the fractional density modulation at a particular drive frequency after integration along the radial axis. This “sonogram” reveals discrete normal modes, the first five of which are shown in Fig. 2A. The spatial Fourier transform, giving the out-of-phase response function, is shown in Fig. 2C. For each normal mode in the box, it features a peak at  $\omega = ck$ . The sound attenuation rate can be seen to increase with  $k$ , revealed in both a broadened frequency response as well as a reduced peak height.

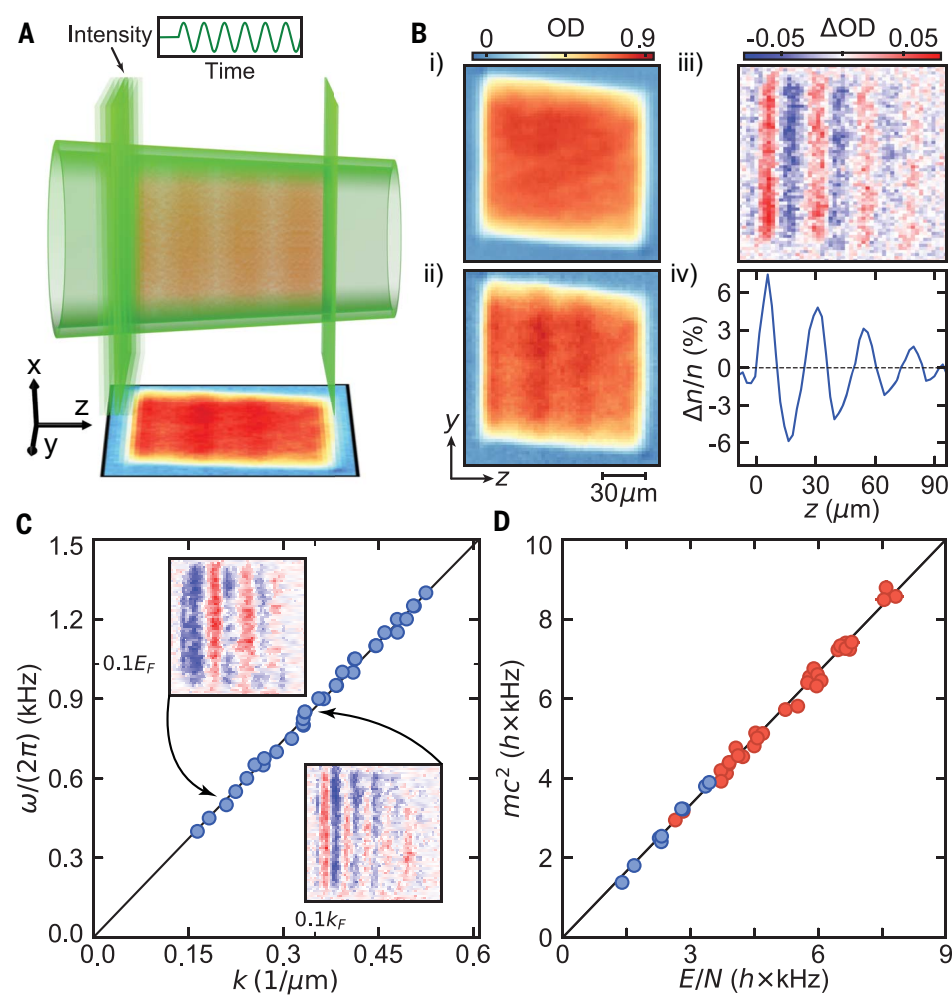


**Fig. 1. Sound waves in a homogeneous unitary Fermi gas.** (A) Fermionic  ${}^6\text{Li}$  atoms are trapped in a three-dimensional cylindrical box made from green laser beams. Sound is excited by modulating the intensity of one of the laser walls. (B) The resulting density wave is observed via an in situ absorption image, shown as optical density (OD) for both an unperturbed (i) and modulated (ii) sample. Here, the modulation frequency is  $2\pi \times 600 \text{ Hz}$ . Taking their difference (iii) and integrating along the homogeneous radial trap axis reveals (iv) a perturbation in the fractional density difference  $\Delta n/n$ , propagating along the axial direction  $z$  and exhibiting a well-defined wave number  $k$  corresponding to the applied modulation frequency  $\omega$ . (C) Dispersion of sound  $\omega(k)$ . The fitted slope (black line) provides the speed of sound. The insets display sound waves observed at  $\omega = 2\pi \times 600 \text{ Hz}$  and  $\omega = 2\pi \times 850 \text{ Hz}$ . Errors in the measured  $k$  are smaller than the point size. (D) Measurement of the universal relation between the measured speed of sound and the energy-per-particle  $E/N$  (see text). The black solid line shows the predicted linear dependence for any nonrelativistic scale invariant system in three dimensions;  $mc^2 = \frac{10}{9}E/N$ . Data are shown for both the normal (red) and the superfluid (blue) phase.

The density response  $\text{Im}[\chi(\omega, k_j)]$  at the wave number  $k_j = j\pi/L$  of the  $j^{\text{th}}$  normal mode of the box is shown in Fig. 3A, along with Lorentzian fits (solid lines). The full-width at half-maximum yields the damping rate of sound  $\Gamma$ , which is shown as a function of  $k$  in Fig. 3B, for gases both above (red and green) and below (blue) the superfluid transition. At temperatures above the superfluid transition temperature  $T_C = 0.17T_F$  (20), we observe  $\Gamma(k)$  to increase quadratically with  $k$  for all explored wave numbers ( $k \lesssim 0.3 mc/\hbar$ ). This establishes diffusive damping of sound in the normal regime, as expected in the collisionally hydrodynamic regime (16, 58).

Below the superfluid transition temperature,  $T < T_C$ , we observe a crossover from quadratic scaling of  $\Gamma(k)$  at wave numbers  $k \lesssim 0.2mc/\hbar$  to linear behavior, indicating a departure from purely hydrodynamic transport at high wave numbers. This is expected when the modulation frequency becomes comparable to the damping rate of thermal phonons  $\Gamma_{\text{ph}}$  (36, 59). Collisionless or Landau damping of sound is caused by nonlinearities resulting from the kinetic energy density carried by sound and the density dependence of the speed of sound. Fermi's golden rule yields a rate  $\Gamma_{\text{ph}} \propto k$  (36, 51) proportional to the energy  $\hbar c k$  carried by a phonon. Including a nonzero damping rate of phonons  $\Gamma_{\text{ph}}$  yields a crossover from hydro-

dynamic to collisionless damping as the sound frequency  $ck$  exceeds  $\Gamma_{\text{ph}}$  (59). The relation  $\Gamma = Dk^2 f(ck/\Gamma_{\text{ph}})$  with  $f(x) = \tan^{-1}(x)/x$  (59) shows a good agreement with the data (solid line). The scale of the fitted relaxation rate  $\Gamma_{\text{ph}} = 0.27(8)k_B T/\hbar$  is on the order of the gas temperature, hinting toward quantum critical damping (27). We note that the observation of quadratic scaling of  $\Gamma$  with  $k$  at low wave numbers implies that sound is primarily attenuated in the bulk, and that edge effects are negligible (53, 60).

As the main result of this work, we present in Fig. 4 the sound diffusivity  $D$  of the unitary Fermi gas. This is obtained as  $D = \Gamma/k^2$  using the  $j = 2$  normal mode, for which  $ck/\Gamma_{\text{ph}}$  is always less than 0.25, ensuring that it is well described by a hydrodynamic framework. The measured values are shown in units of  $\hbar/m$  and, at low temperatures, exhibit a numerical prefactor  $\sim 1$ . This demonstrates universal sound diffusion, with no dependence on microscopic parameters of the gas.

Generally, the sound diffusivity contains contributions from both the bulk and shear viscosity,  $\zeta$  and  $\eta$ , respectively (which damp momentum gradients), and the thermal conductivity  $\kappa$  (which damps temperature gradients) (53). However, for a scale-invariant fluid, the bulk viscosity vanishes (61) and  $D = D_\eta + D_\kappa$  only, with  $D_\eta = 4\eta/(3mn)$  and

$D_\kappa = 4\kappa T/(15P)$  (55). We note that our measurements of  $D$  therefore constrain the relationship between the viscosity and thermal conductivity, which is usually quantified by the Prandtl number  $\text{Pr} = c_p\eta/\kappa$  (53), where  $c_p$  is the specific heat at constant pressure (55).

The solid black line in Fig. 4 shows a prediction  $D = 6.46 (\hbar/m)(T/T_F)^{3/2}$ , which uses the high-temperature results for viscosity (23, 62) and thermal conductivity (23, 25), along with the ideal gas equation of state. This simple model captures the high-temperature behavior well without any free parameters. However, it is expected to underestimate  $D$  when  $T/T_F \lesssim 1$  because it neglects the suppression of scattering arising from Pauli blocking.

As the temperature is reduced,  $D$  smoothly drops to a value  $\sim \hbar/m$ , consistent with Heisenberg-limited diffusivity. Notably, at intermediate temperatures, we observe neither the  $D \sim 1/T^2$  scaling typical of a Fermi liquid nor any sudden change at the superfluid transition. This is further demonstrated by the inset of Fig. 4, where we show a magnified plot of  $D$  (blue points) in the vicinity of the superfluid transition (vertical red line) (20). Also shown is the pair condensate fraction (red points) obtained from the measured pair center-of-mass momentum distribution (63), which

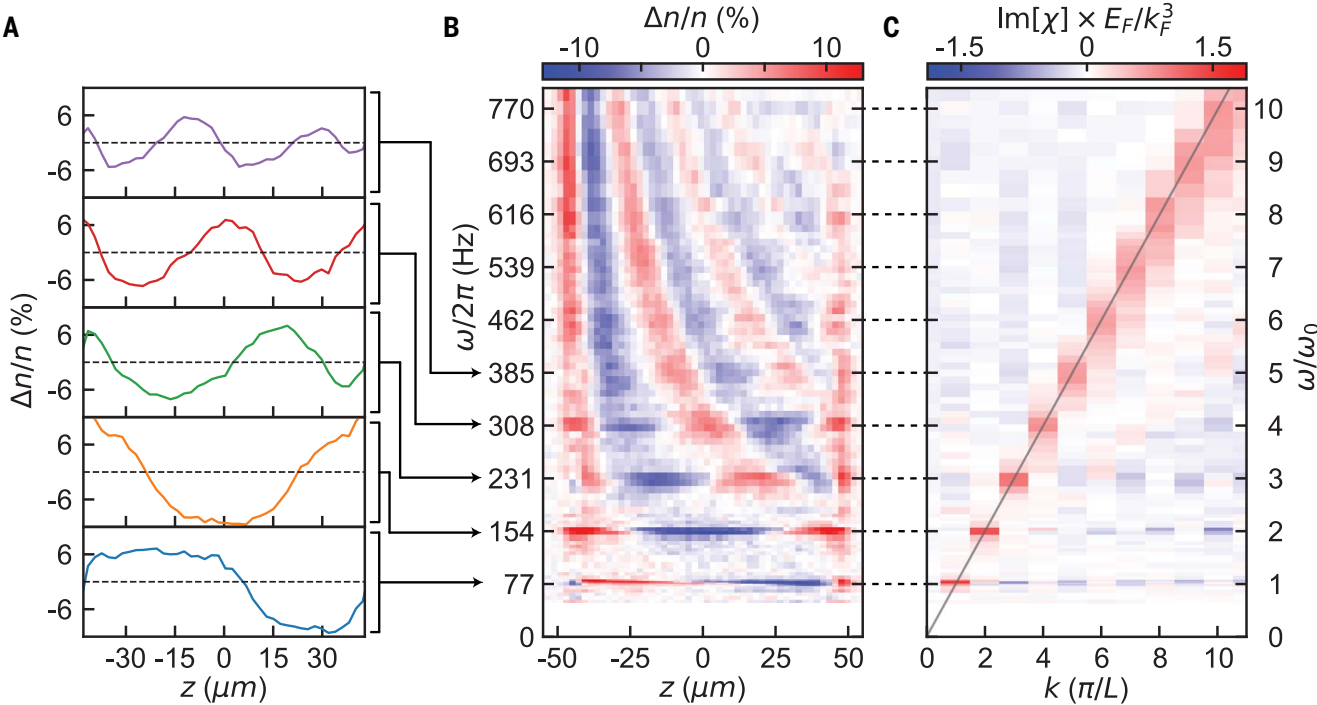


**Fig. 2. Normal modes of the cylindrical box trap.** (A and B) The steady-state density response of the gas is obtained by modulating the container walls at frequency  $\omega$  for 30 cycles of the drive. Standing waves of sound corresponding to the normal modes in the box are observed at frequencies  $\omega_j = j\pi c/L \approx 2\pi j \times 77\text{Hz}$  (where  $j \in \mathbb{Z}$ ), the first five of which are shown in (A). The full sonogram is shown in (B). Here, each row of pixels corresponds to a particular realization of the experiment at a given frequency. (C) The spatial Fourier transform directly yields the density response function  $\text{Im}[\chi(k, \omega)]$ . It reveals well-defined resonance peaks exhibiting both the linear dispersion of sound and increasing widths in frequency at higher wave numbers, corresponding to increased rates of sound attenuation.

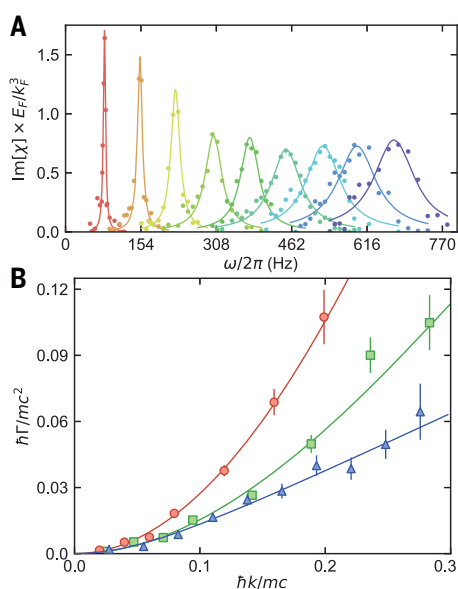


**Fig. 3. Spectral response of sound and its attenuation rate.** (A) The imaginary part of the density response function at each normal mode wave number  $k_j$  displays a well-defined peak in frequency, whose full-width at half-maximum yields the mode damping rate  $\Gamma$ . This is obtained from a Lorentzian fit, shown by solid lines. (B) Damping rate  $\Gamma(k)$  for gas temperatures  $T/T_F = 0.36(5)$  (red circles),  $T/T_F = 0.21(3)$  (green squares), and  $T/T_F = 0.13(2)$  (blue triangles). For all temperatures,  $\Gamma(k)$  displays a quadratic scaling at low momenta characteristic of diffusive damping. For our coldest samples, as  $k$  increases, we observe a deviation from this behavior, revealed by a crossover to linear scaling. At all temperatures and wave numbers, our data are well captured by the model of (59) (solid lines), which accounts for the finite relaxation rate of the fluid. Error bars represent  $1\sigma$  statistical uncertainty.

serves as both an indicator of superfluidity and a robust thermometer in the superfluid phase (15). Despite the definitive onset of pair condensation, we observe no measurable sharp feature in the diffusivity, which remains approximately constant as the temperature is reduced. Our nonvanishing diffusivity therefore contrasts previous measurements of a vanishing viscosity in the low-temperature limit (24).

This behavior can qualitatively be understood as follows. In the superfluid phase, viscosity arises entirely from the normal component, giving a diffusivity  $D \sim (n_n/n)lv$  where  $l = 1/(n_n\sigma)$  is the mean free path of a typical excitation with scattering cross section  $\sigma$ , velocity  $v$ , and density  $n_n$  (30, 64). The dependence on the (strongly temperature-dependent)  $n_n$  therefore cancels, giving  $D \sim v/(\sigma n)$ . At the temperatures studied here, the normal component is dominated by broken pairs (15), whose velocity and cross section are only weakly

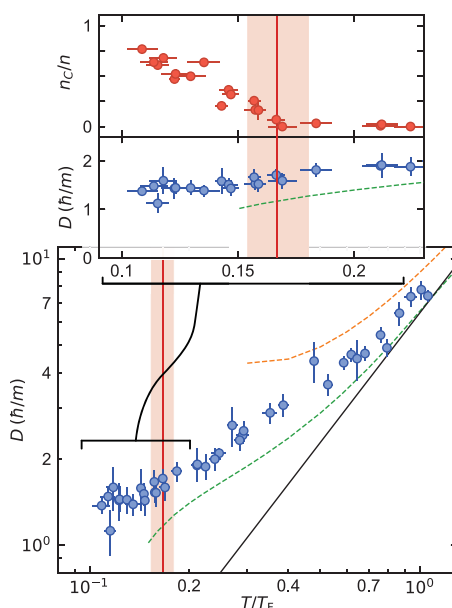


**Fig. 4. Temperature dependence of the sound diffusivity.** For temperatures comparable to the Fermi temperature, the sound diffusivity ( $D$ , normalized by  $\hbar/m$ ; blue circles) approaches the expected high-temperature scaling of  $T^{3/2}$  (solid black line). As the temperature is lowered,  $D$  decreases monotonically and attains a quantum-limited value close to  $\hbar/m$ . Below the superfluid transition [vertical red line, from (20)],  $D$  is observed to be almost independent of temperature and condensate fraction ( $n_c/n$ , red circles in inset). From the transition temperature ( $n_c/n = 0$ ) to the coldest temperatures ( $n_c/n \sim 0.8$ ), the changes in  $D$  are within the standard error of the measurements. Theoretical predictions for  $D$  are as follows: The dashed orange line is from the sound attenuation length calculated in the framework of kinetic theory (25), and the dashed green line is from a calculation of shear viscosity (23), assuming a Prandtl number of 2/3. Bars denote statistical error arising from the uncertainty in  $\Gamma$ . Additionally, the dominant systematic uncertainty in  $D$  is an error of 13% arising from the nonzero width of the endcaps. The red shaded regions represent the uncertainty in the superfluid transition temperature (20).

temperature-dependent. Broken pairs are primarily formed at the Fermi surface, which is broadened by the pairing gap  $\Delta$ . This results in a typical velocity  $v \sim \hbar k_F/m$  and cross section  $\sigma \sim k_F^{-2}(\Delta/E_F)^2$ , where the  $(\Delta/E_F)^2$  accounts for the restriction of phase space available for scattering arising from Pauli blocking. In the unitary Fermi gas,  $\Delta \sim 0.4E_F$  (41, 65), giving a diffusivity  $D \sim \hbar/m$ , consistent with our observations. By contrast, the pairing gap in  ${}^3\text{He}$  is  $\Delta \sim 10^{-3}E_F$ , leading to a much larger value of  $D \sim 5000\hbar/m$  (60, 66).

We have measured the sound diffusivity of the unitary Fermi gas. The diffusivity ap-

proaches a Heisenberg-limited value of  $\hbar/m$  at low temperatures, similar to the strongly interacting, bosonic quantum fluid  ${}^4\text{He}$ . In contrast to Fermi liquid behavior seen in weakly interacting fermionic systems, the diffusivity monotonically increases with increasing temperatures and eventually follows the high-temperature behavior  $D \sim \hbar/m(T/T_F)^{3/2}$ . The measured sound diffusivity constrains the shear viscosity and thermal conductivity of the unitary Fermi gas. In particular, combined with the calculated shear viscosity in (23), we find a Prandtl number strictly lower than unity for all explored temperatures (55). This excludes the existence of a relativistic conformal gravity dual of the unitary Fermi gas (67), because this would require  $\text{Pr} = 1$ . Thanks to the scale invariance of the unitary Fermi gas, the results obtained here apply broadly to other strongly interacting forms of fermionic matter, from hydrodynamic electron flow to nuclei and neutron matter.

## REFERENCES AND NOTES

- P. A. Lee, N. Nagaosa, X.-G. Wen, *Rev. Mod. Phys.* **78**, 17–85 (2006).
- Y. Cao et al., *Nature* **556**, 43–50 (2018).
- M. G. Alford, L. Bovard, M. Hanuske, L. Rezzolla, K. Schwenzer, *Phys. Rev. Lett.* **120**, 041101 (2018).
- A. Adams, L. D. Carr, T. Schäfer, P. Steinberg, J. E. Thomas, *New J. Phys.* **14**, 115009 (2012).
- A. Sommer, M. Ku, G. Roati, M. W. Zwierlein, *Nature* **472**, 201–204 (2011).
- A. B. Bardon et al., *Science* **344**, 722–724 (2014).
- C. Luciuk et al., *Phys. Rev. Lett.* **118**, 130405 (2017).
- K. H. Bennemann, J. B. Ketterson, *The Physics of Liquid and Solid Helium* (Wiley, 1976).
- D. Vollhardt, P. Wölfle, *The Superfluid Phases of Helium 3* (Dover Publications, Inc., 2013).
- V. S. L'vov, L. Skrbek, K. R. Sreenivasan, *Phys. Fluids* **26**, 041703 (2014).
- W. Ketterle, M. W. Zwierlein, in *Ultra-cold Fermi Gases*, vol. 164 of *Proceedings of the International School of Physics “Enrico Fermi”*, M. Inguscio, W. Ketterle, C. Salomon, Eds. (IOS Press, 2007), pp. 95–287.
- I. Bloch, J. Dalibard, W. Zwerger, *Rev. Mod. Phys.* **80**, 885–964 (2008).
- S. Giorgini, L. P. Pitaevskii, S. Stringari, *Rev. Mod. Phys.* **80**, 1215–1274 (2008).
- W. Zwerger, Ed., *The BCS-BEC Crossover and the Unitary Fermi Gas* (Springer, 2012).
- M. W. Zwierlein, *Novel Superfluids* (Oxford Univ. Press, 2014), pp. 269–422.
- K. M. O'Hara, S. L. Hemmer, M. E. Gehm, S. R. Granade, J. E. Thomas, *Science* **298**, 2179–2182 (2002).
- A. Altmeier et al., *Phys. Rev. Lett.* **98**, 040401 (2007).
- M. K. Tey et al., *Phys. Rev. Lett.* **110**, 055303 (2013).
- T.-L. Ho, *Phys. Rev. Lett.* **92**, 090402 (2004).
- M. J. H. Ku, A. T. Sommer, L. W. Cheuk, M. W. Zwierlein, *Science* **335**, 563–567 (2012).
- M. Randeria, E. Taylor, *Annu. Rev. Condens. Matter Phys.* **5**, 209–232 (2014).
- C. Cao et al., *Science* **331**, 58–61 (2011).
- T. Enss, R. Haussmann, W. Zwerger, *Ann. Phys.* **326**, 770–796 (2011).
- J. A. Joseph, E. Elliott, J. E. Thomas, *Phys. Rev. Lett.* **115**, 020401 (2015).
- M. Braby, J. Chao, T. Schäfer, *Phys. Rev. A* **82**, 033619 (2010).
- P. Nikolić, S. Sachdev, *Phys. Rev. A* **75**, 033608 (2007).
- T. Enss, *Phys. Rev. A* **86**, 013616 (2012).
- S. Nascimbène et al., *Phys. Rev. Lett.* **106**, 215303 (2011).
- I. Z. Rothstein, P. Shrivastava, *Phys. Rev. B* **99**, 035101 (2019).

30. H. Smith, H. H. Jensen, *Transport Phenomena* (Clarendon, 1989).
31. M. A. Black, H. E. Hall, K. Thompson, *J. Phys. C Solid State Phys.* **4**, 129–142 (1971).
32. C. N. Archie, T. A. Alvesalo, J. D. Reppy, R. C. Richardson, *J. Low Temp. Phys.* **42**, 295–332 (1981).
33. H. Guo, D. Wu, C.-C. Chien, K. Levin, *New J. Phys.* **13**, 075011 (2011).
34. G. Rupak, T. Schäfer, *Phys. Rev. A* **76**, 053607 (2007).
35. M. Mannarelli, C. Manuel, L. Tolos, *Ann. Phys.* **336**, 12–35 (2013).
36. H. Kurkjian, Y. Castin, A. Sinatra, *Ann. Phys.* **529**, 1600352 (2017).
37. S. Krinner, T. Esslinger, J.-P. Brantut, *J. Phys. Condens. Matter* **29**, 343003 (2017).
38. G. Valtolina et al., *Science* **350**, 1505–1508 (2015).
39. M. Bartenstein et al., *Phys. Rev. Lett.* **92**, 203201 (2004).
40. J. Kinast, S. L. Hemmer, M. E. Gehm, A. Turlapov, J. E. Thomas, *Phys. Rev. Lett.* **92**, 150402 (2004).
41. S. Hoinka et al., *Nat. Phys.* **13**, 943–946 (2017).
42. M. Koschorreck, D. Pertot, E. Vogt, M. Köhl, *Nat. Phys.* **9**, 405–409 (2013).
43. M. Bluhm, J. Hou, T. Schäfer, *Phys. Rev. Lett.* **119**, 065302 (2017).
44. A. L. Gaunt, T. F. Schmidutz, I. Gotlibovich, R. P. Smith, Z. Hadzibabic, *Phys. Rev. Lett.* **110**, 200406 (2013).
45. B. Mukherjee et al., *Phys. Rev. Lett.* **118**, 123401 (2017).
46. K. Hueck et al., *Phys. Rev. Lett.* **120**, 060402 (2018).
47. L. Baird, X. Wang, S. Roof, J. E. Thomas, *Phys. Rev. Lett.* **123**, 160402 (2019).
48. N. Navon, A. L. Gaunt, R. P. Smith, Z. Hadzibabic, *Nature* **539**, 72–75 (2016).
49. J. L. Ville et al., *Phys. Rev. Lett.* **121**, 145301 (2018).
50. S. J. Garratt et al., *Phys. Rev. A (Coll. Park)* **99**, 021601 (2019).
51. P. C. Hohenberg, P. C. Martin, *Ann. Phys.* **34**, 291–359 (1965).
52. P. C. Hohenberg, *J. Low Temp. Phys.* **11**, 745–750 (1973).
53. L. D. Landau, E. M. Lifshitz, *Fluid Mechanics* (Elsevier, 1959).
54. J. A. Tarvin, F. Vidal, T. J. Greytak, *Phys. Rev. B* **15**, 4193–4210 (1977).
55. See supplementary materials.
56. H. Kurkjian, Y. Castin, A. Sinatra, *Phys. Rev. A* **93**, 013623 (2016).
57. Z. Yan et al., *Phys. Rev. Lett.* **122**, 093401 (2019).
58. M. J. Wright et al., *Phys. Rev. Lett.* **99**, 150403 (2007).
59. C. J. Pethick, D. Ter Haar, *Physica* **32**, 1905–1920 (1966).
60. G. Eska et al., *Phys. Rev. Lett.* **44**, 1337–1340 (1980).
61. D. T. Son, *Phys. Rev. Lett.* **98**, 020604 (2007).
62. G. M. Bruun, H. Smith, *Phys. Rev. A* **72**, 043605 (2005).
63. B. Mukherjee et al., *Phys. Rev. Lett.* **122**, 203402 (2019).
64. C. J. Pethick, H. Smith, P. Bhattacharyya, *Phys. Rev. B* **15**, 3384–3400 (1977).
65. A. Schirotzek, Y. I. Shin, C. H. Schunck, W. Ketterle, *Phys. Rev. Lett.* **101**, 140403 (2008).
66. Y. A. Ono, J. Hara, K. Nagai, *J. Low Temp. Phys.* **48**, 167–188 (1982).
67. M. Rangamani, S. F. Ross, D. Son, E. G. Thompson, *J. High Energy Phys.* **2009**, 075 (2009).
68. P. B. Patel et al., Replication data for: Universal sound diffusion in a strongly interacting Fermi gas. Harvard Dataverse (2020); <https://doi.org/10.7910/DVN/UVM2KN>.

**ACKNOWLEDGMENTS**

We thank Y. Castin, T. Enss, T. Schäfer, C. J. Vale, and W. Zwerger for helpful discussions. **Funding:** This work was supported by the National Science Foundation (Center for Ultracold Atoms award nos. PHY-1734011 and PHY-1506019), U.S. Air Force Office of Scientific Research (FA9550-16-1-0324 and MURI Quantum Phases of Matter FA9550-14-1-0035), U.S. Office of Naval Research (N00014-17-1-2257), and the David and Lucile Packard Foundation. J.S. was supported by LabEX ENS-ICFP: ANR-10-LABX-0010/ANR-10-IDEX-0001-02 PSL\*. **Author contributions:** P.B.P., Z.Y., and J.S. performed the experimental measurements and data analysis. All authors contributed to the interpretation of the data and the preparation of the manuscript. **Competing interests:** The authors declare no competing interests. **Data and materials availability:** All data shown in this work can be found at Harvard Dataverse (68).

**SUPPLEMENTARY MATERIALS**

[science.sciencemag.org/content/370/1222/suppl/DC1](https://science.sciencemag.org/content/370/1222/suppl/DC1)  
Materials and Methods  
Supplementary Text  
Figs. S1 and S2  
References (69–73)

20 September 2019; accepted 24 October 2020  
10.1126/science.aaz5756

## Universal sound diffusion in a strongly interacting Fermi gas

Parth B. Patel, Zhenjie Yan, Biswaroop Mukherjee, Richard J. Fletcher, Julian Struck and Martin W. Zwierlein

Science 370 (6521), 1222-1226.  
DOI: 10.1126/science.aaz5756

### Watching sound die out

A gas of strongly interacting fermionic atoms can serve as a model for systems with densities and energies spanning many orders of magnitude. This universality of physics comes about thanks to a property known as scale invariance. Patel *et al.* exploited this concept to draw universal conclusions about the attenuation of sound in such systems by studying a homogeneous gas of lithium-6 atoms at very low temperatures (see the Perspective by Schaefer). They found that below the superfluid transition, the sound diffusivity behaved not unlike what has been observed in helium-4, a fluid of strongly interacting bosons.

Science, this issue p. 1222; see also p. 1162

### ARTICLE TOOLS

<http://science.sciencemag.org/content/370/6521/1222>

### SUPPLEMENTARY MATERIALS

<http://science.sciencemag.org/content/suppl/2020/12/02/370.6521.1222.DC1>

### RELATED CONTENT

<http://science.sciencemag.org/content/sci/370/6521/1162.full>

### REFERENCES

This article cites 66 articles, 5 of which you can access for free  
<http://science.sciencemag.org/content/370/6521/1222#BIBL>

### PERMISSIONS

<http://www.sciencemag.org/help/reprints-and-permissions>

Use of this article is subject to the [Terms of Service](#)

---

Science (print ISSN 0036-8075; online ISSN 1095-9203) is published by the American Association for the Advancement of Science, 1200 New York Avenue NW, Washington, DC 20005. The title *Science* is a registered trademark of AAAS.

Copyright © 2020 The Authors, some rights reserved; exclusive licensee American Association for the Advancement of Science. No claim to original U.S. Government Works

## Supplementary Materials for **Universal sound diffusion in a strongly interacting Fermi gas**

Parth B. Patel, Zhenjie Yan, Biswaroop Mukherjee, Richard J. Fletcher,  
Julian Struck, Martin W. Zwierlein\*

\*Corresponding author. Email: zwierlei@mit.edu

Published 4 December 2020, *Science* **370**, 1222 (2020)  
DOI: 10.1126/science.aaz5756

### This PDF file includes:

Materials and Methods  
Supplementary Text  
Figs. S1 and S2  
References

## Materials and Methods

The strongly interacting unitary Fermi gas was realized using an equal mixture of the first and third lowest hyperfine states of  ${}^6\text{Li}$ ,  $|1\rangle = |m_J = -\frac{1}{2}, m_I = 1\rangle$  and  $|3\rangle = |-\frac{1}{2}, -1\rangle$  respectively, with magnetic fields tuned to an interstate Feshbach resonance centered at  $\sim 690$  G (69, 70). The temperature and density were calibrated using the measured equation of state (20).

Sound waves were generated by sinusoidally modulating the intensity of one of the endcap laser sheets with sharpness  $\sim 4 \mu\text{m}$  (45). This drives the gas at a wide range of wavenumbers ( $k \lesssim 0.5 \mu\text{m}^{-1}$  or  $k/k_F \lesssim 0.15$ ) simultaneously. The sound wave amplitude  $\Delta n/n$  was deliberately kept below 10% to ensure that the response is in the linear regime and the local velocity  $v = (\Delta n/n) c$  is smaller than the critical velocity.

## Supplementary Text

### Thermal conductivity and Prandtl number.

Within hydrodynamics, the change in the energy of a sound wave is given by  $\dot{E} = -Dk^2 E$  with  $D = 4\eta/(3\rho) + \alpha^2 c^2 \kappa T / (\rho c_P^2)$  (53). Here  $\alpha = (1/V)(\partial V / \partial T)|_P$  is the thermal expansivity and  $\rho = mn$  is the mass density. The scale invariance of the unitary Fermi gas implies  $c^2 = 5P/(3\rho)$  and  $c_P = 5P\alpha/(2\rho)$  (15), which simplifies the sound diffusivity to  $D = 4\eta/(3\rho) + 4\kappa T/(15P)$ , valid at all temperatures above  $T_c$ . Below  $T_c$ , coupling to the second sound increases the contribution from viscosity by  $\sim 30\%$  for the unitary Fermi gas (51).

Our measurements of the sound diffusivity constrain the value of the viscosity and thermal conductivity according to  $D = D_\eta + D_\kappa$ , where  $D_\eta = 4\eta/(3\rho)$  and  $D_\kappa = 4\kappa T/(15P)$ . For example, the thermal conductivity  $\kappa = (D - D_\eta)(15P)/(4T)$  can be calculated from the sound diffusivity  $D$  if the equation of state and viscosity are known. We calculate the thermal con-

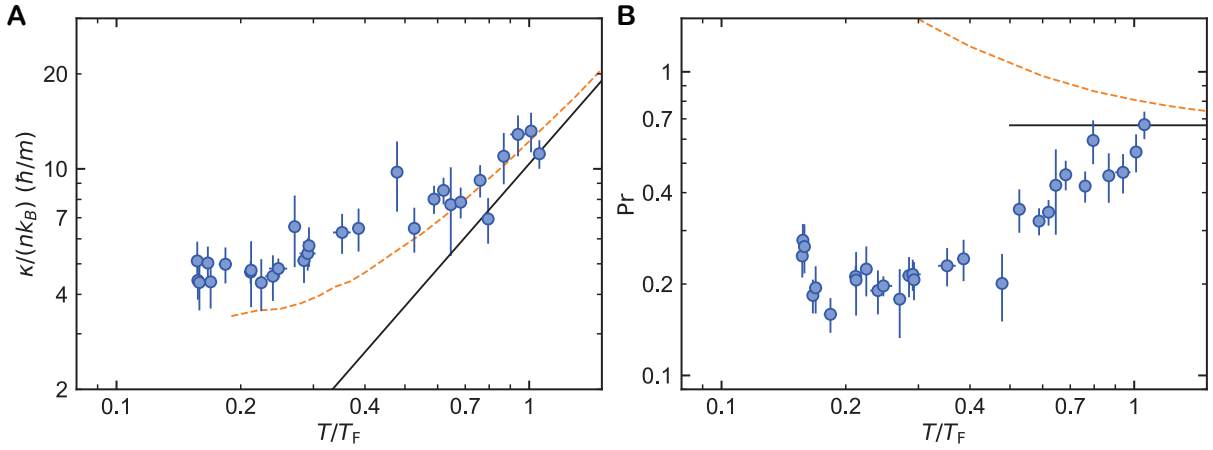


**Figure S1: Thermal conductivity and Prandtl number.** For temperatures comparable to the Fermi temperature ( $T \sim T_F$ ), the thermal conductivity (**A**;  $\kappa/(nk_B)$ , normalized by  $\hbar/m$ ; blue circles) approaches the expected high temperature scaling  $T^{3/2}$  (solid black line) as the Prandtl number (**B**;  $\text{Pr}$ ; blue circles) approaches the predicted high temperature value of  $2/3$  (solid black line). The orange dashed line in both **A** and **B** are theoretical predictions calculated in the framework of kinetic theory (25).

ductivity  $\kappa$  (Fig. S1A) and Prandtl number  $\text{Pr} = c_P \eta / \kappa$  (Fig. S1B) using the measured sound diffusivity, the experimental equation of state (20), and a theoretical calculation for the shear viscosity  $\eta$  above  $T_c$  (23), performed within the same framework that gave excellent agreement with the experimental equation of state (20). Similar to the sound diffusivity and viscosity, the thermal conductivity increases with temperature as  $T^{3/2}$  for  $T \gg T_F$ . The solid black line in Fig. S1A shows the limiting behavior  $\kappa/(nk_B) = 10.38 (\hbar/m) (T/T_F)^{3/2}$  for the thermal conductivity at high temperatures (25), which captures our data well without any free parameters.

The Prandtl number,  $\text{Pr}$ , quantifies the relative importance of viscosity and thermal conductivity for the attenuation of sound in fluids. For compressible fluids such as air, both the viscosity and the thermal conductivity play an important role in the diffusion of sound, resulting in  $\text{Pr}$  being close to unity. In contrast, for incompressible fluids such as water, thermal gradients associated with sound waves are minimal, resulting in a  $\text{Pr} \gg 1$ . The unitary Fermi gas is a compressible fluid, whose  $\text{Pr}$  is predicted to reach the classical limit of  $2/3$  at high

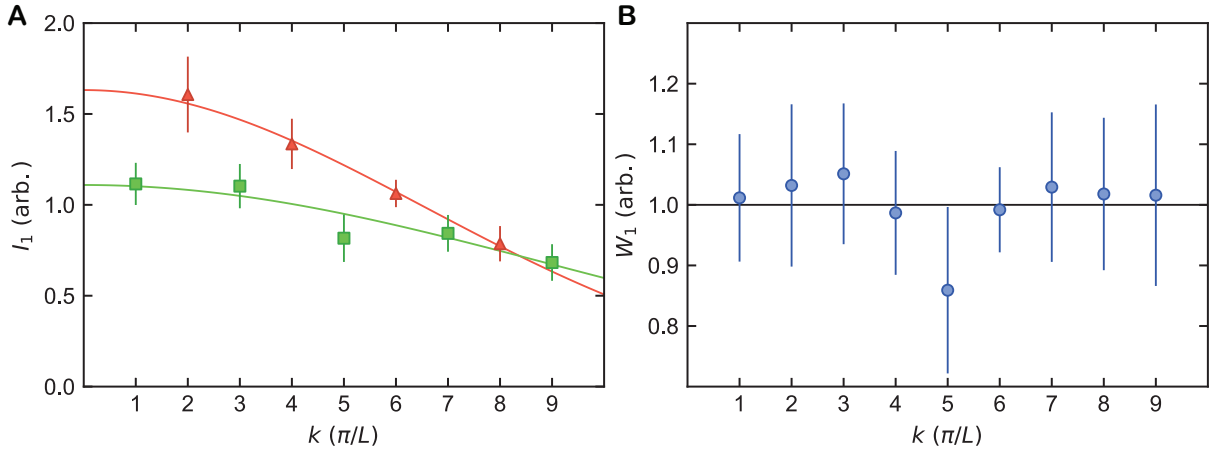


**Figure S2: Weight of the first-sound mode in  $\chi$ .** (A) Integral over the density response  $I_1(k) = \int d\omega \delta n(\omega, k)/\omega$  for even (red triangles) and odd (green square) modes. They are fit with a Gaussian function (solid lines) which models the drive  $V_0(k)$ . (B) The weight of the first sound in the density response function  $W_1(k) = \int d\omega \text{Im}[\chi(\omega, k)]/\omega$  calculated from the measured  $I_1$  and the modelled drive potential,  $W_1(k) = I_1(k)/V_0(k)$ .

temperatures (25). Our data indeed approach this value at high temperatures. We find the  $\text{Pr}$  to be significantly below 1 at all temperatures, excluding the existence of a relativistic conformal gravity dual of the unitary Fermi gas (67).

#### The response function $\chi$ and its normalization

The response function  $\chi$  relates the perturbations in a fluid's number density to the applied external potential,  $\delta n(\omega, k) = \chi(\omega, k)V(\omega, k)$  (51). With knowledge of  $\chi$ , the density response of a fluid to an arbitrary external perturbation can be calculated via a Fourier transform,  $\delta n(t, x) = \int \frac{d\omega'}{2\pi} e^{-i\omega' t} \int \frac{dk}{2\pi} e^{-ikx} \chi(\omega', k)V(\omega', k)$ . For example, the density response to a sinusoidal drive  $V(\omega', k) = -i\pi V_0(k) (\delta(\omega' + \omega) - \delta(\omega' - \omega))$ , with frequency  $\omega$  and amplitude  $V_0(k)$ , is

$$\delta n(t, k) = V_0(k) \sin(\omega t) \text{Re}[\chi(\omega, k)] - V_0(k) \cos(\omega t) \text{Im}[\chi(\omega, k)].$$

Similar to a classical harmonic oscillator, the in-phase and out-of-phase density responses are proportional to  $\text{Re}[\chi]$  and  $\text{Im}[\chi]$  respectively, providing an experimentally convenient tool to

measure the density response function. Data shown in Fig. 2 were taken after 30 complete cycles of the  $\sin(\omega t)$  drive, which was found to be sufficiently long to reach a steady state of the density evolution at all frequencies and temperatures explored. During this drive, the energy injected by the external potential is less than 4% of the energy of the system.

In the vicinity of a sound mode ( $\omega \sim ck$ ), the response of the fluid can be well modeled by a damped driven harmonic oscillator with a resonance frequency  $\omega_0 = ck$  and damping rate  $\Gamma$  (51). The equation of motion of a harmonic oscillator implies a response function  $\chi \sim 1/(\omega^2 - \omega_0^2 + i\Gamma\omega)$  whose imaginary part,  $\text{Im}[\chi] \sim 1/((\omega - \omega_0)^2 + \Gamma^2)$ , has a Lorentzian peak with full-width-at-half-maximum  $\Gamma$  centered at  $\omega = \omega_0$ .

In general, the response function  $\chi$  for a unitary Fermi gas is given by two-fluid hydrodynamics, as discussed in Refs. (51, 52, 71). Fixing  $k$ , the function  $\text{Im}(\chi(\omega, k))/\omega$  contains in general two peaks: one is centered at the first-sound resonance, corresponding to predominantly density waves. The second peak is present when thermal gradients can cause density gradients, which occurs for non-zero expansivity  $\alpha$  or equivalently for a specific heat ratio  $c_P/c_V \neq 1$ . In the normal state, the second peak occurs at zero frequency, corresponding to purely diffusive heat transport coupled to density. In the superfluid regime, this peak moves to finite frequency, corresponding to the emergence of second sound. It is predominantly (for  $c_P/c_V$  not far from 1) a temperature wave that propagates ballistically (72, 73).

An exact sum rule relates the integral of  $\text{Im}(\omega, k)/\omega$  to the isothermal compressibility (51, 71). The integral  $W_1 = \int d\omega \text{Im}[\chi(\omega, k)]/\omega$  over only the first-sound peak is  $n\pi/(2mc^2)$ , related to the speed of sound and thus the isentropic compressibility, independent of the wavenumber. We verify this ‘first sound sum-rule’ in Fig. S2 and utilize it to calibrate the amplitude  $V_0(k)$  of the drive. The measured out-of-phase density response (Fig. 2C and Fig. 3A) is given by  $\delta n(\omega, k) = \text{Im}[\chi(\omega, k)]V_0(k)$ . The weight of the first-sound mode is calculated from the density response,  $W_1 = [\int d\omega \delta n(\omega, k)/\omega]/V_0(k) \equiv I_1/V_0(k)$ , where  $I_1$  is the integral over

the  $\delta n$  (Fig. S2A). We model the shape of the potential wall  $V_0(x)$  by a Gaussian function with a width  $\sigma$  such that  $V_0(k) \sim \exp[-k^2\sigma^2/2]$ . To account for the slight asymmetry between the two endcap potentials, we use  $\sigma = 4.4(1)\mu\text{m}$  and  $3.2\mu\text{m}$  for the even and odd modes, respectively, acquired from Gaussian fits to  $I_1$ . The calculated weight  $W_1(k)$  (Fig 6B) is independent of the wavenumber to within the standard error of the measurements. By requiring the average value of  $W_1(k)$  to be  $n\pi/(2mc^2)$ , we calibrate the amplitude of  $V_0(k)$  and normalize  $\text{Im}[\chi]$  shown in Fig. 3A.

## References and Notes

1. P. A. Lee, N. Nagaosa, X.-G. Wen, Doping a Mott insulator: Physics of high-temperature superconductivity. *Rev. Mod. Phys.* **78**, 17–85 (2006). [doi:10.1103/RevModPhys.78.17](https://doi.org/10.1103/RevModPhys.78.17)
2. Y. Cao, V. Fatemi, S. Fang, K. Watanabe, T. Taniguchi, E. Kaxiras, P. Jarillo-Herrero, Unconventional superconductivity in magic-angle graphene superlattices. *Nature* **556**, 43–50 (2018). [doi:10.1038/nature26160](https://doi.org/10.1038/nature26160) Medline
3. M. G. Alford, L. Bovard, M. Hanuske, L. Rezzolla, K. Schwenzer, Viscous dissipation and heat conduction in binary neutron-star mergers. *Phys. Rev. Lett.* **120**, 041101 (2018). [doi:10.1103/PhysRevLett.120.041101](https://doi.org/10.1103/PhysRevLett.120.041101) Medline
4. A. Adams, L. D. Carr, T. Schäfer, P. Steinberg, J. E. Thomas, Strongly correlated quantum fluids: Ultracold quantum gases, quantum chromodynamic plasmas and holographic duality. *New J. Phys.* **14**, 115009 (2012). [doi:10.1088/1367-2630/14/11/115009](https://doi.org/10.1088/1367-2630/14/11/115009)
5. A. Sommer, M. Ku, G. Roati, M. W. Zwierlein, Universal spin transport in a strongly interacting Fermi gas. *Nature* **472**, 201–204 (2011). [doi:10.1038/nature09989](https://doi.org/10.1038/nature09989) Medline
6. A. B. Bardon, S. Beattie, C. Luciuk, W. Cairncross, D. Fine, N. S. Cheng, G. J. A. Edge, E. Taylor, S. Zhang, S. Trotzky, J. H. Thywissen, Transverse demagnetization dynamics of a unitary Fermi gas. *Science* **344**, 722–724 (2014). [doi:10.1126/science.1247425](https://doi.org/10.1126/science.1247425) Medline
7. C. Luciuk, S. Smale, F. Böttcher, H. Sharum, B. A. Olsen, S. Trotzky, T. Enss, J. H. Thywissen, Observation of quantum-limited spin transport in strongly interacting two-dimensional Fermi gases. *Phys. Rev. Lett.* **118**, 130405 (2017). [doi:10.1103/PhysRevLett.118.130405](https://doi.org/10.1103/PhysRevLett.118.130405) Medline
8. K. H. Bennemann, J. B. Ketterson, *The Physics of Liquid and Solid Helium* (Wiley, 1976).
9. D. Vollhardt, P. Wölfle, *The Superfluid Phases of Helium 3* (Dover Publications, Inc., 2013).
10. V. S. L'vov, L. Skrbek, K. R. Sreenivasan, Viscosity of liquid  $^4\text{He}$  and quantum of circulation: Are they related? *Phys. Fluids* **26**, 041703 (2014). [doi:10.1063/1.4871291](https://doi.org/10.1063/1.4871291)
11. W. Ketterle, M. W. Zwierlein, in *Ultra-cold Fermi Gases*, vol. 164 of *Proceedings of the International School of Physics “Enrico Fermi”*, M. Inguscio, W. Ketterle, C. Salomon, Eds. (IOS Press, 2007), pp. 95–287.
12. I. Bloch, J. Dalibard, W. Zwerger, Many-body physics with ultracold gases. *Rev. Mod. Phys.* **80**, 885–964 (2008). [doi:10.1103/RevModPhys.80.885](https://doi.org/10.1103/RevModPhys.80.885)
13. S. Giorgini, L. P. Pitaevskii, S. Stringari, Theory of ultracold atomic Fermi gases. *Rev. Mod. Phys.* **80**, 1215–1274 (2008). [doi:10.1103/RevModPhys.80.1215](https://doi.org/10.1103/RevModPhys.80.1215)
14. W. Zwerger, Ed., *The BCS-BEC Crossover and the Unitary Fermi Gas* (Springer, 2012).
15. M. W. Zwierlein, *Novel Superfluids* (Oxford Univ. Press, 2014), pp. 269–422.
16. K. M. O'Hara, S. L. Hemmer, M. E. Gehm, S. R. Granade, J. E. Thomas, Observation of a strongly interacting degenerate Fermi gas of atoms. *Science* **298**, 2179–2182 (2002). [doi:10.1126/science.1079107](https://doi.org/10.1126/science.1079107) Medline

17. A. Altmeyer, S. Riedl, C. Kohstall, M. J. Wright, R. Geursen, M. Bartenstein, C. Chin, J. H. Denschlag, R. Grimm, Precision measurements of collective oscillations in the BEC-BCS crossover. *Phys. Rev. Lett.* **98**, 040401 (2007). [doi:10.1103/PhysRevLett.98.040401](https://doi.org/10.1103/PhysRevLett.98.040401) [Medline](#)
18. M. K. Tey, L. A. Sidorenkov, E. R. S. Guajardo, R. Grimm, M. J. H. Ku, M. W. Zwierlein, Y.-H. Hou, L. Pitaevskii, S. Stringari, Collective modes in a unitary Fermi gas across the superfluid phase transition. *Phys. Rev. Lett.* **110**, 055303 (2013). [doi:10.1103/PhysRevLett.110.055303](https://doi.org/10.1103/PhysRevLett.110.055303) [Medline](#)
19. T.-L. Ho, Universal thermodynamics of degenerate quantum gases in the unitarity limit. *Phys. Rev. Lett.* **92**, 090402 (2004). [doi:10.1103/PhysRevLett.92.090402](https://doi.org/10.1103/PhysRevLett.92.090402) [Medline](#)
20. M. J. H. Ku, A. T. Sommer, L. W. Cheuk, M. W. Zwierlein, Revealing the superfluid lambda transition in the universal thermodynamics of a unitary Fermi gas. *Science* **335**, 563–567 (2012). [doi:10.1126/science.1214987](https://doi.org/10.1126/science.1214987) [Medline](#)
21. M. Randeria, E. Taylor, Crossover from Bardeen-Cooper-Schrieffer to Bose-Einstein condensation and the unitary Fermi gas. *Annu. Rev. Condens. Matter Phys.* **5**, 209–232 (2014). [doi:10.1146/annurev-conmatphys-031113-133829](https://doi.org/10.1146/annurev-conmatphys-031113-133829)
22. C. Cao, E. Elliott, J. Joseph, H. Wu, J. Petricka, T. Schäfer, J. E. Thomas, Universal quantum viscosity in a unitary Fermi gas. *Science* **331**, 58–61 (2011). [doi:10.1126/science.1195219](https://doi.org/10.1126/science.1195219) [Medline](#)
23. T. Enss, R. Haussmann, W. Zwerger, Viscosity and scale invariance in the unitary Fermi gas. *Ann. Phys.* **326**, 770–796 (2011). [doi:10.1016/j.aop.2010.10.002](https://doi.org/10.1016/j.aop.2010.10.002)
24. J. A. Joseph, E. Elliott, J. E. Thomas, Shear viscosity of a unitary Fermi gas near the superfluid phase transition. *Phys. Rev. Lett.* **115**, 020401 (2015). [doi:10.1103/PhysRevLett.115.020401](https://doi.org/10.1103/PhysRevLett.115.020401) [Medline](#)
25. M. Braby, J. Chao, T. Schäfer, Thermal conductivity and sound attenuation in dilute atomic Fermi gases. *Phys. Rev. A* **82**, 033619 (2010). [doi:10.1103/PhysRevA.82.033619](https://doi.org/10.1103/PhysRevA.82.033619)
26. P. Nikolić, S. Sachdev, Renormalization-group fixed points, universal phase diagram, and  $1/N$  expansion for quantum liquids with interactions near the unitarity limit. *Phys. Rev. A* **75**, 033608 (2007). [doi:10.1103/PhysRevA.75.033608](https://doi.org/10.1103/PhysRevA.75.033608)
27. T. Enss, Quantum critical transport in the unitary Fermi gas. *Phys. Rev. A* **86**, 013616 (2012). [doi:10.1103/PhysRevA.86.013616](https://doi.org/10.1103/PhysRevA.86.013616)
28. S. Nascimbène, N. Navon, S. Pilati, F. Chevy, S. Giorgini, A. Georges, C. Salomon, Fermi-liquid behavior of the normal phase of a strongly interacting gas of cold atoms. *Phys. Rev. Lett.* **106**, 215303 (2011). [doi:10.1103/PhysRevLett.106.215303](https://doi.org/10.1103/PhysRevLett.106.215303) [Medline](#)
29. I. Z. Rothstein, P. Shrivastava, Symmetry obstruction to Fermi liquid behavior in the unitary limit. *Phys. Rev. B* **99**, 035101 (2019). [doi:10.1103/PhysRevB.99.035101](https://doi.org/10.1103/PhysRevB.99.035101)
30. H. Smith, H. H. Jensen, *Transport Phenomena* (Clarendon, 1989).
31. M. A. Black, H. E. Hall, K. Thompson, The viscosity of liquid helium 3. *J. Phys. C Solid State Phys.* **4**, 129–142 (1971). [doi:10.1088/0022-3719/4/2/001](https://doi.org/10.1088/0022-3719/4/2/001)

32. C. N. Archie, T. A. Alvesalo, J. D. Reppy, R. C. Richardson, Viscosity measurements in superfluid  $^3\text{He}$ -B from 2 to 29 bar. *J. Low Temp. Phys.* **42**, 295–332 (1981).  
[doi:10.1007/BF00120208](https://doi.org/10.1007/BF00120208)
33. H. Guo, D. Wulin, C.-C. Chien, K. Levin, Perfect fluids and bad metals: Insights from ultracold Fermi gases. *New J. Phys.* **13**, 075011 (2011). [doi:10.1088/1367-2630/13/7/075011](https://doi.org/10.1088/1367-2630/13/7/075011)
34. G. Rupak, T. Schäfer, Shear viscosity of a superfluid Fermi gas in the unitarity limit. *Phys. Rev. A* **76**, 053607 (2007). [doi:10.1103/PhysRevA.76.053607](https://doi.org/10.1103/PhysRevA.76.053607)
35. M. Mannarelli, C. Manuel, L. Tolos, Phonon contribution to the shear viscosity of a superfluid Fermi gas in the unitarity limit. *Ann. Phys.* **336**, 12–35 (2013).  
[doi:10.1016/j.aop.2013.05.015](https://doi.org/10.1016/j.aop.2013.05.015)
36. H. Kurkjian, Y. Castin, A. Sinatra, Three-phonon and four-phonon interaction processes in a pair-condensed Fermi gas. *Ann. Phys.* **529**, 1600352 (2017).  
[doi:10.1002/andp.201600352](https://doi.org/10.1002/andp.201600352)
37. S. Krinner, T. Esslinger, J.-P. Brantut, Two-terminal transport measurements with cold atoms. *J. Phys. Condens. Matter* **29**, 343003 (2017). [doi:10.1088/1361-648X/aa74a1](https://doi.org/10.1088/1361-648X/aa74a1) [Medline](#)
38. G. Valtolina, A. Burchianti, A. Amico, E. Neri, K. Xhani, J. A. Seman, A. Trombettoni, A. Smerzi, M. Zaccanti, M. Inguscio, G. Roati, Josephson effect in fermionic superfluids across the BEC-BCS crossover. *Science* **350**, 1505–1508 (2015).  
[doi:10.1126/science.aac9725](https://doi.org/10.1126/science.aac9725) [Medline](#)
39. M. Bartenstein, A. Altmeyer, S. Riedl, S. Jochim, C. Chin, J. H. Denschlag, R. Grimm, Collective excitations of a degenerate gas at the BEC-BCS crossover. *Phys. Rev. Lett.* **92**, 203201 (2004). [doi:10.1103/PhysRevLett.92.203201](https://doi.org/10.1103/PhysRevLett.92.203201) [Medline](#)
40. J. Kinast, S. L. Hemmer, M. E. Gehm, A. Turlapov, J. E. Thomas, Evidence for superfluidity in a resonantly interacting Fermi gas. *Phys. Rev. Lett.* **92**, 150402 (2004).  
[doi:10.1103/PhysRevLett.92.150402](https://doi.org/10.1103/PhysRevLett.92.150402) [Medline](#)
41. S. Hoinka, P. Dyke, M. G. Lingham, J. J. Kinnunen, G. M. Bruun, C. J. Vale, Goldstone mode and pair-breaking excitations in atomic Fermi superfluids. *Nat. Phys.* **13**, 943–946 (2017). [doi:10.1038/nphys4187](https://doi.org/10.1038/nphys4187)
42. M. Koschorreck, D. Pertot, E. Vogt, M. Köhl, Universal spin dynamics in two-dimensional Fermi gases. *Nat. Phys.* **9**, 405–409 (2013). [doi:10.1038/nphys2637](https://doi.org/10.1038/nphys2637)
43. M. Bluhm, J. Hou, T. Schäfer, Determination of the density and temperature dependence of the shear viscosity of a unitary Fermi gas based on hydrodynamic flow. *Phys. Rev. Lett.* **119**, 065302 (2017). [doi:10.1103/PhysRevLett.119.065302](https://doi.org/10.1103/PhysRevLett.119.065302) [Medline](#)
44. A. L. Gaunt, T. F. Schmidutz, I. Gotlibovich, R. P. Smith, Z. Hadzibabic, Bose-Einstein condensation of atoms in a uniform potential. *Phys. Rev. Lett.* **110**, 200406 (2013).  
[doi:10.1103/PhysRevLett.110.200406](https://doi.org/10.1103/PhysRevLett.110.200406) [Medline](#)
45. B. Mukherjee, Z. Yan, P. B. Patel, Z. Hadzibabic, T. Yefsah, J. Struck, M. W. Zwierlein, Homogeneous atomic Fermi gases. *Phys. Rev. Lett.* **118**, 123401 (2017).  
[doi:10.1103/PhysRevLett.118.123401](https://doi.org/10.1103/PhysRevLett.118.123401) [Medline](#)

46. K. Hueck, N. Luick, L. Sobirey, J. Siegl, T. Lompe, H. Moritz, Two-dimensional homogeneous Fermi gases. *Phys. Rev. Lett.* **120**, 060402 (2018).  
[doi:10.1103/PhysRevLett.120.060402](https://doi.org/10.1103/PhysRevLett.120.060402) [Medline](#)
47. L. Baird, X. Wang, S. Roof, J. E. Thomas, Measuring the hydrodynamic linear response of a unitary Fermi gas. *Phys. Rev. Lett.* **123**, 160402 (2019).  
[doi:10.1103/PhysRevLett.123.160402](https://doi.org/10.1103/PhysRevLett.123.160402) [Medline](#)
48. N. Navon, A. L. Gaunt, R. P. Smith, Z. Hadzibabic, Emergence of a turbulent cascade in a quantum gas. *Nature* **539**, 72–75 (2016). [doi:10.1038/nature20114](https://doi.org/10.1038/nature20114) [Medline](#)
49. J. L. Ville, R. Saint-Jalm, É. Le Cerf, M. Aidelsburger, S. Nascimbène, J. Dalibard, J. Beugnon, Sound propagation in a uniform superfluid two-dimensional Bose gas. *Phys. Rev. Lett.* **121**, 145301 (2018). [doi:10.1103/PhysRevLett.121.145301](https://doi.org/10.1103/PhysRevLett.121.145301) [Medline](#)
50. S. J. Garratt, C. Eigen, J. Zhang, P. Turzák, R. Lopes, R. P. Smith, Z. Hadzibabic, N. Navon, From single-particle excitations to sound waves in a box-trapped atomic Bose-Einstein condensate. *Phys. Rev. A (Coll. Park)* **99**, 021601 (2019).  
[doi:10.1103/PhysRevA.99.021601](https://doi.org/10.1103/PhysRevA.99.021601)
51. P. C. Hohenberg, P. C. Martin, Microscopic theory of superfluid helium. *Ann. Phys.* **34**, 291–359 (1965). [doi:10.1016/0003-4916\(65\)90280-0](https://doi.org/10.1016/0003-4916(65)90280-0)
52. P. C. Hohenberg, Density correlation function in superfluid helium near  $T$ ? *J. Low Temp. Phys.* **11**, 745–750 (1973). [doi:10.1007/BF00654455](https://doi.org/10.1007/BF00654455)
53. L. D. Landau, E. M. Lifshitz, *Fluid Mechanics* (Elsevier, 1959).
54. J. A. Tarvin, F. Vidal, T. J. Greytak, Measurements of the dynamic structure factor near the lambda temperature in liquid helium. *Phys. Rev. B* **15**, 4193–4210 (1977).  
[doi:10.1103/PhysRevB.15.4193](https://doi.org/10.1103/PhysRevB.15.4193)
55. See supplementary materials.
56. H. Kurkjian, Y. Castin, A. Sinatra, Concavity of the collective excitation branch of a Fermi gas in the BEC-BCS crossover. *Phys. Rev. A* **93**, 013623 (2016).  
[doi:10.1103/PhysRevA.93.013623](https://doi.org/10.1103/PhysRevA.93.013623)
57. Z. Yan, P. B. Patel, B. Mukherjee, R. J. Fletcher, J. Struck, M. W. Zwierlein, Boiling a unitary Fermi liquid. *Phys. Rev. Lett.* **122**, 093401 (2019).  
[doi:10.1103/PhysRevLett.122.093401](https://doi.org/10.1103/PhysRevLett.122.093401) [Medline](#)
58. M. J. Wright, S. Riedl, A. Altmeyer, C. Kohstall, E. R. S. Guajardo, J. H. Denschlag, R. Grimm, Finite-temperature collective dynamics of a Fermi gas in the BEC-BCS crossover. *Phys. Rev. Lett.* **99**, 150403 (2007). [doi:10.1103/PhysRevLett.99.150403](https://doi.org/10.1103/PhysRevLett.99.150403) [Medline](#)
59. C. J. Pethick, D. Ter Haar, On the attenuation of sound in liquid helium. *Physica* **32**, 1905–1920 (1966). [doi:10.1016/0031-8914\(66\)90157-1](https://doi.org/10.1016/0031-8914(66)90157-1)
60. G. Eska, K. Neumaier, W. Schoepe, K. Uhlig, W. Wiedemann, P. Wölfle, First-sound attenuation and viscosity of superfluid  $^3\text{He-B}$ . *Phys. Rev. Lett.* **44**, 1337–1340 (1980).  
[doi:10.1103/PhysRevLett.44.1337](https://doi.org/10.1103/PhysRevLett.44.1337)

61. D. T. Son, Vanishing bulk viscosities and conformal invariance of the unitary Fermi gas. *Phys. Rev. Lett.* **98**, 020604 (2007). [doi:10.1103/PhysRevLett.98.020604](https://doi.org/10.1103/PhysRevLett.98.020604) Medline
62. G. M. Bruun, H. Smith, Viscosity and thermal relaxation for a resonantly interacting Fermi gas. *Phys. Rev. A* **72**, 043605 (2005). [doi:10.1103/PhysRevA.72.043605](https://doi.org/10.1103/PhysRevA.72.043605)
63. B. Mukherjee, P. B. Patel, Z. Yan, R. J. Fletcher, J. Struck, M. W. Zwierlein, Spectral response and contact of the unitary Fermi gas. *Phys. Rev. Lett.* **122**, 203402 (2019). [doi:10.1103/PhysRevLett.122.203402](https://doi.org/10.1103/PhysRevLett.122.203402) Medline
64. C. J. Pethick, H. Smith, P. Bhattacharyya, Transport processes in superfluid  $^3\text{He}$ -B at low temperatures. *Phys. Rev. B* **15**, 3384–3400 (1977). [doi:10.1103/PhysRevB.15.3384](https://doi.org/10.1103/PhysRevB.15.3384)
65. A. Schirotzek, Y. I. Shin, C. H. Schunck, W. Ketterle, Determination of the superfluid gap in atomic Fermi gases by quasiparticle spectroscopy. *Phys. Rev. Lett.* **101**, 140403 (2008). [doi:10.1103/PhysRevLett.101.140403](https://doi.org/10.1103/PhysRevLett.101.140403) Medline
66. Y. A. Ono, J. Hara, K. Nagai, Shear viscosity of the B phase of superfluid  $^3\text{He}$ . III. *J. Low Temp. Phys.* **48**, 167–188 (1982). [doi:10.1007/BF00681569](https://doi.org/10.1007/BF00681569)
67. M. Rangamani, S. F. Ross, D. Son, E. G. Thompson, Conformal non-relativistic hydrodynamics from gravity. *J. High Energy Phys.* **2009**, 075 (2009). [doi:10.1088/1126-6708/2009/01/075](https://doi.org/10.1088/1126-6708/2009/01/075)
68. P. B. Patel, Z. Yan, B. Mukherjee, R. J. Fletcher, J. Struck, M. W. Zwierlein, Replication data for: Universal sound diffusion in a strongly interacting Fermi gas. Harvard Dataverse (2020); <https://doi.org/10.7910/DVN/UVM2KN>.
69. C. Chin, R. Grimm, P. Julienne, E. Tiesinga, Feshbach resonances in ultracold gases. *Rev. Mod. Phys.* **82**, 1225–1286 (2010). [doi:10.1103/RevModPhys.82.1225](https://doi.org/10.1103/RevModPhys.82.1225)
70. G. Zürn, T. Lompe, A. N. Wenz, S. Jochim, P. S. Julienne, J. M. Hutson, Precise characterization of  $^6\text{Li}$  Feshbach resonances using trap-sideband-resolved RF spectroscopy of weakly bound molecules. *Phys. Rev. Lett.* **110**, 135301 (2013). [doi:10.1103/PhysRevLett.110.135301](https://doi.org/10.1103/PhysRevLett.110.135301) Medline
71. H. Hu, P. Zou, X.-J. Liu, Low-momentum dynamic structure factor of a strongly interacting Fermi gas at finite temperature: A two-fluid hydrodynamic description. *Phys. Rev. A (Coll. Park)* **97**, 023615 (2018). [doi:10.1103/PhysRevA.97.023615](https://doi.org/10.1103/PhysRevA.97.023615)
72. G. Bertaina, L. Pitaevskii, S. Stringari, First and second sound in cylindrically trapped gases. *Phys. Rev. Lett.* **105**, 150402 (2010). [doi:10.1103/PhysRevLett.105.150402](https://doi.org/10.1103/PhysRevLett.105.150402) Medline
73. L. A. Sidorenkov, M. K. Tey, R. Grimm, Y.-H. Hou, L. Pitaevskii, S. Stringari, Second sound and the superfluid fraction in a Fermi gas with resonant interactions. *Nature* **498**, 78–81 (2013). [doi:10.1038/nature12136](https://doi.org/10.1038/nature12136) Medline

## Appendix F

### Geometric squeezing into the lowest Landau level

This appendix contains a reprint of Ref. [54]:

## QUANTUM SIMULATION

# Geometric squeezing into the lowest Landau level

Richard J. Fletcher\*, Airlia Shaffer, Cedric C. Wilson, Parth B. Patel, Zhenjie Yan, Valentin Crépel, Biswaroop Mukherjee, Martin W. Zwierlein

The equivalence between particles under rotation and charged particles in a magnetic field relates phenomena as diverse as spinning atomic nuclei, weather patterns, and the quantum Hall effect. For such systems, quantum mechanics dictates that translations along different directions do not commute, implying a Heisenberg uncertainty relation between spatial coordinates. We implement squeezing of this geometric quantum uncertainty, resulting in a rotating Bose-Einstein condensate occupying a single Landau gauge wave function. We resolve the extent of zero-point cyclotron orbits and demonstrate geometric squeezing of the orbits' centers 7 decibels below the standard quantum limit. The condensate attains an angular momentum exceeding 1000 quanta per particle and an interatomic distance comparable to the cyclotron orbit. This offers an alternative route toward strongly correlated bosonic fluids.

In 1851, Foucault directly demonstrated the rotation of Earth via the precession of a pendulum's oscillation axis. This occurs because in the rotating frame, counter- and corotating motions no longer oscillate at the pendulum's natural frequency  $\omega$ . Instead, their frequencies are increased and decreased, respectively, by Earth's rotation frequency  $\Omega$ , which leads to the bob performing epicycles (Fig. 1A). In Foucault's experiment, for which  $\Omega \ll \omega$ , this manifests as an apparent precession of the oscillation axis. If we imagine instead that  $\Omega = \omega$ , the centrifugal force exactly cancels the restoring force. The pendulum can still perform cyclotron orbits against the frame's rotation, but the motion of the orbit's guiding center is free. In a quantum mechanical description, the energy spectrum is analogous to that of charged particles in a magnetic field and forms discrete Landau levels spaced by  $2\hbar\omega$ , where  $\hbar$  is the reduced Planck constant. The levels correspond to different states of cyclotron motion, each with a large degeneracy arising from the possible guiding-center positions.

An intrinsic characteristic of both neutral particles under rotation and charged particles in a magnetic field is the noncommutativity of space. This can be seen from the quantized Hamiltonian of a pendulum of mass  $m$  viewed in the rotating frame,

$$\hat{H} = \frac{\hat{p}_x^2 + \hat{p}_y^2}{2m} + \frac{1}{2}m\omega^2(\hat{x}^2 + \hat{y}^2) - \Omega\hat{L}_z \quad (1)$$

where  $\hat{p}_{x,y}$  are the canonical momenta along  $x$  and  $y$ , and  $\hat{L}_z$  is the axial angular momentum. The rotational term  $\Omega\hat{L}_z$  mixes spatial and momentum coordinates into new normal modes,

and one decouples Eq. 1 by transforming into cyclotron coordinates  $\xi = \frac{1}{2}[x - (p_y/m\omega)]$  and  $\eta = \frac{1}{2}[y + (p_x/m\omega)]$ , and guiding-center coordinates  $X = \frac{1}{2}[x + (p_y/m\omega)]$  and  $Y = \frac{1}{2}[y - (p_x/m\omega)]$ , yielding

$$\hat{H} = m\omega(\omega + \Omega)\left(\hat{\xi}^2 + \hat{\eta}^2\right) + m\omega(\omega - \Omega)\left(\hat{X}^2 + \hat{Y}^2\right) \quad (2)$$

(1). Because  $\hat{x} = \hat{X} + \hat{\xi}$  and  $\hat{y} = \hat{Y} + \hat{\eta}$ , the particle's motion is the sum of a fast cyclotron motion and a slow drift of the guiding center (Fig. 1A). Crucially, while the absolute spatial coordinates  $\hat{x}$  and  $\hat{y}$  always commute, the two pairs of cyclotron and guiding-center coordinates separately do not. Each pair spans the phase space of a one-dimensional harmonic oscillator, and consequently

$$[\hat{\xi}, \hat{\eta}] = -[\hat{X}, \hat{Y}] = i\ell_B^2 \quad (3)$$

where  $\ell_B = \sqrt{\hbar/(2m\omega)}$  is the rotational analog of the magnetic length. If an applied potential  $\hat{V}(\hat{x}, \hat{y})$  varies little over this length scale, it cannot resolve the cyclotron motion and only couples to the guiding centers. In this case,  $\hat{V}(\hat{x}, \hat{y}) \rightarrow \hat{V}(\hat{X}, \hat{Y})$ , and the resulting dynamics occurs within a noncommutative space (2).

This noncommutativity of guiding-center motion lies at the heart of the Hall effect. Each spatial variable generates translations in the orthogonal direction, meaning that a force along  $X$  effects motion along  $Y$ . Particles therefore drift along isopotentials of  $V$  with a velocity  $\mathbf{v}_d = \boldsymbol{\Omega} \times \nabla V/(2m\Omega\omega)$  in analogy to the  $\mathbf{E} \times \mathbf{B}$  drift of electromagnetism. This flow is divergence-free, reflecting the incompressibility of phase-space distributions (3), and defines a one-to-one mapping between a particle's initial position and its final position. Time evolution therefore always results in a purely geometric, equiareal transformation of the guiding-center distribution.

These concepts are relevant to atomic nuclei (4–6), astrophysical phenomena (7, 8), quantum Hall systems (9), and ultracold atomic quantum gases, which offer a highly versatile experimental arena for studying rotating quantum fluids (10). In Bose-Einstein condensates rotating close to the trap frequency, signatures of the gas approaching the lowest Landau level (LLL) were seen in a softening of the vortex lattice (11, 12). A principal goal is to address the quantum Hall regime, but the exacting requirements on the trap isotropy and rotation speed present a major challenge. Synthetic magnetic fields (13–15) have also been engineered by other methods, such as spin-orbit coupling (16, 17), and by direct phase-imprinting in both optical lattices (18–21) and synthetic dimensions (22). Experiments have shown a transverse Hall response in lattice transport (23) and superfluid collective modes (24), as well as chiral edge states in synthetic dimensions (25, 26).

Here, we directly exploited the noncommutativity of guiding-center motion to realize geometric squeezing, cleanly distilling a single Landau gauge wave function in the lowest Landau level (1). In comparison to previous work in azimuthally symmetric condensates (11), this obviates delicate fine-tuning of trapping and rotation parameters, and offers a complementary “Landau gauge” starting point from which to investigate interaction-driven physics in quantum Hall systems. To begin our experiment, we prepared a condensate of  $N_{\text{Tot}} = 8.1 (\pm 0.1) \times 10^5$  atoms of  $^{23}\text{Na}$  in an elliptical time-orbiting-potential (TOP) trap (27), with trap frequencies  $(\omega_x, \omega_y, \omega_z) = (\sqrt{1+\epsilon}, \sqrt{1-\epsilon}, \sqrt{8})\omega$ . Here,  $\omega = 2\pi \times 88.6 (\pm 0.1)$  Hz and the trap ellipticity is  $\epsilon = 0.125 \pm 0.004$ . We smoothly ramped the trap's rotation frequency from zero to  $\omega$ , waited for a variable time  $t$ , and then obtained an absorption image of the in situ density distribution. Our imaging resolution was sufficient to observe vortices in situ with a contrast of ~60% (1). These have a characteristic size set by the healing length, which is ~300 nm in our system. This is much smaller than the quantum mechanical ground-state size of cyclotron orbits, set by the magnetic length  $\ell_B = 1.6 \mu\text{m}$ .

In the frame rotating at  $\Omega$ , the condensate evolves under both a vector potential and a scalar potential. The vector potential and the associated synthetic magnetic field are induced by the frame rotation (1). The scalar potential  $V = m[(\omega^2 - \Omega^2)(X^2 + Y^2)/2] + m\omega^2[(X^2 - Y^2)/2]$  arises from both the TOP trap and the centrifugal force. For  $\Omega/\omega < \sqrt{1-\epsilon}$ , the isopotentials of  $V$  are closed; the condensate remains confined but deforms into an ellipse. In earlier experiments, unstable density modulations mediated the nucleation of vortices for rotation frequencies  $\Omega/\omega \gtrsim 0.8$  (28, 29). By ramping sufficiently

MIT-Harvard Center for Ultracold Atoms, Research Laboratory of Electronics, and Department of Physics, Massachusetts Institute of Technology, Cambridge, MA 02139, USA.

\*Corresponding author. Email: rfletch@mit.edu

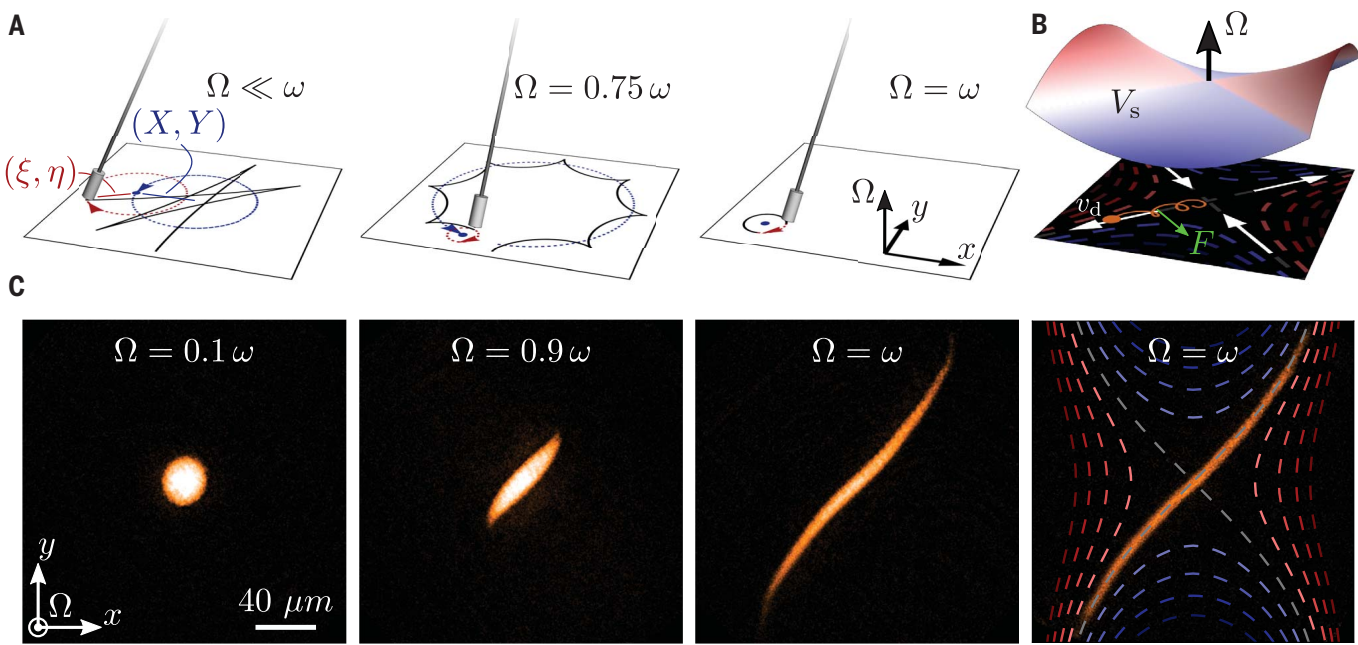


**Fig. 1. Geometric squeezing of a rotating Bose-Einstein condensate.**

(A) Viewed in a frame rotating at  $\Omega$ , the motion of a Foucault pendulum with natural frequency  $\omega$  separates into a slow corotating drift of the guiding center ( $X, Y$ ), in blue, and fast counterrotating cyclotron orbits with relative coordinates  $(\xi, \eta)$ , in red. For  $\Omega < \omega$ , the pendulum performs skipping orbits, whereas if  $\Omega = \omega$ , the guiding-center motion is free. (B) Atoms in an elliptical harmonic trap rotating at  $\Omega = \omega$  evolve under both a vector potential and a scalar saddle

potential  $V_s$ , whose isopotentials are shown as red ( $V_s > 0$ ) and blue ( $V_s < 0$ ) dashed lines. Particles perform cyclotron orbits whose guiding centers drift along isopotentials with a velocity  $v_d$  (white arrows) orthogonal to the local force  $\mathbf{F} = -\nabla V_s$  (green arrow). (C) In situ images of the condensate in the rotating frame. During the hold time at  $\Omega = \omega$ , the atoms flow out along one diagonal and in along the other, mediating squeezing of the distribution in guiding-center phase space. The final image is overlaid with the isopotentials of  $V_s$ .

quickly, we precluded breakup of the condensate while allowing its ellipticity to adiabatically follow the equilibrium value (30).

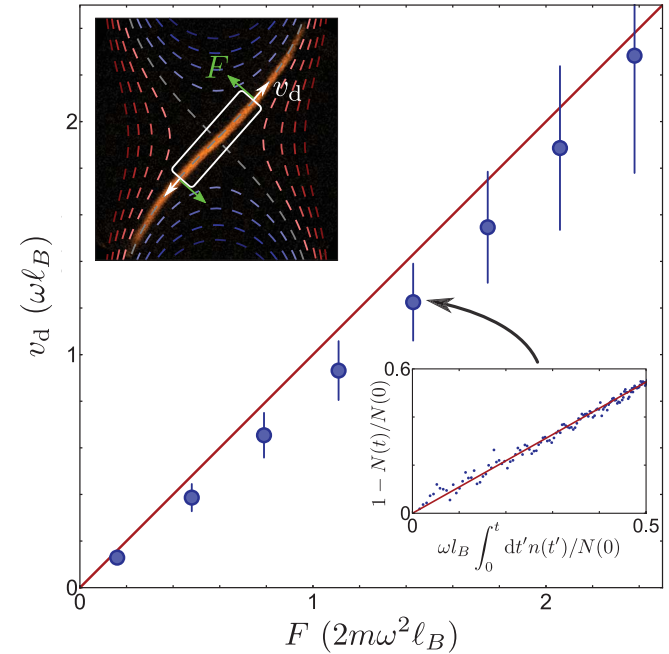
When  $\Omega = \omega$ , the scalar potential forms a saddle  $V_s = m\varepsilon\omega^2(X^2 - Y^2)/2$  (Fig. 1B). Without a vector potential, atoms would be lost along the anti-trapped  $y$ -direction. Instead, the guiding centers drift outward along the  $x = y$  contours and inward along the  $x = -y$  contours. This flow (illustrated by white arrows) mediates squeezing of the spatial distribution. In Fig. 1C we show the evolution of the condensate density viewed in the rotating frame. The final image is overlaid with the known isopotentials of  $V_s$ , whose coincidence with the atomic density provides a qualitative signature of isopotential drift. The small curvature of the diagonal contours arises from the known quartic corrections  $\sim(X^2 + Y^2)^2$  to the trapping potential (27), and the spatial twisting of the condensate lies in close analogy to the twisting in optical phase space induced by the Kerr effect (31).

To measure the transverse Hall response, we obtained the radial drift speed as a function of the azimuthal force, which at a radius  $r$  is  $F(r) = m\varepsilon\omega^2r$ . Our measurements are shown in Fig. 2 along with the theoretical relation  $v_d = F/(2m\omega)$ , valid for any quantum state, which shows good agreement without any free parameters. We used a continuity equation to infer the drift speed; the atom

**Fig. 2. Isopotential drift velocity.**

The main plot shows the particles' radial speed  $v_d$  in response to the azimuthal force  $F$ , measured at distances of (left to right) 4.1  $\mu\text{m}$ , 12  $\mu\text{m}$ , 20  $\mu\text{m}$ , 28  $\mu\text{m}$ , 36  $\mu\text{m}$ , 44  $\mu\text{m}$ , 52  $\mu\text{m}$ , and 60  $\mu\text{m}$  from the trap center. The speed is inferred from changes in the atom number  $N$  inside a bounding box (top inset) and the density  $n$  at its boundary. The bottom inset shows a typical plot constructed from  $N(t)$  and  $n(t)$ , whose slope gives  $v_d$  (see text). The data show good agreement with the theoretical expectation (red line) without any free parameters. The force  $F$  is calculated assuming a harmonic trap, but the quartic corrections to the potential

reduce the velocity along  $x = y$ ; this results in a small downward shift of the data, which is captured by a GP simulation (I). Error bars show the variation in  $v_d$  measured across different time intervals.



number  $N$  inside a bounding box (Fig. 2, white frame in top inset) centered on  $r = 0$  and with length  $2R$  varies as  $\dot{N} = -2v_d n$ , where  $v_d$  and  $n$  are the drift speed and one-dimensional number density at  $r = R$ . Integrating once

gives  $1 - [N(t)/N(0)] = 2v_d \int_0^t dt' [n(t')/N(0)]$ , allowing straightforward evaluation of  $v_d$  as shown in the lower inset. This method offers a convenient protocol for measuring the Hall response of any fluid.

**Fig. 3. Squeezing into the lowest Landau level.**

**(A)** Evolution of the major and minor cloud radii  $\sigma_{\pm}$  in response to ramping the rotational angular frequency  $\Omega$  of the trap from zero to the trap frequency  $\omega$  (top). The gray shading shows the time period for which  $\Omega < \omega$ . The left and right insets show representative in situ images of the cloud at early and late times, respectively. Initially the condensate is approximately isotropic, whereas for long times the spatial aspect ratio exceeds 100. The red line shows the prediction of a hydrodynamic model for which the total atom number is the only free parameter, and whose behavior when  $\Omega = \omega$

follows simple scalings shown by the dashed and dotted lines (see text). The green line shows the result of a Gross-Pitaevskii simulation of our experiment (1) and captures the deviation from classical hydrodynamic behavior as the LLL is approached. The gray data show a small cyclotron breathing oscillation driven by trap imperfections (see text); the blue points are averaged over one period. **(B)** Top: A zoom-in of the minor width evolution. Bottom: The inferred number of occupied Landau levels  $N_{\text{LL}} \equiv \mu/(2\hbar\omega)$ . As the condensate enters the LLL, its width saturates at  $\sigma_{\text{LLL}} = \ell_B/\sqrt{2}$ , shown by a solid line and corresponding to zero-point cyclotron motion. For comparison, the dashed line shows the width of the two-dimensional harmonic oscillator ground state,  $\sigma_0 = \ell_B$ . The blue arrow denotes the measured imaging resolution obtained using vortex cores (1). **(C)** The transverse optical density (OD) profile of the cloud along with fits of Thomas-Fermi (red) and Gaussian (green) functions. At early times, interactions dominate and the profile is Thomas-Fermi in character, whereas when  $N_{\text{LL}} \lesssim 1$  we observe a Gaussian shape, which is characteristic of wave functions in the LLL.

Whereas the drift velocity determines the local response to a force, the specific geometric transformation of the cloud depends upon the global shape of  $V_s$ . Qualitatively, isopotential flow on a saddle in the presence of a magnetic field results in elongation and contraction along orthogonal diagonals. More quantitatively, in terms of the oscillator ladder operators  $\hat{a} = \sqrt{m\omega/\hbar}(\hat{x} + i\hat{y})$  and  $\hat{b} = \sqrt{m\omega/\hbar}(\hat{X} - i\hat{Y})$ , the single-particle Hamiltonian is

$$\hat{H}_s \approx 2\hbar\omega \left( \hat{a}^\dagger \hat{a} + \frac{1}{2} \right) + \frac{\hbar\zeta}{2} \left( \hat{b}^\dagger \hat{b} + \hat{b} \hat{b}^\dagger \right) \quad (4)$$

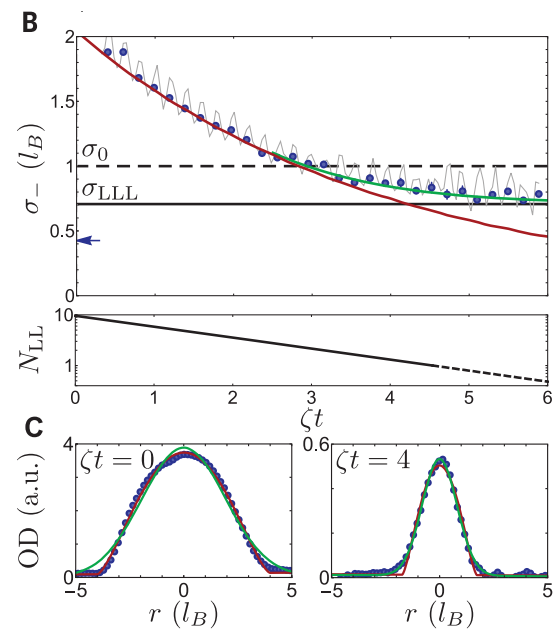
(1), where we define  $\zeta = \varepsilon\omega/2$ . Comparison with the one-mode squeezing operator  $\hat{S}(\alpha) = \exp[(\alpha^* \hat{b} \hat{b} - \alpha \hat{b}^\dagger \hat{b}^\dagger)/2]$  reveals that time evolution under a saddle potential is equivalent to fully coherent squeezing of the guiding-center phase space distribution, analogous to phase squeezing in quantum optics (32–34). Consistent with the perspective based on isopotential flow, the imaginary squeezing parameter  $\alpha = i\zeta t$  describes dilation of the cloud along the diagonals of phase space by factors  $\exp(\pm\zeta t)$ .

In the limit  $\zeta t \gg 1$ , the particles' guiding centers become widely distributed along one diagonal and sharply localized along the other. The residual transverse width of the cloud solely arises from the unsqueezed cyclotron orbits, which have a size  $\sqrt{\langle \xi^2 \rangle} = \ell_B \sqrt{v+1}/2$  in the  $v$ th Landau level. The minimum orbit size

$\sigma_{\text{LLL}} = \ell_B/\sqrt{2}$  occurs in the LLL, where the cyclotron wave function is Gaussian and saturates the Heisenberg uncertainty relation  $\Delta\xi\Delta\eta \geq \ell_B^2/2$ . The density of any condensate in the LLL is therefore a convolution of the guiding-center distribution with a Gaussian of width  $\sigma_{\text{LLL}}$ . In the quantum optics analogy, this directly realizes the Husimi-Q representation of the guiding-center Wigner function (1). In our case, at long times the cloud is an extended strip of transverse width  $\sigma_{\text{LLL}}$ . Geometric squeezing therefore coherently transforms the condensate into a single Landau gauge wave function within the LLL (1).

In Fig. 3A we show images of the condensate before and after squeezing and plot the major and minor cloud widths,  $\sigma_{\pm}$ , which are defined as the  $e^{-1/2}$  radii obtained from a Gaussian fit. Initially the chemical potential is  $\mu_0 \approx h \times 3.4$  kHz, where  $h$  is the Planck constant, and the number of Landau levels admixed into the condensate wave function is  $\sim\mu_0/(2\hbar\omega) \approx 20$ , hence the evolution is well described by a hydrodynamic model that neglects quantum pressure (29). The prediction of this model is shown by the red line, for which the only free parameter is the total atom number (35).

For times  $t > 0$ , the cloud evolves under the squeezing Hamiltonian of Eq. 3 and the major width increases as  $\sigma_{+} \propto \exp(\zeta t)$ , il-



lustrated by the dashed line. However, the minor width decays more slowly. This difference arises because the condensate size contains contributions from both the guiding centers, which are squeezed at a rate  $\zeta$ , and the cyclotron orbits, whose size depends on the number of occupied Landau levels  $N_{\text{LL}} \equiv \mu/(2\hbar\omega)$ . In our experiment,  $\sigma_{-}$  is generally dominated by cyclotron motion and its evolution is captured well by a simple scaling model. The chemical potential is proportional to the atomic number density  $\sim N_{\text{Tot}}/(\sigma_{+}\sigma_{-}\sigma_z)$ , where  $\sigma_z$  is the axial extent of the condensate. The major width always increases as  $\sigma_{+} \propto \exp(\zeta t)$ , and  $\sigma_{-} \propto \sqrt{\mu}$  when  $N_{\text{LL}} \gg 1$ . We therefore predict a time dependence  $\sigma_{-} \propto \exp(-\zeta t/4)$  at early times, which is shown by the dotted line in Fig. 3A. The gray data show a small breathing of the cloud at the cyclotron frequency  $2\omega$ . This is driven by imperfections in the trap, which shows a  $\sim 0.3\%$  root-mean-square variation in  $\omega$  with ellipse orientation, giving a perturbation in the rotating frame with a frequency  $2\Omega$ . The blue points are averaged over one period.

The falling chemical potential  $\mu \propto \exp(-\zeta t/2)$  guarantees that eventually  $\mu < 2\hbar\omega$  and the condensate enters the LLL. As shown in Fig. 3B, we directly observe the saturation of  $\sigma_{-}$  at the zero-point cyclotron width  $\sigma_{\text{LLL}}$  imposed by Heisenberg uncertainty. Because

the hydrodynamic model neglects quantum pressure, it predicts that  $\sigma_- \rightarrow 0$ . On the other hand, the saturation of the cloud width is captured very well by a Gross-Pitaevskii simulation with no free parameters (green solid line) (1). For comparison, the dashed line shows the width  $\sigma_0 = \ell_B$  of the noninteracting harmonic oscillator ground state, which corresponds to minimal, but isotropic, Heisenberg uncertainty in both cyclotron and guiding-center coordinates. This lies above our data at long times, and from the last five data points we infer squeezing of the guiding centers by >7 dB below the standard quantum limit.

In the lower panel of Fig. 3B, we plot the number of occupied Landau levels,  $N_{\text{LL}}$ , inferred from the central density evaluated using the fitted hydrodynamic model. We indeed find that the crossover to LLL behavior occurs for  $N_{\text{LL}} \sim 1$ ; the dashed region corresponds to  $N_{\text{LL}} < 1$ , where the hydrodynamic model is not applicable and this inference is no longer self-consistent. We also see a qualitative change in the shape of the cloud, which changes from a Thomas-Fermi to a Gaussian profile. This is shown in Fig. 3C, where we plot cuts along  $x = -y$  at early and late times. If  $N_{\text{LL}} \gg 1$ , the healing length is much smaller than the magnetic length and the density profile is a Thomas-Fermi function (red line). On the other hand, if  $N_{\text{LL}} < 1$ , the profile is Gaussian (green line), reflecting the cyclotron ground state. We note that at our latest times, the interparticle distance has grown to ~500 nm, close to half the size of a zero-point cyclotron orbit  $\sim \sigma_{\text{LLL}}$ . This signals the approach of the Bose gas toward the strongly correlated regime (10, 15, 36–40).

Microscopically, the squeezing operator mixes higher-angular momentum states into the condensate wave function, in analogy to the admixing of higher Fock states in squeezed light (32). In general, the angular momentum of a superfluid can be carried either by vortices or by deformations that break rotational symmetry (41). Because  $\nabla \times \mathbf{v}_d = 0$ , the induced flow is irrotational, but the large aspect ratio gives a moment of inertia  $\Theta = mN_{\text{Tot}} [(\sigma_+^2 - \sigma_-^2)^2 / (\sigma_+^2 + \sigma_-^2)] \approx mN_{\text{Tot}}\sigma_+^2$  which is close to the rigid-body value (41). For clouds with  $\sigma_+ > 50\ell_B$ , this gives a per-particle angular momentum  $\langle l_z \rangle > 1000\hbar$  despite the absence of any vortices inside the condensate (42).

In the experiments above, geometric squeezing was seen in the evolution of the condensate widths. To directly observe the drift velocity field inside the cloud, we now introduce a dilute gas of vortices that correspond to nodes in the atomic wave function and can serve as “tracer particles” for the local flow. We prepare a ground-state condensate rotating at  $0.8\omega$  in an isotropic trap and instantaneously apply the saddle  $V_s$  rotating at  $\Omega = \omega$ . The initial chemical potential is  $\mu \approx \hbar \times 2.2$  kHz, giving a cyclotron orbit size  $\sim \sqrt{\mu/(2\hbar\omega)}\ell_B = 5.5$   $\mu\text{m}$ .

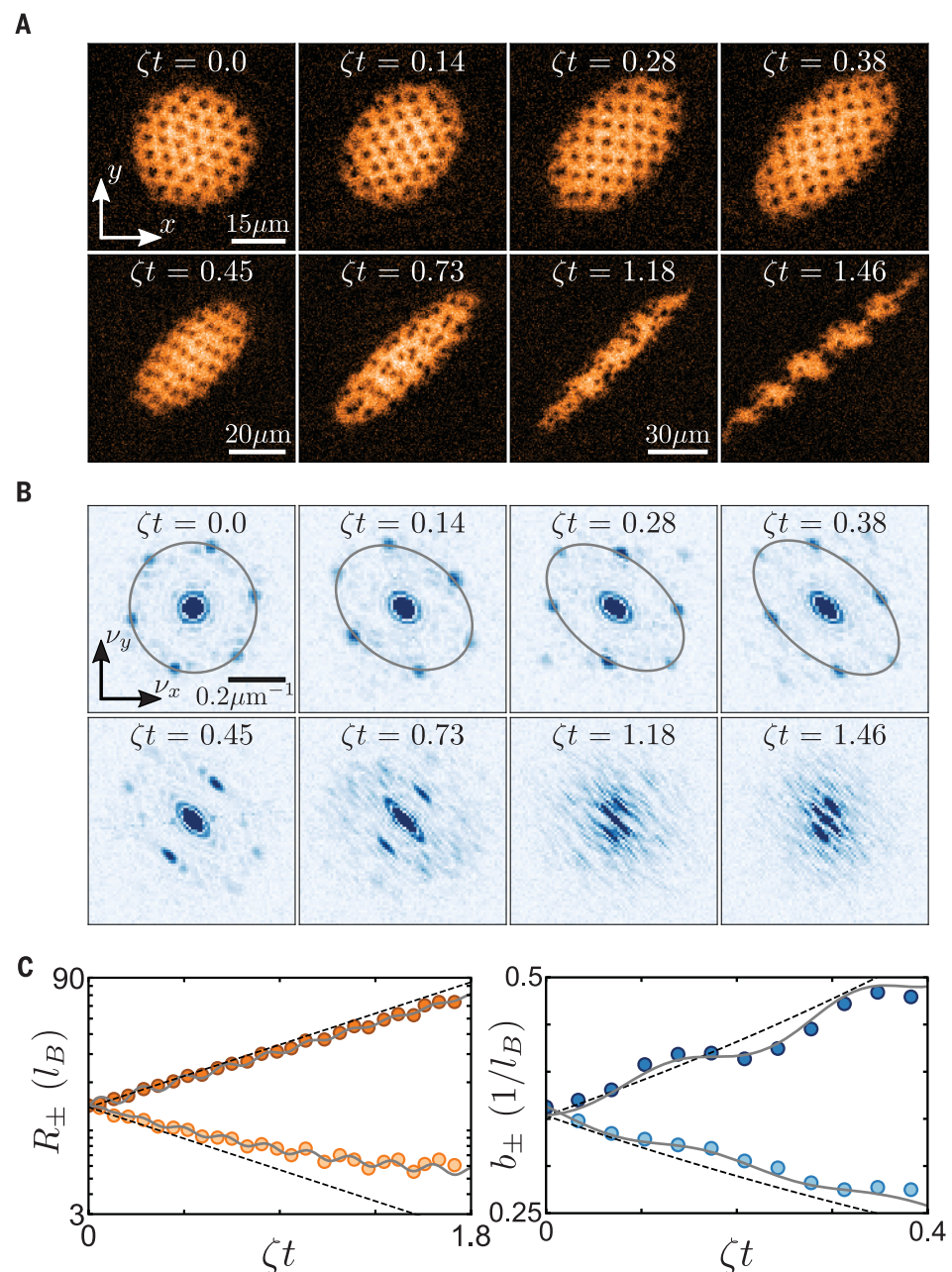


**Fig. 4. Squeezing of a vortex lattice.** (A and B) In situ evolution in real space (A) and reciprocal space (B) after suddenly applying the rotating saddle. Initially the cloud is round, and the reciprocal lattice vectors lie on a circle. Squeezing is evident in both the condensate spatial envelope and the vortex lattice spacing. At longer times, clustering of vortices causes the condensate to break up into droplets. (C) Time evolution of the major and minor Thomas-Fermi radii of the condensate,  $R_{\pm}$ , and the major and minor radii of the ellipse describing the lattice vectors,  $b_{\pm}$ . The black dashed lines show exponential functions  $A \exp(\pm \zeta t)$ , with  $A$  fixed by the data at  $t = 0$ ; the solid lines include the small contributions of quadrupolar collective modes and the nonzero size of the cyclotron orbits (1). The longest squeezing time  $\zeta t = 1.8$  corresponds to  $t \approx 50$  ms. The ellipse widths in reciprocal space are shown for times for which the distribution of vortices remains periodic.

This is much smaller than the cloud’s Thomas-Fermi radius of 21  $\mu\text{m}$ , hence the observed width is dominated by the guiding-center distribution. In Fig. 4, A and B, we show the in situ evolution in both real and reciprocal space. Initially, the condensate is circular and contains a triangular Abrikosov lattice with six-fold-symmetric reciprocal lattice vectors.

Subsequently, squeezing is evident in both the cloud shape and the vortex lattice. Because the vortices are distributed throughout the whole cloud, this indicates that the coordinates of all particles evolve under the same squeezing transformation. For longer times, while the overall spatial envelope continues to squeeze, the density profile exhibits

an intricate evolution. Squeezing of the initially triangular vortex lattice eventually leads to the formation of vortex rows (43, 44). Subsequently, a hydrodynamic instability drives amalgamation of the vortices into clusters, as well as an intriguing fragmentation of the condensate into a persistent array of droplets.

In Fig. 4C, we show the evolution of the major and minor Thomas-Fermi radii of the cloud,  $R_{\pm}$ , and the major and minor radii of an ellipse fitted to the reciprocal lattice vectors,  $b_{\pm}$ . The dashed lines show exponential functions  $A \exp(\pm \zeta t)$  (where the amplitude  $A$  is the only free parameter), which capture the initial evolution well. This confirms both the expected rate of squeezing and the incompressibility of the guiding-center distribution. The solid lines show a fit that includes the excitation of quadrupolar collective modes by the saddle turn-on and trap imperfections (see above) and additionally accounts for the nonzero cyclotron orbit size ( $\mathcal{I}$ ). This results in a slight reduction of the apparent squeezing rate and a slowdown of the decay in  $R_{\pm}$  as the guiding-center width approaches the cyclotron size.

The geometric squeezing protocol established here offers an alternative route to LLL physics in quantum gases. Crucially, simply turning off the saddle potential halts the outward flow of atoms. This controllably prepares an equilibrium condensate ( $\mathcal{I}$ ), which occupies a single Landau gauge wave function whose purely interaction-driven evolution in the flat single-particle dispersion of the LLL can then be cleanly observed. Natural immediate directions concern the collective excitation spectrum (45), quantum hydrodynamic stability, and the appearance of strongly correlated bosonic states (36–40, 42, 46). More generally, the ability to resolve cyclotron motion and vortices *in situ* allows the study of chiral edge states and quantum turbulence in rotating gases. From a metrology perspective, azimuthally squeezed condensates might offer

benefits for rotation sensing and a route to spin-squeezing via a spatially dependent coupling between internal atomic states (47).

## REFERENCES AND NOTES

- See supplementary materials.
- M. Wilkinson, *J. Phys. Math. Gen.* **20**, 1761–1771 (1987).
- Semiclassically, this incompressibility is an instance of Liouville's theorem; the quantum analog of a phase-space distribution is provided by the Wigner function, which is incompressible in the case of a quadratic Hamiltonian (48).
- J. G. Valatin, *Proc. R. Soc. London Ser. A* **238**, 132–141 (1956).
- A. Bohr, *Rev. Mod. Phys.* **48**, 365–374 (1976).
- B. R. Mottelson, *Rev. Mod. Phys.* **48**, 375–383 (1976).
- R. P. Kerr, *Phys. Rev. Lett.* **11**, 237–238 (1963).
- A. Maeder, G. Meynet, *Rev. Mod. Phys.* **84**, 25–63 (2012).
- F. D. M. Haldane, *Phys. Rev. Lett.* **107**, 116801 (2011).
- N. Cooper, *Adv. Phys.* **57**, 539–616 (2008).
- V. Schweikhard, I. Coddington, P. Engels, V. P. Mogendorff, E. A. Cornell, *Phys. Rev. Lett.* **92**, 040404 (2004).
- V. Bretin, S. Stock, Y. Seurin, J. Dalibard, *Phys. Rev. Lett.* **92**, 050403 (2004).
- J. Dalibard, F. Gerbier, G. Juzeliūnas, P. Öhberg, *Rev. Mod. Phys.* **83**, 1523–1543 (2011).
- N. Goldman, G. Juzeliūnas, P. Öhberg, I. B. Spielman, *Rep. Prog. Phys.* **77**, 126401 (2014).
- V. Galitski, G. Juzeliūnas, I. B. Spielman, *Phys. Today* **72**, 38–44 (2019).
- Y.-J. Lin, R. L. Compton, K. Jiménez-García, J. V. Porto, I. B. Spielman, *Nature* **462**, 628–632 (2009).
- V. Galitski, I. B. Spielman, *Nature* **494**, 49–54 (2013).
- J. Struck *et al.*, *Phys. Rev. Lett.* **108**, 225304 (2012).
- M. Aidelsburger *et al.*, *Phys. Rev. Lett.* **111**, 185301 (2013).
- H. Miyake, G. A. Siviloglou, C. J. Kennedy, W. C. Burton, W. Ketterle, *Phys. Rev. Lett.* **111**, 185302 (2013).
- G. Jotzu *et al.*, *Nature* **515**, 237–240 (2014).
- A. Celi *et al.*, *Phys. Rev. Lett.* **112**, 043001 (2014).
- M. Aidelsburger *et al.*, *Nat. Phys.* **11**, 162–166 (2014).
- L. J. LeBlanc *et al.*, *Proc. Natl. Acad. Sci. U.S.A.* **109**, 10811–10814 (2012).
- B. K. Stuhl, H.-I. Lu, L. M. Aycock, D. Genkina, I. B. Spielman, *Science* **349**, 1514–1518 (2015).
- M. Mancini *et al.*, *Science* **349**, 1510–1513 (2015).
- W. Petrich, M. H. Anderson, J. R. Ensher, E. A. Cornell, *Phys. Rev. Lett.* **74**, 3352–3355 (1995).
- K. W. Madison, F. Chevy, V. Bretin, J. Dalibard, *Phys. Rev. Lett.* **86**, 4443–4446 (2001).
- S. Sinha, Y. Castin, *Phys. Rev. Lett.* **87**, 190402 (2001).
- A. Recati, F. Zambelli, S. Stringari, *Phys. Rev. Lett.* **86**, 377–380 (2001).
- G. Kirchmair *et al.*, *Nature* **495**, 205–209 (2013).
- R. Loudon, P. Knight, *J. Mod. Opt.* **34**, 709–759 (1987).
- H. A. Fertig, B. I. Halperin, *Phys. Rev. B* **36**, 7969–7976 (1987).
- S. Vishveshwara, N. R. Cooper, *Phys. Rev. B* **81**, 201306 (2010).
- The hydrodynamic theory of (29) assumes a Thomas-Fermi cloud shape of radius  $R$ . A Thomas-Fermi profile has a fitted Gaussian  $e^{-1/2}$  radius of  $0.46R$ , which is the quantity shown by the red curve in Fig. 3A for direct comparison to our data.
- N. R. Cooper, N. K. Wilkin, J. M. F. Gunn, *Phys. Rev. Lett.* **87**, 120405 (2001).
- S. Sinha, G. V. Shlyapnikov, *Phys. Rev. Lett.* **94**, 150401 (2005).
- X. Chen, Z.-C. Gu, Z.-X. Liu, X.-G. Wen, *Science* **338**, 1604–1606 (2012).
- T. Senthil, M. Levin, *Phys. Rev. Lett.* **110**, 046801 (2013).
- A. Vishwanath, T. Senthil, *Phys. Rev. X* **3**, 011016 (2013).
- F. Zambelli, S. Stringari, *Phys. Rev. A* **63**, 033602 (2001).
- A. Altalion, X. Blanc, N. Lerner, *Phys. Rev. A* **79**, 011603 (2009).
- P. Engels, I. Coddington, P. C. Haljan, E. A. Cornell, *Phys. Rev. Lett.* **89**, 100403 (2002).
- M. Cozzini, S. Stringari, *Phys. Rev. A* **67**, 041602 (2003).
- S. M. Girvin, A. H. MacDonald, P. M. Platzman, *Phys. Rev. Lett.* **54**, 581–583 (1985).
- M. O. Oktel, *Phys. Rev. A* **69**, 023618 (2004).
- D. J. Wineland, J. J. Bollinger, W. M. Itano, D. J. Heinzen, *Phys. Rev. A* **50**, 67–88 (1994).
- E. Moyal, *Math. Proc. Camb. Philos. Soc.* **45**, 99–124 (1949).
- R. J. Fletcher *et al.*, Replication data for "Geometric squeezing into the lowest Landau level". Harvard Dataverse (2021); DOI: 10.7910/DVN/12PEGZ.

## ACKNOWLEDGMENTS

We thank T. Yefsah and J. Struck for early contributions to the planning and construction of the lab space and apparatus and L. Kendrick and J. T. Chamberlin for experimental assistance.

**Funding:** Supported by NSF (Center for Ultracold Atoms award PHY-1734011 and award PHY-1506019), Air Force Office of Scientific Research (FA9550-16-1-0324 and MURI Quantum Phases of Matter FA9550-14-1-0035), Office of Naval Research (N00014-17-1-2257), the DARPA A-Phi program through ARO grant W911NF-19-1-0511, the David and Lucile Packard Foundation, and the Vannevar Bush Faculty Fellowship. Also supported by a MIT Pappalardo Fellowship (R.J.F.) and by NSF GRFP (A.S.). **Author contributions:** R.J.F. and A.S. performed the experimental measurements and data analysis; R.J.F., V.C., B.M., and M.W.Z. developed the theoretical description and numerical calculations; R.J.F., A.S., C.C.W., P.B.P., Z.Y., and B.M. constructed the experimental apparatus; and R.J.F. and M.W.Z. supervised the study. All authors contributed to the interpretation of the data and the preparation of the manuscript. **Competing interests:** The authors declare no competing interests. **Data and materials availability:** All data shown in this work can be found at Harvard Dataverse (49).

## SUPPLEMENTARY MATERIALS

science.sciencemag.org/content/372/6548/1318/suppl/DC1  
Materials and Methods  
Supplementary Text  
Figs. S1 to S4  
References (50–59)  
28 December 2019; resubmitted 3 July 2020  
Accepted 11 May 2021  
10.1126/science.aba7202

## Geometric squeezing into the lowest Landau level

Richard J. FletcherAirlia ShafferCedric C. WilsonParth B. PatelZhenjie YanValentin CrépelBiswaroop MukherjeeMartin W. Zwierlein

Science, 372 (6548), • DOI: 10.1126/science.aba7202

### A spinning quantum gas

Ultracold atomic gases are very good at simulating electrons in solids but lack one essential party trick: charge. Their neutrality makes it challenging to simulate phenomena such as the quantum Hall effect, which, in the case of charged electrons, is easily induced by an external magnetic field. One way to produce a similar effect in a neutral system is to rotate it, but achieving the equivalent of strong magnetic fields remains difficult. Fletcher *et al.* rotated a gas of trapped sodium atoms, reaching a state in which the gas could be described by a single lowest Landau-level wave-function. The system is expected to be a testbed for studying the behavior of strongly interacting many-body states.

Science, aba7202, this issue p. 1318

### View the article online

<https://www.science.org/doi/10.1126/science.aba7202>

### Permissions

<https://www.science.org/help/reprints-and-permissions>

## Supplementary Materials for

### **Geometric squeezing into the lowest Landau level**

Richard J. Fletcher\*, Airlia Shaffer, Cedric C. Wilson, Parth B. Patel, Zhenjie Yan, Valentin Crépel,  
Biswaroop Mukherjee, Martin W. Zwierlein

\*Corresponding author. Email: rfletch@mit.edu

Published 18 June 2021, *Science* **372**, 1318 (2021)  
DOI: 10.1126/science.aba7202

**This PDF file includes:**

Materials and Methods

Supplementary Text

Figs. S1 to S4

References and Notes

## Materials and Methods

### Sample preparation

We prepare a Bose-Einstein condensate of  $N_{\text{Tot}} = 8.1(1) \times 10^5$  atoms of  $^{23}\text{Na}$  in the  $|F = 2, m_F = 2\rangle$  hyperfine state, in a magnetic TOP trap (27) of rms radial frequency  $\omega = 2\pi \times 88.6(1)$  Hz, and with no discernible thermal component. The chemical potential at the cloud center is  $\mu_0 \approx h \times 3.4$  kHz corresponding to a healing length of  $\sqrt{\hbar^2/(2m\mu)} = 250$  nm.

### Imaging calibration

The objective used for our *in situ* imaging has a nominal numerical aperture of  $\text{NA} = 0.5$ . In addition to the diffraction limit, an imaged cloud can also be broadened by optical aberrations, imperfections in the polarisation and frequency of the imaging light, and by motion of the atoms during imaging.

To directly characterize our imaging resolution experimentally, we measure the core structure of a quantum vortex. In Fig. S1A we show a rotating condensate prepared in a circular magnetic trap which has a radial trapping frequency  $\omega = 2\pi \times 88.6(1)$  Hz. The cloud rotation rate is  $\Omega \approx 0.75\omega$ , which is determined from the two-dimensional vortex number density,  $n_v$ , according to  $n_v = m\Omega/(\pi\hbar)$  (50). From the measured Thomas-Fermi radius of the condensate,  $R \approx 22.1$   $\mu\text{m}$ , and using the effective radial trapping frequency of  $\sqrt{\omega^2 - \Omega^2}$ , we infer a central chemical potential  $\mu \approx h \times 1.9$  kHz corresponding to a healing length of 340 nm.

We perform an azimuthal average of the measured two-dimensional atomic number density,  $n$ , around every vortex located within a radius of  $R/2$ . The average of these individual vortex profiles is shown in Fig. S1B, where we compare the data to two models. The dashed curve shows the theoretical vortex core structure, obtained by numerically solving the Gross-Pitaevskii equation for a single vortex within a uniform condensate (51). The solid curve shows a fit function obtained by convolving this profile with a Gaussian of variable  $e^{-1/2}$ -radius  $\sigma$ , which

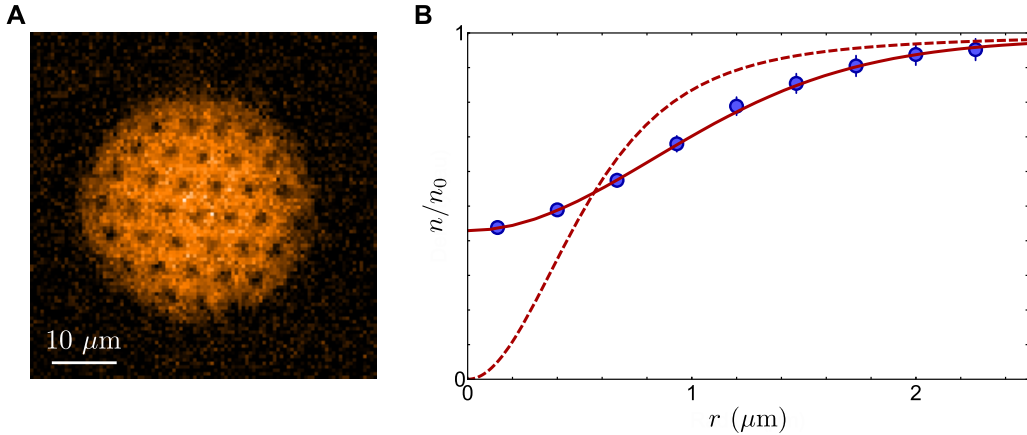


Figure S1: **In situ image of quantum vortices.** (A) An *in situ* image of a condensate containing a vortex lattice. A radial average of the measured density,  $n$ , is performed around the core of each vortex within  $R/2$  of the cloud center, where  $R$  is the Thomas-Fermi radius of the cloud. (B) The average of these profiles is shown by the blue points, where the density,  $n$ , has been normalized to the density of the surrounding condensate,  $n_0$ . We fit the data with a function obtained by convolving the theoretical core structure of a single vortex (see text) with a Gaussian function, whose  $e^{-1/2}$ -radius has an optimal value of 670 nm. The resulting curve is shown by the solid line, while the dashed line shows the theoretical curve without any broadening.

simultaneously captures both the increased width and reduced contrast of the vortex well. The optimum value of  $\sigma = 670$  nm corresponds to the effective broadening of a point source arising from both the diffraction limit and imaging imperfections. It is indicated by a blue arrow in Fig. 3 of the main paper.

For comparison, we measured the point spread function of our imaging system before installation in the machine, using a point source provided by a SNOM optical fibre tip (52). A Gaussian fitted to this function has a  $e^{-1/2}$ -radius of 280 nm. The difference between this value and the observed resolution is approximately accounted for by motion of the atoms during imaging; we use a high-intensity imaging pulse with a duration of 3  $\mu$ s, resulting in diffusion by  $\approx 570$  nm of a  $^{23}\text{Na}$  atom transverse to the imaging axis.

We note that *in situ* detection of vortices has also been reported using, i) dark-field imaging (53), where several vortices within a lattice were detected with a spatial resolution  $\sim 3$   $\mu\text{m}$

and separation of  $9 \mu\text{m}$ , ii) phase-contrast imaging (54), where individual vortices could be detected for separations  $\gtrsim 20 \mu\text{m}$ , and iii) by filling the vortex cores with atoms prepared in a different internal hyperfine state (55), which expanded the core to a radius of  $\sim 7 \mu\text{m}$ . In contrast to these previous methods, our imaging allows us to resolve dense vortex lattices, with an inter-vortex spacing comparable to the vortex size, given by the healing length scale of  $\sim 0.5 \mu\text{m}$ .

## Fit function for vortex lattice squeezing

In Fig. 4C of the main paper, we show the evolution under geometric squeezing of the major and minor widths of the cloud in real space, and the major and minor widths of an ellipse describing the reciprocal vectors of the vortex lattice. While the dashed lines show purely the ideal squeezing evolution  $R_{\pm}, b_{\pm} \sim \exp(\pm\zeta t)$ , the solid line fits include a small admixture of  $m = 0$  and  $m = 2$  quadrupolar collective excitations, which have a natural frequency  $2\omega$  for a cloud rotating at  $\Omega = \omega$  (44). These are excited by both the sudden switch-on of the saddle potential which initiates squeezing of the cloud, and a small ( $\sim 0.3\%$ ) breathing of the trapping frequency  $\omega$  as the trap rotates (see main paper). We also include the non-zero size of cyclotron orbits; these are not squeezed and so their contribution to the cloud width remains constant, while the guiding centers are squeezed at a rate  $\zeta$ . We simultaneously fit the function

$$R_{\pm}(t) = A\sqrt{e^{\pm 2\zeta t} + B^2} + C \sin(2\omega t + \phi_C) \pm D \sin(2\omega t + \phi_D),$$

$$b_{\pm}(t) = E/R_{\pm}(t),$$

to all data sets  $\{R_{\pm}(t), b_{\pm}(t)\}$ .

We find fractional amplitudes  $C/A = 0.047(5)$  and  $D/A = 0.019(5)$  for the  $m = 0$  and  $m = 2$  modes respectively, and a residual cyclotron orbit size  $AB = 7.6(4) \mu\text{m}$ , comparable to an estimate  $\sim \sqrt{\mu/(2\hbar\omega)} \ell_B = 5.5 \mu\text{m}$  obtained from the chemical potential  $\mu \approx h \times 2.2 \text{ kHz}$ .

## Gross-Pitaevskii simulations

Given the experimental results presented in the main paper, it is interesting to explore the experimental protocol within a Gross-Pitaevskii (GP) framework. Stimulated by the experiment, we thus implemented a GP simulation in the rotating frame. In addition to describing well the saturation of the cloud width as the gas enters the LLL (see Fig. 3 of the main paper), we also reproduced several other features of the experiment, examples of which are shown in Fig. S3.

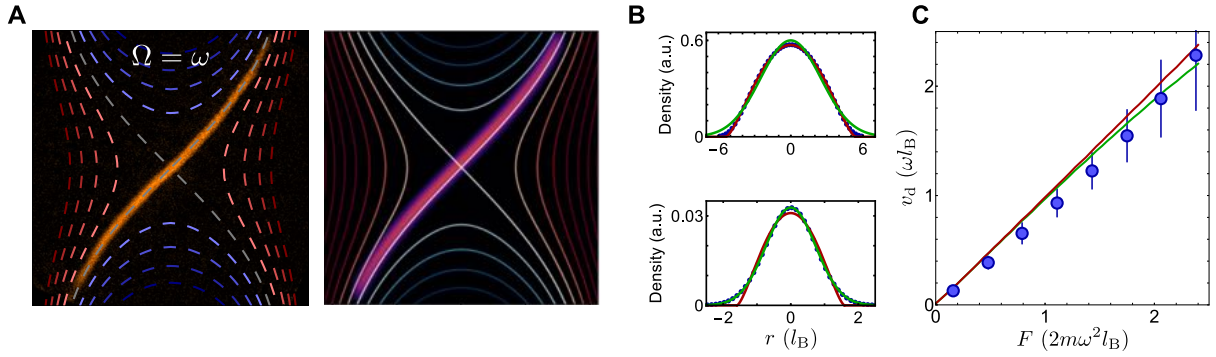


**Figure S2: Gross-Pitaevskii simulation of the geometric squeezing experiment.** **(A)** Quartic corrections to the TOP trap potential (27) lead to a curvature of the cloud as the atoms flow out along isopotentials. We show images from the experiment (left, taken from Fig. 1 of the main paper) and the simulation (right). **(B)** At high densities (top), a cut through the density distribution along the short axis of the cloud is better fitted by a Thomas-Fermi function (red) than a Gaussian (green). At low densities (bottom), the gas occupies the LLL and the density is better fitted by a Gaussian. Corresponding experimental profiles are shown in Fig. 3C of the main paper. **(C)** The drift velocity as a function of the azimuthal force  $F(r) = m\varepsilon\omega^2 r$  felt by atoms flowing out along the diagonal of the saddle potential. The red line shows the simulated drift velocity for a perfectly harmonic trap, and the green line shows the GP result including corrections to the velocity directed along  $x = y$ , which arise from quartic terms in the trapping potential. The blue points show our experimental data, plotted in Fig. 2 of the main paper.

## Supplementary Text

### Geometric squeezing as a route to equilibrium rotating gases

Turning off the saddle potential during geometric squeezing halts the outward flow of atoms. The density of the final condensate can be smoothly varied by changing the duration of the squeezing, and is conveniently parameterized by the number of occupied Landau levels  $N_{\text{LL}} = \mu/(2\hbar\omega)$ . The condensate continues to rotate at  $\Omega = \omega$ , experiencing a synthetic magnetic field but no scalar potential. In the limit  $N_{\text{LL}} \ll 1$  the atoms occupy a single Landau gauge wavefunction within the LLL, whereas in the limit  $N_{\text{LL}} \gg 1$  states from the first  $\sim N_{\text{LL}}$  Landau levels are admixed into the superfluid wavefunction.

In both cases, despite the absence of any scalar potential in the rotating frame, the cloud is stabilized by an effective trap along  $x$ , of frequency  $2\omega$ , where we take the long axis of the condensate to lie along the  $y$ -direction. This can be seen directly from the Hamiltonian in the Landau gauge of a gas rotating at  $\Omega = \omega$  (see Eq. (S17) below),

$$H = \frac{p_x^2}{2m} + \frac{1}{2}m(2\omega)^2(x - k_y\ell_B^2)^2, \quad (\text{S1})$$

where  $k_y$  is the wavevector along the translationally-invariant  $y$ -direction. Physically, the effective trapping arises from the kinetic energy cost imposed by irrotationality of the condensate in the lab frame, which implies a flow profile in the rotating frame  $\vec{v} = (0, -2\omega x)$  (30).

In Fig. S2 we show several examples of condensate evolution after turning off the saddle. The cloud continues to rotate at  $\Omega = \omega$ , but the density profile remains constant. In the rotating frame, the condensate provides a static, equilibrium starting point from which to investigate quantum Hall physics. This equilibrium reflects a balancing of the outward pressure (quantum or mean-field) on each fluid element by the inward Coriolis force arising from the flow profile  $\vec{v}$ . Such stabilization of the cloud by the Coriolis force is reminiscent of the persistence of vortex aggregates in azimuthally-symmetric condensates (56).

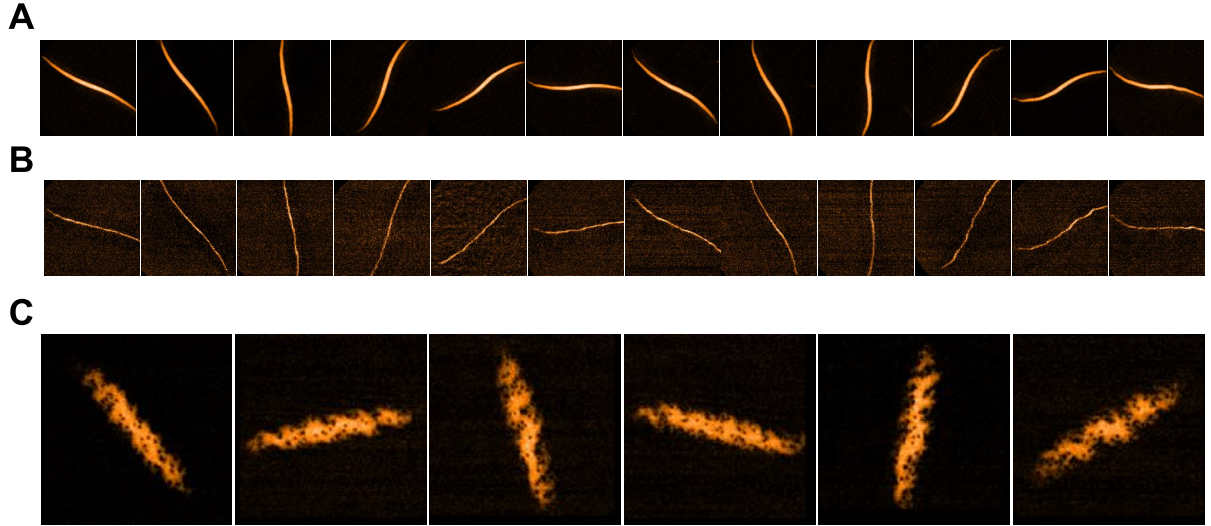


**Figure S3: Preparation of an equilibrium, rotating condensate by geometric squeezing.** Turning off the saddle potential halts geometric squeezing, and freezes the outward flow of atoms. The cloud continues to rotate at  $\Omega = \omega$  and therefore experiences a synthetic magnetic field. Even though it feels no scalar potential, the cloud maintains its shape thanks to the imprinted flow profile in the rotating frame (see text), realizing an equilibrium starting point from which to investigate quantum Hall physics. **(A-B)** The stable evolution of a cloud with  $\mu/(2\hbar\omega) \approx 9$ , and a lower density cloud with  $\mu/(2\hbar\omega) \approx 3$ . The time interval between images is 1 ms, with the first image being taken immediately after turning off the saddle potential. **(C)** The evolution of a cloud supporting quantum vortices, obtained by geometric squeezing of a condensate containing a vortex lattice. The images show the cloud 0 ms, 2 ms, 5 ms, 7 ms, 10 ms, and 20 ms after turning off the saddle.

## Derivation of the Foucault Hamiltonian

The Hamiltonian of a two-dimensional harmonic oscillator viewed in a frame rotating about the  $z$ -axis is

$$H = \frac{p_x^2 + p_y^2}{2m} + \frac{1}{2}m\omega^2(x^2 + y^2) - \Omega L_z, \quad (\text{S2})$$

where  $\omega$  is the natural frequency of the pendulum,  $m$  is the particle's mass,  $p_{x,y}$  are canonical momenta along  $x$  and  $y$ ,  $L_z = xp_y - yp_x$  is the axial angular momentum, and  $\Omega$  is the rotational angular frequency of the reference frame. Although we are describing the quantum problem, we omit hats over all operators for brevity.

The equivalence of Eq. (S2) to the Hamiltonian of a charged particle in a magnetic field is easily seen by completing the square for momentum variables. For the case  $\Omega = \omega$ , where the centrifugal force cancels the trapping force, we obtain

$$H = \frac{(p_x + m\Omega y)^2 + (p_y - m\Omega x)^2}{2m}. \quad (\text{S3})$$

Rotation of the reference frame therefore induces an effective vector potential  $q\vec{A} = m\vec{\Omega} \times \vec{r}$ , corresponding to a uniform magnetic field  $qB = q\vec{\nabla} \times \vec{A} = 2m\Omega$ . Here  $q$  is the particle's charge in the equivalent magnetic problem. In that case, particles perform cyclotron motion at the cyclotron frequency  $qB/m = 2\omega$  and with a typical extent set by the magnetic length  $\ell_B = \sqrt{\hbar/(qB)}$  (57).

The Hamiltonian of the rotating pendulum given in Eq. (S2) is conveniently diagonalized by introducing ladder operators corresponding to the counter-rotating ‘cyclotron’ mode, and the co-rotating ‘guiding center’ mode,

$$a = \frac{a_x + ia_y}{\sqrt{2}}, \quad b = \frac{a_x - ia_y}{\sqrt{2}} \quad (\text{S4})$$

where  $a_x = \sqrt{\frac{m\omega}{2\hbar}}(x + i\frac{p_x}{m\omega})$  and  $a_y = \sqrt{\frac{m\omega}{2\hbar}}(y + i\frac{p_y}{m\omega})$  are ladder operators for the individual  $x$ - and  $y$ -oscillators respectively. One finds

$$H = \hbar(\omega + \Omega)a^\dagger a + \hbar(\omega - \Omega)b^\dagger b + \hbar\omega, \quad (\text{S5})$$

which describes two decoupled oscillators with natural frequencies  $\omega \pm \Omega$ . In terms of the cyclotron coordinates  $(\xi, \eta)$  and the guiding center coordinates  $(X, Y)$  (57),

$$a = \sqrt{\frac{m\omega}{\hbar}}(\xi + i\eta), \quad b = \sqrt{\frac{m\omega}{\hbar}}(X - iY), \quad (\text{S6})$$

where  $(\xi, \eta)$  and  $(X, Y)$  are admixtures of the position and momentum variables of the pendulum bob,

$$\xi = \left(\frac{x}{2} - \frac{p_y}{2m\omega}\right), \quad \eta = \left(\frac{y}{2} + \frac{p_x}{2m\omega}\right)$$

$$X = \left( \frac{x}{2} + \frac{p_y}{2m\omega} \right), \quad Y = \left( \frac{y}{2} - \frac{p_x}{2m\omega} \right). \quad (\text{S7})$$

A particle's absolute position  $(x, y) = (\xi + X, \eta + Y)$  is given by the sum of a fast, counter-rotating motion in  $(\xi, \eta)$ -space, and a slow, co-rotating motion in  $(X, Y)$ -space (see Fig. 1A of the main paper). Since these coordinate pairs each span the phase space of a one-dimensional harmonic oscillator, they do not commute, and

$$[\xi, \eta] = -[X, Y] = i\ell_B^2, \quad (\text{S8})$$

where  $\ell_B = \sqrt{\hbar/(2m\omega)}$  is the rotational analogue of the magnetic length. In terms of these variables, the pendulum Hamiltonian takes the form

$$H = m\omega(\omega + \Omega)(\xi^2 + \eta^2) + m\omega(\omega - \Omega)(X^2 + Y^2), \quad (\text{S9})$$

which reproduces Eq. (1) of the main paper.

## Derivation of the squeezing Hamiltonian

Viewed in a rotating reference frame, the Hamiltonian of an anisotropic harmonic oscillator with trapping frequencies  $\omega\sqrt{1 \pm \varepsilon}$  along the  $x$ - and  $y$ -directions respectively is

$$H_\varepsilon = \frac{p_x^2 + p_y^2}{2m} + \frac{1}{2}m\omega^2(x^2 + y^2) + \frac{1}{2}m\varepsilon\omega^2(x^2 - y^2) - \Omega L_z, \quad (\text{S10})$$

where all quantities are defined as in the previous section. The Hamiltonian is quadratic, and can be decoupled into its normal modes by a gauge transformation, under which wavefunctions transform as  $\psi' = G\psi$ , where  $G = \exp\{-i\kappa xy(m\omega/\hbar)\}$  and  $\kappa = \varepsilon\omega/(2\Omega)$ . The transformed Hamiltonian is

$$H'_\varepsilon = GH_\varepsilon G^\dagger = \frac{p_x^2 + p_y^2}{2m} + \frac{1}{2}m\omega^2(1 + \kappa^2)(x^2 + y^2) - \Omega(xp_y - yp_x) + \kappa\omega(xp_y + yp_x). \quad (\text{S11})$$

We now rescale spatial and momentum variables according to

$$\tilde{x} = (1 + \kappa^2)^{1/4} x, \quad \tilde{p}_x = (1 + \kappa^2)^{-1/4} p_x$$

$$\tilde{y} = (1 + \kappa^2)^{1/4} y, \quad \tilde{p}_y = (1 + \kappa^2)^{-1/4} p_y \quad (\text{S12})$$

which yields

$$H'_\varepsilon = \sqrt{1 + \kappa^2} \left[ \frac{\tilde{p}_x^2 + \tilde{p}_y^2}{2m} + \frac{1}{2} m \omega^2 (\tilde{x}^2 + \tilde{y}^2) \right] - \Omega(\tilde{x}\tilde{p}_y - \tilde{y}\tilde{p}_x) + \kappa\omega(\tilde{x}\tilde{p}_y + \tilde{y}\tilde{p}_x). \quad (\text{S13})$$

The first two terms are simply the Hamiltonian of a rotating isotropic oscillator (see Eq. (S2)).

Analogously to the previous section, we introduce scaled ladder operators,

$$\tilde{a} = \frac{\tilde{a}_x + i\tilde{a}_y}{\sqrt{2}}, \quad \tilde{b} = \frac{\tilde{a}_x - i\tilde{a}_y}{\sqrt{2}} \quad (\text{S14})$$

in terms of which the first term of Eq. (S13) yields  $\hbar\omega\sqrt{1 + \kappa^2}(\tilde{a}^\dagger\tilde{a} + \tilde{b}^\dagger\tilde{b} + 1)$ , the second term  $\hbar\Omega(\tilde{a}^\dagger\tilde{a} - \tilde{b}^\dagger\tilde{b})$  and the third term  $\hbar\kappa\omega(\tilde{a}^\dagger\tilde{a}^\dagger + \tilde{a}\tilde{a} + \tilde{b}^\dagger\tilde{b}^\dagger + \tilde{b}\tilde{b})/2$ . We finally obtain

$$\begin{aligned} H'_\varepsilon = \hbar & \left[ \lambda_+(\tilde{a}^\dagger\tilde{a} + 1/2) - \frac{\kappa\omega}{2}(\tilde{a}^\dagger\tilde{a}^\dagger + \tilde{a}\tilde{a}) \right] \\ & + \hbar \left[ \lambda_-(\tilde{b}^\dagger\tilde{b} + 1/2) + \frac{\kappa\omega}{2}(\tilde{b}^\dagger\tilde{b}^\dagger + \tilde{b}\tilde{b}) \right]. \end{aligned} \quad (\text{S15})$$

The Hamiltonian therefore separates into two decoupled oscillators, each including a squeezing interaction, with natural frequencies  $\lambda_\pm = \omega\sqrt{1 + \kappa^2} \pm \Omega$  and squeezing rate  $\zeta = \kappa\omega$ .

In our case,  $\Omega = \omega$  and so  $\zeta = \varepsilon\omega/2$  and  $\kappa = 0.06$ , corresponding to an anisotropy-induced shift in the normal mode frequencies by  $\sim 10^{-3}\omega$ . To an excellent approximation, because  $\kappa\omega \ll \lambda_+$  we can neglect squeezing of the cyclotron motion and set  $\lambda_+ \rightarrow 2\omega$ . On the other hand, because  $\kappa\omega \gg \lambda_-$  the guiding center motion is completely squeezed, and we set  $\lambda_- \rightarrow 0$ . We also neglect the small ( $\sim 0.1\%$ ) rescaling of spatial and momentum variables. This yields the squeezing Hamiltonian

$$H_s \approx 2\hbar\omega(a^\dagger a + 1/2) + \frac{\hbar\zeta}{2}(b^\dagger b^\dagger + bb), \quad (\text{S16})$$

which recovers Eq. (3) of the main paper.

## Squeezing as effecting a gauge transformation

The rotational origin of the gauge field in Eq. (S3) gives rise to a Hamiltonian expressed in the symmetric gauge. However, one can equally well express the rotating gas Hamiltonian in the Landau gauge. This gauge transformation is accomplished by defining Landau gauge wavefunctions  $\psi_L$ , which are related to their symmetric gauge counterparts  $\psi_s$  by  $\psi_L = U\psi_s$  where  $U = e^{im\Omega xy/\hbar}$ , and whose time evolution is governed by the transformed Hamiltonian  $UHU^\dagger$ . In the case  $\Omega = \omega$ , the symmetric gauge Hamiltonian of Eq. (S3) transforms to

$$H = \frac{p_x^2}{2m} + \frac{1}{2}m(2\omega)^2(x - k_y\ell_B^2)^2, \quad (\text{S17})$$

where we have assumed wavefunctions of the form  $\exp(ik_yy)\psi_L(x)$  due to the translational invariance of Eq. (S17).

This Hamiltonian corresponds to a flat dispersion associated with momentum along the  $y$ -direction, and an effective harmonic oscillator along  $x$ . Physically, the effective trapping arises from the kinetic energy cost imposed by irrotationality of the condensate in the lab frame, which implies a flow profile in the rotating frame  $\vec{v} = (0, -2\omega x)$  (30). Within the Landau gauge, eigenstates are translationally-invariant along  $y$ , and in the LLL are Gaussian along  $x$  with the density showing a  $e^{-1/2}$ -radius of  $\ell_B/\sqrt{2}$ .

Geometric squeezing smoothly evolves the wavefunction from one that is most easily described in the symmetric gauge, to one that is best described in the Landau gauge. As a simple illustration, we calculate the evolution of the non-interacting ground state of the 2D harmonic oscillator under geometric squeezing. We will see how this state coherently evolves into the ground state in the Landau gauge, acquiring a width given by the cyclotron zero-point motion.

The ground state starts out in  $|0, 0\rangle$ , where  $|m, n\rangle$  denotes a state of  $m$  quanta of cyclotron oscillation and  $n$  quanta of guiding center motion. We treat the case, relevant here, of critical rotation  $\Omega = \omega$ . Standard tools of quantum optics (58) allow us to write the time-evolved state

as

$$|\Psi(t)\rangle = \exp\left(-i\frac{\zeta t}{2}(b^\dagger b^\dagger + bb)\right) |0, 0\rangle = \frac{1}{\sqrt{\cosh(\zeta t)}} \exp\left(-\frac{i}{2} \tanh(\zeta t) b^\dagger b^\dagger\right) |0, 0\rangle.$$

The wavefunction at position  $(x, y)$  is  $\langle x, y | \Psi(t) \rangle$ . Noting that  $b^\dagger = z - a$ , with  $z = x + iy$  written in units of the oscillator length  $\sqrt{\hbar/m\omega} = \sqrt{2}l_B$ ,  $[z, a] = 0$ , and  $\langle x, y | 0, 0 \rangle = \frac{1}{\sqrt{\pi}} \exp(-\frac{1}{2}(x^2 + y^2))$ , one finds

$$\langle x, y | \Psi(t) \rangle = \frac{1}{\sqrt{\pi \cosh(\zeta t)}} \exp\left(-\frac{i}{2} \tanh(\zeta t) z^2\right) \exp\left(-\frac{1}{2}|z|^2\right), \quad (\text{S18})$$

from which follows for the density  $n(x, y) = |\langle x, y | \Psi(t) \rangle|^2$

$$n(x, y) = \frac{1}{\pi \cosh \zeta t} \exp\left(-\frac{1}{2}(1 - \tanh(\zeta t))(x + y)^2 + \frac{1}{2}(1 + \tanh(\zeta t))(x - y)^2\right). \quad (\text{S19})$$

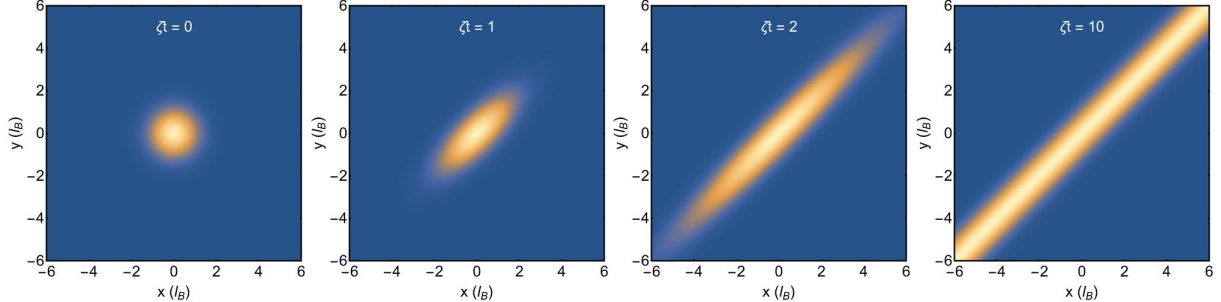


**Figure S4: Geometric squeezing from a symmetric to Landau gauge ground state.** The density plots show the time evolution of the condensate density  $n(x, y)$  according to Eq. (S19). The cloud is coherently transformed from the circular ground state wavefunction of the symmetric gauge, to the elongated Landau gauge ground state.

This describes geometric squeezing along the diagonal  $x = y$ , and the evolution of  $n(x, y)$  is illustrated in Fig. S4. The final state for  $\zeta t \gg 1$  evolves towards

$$|\Psi(\zeta t \gg 1)\rangle \propto \exp\left(-\frac{1}{2}(x - y)^2\right) \exp\left(-\frac{1}{2}i(x^2 - y^2)\right) \quad (\text{S20})$$

which is the ground state Landau gauge wavefunction oriented along the diagonal  $y = x$ , of density  $n(x, y) \propto \exp(-(x - y)^2)$ , featuring a  $e^{-1/2}$ -radius along the narrow axis of  $l_B/\sqrt{2}$ . The

phase profile  $\exp(-\frac{1}{2}i(x^2-y^2)) = \exp(-im\omega uv/\hbar)$ , with  $u = (x+y)/\sqrt{2}$  and  $v = (x-y)/\sqrt{2}$ , is precisely that of a Landau gauge strip when expressed in the symmetric gauge (in which we solved the problem) for  $\Omega = \omega$ .

## Deviations from ideal behavior

The motion of a particle in a rotating frame deviates from the ideal picture of circular cyclotron orbits drifting along isopotentials in two ways (59). First, any applied force not only leads to a transverse drift in  $(X, Y)$ -space, but also a static colinear displacement in  $(\xi, \eta)$ -space. Second, curvature of an applied scalar potential mixes the cyclotron and guiding center modes, resulting in sheared cyclotron orbits.

In our case, atoms are driven outward along the  $x = y$  diagonal of the saddle potential by the azimuthal force  $F(r) = m\varepsilon\omega^2r$ . Cyclotron orbits occur at a frequency  $2\omega$  giving an effective spring constant  $k = 4m\omega^2$ , which implies a spatial displacement in the azimuthal direction of  $F/k = \varepsilon r/4$ . This causes the outward flow of atoms to deviate from the  $x = y$  diagonal by an angle of  $\varepsilon/4 \sim 2^\circ$ .

The shearing of cyclotron orbits follows from Eq. (S15). Rewriting the cyclotron ladder operator in terms of spatial cyclotron variables,  $a = \sqrt{m\omega/\hbar}(\xi + i\eta)$ , yields a cyclotron Hamiltonian  $2m\omega^2[\xi^2(1 - \kappa/2) + \eta^2(1 + \kappa/2)]$ . Atoms therefore perform elliptical trajectories in cyclotron phase-space, of ellipticity  $\kappa/2 = \varepsilon/4 = 0.03$ , giving a ratio of major to minor orbit widths of 1.03.

## Relation of the density distribution to cyclotron and guiding center Wigner functions

In this section, we show that if the particle's wavefunction is separable in guiding center and cyclotron coordinates, then the imaged density distribution is given by the convolution of the guiding center and cyclotron Wigner distributions. In the following we set  $\hbar = 1$  and  $2m\omega = 1$ .

For a one-dimensional particle described by state vector  $|\psi\rangle$  and with position and momentum variables  $(x, p)$ , the Wigner distribution is defined by

$$\mathcal{W}(x, p) = \frac{1}{\pi} \int du e^{2ipu} \psi(x - u) \psi^*(x + u), \quad (\text{S21})$$

and is closely analogous to the phase space distribution of classical physics (48). Whereas  $[x, p] = i$ , the cyclotron and guiding center coordinates instead have commutators  $[\xi, \eta] = i$  and  $[X, Y] = -i$  (see Eq. (S8)), implying corresponding Wigner functions

$$\begin{aligned} \mathcal{W}_c(\xi, \eta) &= \frac{1}{\pi} \int du e^{2i\eta u} \psi_c(\xi - u) \psi_c^*(\xi + u), \\ \mathcal{W}_g(X, Y) &= \frac{1}{\pi} \int du e^{-2iY u} \psi_g(X - u) \psi_g^*(X + u). \end{aligned} \quad (\text{S22})$$

where  $\psi_c(\xi)$  and  $\psi_g(X)$  are the cyclotron and guiding center wavefunctions.

The imaged density is proportional to the particle state vector  $|\Psi\rangle$  projected onto a state of definite  $x$  and  $y$ ,

$$\begin{aligned} n(x, y) &= |\langle x, y | \Psi \rangle|^2 \\ &= \left| \int \frac{dp_y}{2\pi} \langle x, y | x, p_y \rangle \Psi(x, p_y) \right|^2 \\ &= \left| \int \frac{dp_y}{2\pi} e^{ip_y y} \Psi \left( X = \frac{x}{2} + p_y, \xi = \frac{x}{2} - p_y \right) \right|^2, \end{aligned} \quad (\text{S23})$$

where we have inserted the resolution of the identity  $I = \int \frac{dx dp_y}{2\pi} |x, p_y\rangle \langle x, p_y|$ , and used Eq. (S7) to relate absolute spatial and momentum coordinates to cyclotron and guiding center variables.

We now make the assumption of a separable wavefunction, such that  $|\Psi\rangle = |\psi_g\rangle |\psi_c\rangle$ , where  $|\psi_g\rangle$  and  $|\psi_c\rangle$  are the guiding center and cyclotron state vectors respectively. We find

$$n(x, y) = \frac{1}{4\pi^2} \int \int du dv e^{i(u-v)y} \psi_g \left( \frac{x}{2} + u \right) \psi_g^* \left( \frac{x}{2} + v \right) \psi_c \left( \frac{x}{2} - u \right) \psi_c^* \left( \frac{x}{2} - v \right). \quad (\text{S24})$$

Making the coordinate rotation  $u = \alpha + \beta$ ,  $v = \alpha - \beta$  yields

$$n(x, y) = \frac{1}{2\pi^2} \int \int d\alpha d\beta e^{2i\beta y} \psi_g\left(\frac{x}{2} + \alpha + \beta\right) \psi_g^*\left(\frac{x}{2} + \alpha - \beta\right) \psi_c\left(\frac{x}{2} - \alpha - \beta\right) \psi_c^*\left(\frac{x}{2} - \alpha + \beta\right). \quad (\text{S25})$$

We now employ the convolution theorem  $\int \frac{dk}{2\pi} e^{ikx} f(k)g(k) = [\int \frac{dk}{2\pi} e^{ikx} f(k)] * [\int \frac{dk}{2\pi} e^{ikx} g(k)]$ , where the convolution is defined by  $f(x) * g(x) = \int du f(\frac{x}{2} + u) g(\frac{x}{2} - u)$ , yielding

$$\begin{aligned} n(x, y) &= \int \frac{d\alpha}{2\pi} \left[ \frac{1}{\pi} \int d\beta e^{2i\beta y} \psi_g\left(\frac{x}{2} + \alpha + \beta\right) \psi_g^*\left(\frac{x}{2} + \alpha - \beta\right) \right] *_y \left[ \frac{1}{\pi} \int d\beta e^{2i\beta y} \psi_c\left(\frac{x}{2} - \alpha - \beta\right) \psi_c^*\left(\frac{x}{2} - \alpha + \beta\right) \right] \\ &= \int \frac{d\alpha}{2\pi} \mathcal{W}_g\left(\frac{x}{2} + \alpha, y\right) *_y \mathcal{W}_c\left(\frac{x}{2} - \alpha, y\right) \end{aligned} \quad (\text{S26})$$

$$= \mathcal{W}_g(x, y) *_x \mathcal{W}_c(x, y), \quad (\text{S27})$$

where  $*_i$  denotes convolution over the  $i$ -direction.

In the case that the cloud occupies the lowest Landau level, the cyclotron wavefunction corresponds to the ground state of a harmonic oscillator with coordinates  $(\xi, \eta)$  and natural frequency  $2\omega$ , and  $\langle \xi | \psi_c \rangle \sim \exp(-\xi^2/(2\ell_B^2))$ . Evaluating the Wigner function according to Eq. (S22) yields  $\mathcal{W}_c(\xi, \eta) \sim \exp(-(\xi^2 + \eta^2)/\ell_B^2)$ . The experimentally observed density is therefore the convolution of the guiding center Wigner function with a Gaussian, directly visualizing the Husimi-Q representation of the guiding center wavefunction.

## References and Notes

1. See supplementary materials.
2. M. Wilkinson, An exact effective Hamiltonian for a perturbed Landau level. *J. Phys. Math. Gen.* **20**, 1761–1771 (1987). [doi:10.1088/0305-4470/20/7/022](https://doi.org/10.1088/0305-4470/20/7/022)
3. Semi-classically, this incompressibility is an instance of Liouville's theorem; the quantum analog of a phase-space distribution is provided by the Wigner function, which is incompressible in the case of a quadratic Hamiltonian (48).
4. J. G. Valatin, Nucleon motion in a rotating potential. *Proc. R. Soc. London Ser. A* **238**, 132–141 (1956). [doi:10.1098/rspa.1956.0208](https://doi.org/10.1098/rspa.1956.0208)
5. A. Bohr, Rotational motion in nuclei. *Rev. Mod. Phys.* **48**, 365–374 (1976).  
[doi:10.1103/RevModPhys.48.365](https://doi.org/10.1103/RevModPhys.48.365) [Medline](#)
6. B. R. Mottelson, Elementary modes of excitation in the nucleus. *Rev. Mod. Phys.* **48**, 375–383 (1976). [doi:10.1103/RevModPhys.48.375](https://doi.org/10.1103/RevModPhys.48.375) [Medline](#)
7. R. P. Kerr, Gravitational Field of a Spinning Mass as an Example of Algebraically Special Metrics. *Phys. Rev. Lett.* **11**, 237–238 (1963). [doi:10.1103/PhysRevLett.11.237](https://doi.org/10.1103/PhysRevLett.11.237)
8. A. Maeder, G. Meynet, Rotating massive stars: From first stars to gamma ray bursts. *Rev. Mod. Phys.* **84**, 25–63 (2012). [doi:10.1103/RevModPhys.84.25](https://doi.org/10.1103/RevModPhys.84.25)
9. F. D. M. Haldane, Geometrical description of the fractional quantum Hall effect. *Phys. Rev. Lett.* **107**, 116801 (2011). [doi:10.1103/PhysRevLett.107.116801](https://doi.org/10.1103/PhysRevLett.107.116801) [Medline](#)
10. N. Cooper, Rapidly rotating atomic gases. *Adv. Phys.* **57**, 539–616 (2008).  
[doi:10.1080/00018730802564122](https://doi.org/10.1080/00018730802564122)
11. V. Schweikhard, I. Coddington, P. Engels, V. P. Mogendorff, E. A. Cornell, Rapidly rotating Bose-Einstein condensates in and near the lowest Landau level. *Phys. Rev. Lett.* **92**, 040404 (2004). [doi:10.1103/PhysRevLett.92.040404](https://doi.org/10.1103/PhysRevLett.92.040404) [Medline](#)
12. V. Bretin, S. Stock, Y. Seurin, J. Dalibard, Fast rotation of a Bose-Einstein condensate. *Phys. Rev. Lett.* **92**, 050403 (2004). [doi:10.1103/PhysRevLett.92.050403](https://doi.org/10.1103/PhysRevLett.92.050403) [Medline](#)
13. J. Dalibard, F. Gerbier, G. Juzeliūnas, P. Öhberg, Artificial gauge potentials for neutral atoms. *Rev. Mod. Phys.* **83**, 1523–1543 (2011). [doi:10.1103/RevModPhys.83.1523](https://doi.org/10.1103/RevModPhys.83.1523)
14. N. Goldman, G. Juzeliūnas, P. Öhberg, I. B. Spielman, Light-induced gauge fields for ultracold atoms. *Rep. Prog. Phys.* **77**, 126401 (2014). [doi:10.1088/0034-4885/77/12/126401](https://doi.org/10.1088/0034-4885/77/12/126401) [Medline](#)
15. V. Galitski, G. Juzeliūnas, I. B. Spielman, Artificial gauge fields with ultracold atoms. *Phys. Today* **72**, 38–44 (2019). [doi:10.1063/PT.3.4111](https://doi.org/10.1063/PT.3.4111)

16. Y.-J. Lin, R. L. Compton, K. Jiménez-García, J. V. Porto, I. B. Spielman, Synthetic magnetic fields for ultracold neutral atoms. *Nature* **462**, 628–632 (2009). [doi:10.1038/nature08609](https://doi.org/10.1038/nature08609) [Medline](#)
17. V. Galitski, I. B. Spielman, Spin-orbit coupling in quantum gases. *Nature* **494**, 49–54 (2013). [doi:10.1038/nature11841](https://doi.org/10.1038/nature11841) [Medline](#)
18. J. Struck, C. Ölschläger, M. Weinberg, P. Hauke, J. Simonet, A. Eckardt, M. Lewenstein, K. Sengstock, P. Windpassinger, Tunable gauge potential for neutral and spinless particles in driven optical lattices. *Phys. Rev. Lett.* **108**, 225304 (2012). [doi:10.1103/PhysRevLett.108.225304](https://doi.org/10.1103/PhysRevLett.108.225304) [Medline](#)
19. M. Aidelsburger, M. Atala, M. Lohse, J. T. Barreiro, B. Paredes, I. Bloch, Realization of the Hofstadter Hamiltonian with ultracold atoms in optical lattices. *Phys. Rev. Lett.* **111**, 185301 (2013). [doi:10.1103/PhysRevLett.111.185301](https://doi.org/10.1103/PhysRevLett.111.185301) [Medline](#)
20. H. Miyake, G. A. Siviloglou, C. J. Kennedy, W. C. Burton, W. Ketterle, Realizing the Harper Hamiltonian with laser-assisted tunneling in optical lattices. *Phys. Rev. Lett.* **111**, 185302 (2013). [doi:10.1103/PhysRevLett.111.185302](https://doi.org/10.1103/PhysRevLett.111.185302) [Medline](#)
21. G. Jotzu, M. Messer, R. Desbuquois, M. Lebrat, T. Uehlinger, D. Greif, T. Esslinger, Experimental realization of the topological Haldane model with ultracold fermions. *Nature* **515**, 237–240 (2014). [doi:10.1038/nature13915](https://doi.org/10.1038/nature13915) [Medline](#)
22. A. Celi, P. Massignan, J. Ruseckas, N. Goldman, I. B. Spielman, G. Juzeliūnas, M. Lewenstein, Synthetic gauge fields in synthetic dimensions. *Phys. Rev. Lett.* **112**, 043001 (2014). [doi:10.1103/PhysRevLett.112.043001](https://doi.org/10.1103/PhysRevLett.112.043001) [Medline](#)
23. M. Aidelsburger, M. Lohse, C. Schweizer, M. Atala, J. T. Barreiro, S. Nascimbène, N. R. Cooper, I. Bloch, N. Goldman, Measuring the Chern number of Hofstadter bands with ultracold bosonic atoms. *Nat. Phys.* **11**, 162–166 (2014). [doi:10.1038/nphys3171](https://doi.org/10.1038/nphys3171)
24. L. J. LeBlanc, K. Jiménez-García, R. A. Williams, M. C. Beeler, A. R. Perry, W. D. Phillips, I. B. Spielman, Observation of a superfluid Hall effect. *Proc. Natl. Acad. Sci. U.S.A.* **109**, 10811–10814 (2012). [doi:10.1073/pnas.1202579109](https://doi.org/10.1073/pnas.1202579109) [Medline](#)
25. B. K. Stuhl, H.-I. Lu, L. M. Aycock, D. Genkina, I. B. Spielman, Visualizing edge states with an atomic Bose gas in the quantum Hall regime. *Science* **349**, 1514–1518 (2015). [doi:10.1126/science.aaa8515](https://doi.org/10.1126/science.aaa8515) [Medline](#)
26. M. Mancini, G. Pagano, G. Cappellini, L. Livi, M. Rider, J. Catani, C. Sias, P. Zoller, M. Inguscio, M. Dalmonte, L. Fallani, Observation of chiral edge states with neutral fermions in synthetic Hall ribbons. *Science* **349**, 1510–1513 (2015). [doi:10.1126/science.aaa8736](https://doi.org/10.1126/science.aaa8736) [Medline](#)

27. W. Petrich, M. H. Anderson, J. R. Ensher, E. A. Cornell, Stable, Tightly Confining Magnetic Trap for Evaporative Cooling of Neutral Atoms. *Phys. Rev. Lett.* **74**, 3352–3355 (1995). [doi:10.1103/PhysRevLett.74.3352](https://doi.org/10.1103/PhysRevLett.74.3352) [Medline](#)
28. K. W. Madison, F. Chevy, V. Bretin, J. Dalibard, Stationary states of a rotating Bose-Einstein condensate: Routes to vortex nucleation. *Phys. Rev. Lett.* **86**, 4443–4446 (2001). [doi:10.1103/PhysRevLett.86.4443](https://doi.org/10.1103/PhysRevLett.86.4443) [Medline](#)
29. S. Sinha, Y. Castin, Dynamic instability of a rotating Bose-Einstein condensate. *Phys. Rev. Lett.* **87**, 190402 (2001). [doi:10.1103/PhysRevLett.87.190402](https://doi.org/10.1103/PhysRevLett.87.190402) [Medline](#)
30. A. Recati, F. Zambelli, S. Stringari, Overcritical rotation of a trapped Bose-Einstein condensate. *Phys. Rev. Lett.* **86**, 377–380 (2001). [doi:10.1103/PhysRevLett.86.377](https://doi.org/10.1103/PhysRevLett.86.377) [Medline](#)
31. G. Kirchmair, B. Vlastakis, Z. Leghtas, S. E. Nigg, H. Paik, E. Ginossar, M. Mirrahimi, L. Frunzio, S. M. Girvin, R. J. Schoelkopf, Observation of quantum state collapse and revival due to the single-photon Kerr effect. *Nature* **495**, 205–209 (2013). [doi:10.1038/nature11902](https://doi.org/10.1038/nature11902) [Medline](#)
32. R. Loudon, P. Knight, Squeezed Light. *J. Mod. Opt.* **34**, 709–759 (1987). [doi:10.1080/09500348714550721](https://doi.org/10.1080/09500348714550721)
33. H. A. Fertig, B. I. Halperin, Transmission coefficient of an electron through a saddle-point potential in a magnetic field. *Phys. Rev. B* **36**, 7969–7976 (1987). [doi:10.1103/PhysRevB.36.7969](https://doi.org/10.1103/PhysRevB.36.7969) [Medline](#)
34. S. Vishveshwara, N. R. Cooper, Correlations and beam splitters for quantum Hall anyons. *Phys. Rev. B* **81**, 201306 (2010). [doi:10.1103/PhysRevB.81.201306](https://doi.org/10.1103/PhysRevB.81.201306)
35. The hydrodynamic theory of (29) assumes a Thomas-Fermi cloud shape of radius  $R$ . A Thomas-Fermi profile has a fitted Gaussian  $e^{-1/2}$  radius of  $0.46R$ , which is the quantity shown by the red curve in Fig. 3A for direct comparison to our data.
36. N. R. Cooper, N. K. Wilkin, J. M. F. Gunn, Quantum phases of vortices in rotating Bose-Einstein condensates. *Phys. Rev. Lett.* **87**, 120405 (2001). [doi:10.1103/PhysRevLett.87.120405](https://doi.org/10.1103/PhysRevLett.87.120405) [Medline](#)
37. S. Sinha, G. V. Shlyapnikov, Two-dimensional Bose-Einstein condensate under extreme rotation. *Phys. Rev. Lett.* **94**, 150401 (2005). [doi:10.1103/PhysRevLett.94.150401](https://doi.org/10.1103/PhysRevLett.94.150401) [Medline](#)
38. X. Chen, Z.-C. Gu, Z.-X. Liu, X.-G. Wen, Symmetry-protected topological orders in interacting bosonic systems. *Science* **338**, 1604–1606 (2012). [doi:10.1126/science.1227224](https://doi.org/10.1126/science.1227224) [Medline](#)
39. T. Senthil, M. Levin, Integer quantum Hall effect for bosons. *Phys. Rev. Lett.* **110**, 046801 (2013). [doi:10.1103/PhysRevLett.110.046801](https://doi.org/10.1103/PhysRevLett.110.046801) [Medline](#)

40. A. Vishwanath, T. Senthil, Physics of Three-Dimensional Bosonic Topological Insulators: Surface-Deconfined Criticality and Quantized Magnetoelectric Effect. *Phys. Rev. X* **3**, 011016 (2013). [doi:10.1103/PhysRevX.3.011016](https://doi.org/10.1103/PhysRevX.3.011016)
41. F. Zambelli, S. Stringari, Moment of inertia and quadrupole response function of a trapped superfluid. *Phys. Rev. A* **63**, 033602 (2001). [doi:10.1103/PhysRevA.63.033602](https://doi.org/10.1103/PhysRevA.63.033602)
42. A. Aftalion, X. Blanc, N. Lerner, Fast rotating condensates in an asymmetric harmonic trap. *Phys. Rev. A* **79**, 011603 (2009). [doi:10.1103/PhysRevA.79.011603](https://doi.org/10.1103/PhysRevA.79.011603)
43. P. Engels, I. Coddington, P. C. Haljan, E. A. Cornell, Nonequilibrium effects of anisotropic compression applied to vortex lattices in bose-einstein condensates. *Phys. Rev. Lett.* **89**, 100403 (2002). [doi:10.1103/PhysRevLett.89.100403](https://doi.org/10.1103/PhysRevLett.89.100403) [Medline](#)
44. M. Cozzini, S. Stringari, Macroscopic dynamics of a Bose-Einstein condensate containing a vortex lattice. *Phys. Rev. A* **67**, 041602 (2003). [doi:10.1103/PhysRevA.67.041602](https://doi.org/10.1103/PhysRevA.67.041602)
45. S. M. Girvin, A. H. MacDonald, P. M. Platzman, Collective-excitation gap in the fractional quantum Hall effect. *Phys. Rev. Lett.* **54**, 581–583 (1985).  
[doi:10.1103/PhysRevLett.54.581](https://doi.org/10.1103/PhysRevLett.54.581) [Medline](#)
46. M. O. Oktel, Vortex lattice of a Bose-Einstein condensate in a rotating anisotropic trap. *Phys. Rev. A* **69**, 023618 (2004). [doi:10.1103/PhysRevA.69.023618](https://doi.org/10.1103/PhysRevA.69.023618)
47. D. J. Wineland, J. J. Bollinger, W. M. Itano, D. J. Heinzen, Squeezed atomic states and projection noise in spectroscopy. *Phys. Rev. A* **50**, 67–88 (1994).  
[doi:10.1103/PhysRevA.50.67](https://doi.org/10.1103/PhysRevA.50.67) [Medline](#)
48. J. E. Moyal, Quantum mechanics as a statistical theory. *Math. Proc. Camb. Philos. Soc.* **45**, 99–124 (1949). [doi:10.1017/S0305004100000487](https://doi.org/10.1017/S0305004100000487)
49. R. J. Fletcher *et al.*, Replication data for “Geometric squeezing into the lowest Landau level”. Harvard Dataverse (2021); DOI: 10.7910/DVN/I2PEGZ.
50. R. P. Feynman, in *Progress in Low Temperature Physics*, C. J. Gorter, Ed. (North-Holland, 1955), vol. 1, p. 17.
51. C. Pethick, H. Smith, *Bose-Einstein Condensation in Dilute Gases* (Cambridge Univ. Press, 2002).
52. C. Robens, S. Brakhane, W. Alt, F. Kleißler, D. Meschede, G. Moon, G. Ramola, A. Alberti, High numerical aperture ( $NA = 0.92$ ) objective lens for imaging and addressing of cold atoms. *Opt. Lett.* **42**, 1043–1046 (2017). [doi:10.1364/OL.42.001043](https://doi.org/10.1364/OL.42.001043) [Medline](#)
53. K. E. Wilson, Z. L. Newman, J. D. Lowney, B. P. Anderson, *In situ* imaging of vortices in Bose-Einstein condensates. *Phys. Rev. A* **91**, 023621 (2015).  
[doi:10.1103/PhysRevA.91.023621](https://doi.org/10.1103/PhysRevA.91.023621)

54. S. W. Seo, S. Kang, W. J. Kwon, Y. I. Shin, Half-Quantum Vortices in an Antiferromagnetic Spinor Bose-Einstein Condensate. *Phys. Rev. Lett.* **115**, 015301 (2015).  
[doi:10.1103/PhysRevLett.115.015301](https://doi.org/10.1103/PhysRevLett.115.015301) [Medline](#)
55. B. P. Anderson, P. C. Haljan, C. E. Wieman, E. A. Cornell, Vortex precession in Bose-Einstein condensates: Observations with filled and empty cores. *Phys. Rev. Lett.* **85**, 2857–2860 (2000). [doi:10.1103/PhysRevLett.85.2857](https://doi.org/10.1103/PhysRevLett.85.2857) [Medline](#)
56. P. Engels, I. Coddington, P. C. Haljan, V. Schweikhard, E. A. Cornell, Observation of long-lived vortex aggregates in rapidly rotating Bose-Einstein condensates. *Phys. Rev. Lett.* **90**, 170405 (2003). [doi:10.1103/PhysRevLett.90.170405](https://doi.org/10.1103/PhysRevLett.90.170405) [Medline](#)
57. D. Tong, The Quantum Hall Effect. arXiv 1606.06687 [hep-th] (20 September 2016).
58. R. Gilmore, *Lie Groups, Physics, and Geometry: An Introduction for Physicists, Engineers and Chemists* (Cambridge Univ. Press, 2008).
59. Y. Chen, G. Jiang, R. R. Biswas, Geometric response of quantum Hall states to electric fields. *Phys. Rev. B* **103**, 155303 (2021). [doi:10.1103/PhysRevB.103.155303](https://doi.org/10.1103/PhysRevB.103.155303)



## Appendix G

# Crystallization of bosonic quantum Hall states in a rotating quantum gas

This appendix contains a reprint of Ref. [129]:

# Crystallization of bosonic quantum Hall states in a rotating quantum gas

<https://doi.org/10.1038/s41586-021-04170-2>

Received: 21 June 2021

Accepted: 21 October 2021

Published online: 5 January 2022

 Check for updates

Biswaroop Mukherjee<sup>1</sup>, Airlia Shaffer<sup>1</sup>, Parth B. Patel<sup>1</sup>, Zhenjie Yan<sup>1</sup>, Cedric C. Wilson<sup>1</sup>, Valentin Crépel<sup>1</sup>, Richard J. Fletcher<sup>1</sup> & Martin Zwierlein<sup>1</sup>✉

The dominance of interactions over kinetic energy lies at the heart of strongly correlated quantum matter, from fractional quantum Hall liquids<sup>1</sup>, to atoms in optical lattices<sup>2</sup> and twisted bilayer graphene<sup>3</sup>. Crystalline phases often compete with correlated quantum liquids, and transitions between them occur when the energy cost of forming a density wave approaches zero. A prime example occurs for electrons in high-strength magnetic fields, where the instability of quantum Hall liquids towards a Wigner crystal<sup>4–9</sup> is heralded by a roton-like softening of density modulations at the magnetic length<sup>7,10–12</sup>. Remarkably, interacting bosons in a gauge field are also expected to form analogous liquid and crystalline states<sup>13–21</sup>. However, combining interactions with strong synthetic magnetic fields has been a challenge for experiments on bosonic quantum gases<sup>18,21</sup>. Here we study the purely interaction-driven dynamics of a Landau gauge Bose–Einstein condensate<sup>22</sup> in and near the lowest Landau level. We observe a spontaneous crystallization driven by condensation of magneto-rotons<sup>7,10</sup>, excitations visible as density modulations at the magnetic length. Increasing the cloud density smoothly connects this behaviour to a quantum version of the Kelvin–Helmholtz hydrodynamic instability, driven by the sheared internal flow profile of the rapidly rotating condensate. At long times the condensate self-organizes into a persistent array of droplets separated by vortex streets, which are stabilized by a balance of interactions and effective magnetic forces.

When electrons are placed in a magnetic field, their kinetic energy is quenched. The single particle states form discrete, highly degenerate Landau levels, and correspond to wavepackets localized to the magnetic length  $\ell_B$ . In the presence of interactions between electrons, owing to the absence of kinetic energy, one naturally expects the formation of a Wigner crystal of periodicity  $\sim \ell_B$  (refs. <sup>4–6,8,9,23</sup>). Famously, however, the interplay of the macroscopic degeneracy and interactions instead typically favours the strongly correlated fractional quantum Hall liquids, which host fractional charges, anyonic exchange statistics and topologically protected transport properties<sup>1</sup>. The tendency to crystallize is still apparent in a pronounced minimum in the collective excitation spectrum at wavevectors  $k \sim 1/\ell_B$  (refs. <sup>7,10–12</sup>). In analogy with the roton minimum in <sup>4</sup>He, also considered a precursor of solidification<sup>24</sup>, these excitations are called magneto-rotons<sup>7,11,12</sup>.

The fate of interacting bosons in the presence of a gauge field is of fundamental importance in the classification of topological states of matter<sup>19</sup>. Quantum Hall states<sup>13,16,20</sup>, exotic vortex lattices<sup>14</sup> and vortex-free states under extreme fields<sup>17</sup> were predicted. Quantum phase transitions between such states were found to be signalled by the softening of a roton-like collective mode<sup>15,25</sup>.

Bosonic quantum gases in artificial magnetic fields<sup>18,21</sup> have been generated via spin–orbit coupling<sup>21,26,27</sup>, phase imprinting in lattices<sup>28–32</sup> and by rotation of the trapped gas<sup>16,22,33,34</sup>. The latter approach uses the analogy between the Lorentz force on a charged particle in a magnetic field, and the Coriolis force on a massive particle in a frame rotating at

frequency  $\Omega$ , giving  $\omega_c = 2\Omega$  and  $\ell_B = \sqrt{\hbar/(m\omega_c)}$  as the rotational analogue of the cyclotron frequency and the magnetic length, respectively.

Signatures of physics near the lowest Landau level (LLL) have been observed in rotating Bose gases<sup>33,34</sup>. In recent work at MIT, condensates have been prepared directly in the lowest Landau gauge wavefunction using geometric squeezing<sup>22</sup>. In this mean-field quantum Hall regime<sup>13</sup>, all bosons occupy a single wavefunction, whose subsequent dynamics subject to a gauge field can be studied, offering a microscopic insight into the individual building blocks of quantum Hall systems. An advantage of rotation is that the interactions between atoms are decoupled from the induced gauge potential, in contrast to other methods for which the effective magnetic field appears within a dressed-atom picture, leading to additional unwanted interaction terms<sup>35</sup>.

Here we directly observe the evolution of an interacting Bose–Einstein condensate occupying a single Landau gauge wavefunction in the LLL. We find that the Landau gauge condensate is unstable under the influence of interactions, exhibiting spontaneous growth of a snaking mode leading to a persistent density wave order at the magnetic length  $\ell_B$  as illustrated in Fig. 1. At the heart of this crystallization is the coupling between the relative momentum and spatial overlap of two particles in a gauge field. This lowers the interaction energy cost of populating higher-momentum states, and leads to the dynamical instability of the lowest (Goldstone) collective excitation branch<sup>15</sup> (see Supplementary Information). The ensuing proliferation of excitations at momenta near

<sup>1</sup>MIT-Harvard Center for Ultracold Atoms, Research Laboratory of Electronics, Department of Physics, Massachusetts Institute of Technology, Cambridge, MA, USA. ✉e-mail: zwierlein@mit.edu

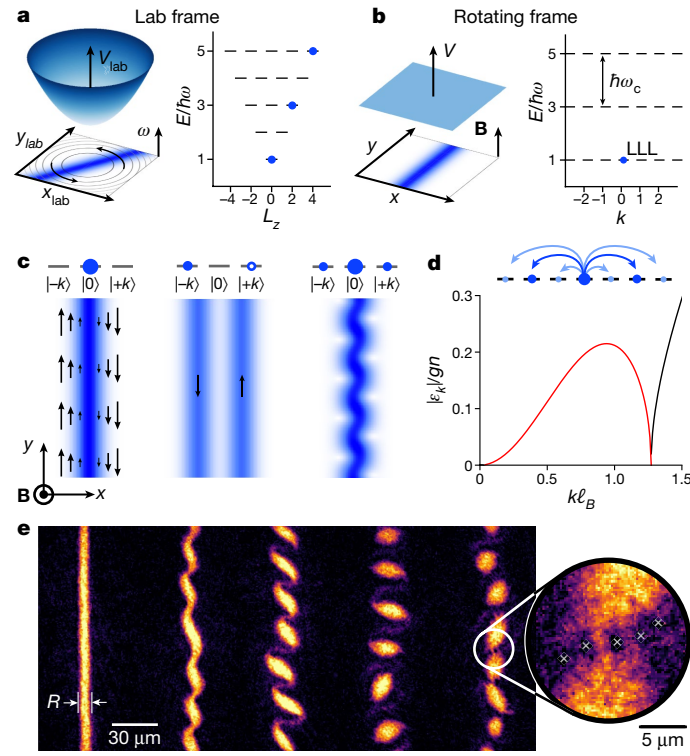


**Fig. 1 | Spontaneous crystallization of an interacting Bose–Einstein condensate in an artificial magnetic field.** **a**, In the laboratory frame, the condensate freely rotates in a circularly symmetric harmonic trap at the trapping frequency  $\omega$ . Occupied states in the energy spectrum are sketched ( $L_z$ , angular momentum). **b**, In the rotating frame, the condensate experiences an effective magnetic field  $B$  but no scalar potential. The energy spectrum is flattened into Landau levels ( $k$ , momentum along  $y$ ). Only the  $k = 0$  Landau gauge wavefunction is occupied. **c**, The irrotationality of the condensate in the laboratory frame imposes a sheared velocity profile in the rotating frame, which is dynamically unstable towards a periodic density modulation. Motion with momentum  $\hbar k$  along the  $y$ -direction is tied to sideways displacement of the wavefunction along  $x$ . The reduced overlap of  $|k\rangle > 0$  states with the  $k = 0$  condensate lowers the interaction energy cost of collective excitations, leading to spontaneous population of  $\pm k$  pairs whose interference with the condensate results in a density modulation. **d**, This dynamical instability is reflected in a (Goldstone) collective excitation branch, which is imaginary across a range of wavevectors, shown by a red line. The spectrum shown is calculated for a condensate in the LLL, for which the interaction energy  $gn$  provides the only relevant energy scale and the magnetic length  $\ell_B = 1.6 \mu\text{m}$  sets the lengthscale. Here  $g$  is the mean-field coupling constant, and  $n = n_{2D}(0)$  is the peak two-dimensional density. **e**, Absorption images of the evolution of the condensate density in the rotating frame, displaying a snake-like instability and the formation of droplet arrays. Here the cloud width is  $R = 2.34\ell_B$ , and the frames are taken at 0, 5, 6.2, 8.5 and 10 cyclotron periods ( $2\pi/\omega_c = 5.6 \text{ ms}$ ). The magnification reveals vortex streets between adjacent droplets (grey crosses), indicating counterflow at their interface.

$\hbar/\ell_B$  can be viewed as condensation of magneto-rotons, in analogy with the Wigner crystal instability of quantum Hall systems<sup>4–9</sup>.

Condensation at non-zero momentum has been predicted in superfluid helium above a critical velocity<sup>36–38</sup>. Roton-like excitations and instabilities in Bose–Einstein condensates have been induced via cavity-mediated interactions<sup>39,40</sup>, spin–orbit coupling<sup>41,42</sup>, shaken optical lattices<sup>43,44</sup>, driven interactions<sup>45</sup> and dipolar interactions<sup>46–48</sup>. These instabilities are tightly connected to evidence for supersolidity, the simultaneous existence of spatial and superfluid order<sup>38,40,42,49–51</sup>. In our case, the instability of density-wave order arises purely from the interplay of contact interactions and a gauge field. No external

drive is present, nor is there any residual scalar potential in the rotating frame. The absence of kinetic energy in the LLL directly implies that the crystallization rate is set solely by the interaction energy of the gas.

By increasing the condensate density such that many Landau levels become populated, we observe a crossover from LLL behaviour to a hydrodynamic instability driven by the sheared internal velocity profile. Analogous phenomena are ubiquitous throughout hydrodynamics, from the diocotron instability in charged plasmas<sup>52</sup> and fragmentation of electron beams<sup>53</sup>, to the Kelvin–Helmholtz instability in atmospheric and astrophysical systems<sup>54,55</sup>. In the context of superfluids, for which the circulation is quantized, the Kelvin–Helmholtz instability has been detected in liquid helium<sup>56</sup>, and theoretically predicted at the boundary between counterflowing condensates<sup>57</sup>. In our superfluid hydrodynamic setting, we directly observe streets of quantized vortices separating emergent droplets, revealing the quantum nature of the instability at the most microscopic level.

To analyse the instability, consider the condensate in the frame rotating at the frequency  $\omega$  of the isotropic harmonic trap, where it experiences a synthetic magnetic field but no scalar potential (see Fig. 1a, b), and thus evolves under the Hamiltonian

$$\hat{H} = \int d^2r \hat{\psi}^\dagger \left[ \frac{(\hat{\mathbf{p}} - q\mathbf{A})^2}{2m} + \frac{g}{2} \hat{\psi}^\dagger \hat{\psi} \right] \hat{\psi}. \quad (1)$$

Here  $\hat{\psi}^\dagger(\mathbf{r})$  is the bosonic field operator,  $\hat{\mathbf{p}}$  is the canonical momentum,  $q$  and  $\mathbf{A}$  are the charge and vector potential in the equivalent magnetic problem, and  $g$  is the two-dimensional mean-field coupling constant. Geometric squeezing prepares a translationally invariant condensate most conveniently described within the Landau gauge  $q\mathbf{A} = (0, m\omega_c x)$  (ref. <sup>22</sup>) for which the Hamiltonian becomes

$$\hat{H} = \int d^2r \hat{\psi}^\dagger \left[ \frac{\hat{p}_x^2}{2m} + \frac{1}{2} m\omega_c^2 \left( \hat{x} - \frac{\hat{p}_y \ell_B^2}{\hbar} \right)^2 + \frac{g}{2} \hat{\psi}^\dagger \hat{\psi} \right] \hat{\psi}. \quad (2)$$

Cyclotron motion of the atoms is reflected in an effective harmonic oscillator along the  $x$ -direction of frequency  $\omega_c = 2\omega$ , the non-interacting energy states of which correspond to different Landau levels (see Fig. 1b). Each level is macroscopically degenerate since it costs no energy to translate the centres of cyclotron orbits. Initially, the  $y$  momentum of all atoms is zero, and their cyclotron motion is centred at  $x = 0$  with a two-dimensional number density  $n_{2D}(x)$ . The condensate has uniform phase and thus features a sheared velocity profile  $\mathbf{v} = -q\mathbf{A}/m = (0, -\omega_c x)$  proportional to the vector potential (see Fig. 1c). We parameterize the crossover from LLL to hydrodynamic behaviour by the ratio  $\frac{gn}{\hbar\omega_c}$ , the condensate's mean-field energy of  $\sim gn$  to the Landau level spacing  $\hbar\omega_c$ , giving a measure for the number of occupied Landau levels<sup>22,33</sup>. Here  $n = n_{2D}(0)$  is the peak density. In our experiment  $\frac{gn}{\hbar\omega_c}$  varies from 0.6 to 7.3, corresponding to a central filling fraction  $n\ell_B^2$  of 50 and higher, meaning the condensate lies within the mean-field quantum Hall regime<sup>13,16</sup>.

The dynamical instability illustrated in Fig. 1 can be understood in the low- and high-density limits as follows. When  $gn \lesssim \hbar\omega_c$ , the condensate is restricted to the LLL and shows a Gaussian transverse density profile with a 1/e radius of  $\ell_B$  (ref. <sup>22</sup>; see Supplementary Information). A Bogoliubov analysis around this state generically results in a Hamiltonian of the form<sup>15</sup>

$$\hat{H}_{\text{LLL}} = \sum_{k>0} A_k (\hat{a}_k^\dagger \hat{a}_k + \hat{a}_{-k}^\dagger \hat{a}_{-k}) + B_k (\hat{a}_k^\dagger \hat{a}_{-k}^\dagger + \hat{a}_k \hat{a}_{-k}), \quad (3)$$

where  $\hat{a}_k$  is the annihilation operator for a particle with momentum  $\hbar k$  along the  $y$ -direction. This Hamiltonian describes pairs of modes  $\pm k$  with natural frequency  $A_k/\hbar$  and coupled by a pair-creation operator of strength  $B_k$ , which corresponds to a two-mode squeezing interaction

# Article

in the language of quantum optics. In a non-rotating uniform condensate,  $A_k = \frac{\hbar^2 k^2}{2m} + gn$  and  $B_k = gn$  (ref. <sup>58</sup>), and hence pair creation is always weaker than the mode energy, leading to stable excitations. However, the effective magnetic field profoundly changes this picture. First, in the LLL there is no kinetic energy contribution to  $A_k$ . Second, as illustrated in Fig. 1c, the coupling between momentum and position means that states with  $k \neq 0$  have a reduced overlap with the condensate and a correspondingly lower interaction energy. One finds<sup>15</sup>  $A_k = gn[2\exp(-k^2\ell_B^2/2) - 1]/\sqrt{2}$  and  $B_k = gn\exp(-k^2\ell_B^2)/\sqrt{2}$ , and the resulting dispersion  $\varepsilon_k = \sqrt{|A_k|^2 - |B_k|^2}$  is shown in Fig. 1d. The spectrum is imaginary for an entire range of wavevectors  $k > 0$  beyond the zero-energy Goldstone mode at  $k = 0$ , indicating dynamical instability of the Goldstone branch and correlated exponential growth of  $\pm k$  pairs of these modes. Their interference with the  $k = 0$  condensate results in a density modulation (see Fig. 1c). The fastest growth occurs at a wavevector  $-1/\ell_B$  giving a spatial modulation wavelength  $\sim 2\pi$  times the magnetic length. This mode eventually becomes macroscopically occupied, corresponding to condensation of magneto-rotons and yielding a density modulation contrast of order unity. Crucially, since interactions provide the only energy scale in the LLL, the instability growth rate is determined purely by the interaction energy  $gn$ .

In the high-density limit where  $gn \gg \hbar\omega_c$ , a hydrodynamic description that neglects quantum pressure is valid. In this regime, the condensate initially exhibits a Thomas–Fermi density profile  $n_{2D} \propto 1 - x^2/R_{TF}^2$  where  $R_{TF} = \sqrt{\frac{2gn}{m\omega_c^2}} = \sqrt{\frac{2gn}{m\omega_c}} \ell_B$  (ref. <sup>59</sup>; see Supplementary Information).

The Coriolis force  $2mv \times \Omega$  on each fluid element resulting from the shear flow  $v = (0, -\omega_c x)$  perfectly balances the local gradient of mean-field energy, resulting in an inhomogeneous equilibrium density despite the absence of any scalar potential. Our hydrodynamic stability analysis about this equilibrium state reveals a dynamical snaking instability of the cloud (see Supplementary Information), in analogy with the Kelvin–Helmholtz instability of counterflow in fluid layers<sup>54,55</sup>, and the diocotron instability of charged plasmas and electron beams<sup>52,53</sup>. The absence of quantum pressure means that the Thomas–Fermi radius and cyclotron frequency provide the only lengthscale and rate. Within the hydrodynamic analysis the instability develops at a wavevector set by the condensate width, as in the LLL, but at a density-independent rate proportional to  $\omega_c$ , in striking qualitative contrast to the growth rate in the LLL.

From these arguments, for all condensate densities we anticipate an emergent density modulation with a lengthscale set by the width of the initial cloud. For a quantitative analysis, from our experimental images (see Fig. 1e) we obtain the static structure factor  $S_k \equiv |n_k|^2/N$ , where  $n_k = \int dy n_{1D}(y)e^{-iky}$  is the Fourier transform of the one-dimensional number density  $n_{1D}(y)$  and  $N = \int dy n_{1D}(y)$  (ref. <sup>47</sup>). In Fig. 2a we show examples of  $S_k$  obtained once the density modulation has fully developed, which show a well defined peak at a wavevector  $k_{\max}$ . We attribute the much smaller secondary peak at  $2k_{\max}$  to the contiguous traces of condensate linking adjacent droplets. In Fig. 2c we show  $k_{\max}$  as a function of the condensate density, which is parameterized by the ratio  $R/\ell_B$  where  $R$  is the full-width at half-maximum of the initial cloud divided by  $2\sqrt{\log 2}$ . This normalization is chosen such that  $R/\ell_B \rightarrow 1$  for vanishing  $gn$ , and in the high-density limit  $R/\ell_B = \sqrt{gn/(\hbar\omega_c \log 2)}$ . At all densities, we indeed find an instability lengthscale of order the cloud width,  $k_{\max} \sim 1/R$ . The star indicates the LLL prediction  $k_{\max} = 0.98/\ell_B$  and the dashed line shows the hydrodynamic result  $k_{\max} = 0.95/R$  neglecting quantum pressure (see Supplementary Information). The solid line presents  $k_{\max}$  that we obtain from a numerical solution of the Bogoliubov equations (see Supplementary Information) showing excellent agreement with the data without any free parameters.

Although the cloud width sets the instability lengthscale in both the LLL and hydrodynamic regimes, the growth rate shows qualitatively different behaviour. In Fig. 3a, we show  $S_k$  as a function of time for several

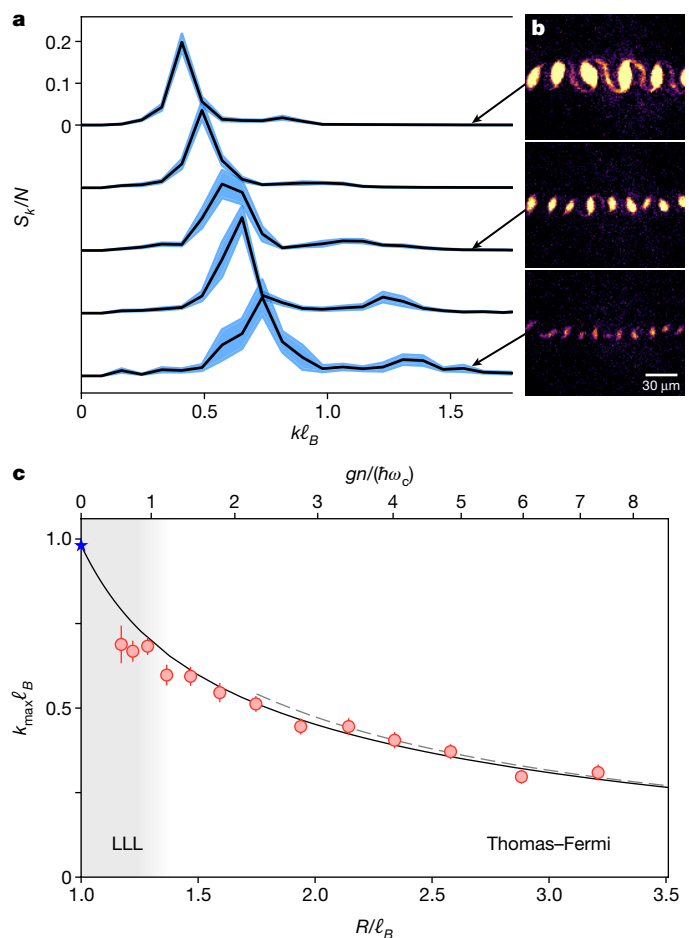


**Fig. 2 | Structure factor and lengthscale of the emergent crystal.** **a**, The static structure factor,  $S_k$ , measured once the density modulation has reached steady state for condensates with initial widths  $R/\ell_B = 2.58, 1.75, 1.59, 1.28$  and  $1.02$  (top to bottom). The prominent peak reflects the periodic modulation of the cloud density. **b**, Corresponding images of the steady-state crystal, illustrating the decrease in the modulation lengthscale with falling condensate density. **c**, Dependence of the dominant modulation wavevector,  $k_{\max}$ , on the cloud width,  $R/\ell_B$ . The LLL and hydrodynamic results are indicated by the star and dashed line, respectively (see text). The solid line shows the prediction of our Bogoliubov analysis (see Supplementary Information), which shows excellent agreement with our data with no free parameters.

different condensate densities. In addition to the decrease in the instability lengthscale at lower densities, we observe a concurrent reduction of the growth rate. At each wavevector we fit the time evolution of the structure factor with the theoretically expected function  $S_k(t) = \text{Acosh}(2t)$  (see Supplementary Information), and extract the instability growth rate  $\Gamma(k)$ . This is reported in Fig. 3b, along with the imaginary component of the corresponding Bogoliubov spectrum, which shows good agreement without any free parameters. We note that the experimental data also reveal some growth in  $S_k$  at higher wavevectors than the unstable region predicted by the linear Bogoliubov analysis. We attribute this to nonlinear effects, and have performed numerical simulations of the Gross–Pitaevskii equation, finding that these exhibit the same behaviour (see Supplementary Information).

We capture the typical crystallization rate corresponding to a particular condensate density by the growth rate of the dominant instability,  $\Gamma(k_{\max})$ , and in Fig. 3c plot this as a function of  $R/\ell_B$ . When  $R/\ell_B \gg 1$  the rate is density-independent and consistent with our hydrodynamic result  $\Gamma = 0.14\omega_c$ , shown by the dashed line. However, for lower interaction energies the gas enters the LLL where  $gn$  provides the only energy scale. We observe a concurrent slowing down of the instability, and the data

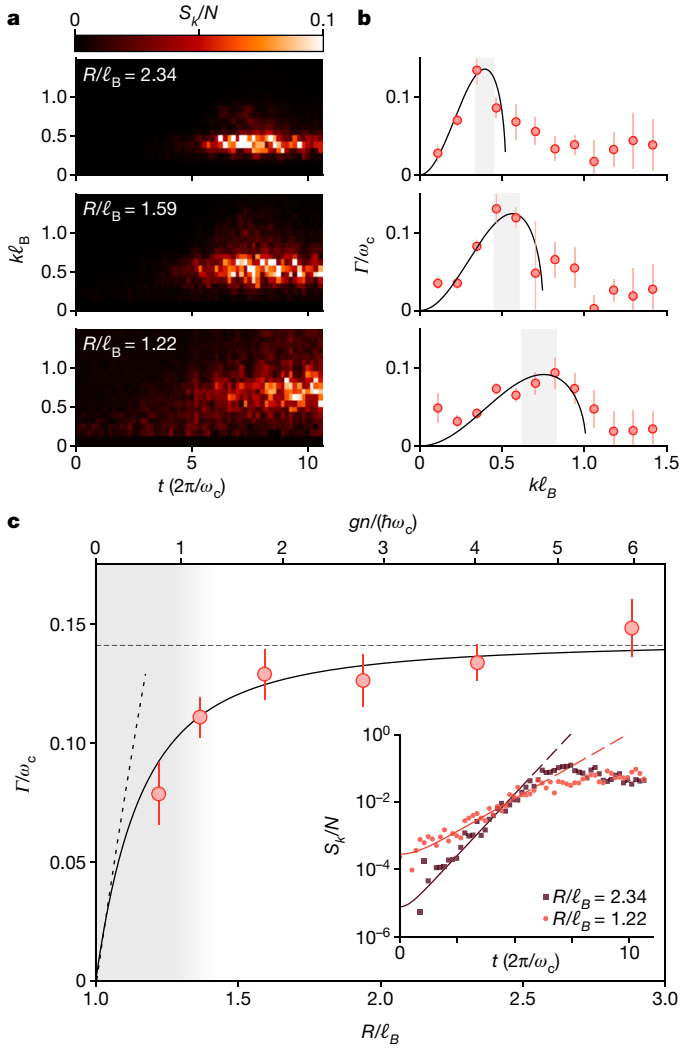


**Fig. 3 | Instability growth dynamics.** **a**, The temporal evolution of the static structure factor,  $S_k(t)$ , for condensates with different initial widths, which reveals a density dependence of both the modulation lengthscale and the growth rate. **b**, The measured instability growth rate,  $\Gamma$ , as a function of wavevector. The solid line shows the rate obtained from our Bogoliubov analysis (see Supplementary Information) and captures the data well with no free parameters. **c**, The instability growth rate at the dominant unstable wavevector shown as a function of the condensate width. The growth rate is obtained by averaging points from the shaded regions in **b**. At high densities we find good agreement with the density-independent hydrodynamic rate  $\Gamma = 0.14\omega_c$  (dashed line). As the density falls, we observe a crossover to the LLL scaling  $\Gamma = 0.21gn/\hbar$  (dotted line). Solid line, Bogoliubov analysis (see Supplementary Information). The inset shows  $S_k(t)$  at  $k_{\max}$  for condensates in the hydrodynamic regime (dark red) and the LLL (light red), along with the corresponding fits used to extract the rate (see text).

approach the LLL prediction  $\Gamma = 0.21gn/\hbar$  indicated by a dotted line. At all densities, the data show good agreement with the rate obtained from our Bogoliubov analysis, reported as the solid line.

After its initial hyperbolic growth,  $S_k$  reaches a steady state, as shown in the inset of Fig. 3c. The emergent crystal is long-lived, with each droplet stabilized by a balance of the outward mean-field pressure and an inwards Coriolis force. This arises from the circulating flow within each droplet which is imposed by the gauge field, and is evident from vortices intersecting adjacent droplets (see Fig. 1e). The counterflow speed at the interface of two droplets of radius  $R$  is  $\sim\omega_cR$ , giving a gradient of  $m\omega_cR/\hbar$  in the relative phase and a vortex spacing of  $2\pi\ell_B^2/R$ . Adjacent droplets are therefore separated by  $\sim(R/\ell_B)^2$  vortices. In the limit

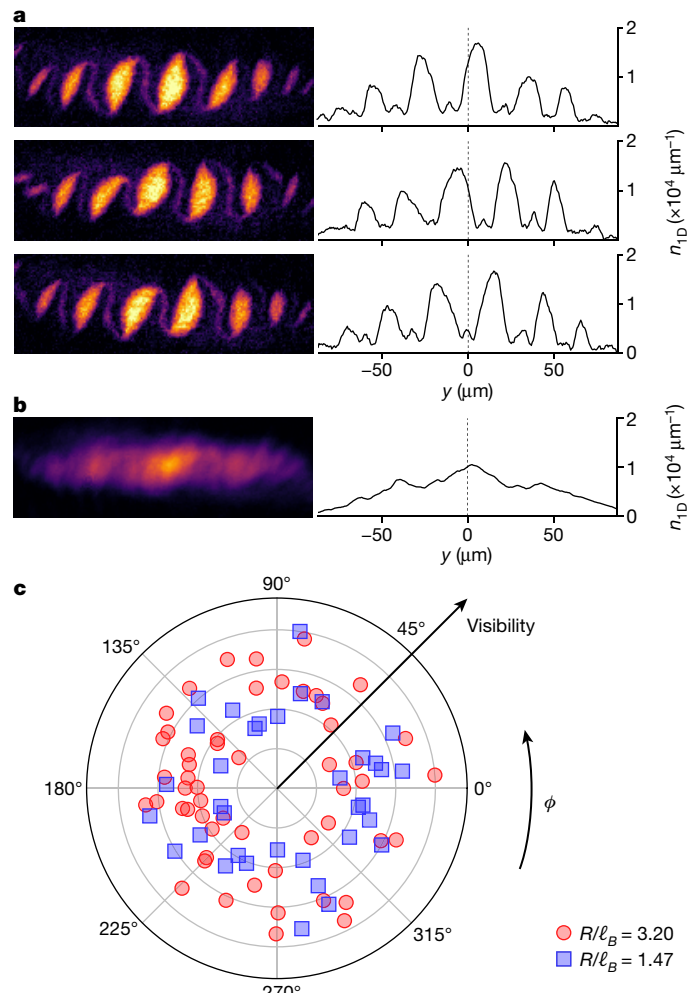


**Fig. 4 | Spontaneous breaking of translational symmetry.** **a**, Images of the emergent crystal in three experimental iterations, along with the integrated one-dimensional density profiles  $n_{1D}(y)$ . The vertical dashed line shows the position of the centre-of-mass of the cloud, relative to which the modulation phase is random. **b**, An image of the cloud averaged over 60 iterations, in which the density modulation is no longer visible. **c**, The phase,  $\phi$ , and visibility of the density modulation measured for multiple iterations of the experiment, for two different initial condensate densities. The visibility appears largely independent of the phase chosen by the modulation. The phase is randomly distributed between 0 and  $2\pi$ , indicating spontaneous breaking of the initial translational symmetry of the cloud.

of classical hydrodynamics this number is large and the quantization of circulation is irrelevant, whereas in the LLL adjacent droplets are separated by a single vortex<sup>15</sup>.

Although the dynamical instability drives the growth of a density modulation, the initial seeding of the unstable mode must arise from thermal or quantum fluctuations in the gas density at  $t = 0$  (see Supplementary Information). Since the phase of these fluctuations is random, this results in spontaneous breaking of the initial translational symmetry of the condensate. In Fig. 4 we show the phase and visibility of the density modulation observed in different iterations of our experiment. To account for small fluctuations in the overall cloud position, we fit the one-dimensional density profile with a sinusoidal function modulated by a Gaussian envelope, and obtain the modulation phase  $\phi$  relative to the centre of mass of the cloud. At all densities we find that the phase is uncorrelated between different experimental realizations, indicating spontaneous breaking of the initial translational symmetry.

The emergent crystallization observed here offers a pristine example of collective physics arising purely from the interplay of interparticle interactions and a gauge field. The steady state breaks both the  $U(1)$  symmetry associated with the phase of the wavefunction and translational symmetry, and thus displays supersolid properties<sup>38</sup>. A natural immediate direction concerns the Goldstone mode associated with the spontaneous breaking of translational symmetry, corresponding to magneto-phonons in the droplet array<sup>9</sup>. This would be a remarkable instance of a propagating mode arising intrinsically from interactions, in the absence of any single-particle dynamics. Although the densities in our experiment correspond to tens of atoms per flux quantum, our protocol can be straightforwardly extended to prepare clouds of lower filling fractions, which are expected to host beyond-mean-field, strongly correlated bosonic quantum Hall states<sup>13–17,19,20,59</sup>.

## Online content

Any methods, additional references, Nature Research reporting summaries, source data, extended data, supplementary information, acknowledgements, peer review information; details of author contributions and competing interests; and statements of data and code availability are available at <https://doi.org/10.1038/s41586-021-04170-2>.

1. Stormer, H. L., Tsui, D. C. & Gossard, A. C. The fractional quantum Hall effect. *Rev. Mod. Phys.* **71**, S298–S305 (1999).
2. Bloch, I., Dalibard, J. & Zwerger, W. Many-body physics with ultracold gases. *Rev. Mod. Phys.* **80**, 885–964 (2008).
3. Cao, Y. et al. Unconventional superconductivity in magic-angle graphene superlattices. *Nature* **556**, 43–50 (2018).
4. Wigner, E. On the interaction of electrons in metals. *Phys. Rev.* **46**, 1002–1011 (1934).
5. Yoshioka, D. & Fukuyama, H. Charge density wave state of two-dimensional electrons in strong magnetic fields. *J. Phys. Soc. Jpn.* **47**, 394–402 (1979).
6. Lam, P. K. & Girvin, S. M. Liquid–solid transition and the fractional quantum-Hall effect. *Phys. Rev. B* **30**, 473–475 (1984).
7. Girvin, S. M., MacDonald, A. H. & Platzman, P. M. Magneto-roton theory of collective excitations in the fractional quantum Hall effect. *Phys. Rev. B* **33**, 2481–2494 (1986).
8. Jiang, H. W. et al. Quantum liquid versus electron solid around  $v = 1/5$  Landau-level filling. *Phys. Rev. Lett.* **65**, 633–636 (1990).
9. Jang, J., Hunt, B. M., Pfeiffer, L. N., West, K. W. & Ashoori, R. C. Sharp tunnelling resonance from the vibrations of an electronic Wigner crystal. *Nat. Phys.* **13**, 340–344 (2017).
10. Haldane, F. D. M. & Rezayi, E. H. Finite-size studies of the incompressible state of the fractionally quantized Hall effect and its excitations. *Phys. Rev. Lett.* **54**, 237–240 (1985).
11. Pinczuk, A., Dennis, B. S., Pfeiffer, L. N. & West, K. Observation of collective excitations in the fractional quantum Hall effect. *Phys. Rev. Lett.* **70**, 3983–3986 (1993).
12. Kukushkin, I. V., Smet, J. H., Scarola, V. W., Umansky, V. & von Klitzing, K. Dispersion of the excitations of fractional quantum Hall states. *Science* **324**, 1044–1047 (2009).
13. Ho, T.-L. Bose–Einstein condensates with large number of vortices. *Phys. Rev. Lett.* **87**, 060403 (2001).
14. Oktel, M. Ö. Vortex lattice of a Bose–Einstein condensate in a rotating anisotropic trap. *Phys. Rev. A* **69**, 023618 (2004).
15. Sinha, S. & Shlyapnikov, G. V. Two-dimensional Bose–Einstein condensate under extreme rotation. *Phys. Rev. Lett.* **94**, 150401 (2005).
16. Cooper, N. R. Rapidly rotating atomic gases. *Adv. Phys.* **57**, 539–616 (2008).
17. Aftalion, A., Blanc, X. & Lerner, N. Fast rotating condensates in an asymmetric harmonic trap. *Phys. Rev. A* **79**, 011603 (2009).
18. Dalibard, J., Gerbier, F., Juzeliūnas, G. & Öhberg, P. Artificial gauge potentials for neutral atoms. *Rev. Mod. Phys.* **83**, 1523–1543 (2011).
19. Chen, X., Gu, Z.-C., Liu, Z.-X. & Wen, X.-G. Symmetry-protected topological orders in interacting bosonic systems. *Science* **338**, 1604–1606 (2012).
20. Senthil, T. & Levin, M. Integer quantum Hall effect for bosons. *Phys. Rev. Lett.* **110**, 046801 (2013).
21. Goldman, N., Juzeliūnas, G., Öhberg, P. & Spielman, I. B. Light-induced gauge fields for ultracold atoms. *Rep. Prog. Phys.* **77**, 126401 (2014).
22. Fletcher, R. J. et al. Geometric squeezing into the lowest Landau level. *Science* **372**, 1318–1322 (2021).
23. Tsui, D. C., Stormer, H. L. & Gossard, A. C. Two-dimensional magnetotransport in the extreme quantum limit. *Phys. Rev. Lett.* **48**, 1559–1562 (1982).
24. Nozières, P. Is the roton in superfluid  $^4\text{He}$  the ghost of a Bragg spot? *J. Low Temp. Phys.* **137**, 45–67 (2004).
25. Graß, T. et al. Fractional quantum Hall phases of bosons with tunable interactions: from the Laughlin liquid to a fractional Wigner crystal. *Phys. Rev. Lett.* **121**, 253403 (2018).
26. Galitski, V. & Spielman, I. B. Spin–orbit coupling in quantum gases. *Nature* **494**, 49–54 (2013).
27. Chalopin, T. et al. Probing chiral edge dynamics and bulk topology of a synthetic Hall system. *Nat. Phys.* **16**, 1017–1021 (2020).
28. Struck, J. et al. Tunable gauge potential for neutral and spinless particles in driven optical lattices. *Phys. Rev. Lett.* **108**, 225304 (2012).
29. Jotzu, G. et al. Experimental realization of the topological Haldane model with ultracold fermions. *Nature* **515**, 237–240 (2014).
30. Aidelsburger, M. et al. Measuring the Chern number of Hofstadter bands with ultracold bosonic atoms. *Nat. Phys.* **11**, 162–166 (2015).
31. Stuhl, B. K., Lu, H.-I., Aycock, L. M., Genkina, D. & Spielman, I. B. Visualizing edge states with an atomic Bose gas in the quantum Hall regime. *Science* **349**, 1514–1518 (2015).
32. Mancini, M. et al. Observation of chiral edge states with neutral fermions in synthetic Hall ribbons. *Science* **349**, 1510–1513 (2015).
33. Schweikhard, V., Coddington, I., Engels, P., Mogendorff, V. P. & Cornell, E. A. Rapidly rotating Bose–Einstein condensates in and near the lowest Landau level. *Phys. Rev. Lett.* **92**, 040404 (2004).
34. Bretin, V., Stock, S., Seurin, Y. & Dalibard, J. Fast rotation of a Bose–Einstein condensate. *Phys. Rev. Lett.* **92**, 050403 (2004).
35. Bukov, M., D’Alessio, L. & Polkovnikov, A. Universal high-frequency behavior of periodically driven systems: from dynamical stabilization to Floquet engineering. *Adv. Phys.* **64**, 139–226 (2015).
36. Iordanskii, S. V. & Pitaevskii, L. P. Bose condensation of moving rotors. *Sov. Phys. Usp.* **23**, 317–318 (1980).
37. Pitaevskii, L. P. Layered structure of superfluid  $^4\text{He}$  with super-critical motion. *JETP Lett.* **39**, 511–514 (1984).
38. Martone, G. I., Recati, A. & Pavloff, N. Supersolidity of cnoidal waves in an ultracold Bose gas. *Phys. Rev. Res.* **3**, 013143 (2021).
39. Mottl, R. et al. Roton-type mode softening in a quantum gas with cavity-mediated long-range interactions. *Science* **336**, 1570–1573 (2012).
40. Léonard, J., Morales, A., Zupancic, P., Esslinger, T. & Donner, T. Supersolid formation in a quantum gas breaking a continuous translational symmetry. *Nature* **543**, 87–90 (2017).
41. Ji, S.-C. et al. Softening of roton and phonon modes in a Bose–Einstein condensate with spin–orbit coupling. *Phys. Rev. Lett.* **114**, 105301 (2015).
42. Li, J.-R. et al. A stripe phase with supersolid properties in spin–orbit-coupled Bose–Einstein condensates. *Nature* **543**, 91–94 (2017).
43. Ha, L.-C., Clark, L. W., Parker, C. V., Anderson, B. M. & Chin, C. Roton-maxon excitation spectrum of Bose condensates in a shaken optical lattice. *Phys. Rev. Lett.* **114**, 055301 (2015).
44. Feng, L., Clark, L. W., Gaj, A. & Chin, C. Coherent inflationary dynamics for Bose–Einstein condensates crossing a quantum critical point. *Nat. Phys.* **14**, 269–272 (2018).
45. Zhang, Z., Yao, K.-X., Feng, L., Hu, J. & Chin, C. Pattern formation in a driven Bose–Einstein condensate. *Nat. Phys.* **16**, 652–656 (2020).
46. Petter, D. et al. Probing the roton excitation spectrum of a stable dipolar Bose gas. *Phys. Rev. Lett.* **122**, 183401 (2019).
47. Hertkorn, J. et al. Density fluctuations across the superfluid–supersolid phase transition in a dipolar quantum gas. *Phys. Rev. X* **11**, 011037 (2021).
48. Schmidt, J.-N. et al. Roton excitations in an oblate dipolar quantum gas. *Phys. Rev. Lett.* **126**, 193002 (2021).
49. Guo, M. et al. The low-energy Goldstone mode in a trapped dipolar supersolid. *Nature* **574**, 386–389 (2019).
50. Tanzi, L. et al. Supersolid symmetry breaking from compressional oscillations in a dipolar quantum gas. *Nature* **574**, 382–385 (2019).
51. Chomaz, L. et al. Long-lived and transient supersolid behaviors in dipolar quantum gases. *Phys. Rev. X* **9**, 21012 (2019).
52. Davidson, R. C., Chan, H.-W., Chen, C. & Lund, S. Equilibrium and stability properties of intense non-neutral electron flow. *Rev. Mod. Phys.* **63**, 341–374 (1991).
53. Cerfon, A. J. Vortex dynamics and shear-layer instability in high-intensity cyclotrons. *Phys. Rev. Lett.* **116**, 174801 (2016).
54. Chandrasekhar, S. *Hydrodynamic and Hydromagnetic Stability* (Clarendon Press, 1961).
55. Landau, L. D. & Lifshitz, E. M. *Fluid Mechanics* (Pergamon Press, 1987).
56. Finne, A. P. et al. Dynamics of vortices and interfaces in superfluid  $^3\text{He}$ . *Rep. Prog. Phys.* **69**, 3157–3230 (2006).
57. Baggaley, A. W. & Parker, N. G. Kelvin–Helmholtz instability in a single-component atomic superfluid. *Phys. Rev. A* **97**, 053608 (2018).
58. Fetter, A. L. & Walecka, J. D. *Quantum Theory of Many-particle Systems* (McGraw-Hill, 1971).
59. Recati, A., Zambelli, F. & Stringari, S. Overcritical rotation of a trapped Bose–Einstein condensate. *Phys. Rev. Lett.* **86**, 377–380 (2001).

**Publisher’s note** Springer Nature remains neutral with regard to jurisdictional claims in published maps and institutional affiliations.

© The Author(s), under exclusive licence to Springer Nature Limited 2022

## Methods

### Preparation of Landau gauge condensates

We prepare condensates occupying a single Landau gauge wavefunction using the geometric squeezing protocol described in ref.<sup>22</sup>. We begin with a condensate of  $8.1(1) \times 10^5$  atoms of <sup>23</sup>Na in an elliptical time-orbiting-potential (TOP) trap<sup>60</sup>, with an root-mean-square (r.m.s.) radial frequency  $\omega = 2\pi \times 88.6(1)$  Hz, ellipticity 0.125(4), and axial frequency  $2.8\omega$ . We then rotate the ellipticity of the trap, ramping the rotation frequency from zero to  $\omega$ . In the rotating frame, atoms experience both a synthetic magnetic field and a scalar saddle potential. Isopotential flow on this saddle, in analogy to the  $\mathbf{E} \times \mathbf{B}$  Hall drift of electromagnetism, leads to elongation and contraction of the condensate along orthogonal directions and effecting unitary squeezing of the atomic density distribution<sup>22</sup>. We then turn off the saddle potential by setting the trap ellipticity to zero, which halts the outward flow of atoms. This results in an equilibrium, quasi-translationally invariant condensate freely rotating at  $\omega$ , which we allow to evolve for a variable time  $t$ . Finally, we obtain an absorption image of the in situ density distribution.

### Imaging setup

Our imaging resolution is sufficient to observe vortices in situ with a contrast of ~60% (ref. <sup>22</sup>). In the Thomas–Fermi regime, these have a characteristic size set by the healing length, which is ~300 nm in our system. This is substantially smaller than the quantum mechanical ground state size of cyclotron orbits, set by the rotational analogue of the magnetic length,  $\ell_B = \sqrt{\hbar/(2m\omega)} = 1.6$  μm.

### Coupling constant

Given interaction energies close to the LLL, the axial motion at frequency  $2.8\omega$  is predominantly in its ground state. The coupling constant is then  $g = \frac{4\pi\hbar^2 a}{m} \int dz |\phi(z)|^4$ , where  $a$  is the three-dimensional s-wave scattering length,  $m$  denotes the atomic mass of <sup>23</sup>Na and  $\phi(z)$  is the axial wavefunction with normalization  $\int dz |\phi(z)|^2 = 1$ .

### Stability analysis

To theoretically investigate the crystallization process, we perform a stability analysis of the initial Landau gauge condensate. In the Thomas–Fermi limit, we may neglect the quantum pressure term in the superfluid hydrodynamic equations. We linearize the equations about the original unperturbed condensate<sup>61</sup>, and find an exact analytical solution for the density and the velocity perturbations in terms of the Heun function<sup>62</sup>. The initial counterflow leads to an instability of Kelvin–Helmholtz type, and the analysis displays a dynamical instability with a most critical wavevector at  $k_{\max} = 1.12/R_{\text{TF}} = 0.95/R$  and a rate  $\Gamma = 0.14\omega_c$ . To treat the entire region from the LLL to the Thomas–Fermi regime, we perform a numerical Bogoliubov analysis. In the LLL limit, the crystallization growth rate is given by  $\Gamma = 0.21gn/\hbar$ , and the most critical wavevector is  $k_{\max} > 0.981/\ell_B$ . The Bogoliubov analysis shows that the growth rate of the dominant wavevector evolves smoothly from being interaction-dominated ( $\Gamma \approx 0.21gn/\hbar$ ) in the LLL regime, to being set by the cyclotron frequency ( $\Gamma \approx \omega_c$ ) in the Thomas–Fermi regime. Further details are provided in the Supplementary Information.

### Gross–Pitaevskii simulation

To provide insight into the crystallization dynamics beyond what can be captured in the linear stability analysis, we perform a numerical simulation of our experiment based upon the Gross–Pitaevskii (GP) equation. Within a single-mode approximation, the condensate wavefunction  $\psi(r, t)$  evolves in the rotating frame as

$$i\hbar \frac{\partial}{\partial t} \psi = \left[ -\frac{\hbar^2 \nabla^2}{2m} + V + g|\psi|^2 - \boldsymbol{\Omega} \cdot \mathbf{L} \right] \psi. \quad (4)$$

Here  $g = \sqrt{8\pi} \frac{\hbar^2 a_s}{ml_z}$  is the two-dimensional mean-field coupling constant,  $a_s = 3.3$  nm is the scattering length,  $l_z = \sqrt{\frac{\hbar}{m\omega_z}}$  is the harmonic oscillator length of the axial trap,  $\omega_z = 2.8\omega$  is the trap frequency in the  $z$  direction,  $\omega = 2\pi \times 88.6$  Hz is the r.m.s. radial trap frequency,  $\boldsymbol{\Omega} = \boldsymbol{\Omega}(t)\hat{z}$  is the angular velocity,  $\mathbf{L}$  is the angular momentum operator, and  $V$  is a complex scalar potential. The real part  $\text{Re}(V) = \frac{1}{2}m\omega^2[(1+\varepsilon)x^2 + (1-\varepsilon)y^2]$  is the radial trapping potential with ellipticity  $\varepsilon$ , and the imaginary part  $\text{Im}(V) \propto 1 + \text{erf}[(r - R_\infty)/\sigma]$  serves as an absorbing circular boundary. The absorbing radius  $R_\infty$  is chosen to be much larger than the transverse size of the condensate, and we use a wall thickness  $\sigma = R_\infty/10$ . We implement the evolution of equation (4) on a square grid using the time-splitting spectral method<sup>63</sup> and accelerate the simulation by performing the bulk of the computation on a graphics processing unit (GPU).

The simulated experimental sequence is identical to the experiment. We first perform geometric squeezing of an initially circular condensate<sup>22</sup>, before setting the trap ellipticity  $\varepsilon \rightarrow 0$  after which the condensate evolves freely for a time  $t$  in the rotating frame.

We find that without the explicit addition of noise, the condensate does not exhibit any instability except near the boundaries, owing to residual edge effects not mitigated by the absorbing potential (see Extended Data Fig. 1a). On the other hand, seeding of the dynamical instability by the addition of Gaussian phase noise at time  $t = 0$  results in a very similar simulated evolution (Extended Data Fig. 1b) compared to the experiment (Extended Data Fig. 1c).

We perform an identical analysis procedure as in the experiment (see main text) on the simulated density profiles in order to obtain the structure factor  $S_k(t)$ , shown in Extended Data Fig. 1d, e, and the instability growth rate shown in Extended Data Fig. 1f. The red points show the experimental instability growth rate as a function of wavevector  $k$ , and the black line shows the prediction of our Bogoliubov analysis. For comparison, the blue line shows the rate extracted from the simulation, which captures the observed growth at higher wavevectors than the unstable range predicted by the Bogoliubov approach. This suggests that such growth can indeed be attributed to nonlinear effects, which are not captured by the perturbative Bogoliubov approach. In addition to oscillations in  $S_k$  at the cyclotron frequency  $\omega_c$ , a slower modulation is also observed. We attribute this oscillation to rotation of the individual droplets in the crystal.

In both experiment and simulation the emergent crystal is long-lived, persisting for  $\omega_c t / (2\pi) > 20$ . In the experiment the lifetime is only limited by the weak  $\propto r^4$  anharmonicities in the trapping potential, leading to a slow S-shaped distortion of the linear crystal, similar to the Kerr effect on nonclassical states in quantum optics.

### Vortex detection and phase profile

In the rotating frame, each droplet exhibits an irrotational flow profile, with vortices surrounding the droplets. These vortices are directly visible in the experimental density image, and can be used to reconstruct the phase profile of the crystal in the rotating frame (see Extended Data Fig. 2a, c, e). The phase is determined by the locations of the vortices, which are assumed to each have a single unit of circulation  $2\pi\hbar/m$ . Most vortices are outside of the bulk of the condensate, making their detection challenging. Nevertheless, a numerical solution of the GP equation shows similarly located vortices (Extended Data Fig. 2d), as well as a similar irrotational flow profile in the rotating frame (Extended Data Fig. 2f).

### Data availability

All data files are available from the corresponding author upon request. Accompanying data, including those for figures, are available from Zenodo (<https://doi.org/10.5281/zenodo.5533142>).

# Article

## Code availability

The simulation and analysis code are available from the corresponding author upon reasonable request.

60. Petrich, W., Anderson, M. H., Ensher, J. R. & Cornell, E. A. Stable, tightly confining magnetic trap for evaporative cooling of neutral atoms. *Phys. Rev. Lett.* **74**, 3352–3355 (1995).
61. Sinha, S. & Castin, Y. Dynamic instability of a rotating Bose–Einstein condensate. *Phys. Rev. Lett.* **87**, 190402 (2001).
62. Ronveaux, A. (ed.) *Heun's Differential Equations* (Oxford Univ. Press, 1995).
63. Bao, W. & Wang, H. An efficient and spectrally accurate numerical method for computing dynamics of rotating Bose–Einstein condensates. *J. Comput. Phys.* **217**, 612–626 (2006).

**Acknowledgements** We thank T. Pfau and his research group, J. Dunkel, A. Fetter, T. Senthil, T. Simula and W. Zwerger for discussions. This work was supported by the National Science Foundation (Center for Ultracold Atoms and grant no. PHY-2012110), Air Force Office of Scientific Research (FA9550-16-1-0324 and MURI Quantum Phases of Matter FA9550-14-1-

0035), Office of Naval Research (N00014-17-1-2257), the DARPA A-Phi program through ARO grant W911NF-19-1-0511, and the Vannevar Bush Faculty Fellowship. A.S. acknowledges support from the NSF GRFP. M.Z. acknowledges funding from the Alexander von Humboldt Foundation.

**Author contributions** B.M., A.S., C.C.W., P.B.P., Z.Y. and R.J.F. constructed the apparatus. B.M., A.S., C.C.W. and R.J.F. performed the measurements. B.M. and A.S. analysed the data. B.M. contributed the GP numerical simulations. V.C., R.J.F. and M.Z. developed the theoretical description. R.J.F. and M.Z. supervised the project. All authors contributed to interpretation of the results and preparation of the manuscript.

**Competing interests** The authors declare no competing interests.

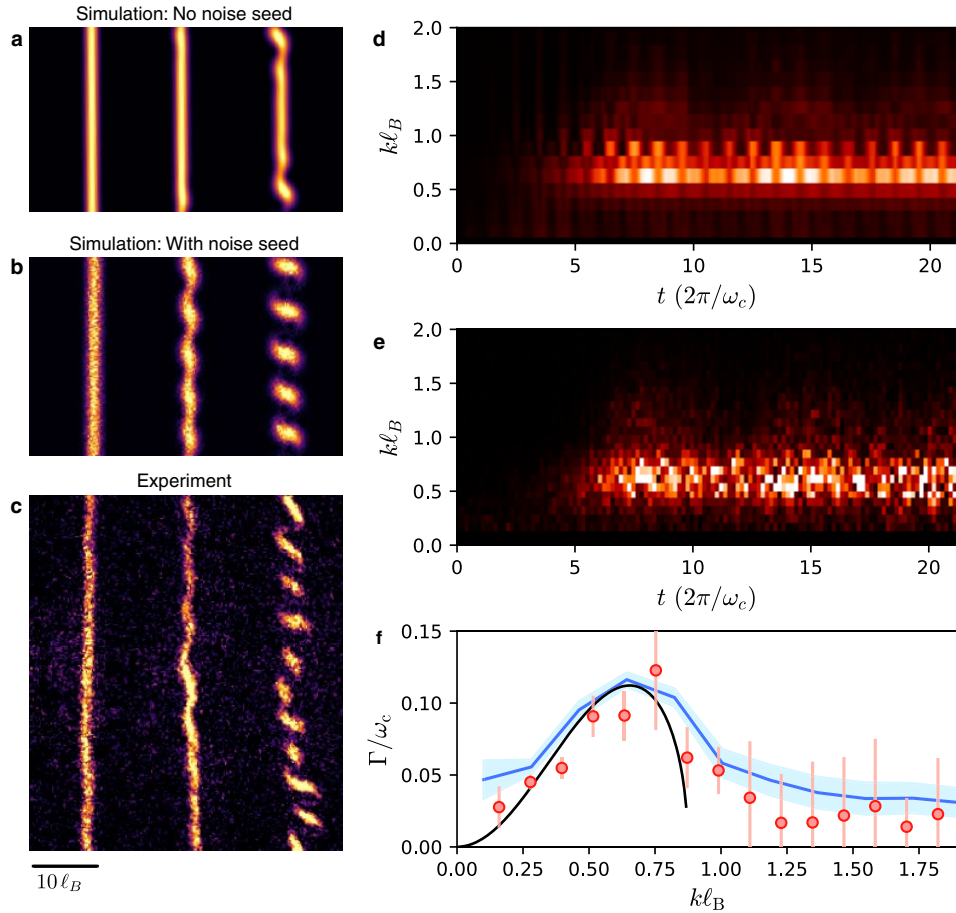
## Additional information

**Supplementary information** The online version contains supplementary material available at <https://doi.org/10.1038/s41586-021-04170-2>.

**Correspondence and requests for materials** should be addressed to Martin Zwierlein.

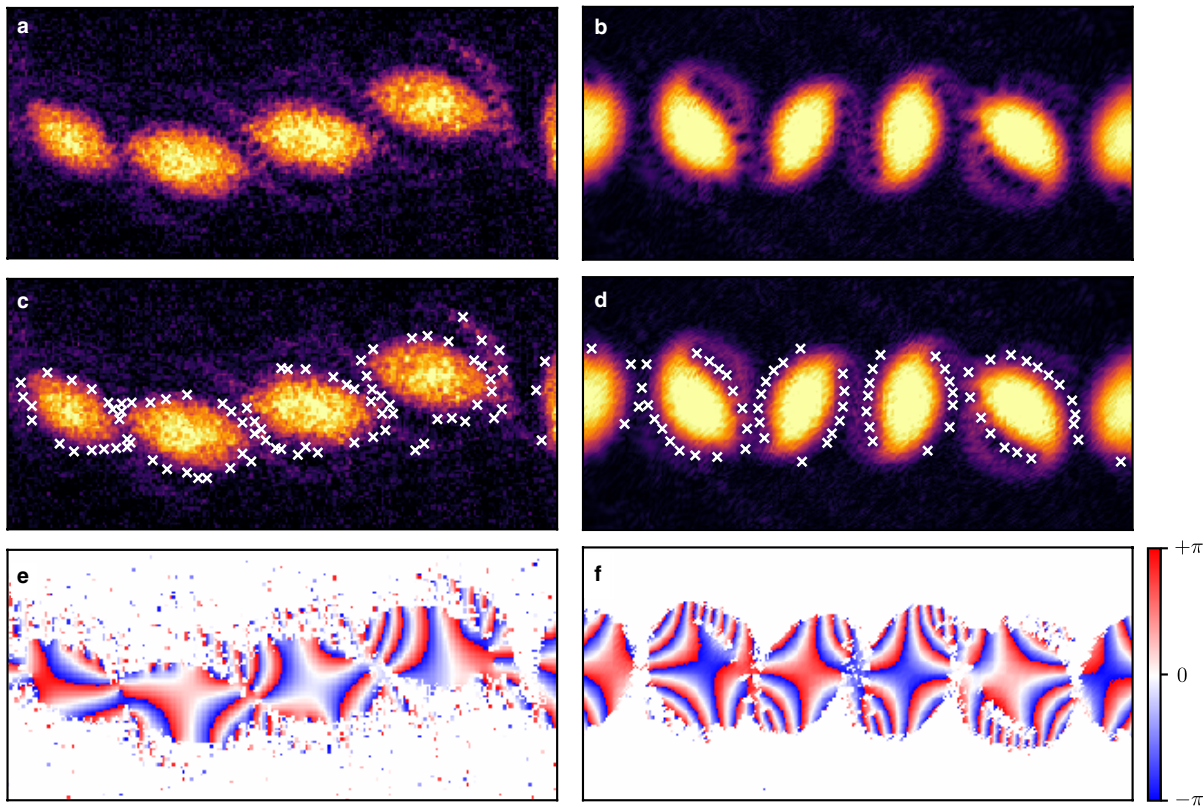
**Peer review information** *Nature* thanks Alessio Recati and the other, anonymous, reviewer(s) for their contribution to the peer review of this work.

**Reprints and permissions information** is available at <http://www.nature.com/reprints>.



**Extended Data Fig. 1 | Numerical GP simulation of the condensate evolution in the rotating frame.** **a–c**, Time evolution of the condensate density without the addition of noise (top), with added phase noise (middle), and in the experiment (bottom). The frames correspond to times  $\omega_c t/(2\pi) = 0, 4$  and  $6$ . **d–e**, Evolution of the structure factor  $S_k(t)$  extracted from the simulation (**d**) and the experiment (**e**) which show good agreement. **f**, The extracted

instability growth rate as a function of wavevector  $k$ . The experimental measurements are shown by red points, and the Bogoliubov prediction by the black line. The blue line shows the result of the GP simulation. Here, the blue shading and the red error bars indicate  $1\sigma$  standard error. This model captures the experimentally measured growth at wavevectors above the instability region provided by the linear Bogoliubov description.



**Extended Data Fig. 2 | Phase profile of the crystal.** **a, b,** The density profiles of the crystals in the experiment (**a**) and GP simulation (**b**) appear to contain vortices, which are marked in **c** and **d**. **e,** The phase of the macroscopic wavefunction can be inferred from the locations of the vortices in the

experimental image. Note that additional contributions from undetected vortices may exist. **f,** The simulated phase profile from a GP simulation shows a similar structure of irrotational flow within each segment of the crystal. In both **e** and **f**, the phase shown is in the rotating frame.

---

## Supplementary information

---

# Crystallization of bosonic quantum Hall states in a rotating quantum gas

---

In the format provided by the  
authors and unedited

---

## Supplementary information

---

# Crystallization of bosonic quantum Hall states in a rotating quantum gas

---

In the format provided by the  
authors and unedited

# Crystallization of Bosonic Quantum Hall States in a Rotating Quantum Gas

## Supplementary Information

Biswaroop Mukherjee, Airlia Shaffer, Parth B. Patel, Zhenjie Yan,

Cedric C. Wilson, Valentin Crépel, Richard J. Fletcher, Martin Zwierlein

*MIT-Harvard Center for Ultracold Atoms, Research Laboratory of Electronics, and Department of Physics, Massachusetts Institute of Technology, Cambridge, Massachusetts 02139, USA*

### BOGOLIUBOV STABILITY ANALYSIS OF LANDAU GAUGE CONDENSATES

A condensate prepared to have uniform phase in the Landau gauge - a “Landau gauge condensate” - is energetically unstable: an infinitely extended Bose gas has lower energy. However, in the absence of dissipation - as in the experiment - this does not itself lead to an instability. The question is whether the system is dynamically unstable, which would cause exponential growth of excitations and an isoenergetic transition into a new state. To search for dynamically unstable modes and to obtain their growth rate and spatial structure we perform a stability analysis of Landau gauge condensates via the Bogoliubov approach [1–3]. We expect the initial unmodulated condensate to be well-described within a single-mode framework, and expand the Hamiltonian in the Landau gauge, Eq. 2 of the main text, to second order in small fluctuations  $\delta\hat{\psi}$  of the bosonic field  $\hat{\Psi} = \psi_0 + \delta\hat{\psi}$  about the initial condensate wavefunction  $\psi_0$  [1–3]. To ensure number conservation one employs the grand-canonical Hamiltonian  $\hat{K} = \hat{H} - \mu\hat{N}$  with chemical potential  $\mu$ :

$$\hat{K} = \hat{H} - \mu\hat{N} \approx \text{const.} + \int d^2r \delta\hat{\psi}^\dagger \left( \hat{h} - \mu_0 + 2g|\psi_0|^2 \right) \delta\hat{\psi} + \frac{1}{2}g \int d^2r \left( \psi_0^{*2} \delta\hat{\psi} \delta\hat{\psi} + \delta\hat{\psi}^\dagger \delta\hat{\psi}^\dagger \psi_0^2 \right). \quad (1)$$

with the single-particle Hamiltonian in the Landau gauge  $\hat{h} = \frac{\hat{p}_x^2}{2m} + \frac{1}{2}m\omega_c^2 \left( \hat{x} - \frac{\hat{p}_y l_B^2}{\hbar} \right)^2$  and the constant term a function of  $\psi_0$ . Terms first order in  $\delta\hat{\psi}$  vanish if  $\psi_0$  obeys the stationary Gross-Pitaevskii (GP) equation  $\hat{h}\psi_0 + g|\psi_0|^2\psi_0 = \mu_0\psi_0$ . Since the initial wavefunction  $\psi_0 = \psi_0(x)$  is translationally invariant along  $y$ , this reads

$$\left( -\frac{\hbar^2}{2m} \frac{d^2}{dx^2} + \frac{1}{2}m\omega_c^2 x^2 + g|\psi_0(x)|^2 \right) \psi_0(x) = \mu_0\psi_0(x), \quad (2)$$

which is formally equivalent to the GP equation of a Bose-Einstein condensate in a one-dimensional harmonic oscillator (h.o.) potential of frequency  $\omega_c$ . We solve Eq. 2 numerically via imaginary time evolution, choosing  $\psi_0(x)$  to be real and normalized such that  $\int dx |\psi_0(x)|^2 = n_{1D}$ , where  $n_{1D}$  is the initial one-dimensional number density. A dimensionless quantity measuring the interaction energy, relative to the cyclotron level spacing  $\hbar\omega_c$ , is  $\tilde{g} \equiv \frac{gn_{1D}}{l_B\hbar\omega_c}$ . Near the lowest Landau level, the interaction is a small perturbation, resulting in the gaussian density  $\psi_0^2(x) = \frac{n_{1D}}{\sqrt{\pi}l_B} e^{-x^2/l_B^2}$  and  $\mu_0 \approx \frac{\hbar\omega_c}{2} \left( 1 + \sqrt{\frac{2}{\pi}}\tilde{g} \right)$ , close to the ground-state cyclotron energy. In the Thomas-Fermi regime, where the term  $\hat{p}_x^2/2m$  can be neglected, one obtains  $g\psi_0^2(x) = \mu_0 - \frac{1}{2}m\omega_c^2 x^2$  with  $\mu_0 = \frac{1}{2}\hbar\omega_c \left( \frac{3}{2}\tilde{g} \right)^{2/3}$ .

Translation invariance of  $\psi_0(x)$  and  $\hat{h}$  along  $y$  allows expanding  $\delta\hat{\psi} = \sum_k \frac{1}{\sqrt{L}} e^{iky} \hat{\phi}_k(x)$  into bosonic fields  $\hat{\phi}_k(x)$  of well-defined  $y$ -momentum  $\hbar k$ , with  $L$  the spatial extent of the system in the  $y$ -direction. The quadratic part of Eq. 1 then becomes, using matrix notation,

$$\begin{aligned} \hat{K}_2 &= \frac{1}{2} \sum_k \int dx \left( \hat{\phi}_k^\dagger \hat{\phi}_{-k} \right) \begin{pmatrix} \hat{h}_k - \mu_0 + 2g\psi_0^2 & g\psi_0^2 \\ g\psi_0^2 & \hat{h}_{-k} - \mu_0 + 2g\psi_0^2 \end{pmatrix} \begin{pmatrix} \hat{\phi}_k \\ \hat{\phi}_{-k}^\dagger \end{pmatrix} \\ &= \frac{1}{2} \sum_k \langle \hat{\Phi}_k | \hat{\mathbf{H}}_k | \hat{\Phi}_k \rangle \end{aligned} \quad (3)$$

with  $\hat{h}_k = \frac{\hat{p}_x^2}{2m} + \frac{1}{2}m\omega_c^2 (x - kl_B^2)^2$ ,  $\hat{\Phi}_k = \left( \hat{\phi}_k \hat{\phi}_{-k}^\dagger \right)^T$ ,  $\hat{\mathbf{H}}_k(x)$  the  $2 \times 2$  matrix operator of the first line in Eq. 3, and  $\langle \mathbf{f} | \mathbf{g} \rangle = \int dx \mathbf{f}^\dagger(x) \cdot \mathbf{g}(x)$  for vectors  $\mathbf{f}, \mathbf{g}$ . Momentum conservation along  $y$  ensures that allowed scattering processes result in either the simultaneous creation or simultaneous annihilation of a pair of states with momenta  $k$  and  $-k$ . Consequently the Hamiltonian only mixes a particle with  $y$ -momentum  $k$  with a hole of  $y$ -momentum  $-k$ , as is explicit in the  $2 \times 2$  particle/hole matrix notation. The Bogoliubov Hamiltonian  $\hat{\mathbf{H}}_k(x)$  in Eq. 3 is Hermitian, has only real eigenvalues (bounded from below

by  $-\mu_0$ ) and thus  $\hat{K}_2$  has only real expectation values in any state. However, the time evolution of the bosonic field operators  $\hat{\phi}_k(x, t)$  evolving under the grand-canonical Hamiltonian  $\hat{K}$  is given by  $i\hbar \frac{\partial}{\partial t} \hat{\phi}_k = [\hat{\phi}_k, \hat{K}]$ , and with the bosonic commutation relations  $[\hat{\phi}_k(x), \hat{\phi}_{k'}^\dagger(x')] = \delta_{k,k'} \delta(x - x')$  we have

$$i\hbar \frac{\partial}{\partial t} \hat{\Phi}_k = \begin{pmatrix} \hat{h}_k - \mu_0 + 2g\psi_0^2 & g\psi_0^2 \\ -g\psi_0^2 & -(\hat{h}_{-k} - \mu_0 + 2g\psi_0^2) \end{pmatrix} \hat{\Phi}_k = \eta \hat{\mathbf{H}}_k \hat{\Phi}_k \quad (4)$$

with  $\eta = \begin{pmatrix} 1 & 0 \\ 0 & -1 \end{pmatrix}$  acting in particle-hole space [4, 5]. The evolution of the field operators is thus governed by an operator  $\eta \hat{\mathbf{H}}_k$  that is in general *non-Hermitian* and can thus feature complex eigenvalues, leading to exponential growth of fluctuations - the system features dynamical instabilities [6].

### Symmetries, eigenvectors and eigenvalues of $\eta \hat{\mathbf{H}}_k$

For each  $k$ , the Hamiltonian matrix  $\hat{\mathbf{H}}_k$  is real,  $\hat{\mathbf{H}}_k^* = \hat{\mathbf{H}}_k$ , and symmetric under simultaneous reflection of space  $\hat{R}$  (i.e.  $\hat{R}x\hat{R} = -x$ ) and exchange of particles and holes, i.e.  $\hat{\mathbf{H}}_k = \gamma \hat{R} \hat{\mathbf{H}}_k \hat{R} \gamma$  with  $\gamma = \begin{pmatrix} 0 & 1 \\ 1 & 0 \end{pmatrix}$  exchanging particles and holes. It follows that given an eigenvector  $\mathbf{V}_{k,n}$  of  $\eta \hat{\mathbf{H}}_k$  with eigenvalue  $\epsilon_{k,n}$ , the vector  $\mathbf{V}_{k,n}^*$  is also an eigenvector with eigenvalue  $\epsilon_{k,n}^*$ , and  $\gamma \hat{R} \mathbf{V}_{k,n}$  and  $\gamma \hat{R} \mathbf{V}_{k,n}^*$  are eigenvectors with eigenvalues  $-\epsilon_{k,n}$  and  $-\epsilon_{k,n}^*$ , respectively. The latter follows from  $\gamma \eta = -\eta \gamma$ . We also note that  $\hat{\mathbf{H}}_{-k} = \hat{R} \hat{\mathbf{H}}_k \hat{R}$  implying that  $\hat{R} \mathbf{V}_{k,n} \equiv \mathbf{V}_{-k,n}$  is eigenvector of  $\eta \hat{\mathbf{H}}_{-k}$  with eigenvalue  $\epsilon_{-k,n} = \epsilon_{k,n}$ . In general, the four values  $\epsilon_{k,n}$ ,  $\epsilon_{k,n}^*$ ,  $-\epsilon_{k,n}$  and  $-\epsilon_{k,n}^*$  are all different, implying an oscillatory evolution of exponentially increasing and decreasing amplitudes. The instability studied in the present work concerns the mode of lowest  $|\epsilon_{k,n}|$  for given  $k$ , the Goldstone branch which we label by  $n=0$ . It is smoothly connected to the Goldstone mode at  $k=0$  of zero frequency,  $\epsilon_{0,0}=0$ , that reflects the free choice of the overall phase of the condensate, i.e. its  $U(1)$  symmetry. An associated second mode with zero eigenvalue of  $(\eta \hat{\mathbf{H}}_0)^2$  describes the global phase fluctuations [7]. The next excited mode,  $n=1$ , is correlated near  $k=0$  with the cyclotron oscillation. At  $k=0$  the  $n=1$  mode lies precisely at the cyclotron energy  $\epsilon_{0,1} = \hbar\omega_c$ , according to Kohn's theorem [8, 9]. The modes at  $k>0$  of the Goldstone branch, connecting to the Goldstone density and phase modes at  $k=0$ , are thus well separated from any other excitations, so that this branch is described by only two, not four, distinct eigenvalues. This implies that either  $\epsilon_{k,0} = \epsilon_{k,0}^*$ , i.e. one has two real eigenvalues  $\pm \epsilon_{k,0}$ , or  $\epsilon_{k,0} = -\epsilon_{k,0}^*$ , i.e. one has two purely imaginary eigenvalues  $\pm i\epsilon_{k,0}$ . For excitations of non-rotating condensates in their ground state, only the first case occurs and corresponds to the usual Bogoliubov phonon excitations. Here, instead, we find, in an entire range of momenta between  $k = 0$  and a maximum  $k = k_c$ , the case of purely imaginary frequencies  $\epsilon_{k,0}$ , corresponding to the exponential growth of correlated excitations at  $\pm k$  that causes the “snake-like” dynamical instability. Results of the numerical solution of  $\eta \hat{\mathbf{H}}_k \mathbf{V}_{k,n} = \epsilon_{k,n} \mathbf{V}_{k,n}$  are shown in Fig. 1, from deep in the lowest Landau level ( $\tilde{g} \lesssim 1$ ) to the Thomas-Fermi regime ( $\tilde{g} \gg 1$ ).

### Relation between eigenvalues of $\hat{\mathbf{H}}_k$ and $\eta \hat{\mathbf{H}}_k$

The difference between stable and dynamically unstable excitations is analogous to the difference between the stable motion in a harmonic oscillator potential and the unstable motion of a particle in an inverted harmonic oscillator. The correspondence becomes explicit if we introduce the Hermitian operators  $\hat{Q}_k(x) = (\hat{\phi}_k(x) + \hat{\phi}_k^\dagger(x)) / \sqrt{2}$  and  $\hat{P}_k(x) = -i(\hat{\phi}_k(x) - \hat{\phi}_k^\dagger(x)) / \sqrt{2}$  obeying  $[\hat{Q}_k(x), \hat{P}_{k'}(x')] = i\delta_{k,k'} \delta(x - x')$ . They are related to the density and current fluctuations of the condensate, as the density operator is

$$\hat{n}(x, y) = \hat{\Psi}^\dagger \hat{\Psi} \approx |\psi_0|^2 + \psi_0(\delta\hat{\psi} + \delta\hat{\psi}^\dagger) = |\psi_0|^2 + \psi_0 \sqrt{\frac{2}{L}} \sum_k \cos(ky) \hat{Q}_k(x) - \sin(ky) \hat{P}_k(x)$$

and  $\hat{\mathbf{j}} \approx |\psi_0|^2 \nabla \hat{\Theta}$  with the linear fluctuation part of the velocity potential operator [2]

$$\hat{\Theta} = \frac{\hbar}{2mi\psi_0} (\delta\hat{\psi} - \delta\hat{\psi}^\dagger) = \frac{\hbar}{2m\psi_0} \sqrt{\frac{2}{L}} \sum_k \cos(ky) \hat{P}_k(x) + \sin(ky) \hat{Q}_k(x)$$

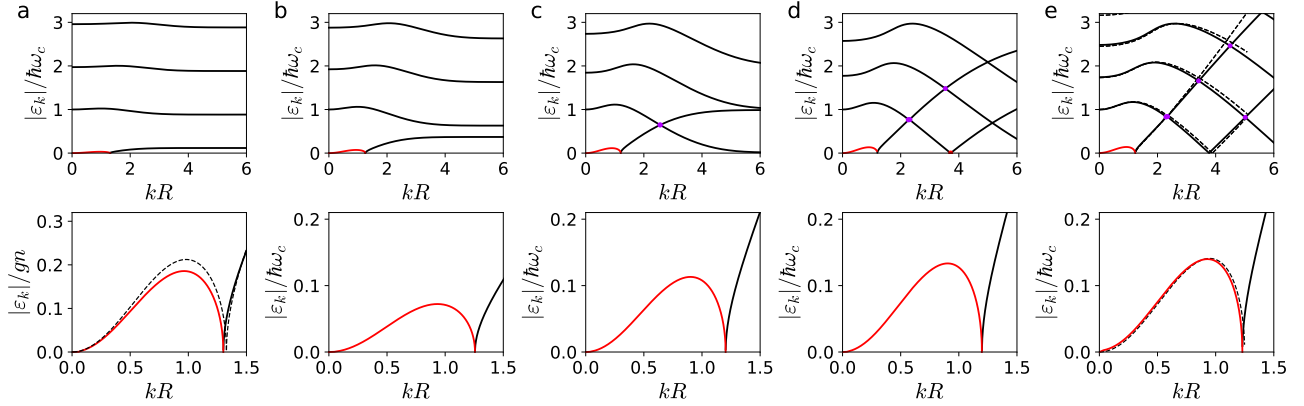


FIG. 1. Bogoliubov spectra from the Lowest Landau Level to the Thomas-Fermi regime. The interaction parameters  $\tilde{g} \equiv \frac{g n_{1D}}{l_B \hbar \omega_c}$  for (a-e) are 0.3, 1, 3, 10, 40, corresponding to  $R/l_B = 1.04, 1.14, 1.39, 2.01, 3.28$ , capturing the evolution from the flat spectra deep in the LLL to the more intricate crossings in the Thomas-Fermi regime. The bottom panel shows a zoomed-in region focusing on the unstable Goldstone branch (red). In the bottom panel of (a), the growth rate/excitation frequencies are normalized by  $gn$ , with  $n = |\psi_0(0)|^2 = n_{1D}/(\sqrt{\pi} l_B)$  the central 2D density in the LLL. The dashed line in this panel shows the result in the deep LLL limit using [10]. In the Thomas-Fermi regime, the dashed line in e) shows the result of the hydrodynamic calculation (see text). Note the existence of complex eigenvalues with  $\text{Re}(\epsilon_k) \neq 0$  near the curve crossings, indicated by purple lines.

In terms of  $\hat{Q}_k$  and  $\hat{P}_k$ , we have  $\hat{K}_2 = \frac{1}{4} \sum_k \langle \hat{Q}_k | \hat{H}_k | \hat{Q}_k \rangle + \langle \hat{P}_k | \eta \hat{H}_k \eta | \hat{P}_k \rangle$  with  $\hat{Q}_k^T = (\hat{Q}_k \ \hat{Q}_{-k})$  and  $\hat{P}_k^T = (\hat{P}_k \ \hat{P}_{-k})$ . So we can think of  $\hat{H}_k$  as representing the matrix of “spring constants” and  $\eta \hat{H}_k \eta$  the matrix of “inverse masses” in the oscillator analogy. Dynamical instabilities can arise in an oscillator when either a spring constant becomes negative, while the mass remains positive, or vice versa.

The time evolution  $\frac{d}{dt} \hat{Q}_k = [\hat{Q}_k, \hat{K}_2] = \eta \hat{H}_k \eta \hat{P}_k$  and  $\frac{d}{dt} \hat{P}_k = -\hat{H}_k \hat{Q}_k$  yields  $\frac{d^2}{dt^2} \hat{Q}_k = -\eta \hat{H}_k \eta \hat{H}_k \hat{Q}_k \stackrel{!}{=} -\epsilon_k^2 \hat{Q}_k$  showing that eigenfrequencies of the motion correspond indeed to the eigenvalues of the operator  $\eta \hat{H}_k$ . The Hermitian operators  $\hat{H}_k$  and  $\eta \hat{H}_k \eta$  share their (real) eigenvalues, and if  $\mathbf{U}_{k,n}$  is an eigenvector of  $\hat{H}_k$  of eigenvalue  $E_{k,n}$ , then  $\eta \mathbf{U}_{k,n}$  is the eigenvector of  $\eta \hat{H}_k \eta$  with that same eigenvalue. With  $\mathcal{O}_{k,nm} = \langle \mathbf{U}_{k,n} | \eta | \mathbf{U}_{k,m} \rangle = \int dx \mathbf{U}_{k,n}(x) \eta \mathbf{U}_{k,m}(x)$  the matrix effecting the basis change, which is symmetric and orthonormal (so  $\mathcal{O}_k^2 = \mathbb{1}$ ), we have  $\langle \mathbf{U}_{k,n} | \eta \hat{H}_k \eta | \mathbf{U}_{k,m} \rangle = \sum_l \mathcal{O}_{k,nl} E_{k,l} \mathcal{O}_{k,lm} = (\mathcal{O}_k \mathcal{E}_k \mathcal{O}_k)_{nm}$ , with  $\mathcal{E}_k$  the diagonal matrix of eigenvalues of  $\hat{H}_k$  (the “spring constants”). The squared eigenfrequencies  $\epsilon_k^2$  are thus eigenvalues of  $\mathcal{O}_k \mathcal{E}_k \mathcal{O}_k$ , and so the eigenfrequencies  $\epsilon_k$  themselves are eigenvalues of  $\mathcal{O}_k \mathcal{E}_k$ , the matrix describing  $\eta \hat{H}_k$  in the basis of eigenvectors of  $\hat{H}_k$ . Importantly, whenever a “spring constant” or “inverse mass” equals zero, i.e. one of the eigenvalues of  $\hat{H}_k$  equals zero, one eigenfrequency  $\epsilon_k$  of  $\eta \hat{H}_k$  also equals zero. Regions in the variable  $k$  featuring dynamical instabilities with purely imaginary eigenfrequency are thus bounded by values of  $k$  where consecutive eigenvalues  $E_k$  of  $\hat{H}_k$  equal zero. This is analogous to a harmonic oscillator slowing down and becoming dynamically unstable as its spring constant changes from positive to negative, followed by its mass diverging and changing sign to yield again a dynamically stable, but thermodynamically unstable, oscillator. A famous example of the latter situation is the magnetron motion in Penning traps [11].

Since  $\hat{H}_k$  commutes with simultaneous reflection and particle-hole exchange, i.e. with  $\gamma \hat{R}$ , eigenvectors of  $\hat{H}_k$  can be found as eigenvectors of  $\gamma \hat{R}$  with eigenvalue  $\sigma = +1$  or  $-1$ , which are states of the form  $\mathbf{U}_\pm = (u(x), \pm u(-x))^T$ , leading to the two eigenequations

$$(\hat{h}_k - \mu_0 + 2g\psi_0^2)u_{k,n\pm}(x) \pm g\psi_0^2 u_{k,n\pm}(-x) = E_{k,n\pm} u_{k,n\pm}(x)$$

The lowest energy for  $\sigma = -1$  and  $k=0$  is  $E_{0,0-}=0$ , for  $u(x) = \psi_0(x)$ , and  $\mathbf{U}_{0,0-}(x) = (\psi_0(x), -\psi_0(x))^T / \sqrt{2}$  is the Goldstone mode. Since  $\psi_0(x)$  is the ground state for a condensate trapped in a 1D harmonic oscillator, the Hamiltonian  $\hat{H}_0$ , describing fluctuations that are translation invariant along  $y$ , is positive semi-definite, with eigenvalues  $E_{0,n\pm}$  all positive or zero. For  $k > 0$ , the decreasing overlap of the eigenfunction  $u_{k,0-}$  with the condensate centered at  $x = 0$  causes the eigenvalue  $E_{k,0-}$  to become negative, corresponding to the case of a negative spring constant.  $\hat{K}_2$  then contains a term corresponding to an inverted oscillator potential,  $\frac{1}{2} E_{k,0-} \hat{Q}_{k,0-}^2$  with  $\hat{Q}_{k,n\sigma} \equiv \langle \mathbf{U}_{k,n\sigma} | \hat{Q}_k \rangle$  the “position” operators, with the canonically conjugate “momentum” operators  $\hat{P}_{k,n\sigma} \equiv \langle \mathbf{U}_{k,n\sigma} | \hat{P}_k \rangle$  and commutation relations  $[\hat{Q}_{k,n\sigma}, \hat{P}_{k,m\sigma'}] = i\delta_{nm}\delta_{\sigma\sigma'}$ .

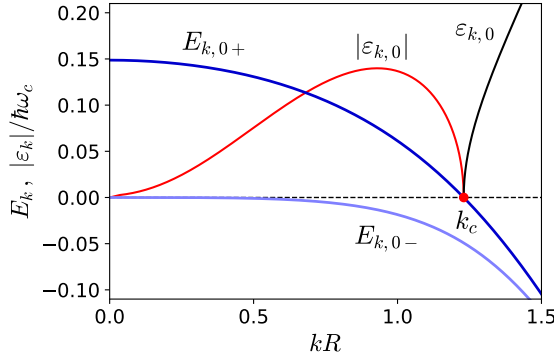


FIG. 2. Relation between Goldstone branch instability and eigenenergies of the Bogoliubov Hamiltonian  $\hat{H}_k$ . The decrease of overlap with the condensate at non-zero  $k$  renders the lowest eigenvalue  $E_{k,0-}$  of  $\hat{H}_k$  negative, corresponding to an inverted oscillator potential (negative spring constant). The Goldstone branch is unstable,  $\epsilon_{k,0}$  being purely imaginary, until the second eigenvalue  $E_{k,0+}$  of  $\hat{H}_k$  becomes negative, corresponding to a negative mass oscillator and resulting in stable motion, with  $\epsilon_{k,0}$  real.

To obtain the matrix of inverse masses, we note that since  $\eta$  anti-commutes with particle-hole exchange,  $\eta\gamma = -\gamma\eta$ , it only connects states of opposite  $\gamma\hat{R}$  symmetry, so  $\langle U_{k,n+} | \eta | U_{k,m+} \rangle = \langle U_{k,n-} | \eta | U_{k,m-} \rangle = 0$ . With  $\mathcal{O}_{k,nm}^{+-} \equiv \langle \mathbf{U}_{k,n+} | \eta | \mathbf{U}_{k,m-} \rangle = \int dx u_{k,n+}(x) u_{k,m-}(x) = \mathcal{O}_{k,mn}^{-+}$  we find for the “inverse mass” matrix  $\langle \mathbf{U}_{k,n+} | \eta \hat{H}_k \eta | \mathbf{U}_{k,m+} \rangle = (\mathcal{O}_k^{-+} \mathcal{E}_{k+} \mathcal{O}_k^{+-})_{nm}$  and  $\langle \mathbf{U}_{k,n-} | \eta \hat{H}_k \eta | \mathbf{U}_{k,m-} \rangle = (\mathcal{O}_k^{-+} \mathcal{E}_{k+} \mathcal{O}_k^{+-})_{nm}$  with  $\mathcal{E}_{k\sigma}$  the diagonal matrix of eigenvalues  $E_{k,\sigma}$ . The squared Bogoliubov eigenfrequencies  $\epsilon_k^2$  are thus eigenvalues of the matrix  $\mathcal{O}_k^{-+} \mathcal{E}_{k+} \mathcal{O}_k^{+-} \mathcal{E}_{k-}$ .

Fig. 2 shows the generic case. The branch  $E_{k,0-}$ , the lowest eigenvalue of  $\hat{H}_k$ , is negative for any non-zero  $k$ , and the Goldstone branch  $\epsilon_{k,0}$  (eigenvalue of  $\eta \hat{H}_k$ ) is correspondingly purely imaginary and thus dynamical unstable, until at  $k=k_c$  the second branch  $E_{k,0+}$  crosses zero, and  $\epsilon_{k,0}$  becomes real. This is the situation of having both a negative mass and a negative spring constant, corresponding to dynamically stable motion. The point at  $k=k_c$  is called an exceptional point in the theory of non-Hermitian physics [6].  $k_c$  is always on the order of the inverse cloud radius  $k_c \sim 1/R$ , and the maximum instability growth rate  $|\epsilon_{k,0}|$  is also only slightly below  $k_c$ .

### Normal form of $\hat{K}_2$

An inverted harmonic oscillator Hamiltonian  $H = \frac{p^2}{2m} - \frac{1}{2}\kappa q^2$  with negative spring constant ( $-\kappa < 0$ ), and mass  $m > 0$  can be canonically transformed via  $q' = \frac{1}{\sqrt{2m\Gamma}}p + \sqrt{\frac{\kappa}{2\Gamma}}q$  and  $p' = \frac{1}{\sqrt{2m\Gamma}}p - \sqrt{\frac{\kappa}{2\Gamma}}q$  into  $H = \frac{1}{2}\Gamma(q'p' + p'q')$ , where  $\Gamma = \sqrt{\kappa/m}$ , with equations of motion  $\frac{d}{dt}q' = \Gamma q'$  and  $\frac{d}{dt}p' = -\Gamma p'$ , generating squeezing of  $p'$  and exponential growth of  $q'$ . In terms of bosonic operators  $a = (q' + ip')/\sqrt{2}$  and  $a^\dagger = (q' - ip')/\sqrt{2}$  with  $[a, a^\dagger] = 1$  the Hamiltonian is of the squeezing form  $H = \Gamma \frac{1}{2i}(aa - a^\dagger a^\dagger)$ . Analogously we will find that  $\hat{K}_2$ , in the dynamically unstable region  $0 < k < k_c$ , will contain a term of the squeezing form,  $\sum_k \Gamma_k (\hat{a}_k \hat{a}_{-k} + \hat{a}_k^\dagger \hat{a}_{-k}^\dagger)$  associated with the spontaneous pairwise creation of excitations at  $\pm k$ . Here,  $\epsilon_k = i\Gamma_k$  with  $\Gamma_k > 0$  is purely imaginary (we omit the index 0 in  $\epsilon_{k,0}$  for simplicity), and we have, since  $\epsilon_k = -\epsilon_k^*$ , two instead of four associated eigenvectors of  $\eta \hat{H}_k$ , labelled  $\mathbf{V}_k$  and  $\mathbf{W}_k = \mathbf{V}_k^*$ , associated with the different eigenvalues  $\epsilon_k$  and  $\epsilon_k^* = -\epsilon_k$ . To have  $\epsilon_k = -\epsilon_k^*$ ,  $\mathbf{V}_k$  and  $\gamma\hat{R}\mathbf{V}_k^* = \gamma\mathbf{V}_{-k}^*$  must be linearly dependent, related by a complex phase  $e^{i\theta}$ . Choosing this phase corresponds to a particular choice of the spatial phase of the emergent crystal. We here set  $\mathbf{V}_k = -\gamma\hat{R}\mathbf{V}_k^*$ , and we then also have  $\mathbf{W}_k = -\gamma\hat{R}\mathbf{W}_k^*$ . From this follows that  $\mathbf{V}_k = (u_k(x), -u_k^*(-x))^T$  and  $\mathbf{W}_k = (u_k^*(x), -u_k(-x))^T$ . We see  $\langle \mathbf{V}_k | \eta | \mathbf{V}_k \rangle = 0 = \langle \mathbf{W}_k | \eta | \mathbf{W}_k \rangle$  but we can choose the normalization of  $u_k(x)$  such that  $\langle \mathbf{W}_k | \eta | \mathbf{V}_k \rangle = \int dx (u_k(x)^2 - u_k^*(x)^2) = i$ . Then the action of  $\hat{H}_k$  on the subspace relevant to  $\epsilon_k$  is

$$\hat{H}_k = \Gamma_k \eta | \mathbf{V}_k \rangle \langle \mathbf{W}_k | \eta + \Gamma_k \eta | \mathbf{W}_k \rangle \langle \mathbf{V}_k | \eta + \dots$$

with  $\dots$  the part of  $\hat{\mathbf{H}}_k$  corresponding to modes with  $n > 0$ . Inserting this in Eq. 3, and noting that  $\mathbf{V}_{-k} = \hat{R}\mathbf{V}_k$  and so  $u_{-k}(x) = u_k(-x)$  gives

$$\begin{aligned}\hat{K}_2 &= \frac{1}{2} \sum_k \Gamma_k \left( \langle \hat{\Phi}_k | \eta | \mathbf{V}_k \rangle \langle \mathbf{W}_k | \eta | \hat{\Phi}_k \rangle + \langle \hat{\Phi}_k | \eta | \mathbf{W}_k \rangle \langle \mathbf{V}_k | \eta | \hat{\Phi}_k \rangle \right) + \dots \\ &= \frac{1}{2} \sum_k \Gamma_k (\hat{p}_k \hat{q}_{-k} + \hat{q}_k \hat{p}_{-k}) + \dots \\ &= \sum_{k>0} \Gamma_k \frac{1}{i} \left( \hat{a}_k \hat{a}_{-k} - \hat{a}_k^\dagger \hat{a}_{-k}^\dagger \right) + \dots\end{aligned}$$

where the dots denote contributions from stable modes of higher excitation energies  $|\epsilon_{k,n}|$  and the  $k=0$  Goldstone mode's "kinetic energy" term corresponding to free global phase diffusion [7], and we defined

$$\begin{aligned}\hat{p}_k &\equiv \langle \hat{\Phi}_k | \eta | \mathbf{V}_k \rangle = \int dx \left( u_k(x) \phi_k^\dagger + u_k^*(x) \phi_{-k} \right) \\ \hat{q}_k &\equiv \langle \hat{\Phi}_k | \eta | \mathbf{W}_k \rangle = \int dx \left( u_k^*(x) \phi_k^\dagger + u_k(-x) \phi_{-k} \right) \\ \hat{p}_k^\dagger &\equiv \langle \mathbf{V}_k | \eta | \hat{\Phi}_k \rangle = \int dx \left( u_k^*(x) \phi_k + u_k(-x) \phi_{-k}^\dagger \right) = \hat{p}_{-k} \\ \hat{q}_k^\dagger &\equiv \langle \mathbf{W}_k | \eta | \hat{\Phi}_k \rangle = \int dx \left( u_k(x) \phi_k + u_k^*(-x) \phi_{-k}^\dagger \right) = \hat{q}_{-k}\end{aligned}$$

with  $[\hat{q}_k, \hat{p}_{-k}] = i$  and other commutators zero and  $\hat{a}_k = (\hat{q}_k + i\hat{p}_k)/\sqrt{2}$ , accordingly  $\hat{a}_k^\dagger = (\hat{q}_k^\dagger - i\hat{p}_k^\dagger)/\sqrt{2} = (\hat{q}_{-k} - i\hat{p}_{-k})/\sqrt{2}$  and  $[\hat{a}_k, \hat{a}_k^\dagger] = 1$  with other commutators zero. Other choices of the phase between  $\mathbf{V}_k$  and  $\gamma \mathbf{V}_{-k}^*$  yield equivalent forms of the squeezing Hamiltonian [12] such as  $\Gamma_k (\hat{a}_k \hat{a}_{-k} + \hat{a}_k^\dagger \hat{a}_{-k}^\dagger)$ . The time-dependence of the operators is then:

$$\begin{aligned}\hat{a}_k(t) &= \cosh(\Gamma_k t) \hat{a}_k(0) - i \sinh(\Gamma_k t) \hat{a}_{-k}^\dagger(0), \\ \hat{a}_{-k}^\dagger(t) &= \cosh(\Gamma_k t) \hat{a}_{-k}^\dagger(0) + i \sinh(\Gamma_k t) \hat{a}_k(0).\end{aligned}\tag{5}$$

### Structure factor

The structure factor  $S_k$  is obtained as follows. From the density operator  $\hat{n}(x, y)$  we obtain the density fluctuation operator, only retaining the contribution from unstable modes

$$\delta\hat{n}(x, y) = \psi_0(x) \frac{1}{\sqrt{L}} \sum_k \left( \bar{u}_k(x) e^{iky} \hat{a}_k + \bar{v}_k^*(x) e^{iky} \hat{a}_{-k}^\dagger + \bar{u}_k^*(x) e^{-iky} \hat{a}_k^\dagger + \bar{v}_k(x) e^{-iky} \hat{a}_{-k} \right),\tag{6}$$

where  $\bar{u}_k = (u_k^* - iu_k)/\sqrt{2}$  and  $\bar{v}_k = -(u_k - iu_k^*)/\sqrt{2}$ . Integrating along  $x$  and taking the Fourier transform along  $y$  yields the Fourier component of the one-dimensional density profile with a wavevector  $q$  in the  $y$ -direction,

$$\begin{aligned}\delta\hat{n}_q &= \int dx \int dy \delta\hat{n}(x, y) e^{-iqy} \\ &= \sqrt{n_{1D}} \int dx \tilde{\psi}_0(x) \left[ (\bar{u}_q(x) + \bar{v}_{-q}(x)) \hat{a}_q + (\bar{u}_{-q}^*(x) + \bar{v}_q^*(x)) \hat{a}_{-q}^\dagger \right]\end{aligned}\tag{7}$$

Here we define  $\psi_0 = \sqrt{n_{1D}} \tilde{\psi}_0$  such that  $\int dx |\tilde{\psi}_0(x)|^2 = 1$ . We also have  $\int dx (|\bar{u}_k(x)|^2 - |\bar{v}_{-k}(x)|^2) = 1$ . The structure factor is defined as [13]

$$\begin{aligned}S_q &= \frac{1}{N} \langle \delta\hat{n}_q \delta\hat{n}_q^\dagger \rangle \\ &= \langle (A_q \hat{a}_q + A_q^* \hat{a}_{-q}^\dagger) (A_q^* \hat{a}_q^\dagger + A_q \hat{a}_{-q}) \rangle \\ &= |A_q|^2 \left( \langle 1 + \hat{a}_q^\dagger \hat{a}_q + \hat{a}_{-q}^\dagger \hat{a}_{-q} \rangle + \frac{1}{i} \langle \hat{a}_q \hat{a}_{-q} - \hat{a}_q^\dagger \hat{a}_{-q}^\dagger \rangle \right) \\ &= |A_q|^2 (1 + \nu) \cosh(2\Gamma_k t)\end{aligned}\tag{8}$$

where  $N = L n_{1D}$  is the total atom number. Since  $\langle \hat{a}_q \hat{a}_{-q} - \hat{a}_q^\dagger \hat{a}_{-q}^\dagger \rangle$  is an expectation value of an operator which commutes with the Hamiltonian, it is a constant of motion and here taken to be zero. The terms  $\langle \hat{a}_q^\dagger \hat{a}_q \rangle$  and  $\langle \hat{a}_{-q}^\dagger \hat{a}_{-q} \rangle$  correspond to the occupation numbers of modes  $\pm q$ . They are related to their values at  $t = 0$  using the operator time-dependence given in Eq. (5), and we denote the initial mode populations by  $\nu = \langle \hat{a}_q^\dagger(0) \hat{a}_q(0) \rangle + \langle \hat{a}_{-q}^\dagger(0) \hat{a}_{-q}(0) \rangle$ . The contribution of a single quantum to  $S_k$  is determined by the overlap integral  $A_q = A_{-q} = \int dx \tilde{\psi}_0(x)(\bar{u}_q(x) + \bar{v}_{-q}(x))$ .

### Limit of the Lowest Landau Level

The Bogoliubov analysis in the lowest Landau level was performed in [10], focussing on the stable regime occurring in a rotating saddle potential  $V(x, y) = \frac{1}{2}m\epsilon\omega^2(x^2 - y^2)$  (in the rotating frame coordinates). The rotation frequency was chosen such that the centrifugal force precisely cancelled the trapping force in the weaker ( $y$ -)direction, i.e.  $\Omega = \omega\sqrt{1-\epsilon}$ . The experiment performed here corresponds to no rotating saddle at all, i.e.  $\epsilon = 0$ . The Bogoliubov Hamiltonian is

$$\hat{K}_2 = \sum_k \left( \frac{\hbar^2 k^2}{2m^*} + 2g^* n_{1D} e^{-k^2 l_B^2/2} \right) \hat{a}_k^\dagger \hat{a}_k + \frac{g^* n_{1D}}{2} \sum_k e^{-k^2 l_B^2} \left( \hat{a}_k^\dagger \hat{a}_{-k}^\dagger + \hat{a}_k \hat{a}_{-k} \right)$$

with an effective 1D coupling constant  $g^* = g/\sqrt{2\pi l_B}$  and where the effective mass  $m^*$  of excitations is given by  $1/m^* = 1/m \left( 1 - \frac{4\Omega^2}{\omega_c^2} \right)$  with the cyclotron frequency  $\omega_c = \omega\sqrt{4-2\epsilon}$  modified by the anharmonic potential. One has  $m^* \approx \frac{2}{\epsilon}m$  for small  $\epsilon$ . We see that in the case relevant to the present experiment  $\epsilon = 0$  we have  $1/m^* = 0$ , corresponding to “infinitely heavy” excitations, i.e. a flat band without a kinetic mass term. Importantly, although only contact interactions are present, evolution in the rotating frame yields a  $k$ -dependent effective interaction, and correspondingly a magneto-roton minimum which evolves into a dynamical instability as the anharmonicity  $\epsilon$  decreases. The excitation spectrum follows as [10]

$$\epsilon_k^2 = \left[ \frac{\hbar^2 k^2}{2m^*} + g^* n_{1D} \left( 2e^{-k^2 l_B^2/2} - 1 \right) \right]^2 - g^{*2} n_{1D}^2 e^{-2k^2 l_B^2} \quad (9)$$

In the limit  $\epsilon = 0$  one has an unstable Goldstone branch between  $k = 0$  and  $k = k_c = \sqrt{2 \log \left( \frac{1}{\sqrt{2}-1} \right)} / l_B = 1.33 / l_B$ . The maximum growth rate of the instability occurs at  $k_{\max} l_B = \sqrt{2 \log \left( \frac{2}{\sqrt{5}-1} \right)} = 0.98$  and is  $\Gamma_{k_{\max}} = \sqrt{\frac{5}{2}\sqrt{5} - \frac{11}{2}} g^* n_{1D} = 0.3 g^* n_{1D} = 0.21gn$ . This is shown in Fig. 1a).

### Evolution from stable magneto-roton excitations to dynamical instability

The expression Eq. 9 allows us to follow the excitation spectrum in the 1D regime of motion in a rotating anharmonic saddle as  $\epsilon \rightarrow 0$ . This evolution is shown in Fig. 3, varying the parameter introduced in [10]  $\beta = \frac{n_{1D} g^*}{\hbar^2 / 2m^* l_B^2}$ , comparing the interaction energy to the kinetic energy of excitations at momentum  $\sim 1/l_B$ . The present experiment corresponds to  $\beta = \infty$ , i.e. zero kinetic energy, infinite effective mass of excitations and purely interaction-driven dynamics. The figure shows how an initially stable branch consisting of phonons at low momenta  $k$  develops a magneto-roton minimum at  $k \approx 1/l_B$ . This minimum lowers in energy as it becomes more and more favorable to create magneto-rotions, excitations which avoid the condensate mean-field repulsion due to their spatial shift by  $kl_B^2 \approx l_B$ . Beyond a critical  $\beta = 4.9$ , a dynamical instability near  $k \sim 1/l_B$  develops, corresponding to the onset of magneto-roton condensation - in analogy to roton condensation considered in [14, 15]. Eventually, for  $\beta \rightarrow \infty$ , the case of the present experiment, the entire Goldstone branch up to  $k = k_c$  is dynamically unstable, with maximum growth at  $k = k_{\max} \sim 1/l_B$ .

### Thomas-Fermi limit - Hydrodynamics

The Gross-Pitaevskii equation for the wavefunction  $\psi = \sqrt{\rho} e^{iS}$  can be equivalently rewritten as hydrodynamic equations for the density  $\rho = |\psi|^2$  and the velocity  $\mathbf{v} = \frac{\hbar}{m} \nabla S$ . The equation for the velocity is:

$$\frac{\partial \mathbf{v}}{\partial t} = -\nabla \left( -\frac{\hbar^2}{2m^2 \sqrt{\rho}} \nabla^2 \sqrt{\rho} + \frac{1}{2} \mathbf{v}^2 - \mathbf{v} \cdot (\boldsymbol{\Omega} \times \mathbf{r}) + \frac{1}{m} U + \frac{g\rho}{m} \right). \quad (10)$$

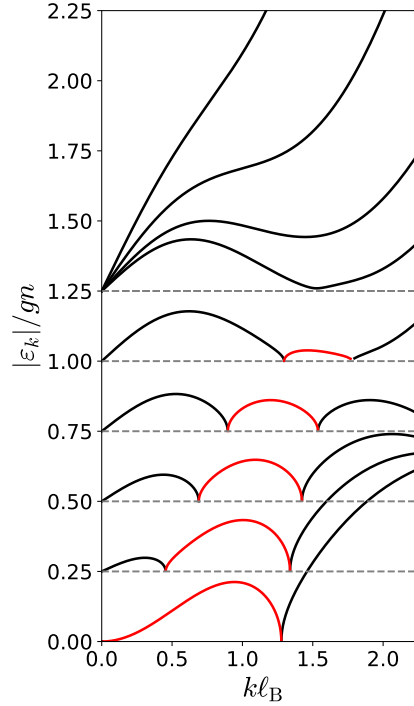


FIG. 3. Evolution from stable phonon and magneto-roton excitations to dynamically unstable excitations as the anharmonicity  $\epsilon$  of a rotating saddle potential is reduced to zero. From top to bottom, the value of the parameter  $\beta$ , measuring the strength of interaction energy to kinetic energy, is varied from  $\beta = 1, 2, 3.5, 4.9$  (the critical value where the magneto-roton minimum touches zero [10]),  $5.1, 7, 10, 20, 100000$ .

Here,  $U(\vec{r}, t) = \frac{1}{2}m\omega^2(x^2(1+\epsilon) + y^2(1-\epsilon))$  is a rotating anisotropic potential - in the experiment  $\epsilon = 0$ . Introducing the “convective derivative” moving with a fluid element,

$$\frac{D}{Dt} = \frac{\partial}{\partial t} + (\mathbf{v}_{\text{rot}} \cdot \nabla) \quad (11)$$

this can be written as

$$m \frac{D\mathbf{v}_{\text{rot}}}{Dt} = 2m\mathbf{v}_{\text{rot}} \times \boldsymbol{\Omega} + m\Omega^2\mathbf{r} - \nabla \left( -\frac{\hbar^2}{2m\sqrt{\rho}} \nabla^2 \sqrt{\rho} + U + g\rho \right). \quad (12)$$

with  $\mathbf{v}_{\text{rot}} = \mathbf{v} - \boldsymbol{\Omega} \times \mathbf{r}$  the velocity in the rotating frame. This is Newton’s law in the rotating frame, featuring the Coriolis force  $2m\mathbf{v}_{\text{rot}} \times \boldsymbol{\Omega}$ , the centrifugal force  $m\Omega^2\mathbf{r}$  and the force acting on a fluid particle derived from the quantum pressure  $-\frac{\hbar^2}{2m\sqrt{\rho}} \nabla^2 \sqrt{\rho}$ , the mean-field potential  $g\rho$ , and the external potential  $U$ . The continuity equation in the rotating frame  $\frac{\partial \rho}{\partial t} = -\nabla \cdot (\rho \mathbf{v}_{\text{rot}})$  can also be written using the convective derivative:

$$\frac{D\rho}{Dt} = -\rho \nabla \cdot \mathbf{v}_{\text{rot}}. \quad (13)$$

Linearizing the hydrodynamic equations - including the quantum pressure term - is equivalent to the Bogoliubov approach [2]. We now drop the quantum pressure term, considering the Thomas-Fermi limit.

We perturb the density and phase around stationary solutions  $\rho_c$  and  $S_c$

$$\begin{aligned} \rho &= \rho_c + \delta\rho \\ S &= S_c + \delta S \end{aligned} \quad (14)$$

and obtain the linearized hydrodynamic equations [16]

$$\begin{aligned} \frac{D\delta\rho}{Dt} &= -\frac{\hbar}{m} \nabla \cdot (\rho_c \nabla \delta S) \\ \hbar \frac{D\delta S}{Dt} &= -g\delta\rho \end{aligned} \quad (15)$$

### Hydrodynamics in the Landau gauge

The Landau gauge corresponds to setting  $S_c = -\frac{m\Omega}{\hbar}xy$ , and we specialize to  $\Omega = \omega\sqrt{1-\epsilon}$ , where the centrifugal potential exactly cancels the ( $y$ -)direction of weak confinement. The case in the experiment is  $\epsilon = 0$ . Neglecting the quantum pressure term (Thomas-Fermi limit), the stationary density profile is  $g\rho_c(x) = \mu - \frac{1}{2}m\omega_c^2x^2$ , the velocity profile is  $\mathbf{v}_c = \frac{\hbar}{m}\nabla S_c$  and we have  $\mathbf{v}_{\text{rot}} = \mathbf{v}_c - \boldsymbol{\Omega} \times \mathbf{r} = -2\Omega x \hat{\mathbf{y}}$ . The coupled linearized hydrodynamic equations become

$$\begin{aligned}\frac{\partial \delta\rho}{\partial t} - 2\Omega x \partial_y \delta\rho &= -\frac{\hbar}{m} \partial_x (\rho_c(x) \partial_x \delta S) - \frac{\hbar}{m} \rho_c(x) \partial_y^2 \delta S \\ \frac{\partial \delta S}{\partial t} - 2\Omega x \partial_y \delta S &= -\frac{1}{\hbar} g \delta\rho\end{aligned}\quad (16)$$

As there is no explicit dependence on  $y$ , one may choose  $\delta\rho = \text{Re}(e^{iky}\delta\rho_k)$  and  $\delta S = \text{Re}(e^{iky}\delta S_k)$ . We omit the index  $k$  in the following and find

$$\begin{aligned}\frac{\partial \delta\rho}{\partial t} - 2i\Omega kx \delta\rho &= -\frac{\hbar}{m} \partial_x (\rho_c(x) \partial_x \delta S) + \frac{\hbar k^2}{m} \rho_c(x) \delta S \\ \frac{\partial \delta S}{\partial t} - 2i\Omega kx \delta S &= -\frac{1}{\hbar} g \delta\rho\end{aligned}\quad (17)$$

Using  $g\rho_c(x) = \mu - \frac{1}{2}m\omega_c^2x^2$  and  $\partial_x g\rho_c(x) = -m\omega_c^2x$  we have

$$\frac{\partial g\delta\rho}{\partial t} - 2i\Omega kx g\delta\rho = \omega_c^2 x \partial_x \hbar \delta S - \frac{1}{m} \left( \mu - \frac{1}{2}m\omega_c^2x^2 \right) (\partial_x^2 - k^2) \hbar \delta S \quad (18)$$

Measuring rates and inverse times in units of  $\omega_c$  (such as  $\tilde{\Omega} = \Omega/\omega_c$ ), energies in units of  $\hbar\omega_c$  (writing  $\delta\tilde{\rho} = g\delta\rho/(\hbar\omega_c)$ ), and lengths in units of the Thomas-Fermi radius  $R_{\text{TF}} = \sqrt{2\mu/(m\omega_c^2)}$ , the equations become (tildes are dropped for brevity)

$$\begin{aligned}\frac{\partial \delta\rho}{\partial t} - 2i\Omega kx \delta\rho &= \left( x \partial_x - \frac{1}{2}(1-x^2)(\partial_x^2 - k^2) \right) \delta S \\ \frac{\partial \delta S}{\partial t} - 2i\Omega kx \delta S &= -\delta\rho\end{aligned}\quad (19)$$

The operator  $\mathcal{L} \equiv x \partial_x - \frac{1}{2}(1-x^2)\partial_x^2 = -\frac{1}{2}\partial_x((1-x^2)\partial_x)$  is Legendre's differential operator, whose eigenfunctions are the Legendre polynomials  $P_n(x)$ :

$$\mathcal{L}P_n(x) = \frac{1}{2}n(n+1)P_n(x) \quad (20)$$

In terms of  $\mathcal{L}$ , the coupled equations are

$$\begin{aligned}\frac{\partial \delta\rho}{\partial t} - 2i\Omega kx \delta\rho &= \left( \mathcal{L} + \frac{k^2}{2}(1-x^2) \right) \delta S \\ \frac{\partial \delta S}{\partial t} - 2i\Omega kx \delta S &= -\delta\rho\end{aligned}\quad (21)$$

Looking for a time-dependence  $\sim e^{-i\omega t}$ , the equations become

$$\begin{aligned}-i(\omega + 2\Omega kx)\delta\rho &= \left( \mathcal{L} + \frac{k^2}{2}(1-x^2) \right) \delta S \\ -i(\omega + 2\Omega kx)\delta S &= -\delta\rho\end{aligned}\quad (22)$$

and thus

$$(\omega + 2\Omega kx)^2 \delta S = \left( \mathcal{L} + \frac{k^2}{2}(1-x^2) \right) \delta S \quad (23)$$

The equation is formally solved by the confluent Heun function [17], with eigenfrequencies obtained by demanding the solution to be regular everywhere inside the Thomas-Fermi radius ( $|x| < 1$ ). In particular, for  $\epsilon = 0$  and so  $2\Omega = \omega_c$  we have  $\delta S = e^{\sqrt{3}kx} H_C [2(k^2 + k(\sqrt{3} - 2\omega) + \omega^2), 4k(\sqrt{3} - 2\omega), 1, 1, 4\sqrt{3}k, \frac{1+x}{2}]$ , where  $H_C [q, \alpha, \gamma, \delta, \kappa, z]$  satisfies the confluent Heun differential equation  $z(z-1)y'' + (\gamma(z-1) + \delta z + z(z-1)\kappa)y' + (\alpha z - q)y = 0$  [17]. Notably, exceptional points where  $\omega = 0$  are obtained as special zeroes of the confluent Heun function:  $H_C [2k^2 + 2\sqrt{3}k, 4\sqrt{3}k, 1, 1, 4\sqrt{3}k, \frac{1}{2}] = 0$ . The critical  $k = k_c$  separating the dynamically unstable modes for  $0 < k < k_c$  and the stable excitations for  $k > k_c$  is obtained as the first zero of this particular Heun function, at  $k_c = 1.47/R_{\text{TF}} = 1.25/R$ . Below we find limiting cases, a series expansion for the solution, and identify the minimal set of modes responsible for the instability: The Goldstone mode, dipole mode and breathing mode of the unperturbed condensate.

### Solution for $k \rightarrow 0$

For  $k = 0$  the problem is just that of finding the excitation spectrum of a Bose-Einstein condensate in a one-dimensional harmonic oscillator:

$$\omega^2 \delta S = \mathcal{L} \delta S \quad (24)$$

with eigenvalues  $\omega_n = \sqrt{\frac{1}{2}n(n+1)}$ , in units of  $\omega_c$ , and eigenfunctions  $\delta S = P_n(x)$ . The case  $n = 1$  is the sloshing mode, oscillating at the cyclotron frequency with  $\omega_1 = \omega_c$ , unshifted from the result for the non-interacting harmonic oscillator, in accordance with Kohn's theorem [8, 9]. Including the long-wavelength modulation  $\propto \sin(ky)$ , the mode is described by

$$\begin{aligned} \delta S(x, y, t) &\propto x \cos(\omega_c t) \sin(ky) \\ \delta \rho(x, y, t) &\propto x \sin(\omega_c t) \sin(ky) \end{aligned}$$

which is a time-dependent “snaking” mode, sloshing back and forth along  $x$  at frequency  $\omega_c$ .

The case  $n = 2$  is the breathing mode, at  $\omega_2 = \sqrt{3}\omega_c$ , shifted from the non-interacting case ( $2\omega_c$ ) by the interactions, and describing a time-dependent compression / decompression mode that periodically alternates along  $y$ .

The case  $n = 0$  and  $k = 0$  is the Goldstone mode at  $\omega_0 = 0$ , with  $\delta S(x) = \text{const.}$  a constant phase offset, and  $\delta \rho = 0$ , i.e. no density modulation, describing the zero cost of changing the phase of the wavefunction globally. For the case in the experiment  $\epsilon = 0$ , i.e.  $\Omega = \omega$ , and neglecting coupling to the breathing mode, one still has the zero-energy solution  $\omega_0 = 0$ , since there is zero energy cost to displace the wavefunction along  $x$ . The mode profile is  $\delta \rho(x, y, t) \propto \Omega k x \cos(ky)$ , corresponding to a stationary “snake”-like deformation. With coupling to the breathing mode, it will grow exponentially.

### Solution by expansion in Legendre polynomials

To solve the equations for  $\delta \rho$  and  $\delta S$ , we expand them in the basis of normalized Legendre polynomials  $p_n(x) \equiv \sqrt{\frac{2n+1}{2}} P_n(x)$  (with  $P_n(x)$  the traditional Legendre polynomials):

$$\begin{aligned} \delta \rho(x) &= \sum_n \rho_n p_n(x) \\ \delta S(x) &= \sum_n s_n p_n(x) \end{aligned}$$

The  $p_n(x)$  are orthonormal for integration over  $x \in [-1, 1]$  (while the  $P_n(x)$  are not):

$$\langle n | m \rangle = \int_{-1}^1 dx p_n(x) p_m(x) = \delta_{n,m}$$

where  $\langle f | g \rangle = \int_{-1}^1 dx f(x) g(x)$  defines a scalar product. The  $p_n(x)$  are eigenfunctions of  $\mathcal{L}$ , but the terms in  $x$  and in  $x^2$  in the equations 22 couple Legendre polynomials whose index differs by 1 or 2, respectively. A recurrence relation for Legendre polynomials gives

$$x P_n = \frac{n+1}{2n+1} P_{n+1} + \frac{n}{2n+1} P_{n-1}$$

which for the orthonormal  $p_n$  reads

$$x p_n = \frac{n+1}{\sqrt{(2n+1)(2n+3)}} p_{n+1} + \frac{n}{\sqrt{(2n+1)(2n-1)}} p_{n-1}$$

from which one finds

$$X_{nm} \equiv \langle n | x | m \rangle = \int_{-1}^1 dx p_n(x) x p_m(x) = \frac{1}{\sqrt{(2n+1)(2m+1)}} (n \delta_{m,n-1} + m \delta_{n,m-1})$$

$$\begin{aligned}
(X^2)_{nm} &= \langle n|x^2|m \rangle = \sum_j \langle n|x|j \rangle \langle j|x|m \rangle = \sum_j X_{nj} X_{jm} \\
&= \sum_j \frac{1}{\sqrt{(2n+1)(2m+1)}} \frac{1}{2j+1} (n\delta_{j,n-1} + j\delta_{n,j-1}) (j\delta_{m,j-1} + m\delta_{j,m-1}) \\
&= \frac{(2n(n+1)-1)}{(2n-1)(2n+3)} \delta_{n,m} + \frac{1}{\sqrt{(2n+1)(2m+1)}} \left( \frac{m(m-1)}{(2m-1)} \delta_{m,n+2} + \frac{n(n-1)}{(2n-1)} \delta_{n,m+2} \right)
\end{aligned}$$

The equations 22 can then be written

$$\begin{aligned}
\frac{\partial \rho_n}{\partial t} &= i2\Omega k X_{nm} \rho_m + \mathcal{L}_{nm}^{(k)} s_m \\
\frac{\partial s_n}{\partial t} &= i2\Omega k X_{nm} s_m - \rho_n
\end{aligned} \tag{25}$$

(using convention to sum over repeated indices) or in vector notation  $\vec{\rho} = (\rho_0, \rho_1, \dots)^T$

$$\begin{aligned}
\frac{\partial \vec{\rho}}{\partial t} &= i2\Omega k X \vec{\rho} + \mathcal{L}^{(k)} \vec{s} \\
\frac{\partial \vec{s}}{\partial t} &= i2\Omega k X \vec{s} - \vec{\rho}
\end{aligned} \tag{26}$$

where  $X$  is the matrix with entries  $X_{nm}$ , and where

$$\mathcal{L}_{nm}^{(k)} = \left( \frac{1}{2} n(n+1) + \frac{k^2}{2} \right) \delta_{nm} - \frac{k^2}{2} (X^2)_{nm}$$

This linear system is solved by choosing a cutoff in the degree  $n$  of polynomials used in the expansion. Alternatively, we can start with Eq. 23, which is particularly useful for the case relevant to the present experiment  $\epsilon = 0$ , so  $2\Omega = \omega_c \equiv 1$  in dimensionless units. We have

$$(\omega + kx)^2 - \frac{k^2}{2}(1-x^2) = \omega^2 + 2\omega kx + k^2 \left( \frac{3}{2}x^2 - \frac{1}{2} \right) = \omega^2 P_0 + 2\omega k P_1 + k^2 P_2$$

since  $P_2(x) = \frac{3}{2}x^2 - \frac{1}{2}$ . So the equation to solve is

$$\mathcal{L} \delta S = (k^2 P_2 + 2\omega k P_1 + \omega^2 P_0) \delta S$$

This way of writing the equation makes it explicit that the cause of the instability of the Goldstone mode ( $\omega = 0$  for  $k = 0$ ) is coupling to the breathing mode with  $n = 2$ , caused by  $P_2$ . The term multiplying  $P_1$ , which could in principle couple the Goldstone to the dipole mode, is zero for  $\omega = 0$  and thus is not responsible for the instability. In the basis of orthonormal Legendre polynomials, we have

$$(P_2(x))_{nm} = \frac{3}{2} (X^2)_{nm} - \frac{1}{2} \delta_{nm}. \tag{27}$$

On the off-diagonals, it acts like  $\frac{3}{2}(X^2)_{nm}$ , but on the diagonal one finds the simpler

$$(P_2(x))_{nn} = \frac{n(n+1)}{(2n-1)(2n+3)} \tag{28}$$

This yields the equation for the  $s_n$ :

$$\begin{aligned}
\left( \frac{1}{2} n(n+1) \left( 1 - \frac{2k^2}{(2n-1)(2n+3)} \right) - \omega^2 \right) s_n &= 2\omega k X_{nm} s_m + \frac{3}{2} k^2 \sum_{m \neq n} (X^2)_{nm} s_m \\
&= 2\omega k \left( \frac{n}{\sqrt{(2n-1)(2n+1)}} s_{n-1} + \frac{n+1}{\sqrt{(2n+1)(2n+3)}} s_{n+1} \right) \\
&\quad + \frac{3}{2} k^2 \left( \frac{(n+1)(n+2)}{(2n+3)\sqrt{(2n+1)(2n+5)}} s_{n+2} + \frac{n(n-1)}{(2n-1)\sqrt{(2n-3)(2n+1)}} s_{n-2} \right)
\end{aligned}$$

With a finite cutoff in the polynomial degree  $n$  this represents a sparse matrix, and eigenfrequencies are found by setting its determinant to zero. In general, eigenfrequencies can be complex and one finds an unstable Goldstone branch. The result is shown as the dashed lines in Fig. 1e).

*Minimal model*

Insight is obtained by truncating the Hilbert space. Including the Goldstone, dipole and breathing mode, so  $p_0$ ,  $p_1$  and  $p_2$  gives equations for the coefficients  $(s_0, s_1, s_2)$

$$\begin{pmatrix} \omega^2 & \frac{2k\omega}{\sqrt{3}} & \frac{k^2}{\sqrt{5}} \\ \frac{2k\omega}{\sqrt{3}} & \frac{2k^2}{5} + \omega^2 - 1 & \frac{4k\omega}{\sqrt{15}} \\ \frac{k^2}{\sqrt{5}} & \frac{4k\omega}{\sqrt{15}} & \frac{2k^2}{7} + \omega^2 - 3 \end{pmatrix} \begin{pmatrix} s_0 \\ s_1 \\ s_2 \end{pmatrix} = 0$$

This minimal model already yields a dynamically unstable Goldstone branch which will lead to exponential growth for small  $k$ . To find the critical  $k=k_c$  where  $\omega=0$  one solves

$$\begin{vmatrix} 0 & 0 & \frac{k^2}{\sqrt{5}} \\ 0 & \frac{2k^2}{5} - 1 & 0 \\ \frac{k^2}{\sqrt{5}} & 0 & \frac{2k^2}{7} - 3 \end{vmatrix} = 0 \quad (29)$$

from which one finds  $k_c R_{\text{TF}} = \sqrt{\frac{5}{2}} = 1.58$ . This is already close to the exact result  $k_c R_{\text{TF}} = 1.47$ . The maximum instability is found at  $k_{\max} R_{\text{TF}} \approx 1.18$  with  $\text{Im } \omega = 0.148 \omega_c$ , close to the exact maximum in the Thomas-Fermi limit at  $k_{\max} R_{\text{TF}} = 1.12\dots$  with  $\text{Im } \omega = 0.141 \omega_c$ .

- [1] N. N. Bogoliubov, “On the theory of superfluidity,” *J. Phys. (USSR)* **11**, 23 (1947).
- [2] A. L. Fetter, “Ground state and excited states of a confined condensed Bose gas,” *Phys. Rev. A* **53**, 4245 (1996).
- [3] Yuki Kawaguchi and Masahito Ueda, “Spinor bose-einstein condensates,” *Physics Reports* **520**, 253–381 (2012), spinor Bose-Einstein condensates.
- [4] Jean-Paul Blaizot and Georges Ripka, *Quantum Theory of Finite Systems* (MIT Press, 1986).
- [5] R. Barnett, “Edge-state instabilities of bosons in a topological band,” *Phys. Rev. A* **88**, 063631 (2013).
- [6] Y. Ashida, Z Gong, and M Ueda, “Non-hermitian physics,” *Advances in Physics* **69**, 249–435 (2020).
- [7] Y. Castin and R. Dum, “Low-temperature Bose-Einstein condensates in time-dependent traps: Beyond the u(1) symmetry-breaking approach,” *Phys. Rev. A* **57**, 3008 (1998).
- [8] W. Kohn, “Cyclotron resonance and de haas-van alphen oscillations of an interacting electron gas,” *Phys. Rev.* **123**, 1242–1244 (1961).
- [9] Alexander L. Fetter and Daniel Rokhsar, “Excited states of a dilute bose-einstein condensate in a harmonic trap,” *Phys. Rev. A* **57**, 1191–1201 (1998).
- [10] S. Sinha and G. V. Shlyapnikov, “Two-dimensional Bose-Einstein condensate under extreme rotation,” *Phys. Rev. Lett.* **94**, 150401 (2005).
- [11] H.G. Dehmelt, “Radiofrequency spectroscopy of stored ions i: Storage\*\*part ii: Spectroscopy is now scheduled to appear in volume v of this series.” (Academic Press, 1968) pp. 53–72.
- [12] L. J. Garay, J. R. Anglin, J. I. Cirac, and P. Zoller, “Sonic Analog of Gravitational Black Holes in Bose-Einstein Condensates,” *Phys. Rev. Lett.* **85**, 4643–4647 (2000).
- [13] L. Pitaevskii and S. Stringari, *Bose-Einstein Condensation* (Oxford University Press, Oxford, 2003).
- [14] S V Iordanskii and Lev P Pitaevskii, “Bose condensation of moving rottons,” *Soviet Physics Uspekhi* **23**, 317–318 (1980).
- [15] L P Pitaevskii, “Layered structure of superfluid  ${}^4\text{He}$  with supercritical motion,” *JETP Letters* **39**, 511–514 (1984).
- [16] Subhasis Sinha and Yvan Castin, “Dynamic instability of a rotating Bose-Einstein condensate,” *Phys. Rev. Lett.* **87**, 190402 (2001).
- [17] A. Ronveaux, ed., *Heun’s Differential Equations* (Oxford University Press, New York, 1995).



# Bibliography

- [1] Nonlinear standing waves in closed tubes. In Bengt O. Enflo and Claes M. Hedberg, editors, *Theory of Nonlinear Acoustics in Fluids*, Fluid Mechanics and Its Applications, pages 219–250. Springer Netherlands, Dordrecht, 2002.
- [2] A A Abrikosov and I M Khalatnikov. The theory of a fermi liquid (the properties of liquid  $^3\text{He}$  at low temperatures). *Rep. Prog. Phys.*, 22(1):329–367, January 1959.
- [3] Allan Adams, Lincoln D. Carr, Thomas Schäfer, Peter Steinberg, and John E. Thomas. Strongly correlated quantum fluids: Ultracold quantum gases, quantum chromodynamic plasmas and holographic duality. *New J. Phys.*, 14(11):115009, November 2012.
- [4] M. H. Anderson, J. R. Ensher, M. R. Matthews, C. E. Wieman, and E. A. Cornell. Observation of Bose-Einstein Condensation in a Dilute Atomic Vapor. *Science*, July 1995.
- [5] Nils Andersson. A Superfluid Perspective on Neutron Star Dynamics. *Universe*, 7(1):17, January 2021.
- [6] Neil W. Ashcroft and N. David Mermin. *Solid State Physics*. Cengage Learning, 2011.
- [7] Lorin Baird, Xin Wang, Stetson Roof, and J. E. Thomas. Measuring the Hydrodynamic Linear Response of a Unitary Fermi Gas. *Phys. Rev. Lett.*, 123(16):160402, October 2019.
- [8] M. A. Baranov, Klaus Osterloh, and M. Lewenstein. Fractional Quantum Hall States in Ultracold Rapidly Rotating Dipolar Fermi Gases. *Phys. Rev. Lett.*, 94(7):070404, February 2005.
- [9] J. Bardeen, L. N. Cooper, and J. R. Schrieffer. Theory of Superconductivity. *Phys. Rev.*, 108(5):1175–1204, December 1957.
- [10] A. B. Bardon, S. Beattie, C. Luciuk, W. Cairncross, D. Fine, N. S. Cheng, G. J. A. Edge, E. Taylor, S. Zhang, S. Trotzky, and J. H. Thywissen. Transverse Demagnetization Dynamics of a Unitary Fermi Gas. *Science*, May 2014.

- [11] M. Bartenstein, A. Altmeyer, S. Riedl, S. Jochim, C. Chin, J. Hecker Denschlag, and R. Grimm. Collective Excitations of a Degenerate Gas at the BEC-BCS Crossover. *Phys. Rev. Lett.*, 92(20):203201, May 2004.
- [12] I. Bausmerth, A. Recati, and S. Stringari. Chandrasekhar-Clogston limit and phase separation in Fermi mixtures at unitarity. *Phys. Rev. A*, 79(4):043622, April 2009.
- [13] Gordon Baym and Christopher Pethick. *Landau Fermi-Liquid Theory: Concepts and Applications*. John Wiley & Sons, September 2008.
- [14] K. H. Bennemann, John Boyd Ketterson, and J. B. Ketterson. *The Physics of Liquid and Solid Helium*. Wiley, 1976.
- [15] Karl-Heinz Bennemann and John B. Ketterson. *Novel Superfluids: Volume 2*. OUP Oxford, November 2014.
- [16] Hannes Bernien, Sylvain Schwartz, Alexander Keesling, Harry Levine, Ahmed Omran, Hannes Pichler, Soonwon Choi, Alexander S. Zibrov, Manuel Endres, Markus Greiner, Vlastan Vuletić, and Mikhail D. Lukin. Probing many-body dynamics on a 51-atom quantum simulator. *Nature*, 551(7682):579–584, November 2017.
- [17] A. Bijl, J. de Boer, and A. Michels. Properties of liquid helium II. *Physica*, 8(7):655–675, July 1941.
- [18] Hauke Biss, Lennart Sobirey, Niclas Luick, Markus Bohlen, Jami J. Kinnunen, Georg M. Bruun, Thomas Lompe, and Henning Moritz. Excitation Spectrum and Superfluid Gap of an Ultracold Fermi Gas. May 2021.
- [19] Leif Bjørnø. Introduction to nonlinear acoustics. *Physics Procedia*, 3(1):5–16, January 2010.
- [20] Immanuel Bloch, Jean Dalibard, and Sylvain Nascimbène. Quantum simulations with ultracold quantum gases. *Nature Phys*, 8(4):267–276, April 2012.
- [21] Immanuel Bloch, Jean Dalibard, and Wilhelm Zwerger. Many-body physics with ultracold gases. *Rev. Mod. Phys.*, 80(3):885–964, July 2008.
- [22] Marcus Bluhm, Jiaxun Hou, and Thomas Schäfer. Determination of the Density and Temperature Dependence of the Shear Viscosity of a Unitary Fermi Gas Based on Hydrodynamic Flow. *Phys. Rev. Lett.*, 119(6):065302, August 2017.
- [23] Markus Bohlen, Lennart Sobirey, Niclas Luick, Hauke Biss, Tilman Enss, Thomas Lompe, and Henning Moritz. Sound Propagation and Quantum-Limited Damping in a Two-Dimensional Fermi Gas. *Phys. Rev. Lett.*, 124(24):240403, June 2020.

- [24] Martin Boll, Timon A. Hilker, Guillaume Salomon, Ahmed Omran, Jacopo Nespolo, Lode Pollet, Immanuel Bloch, and Christian Gross. Spin- and density-resolved microscopy of antiferromagnetic correlations in Fermi-Hubbard chains. *Science*, September 2016.
- [25] Matt Braby, Jingyi Chao, and Thomas Schäfer. Thermal conductivity and sound attenuation in dilute atomic Fermi gases. *Phys. Rev. A*, 82(3):033619, September 2010.
- [26] Jean-Philippe Brantut, Charles Grenier, Jakob Meineke, David Stadler, Sebastian Krinner, Corinna Kollath, Tilman Esslinger, and Antoine Georges. A Thermoelectric Heat Engine with Ultracold Atoms. *Science*, November 2013.
- [27] Jean-Philippe Brantut, Jakob Meineke, David Stadler, Sebastian Krinner, and Tilman Esslinger. Conduction of Ultracold Fermions Through a Mesoscopic Channel. *Science*, August 2012.
- [28] G. M. Bruun. Spin diffusion in Fermi gases. *New J. Phys.*, 13(3):035005, March 2011.
- [29] G. M. Bruun and H. Smith. Viscosity and thermal relaxation for a resonantly interacting Fermi gas. *Phys. Rev. A*, 72(4):043605, October 2005.
- [30] Iulia Buluta and Franco Nori. Quantum Simulators. *Science*, October 2009.
- [31] C. Cao, E. Elliott, J. Joseph, H. Wu, J. Petricka, T. Schäfer, and J. E. Thomas. Universal Quantum Viscosity in a Unitary Fermi Gas. *Science*, January 2011.
- [32] Yuan Cao, Valla Fatemi, Shiang Fang, Kenji Watanabe, Takashi Taniguchi, Efthimios Kaxiras, and Pablo Jarillo-Herrero. Unconventional superconductivity in magic-angle graphene superlattices. *Nature*, 556(7699):43–50, April 2018.
- [33] C. Carcy, S. Hoinka, M. G. Lingham, P. Dyke, C. C. N. Kuhn, H. Hu, and C. J. Vale. Contact and Sum Rules in a Near-Uniform Fermi Gas at Unitarity. *Phys. Rev. Lett.*, 122(20):203401, May 2019.
- [34] Yvan Castin. Exact scaling transform for a unitary quantum gas in a time dependent harmonic potential. *Comptes Rendus Physique*, 5(3):407–410, April 2004.
- [35] N. Chamel. Crustal Entrainment and Pulsar Glitches. *Phys. Rev. Lett.*, 110(1):011101, January 2013.
- [36] B. S. Chandrasekhar. A note on the maximum critical field of high-field superconductors. *Appl. Phys. Lett.*, 1(1):7–8, September 1962.
- [37] Lawrence W. Cheuk, Matthew A. Nichols, Katherine R. Lawrence, Melih Okan, Hao Zhang, Ehsan Khatami, Nandini Trivedi, Thereza Paiva, Marcos Rigol, and Martin W. Zwierlein. Observation of spatial charge and spin correlations in the 2D Fermi-Hubbard model. *Science*, September 2016.

- [38] Ananth P Chikkatur. *Colliding and Moving Bose-Einstein Condensates: Studies of Superfluidity and Optical Tweezers for Condensate Transport*. PhD thesis, Massachusetts Institute of Technology, 2002.
- [39] Cheng Chin, Rudolf Grimm, Paul Julienne, and Eite Tiesinga. Feshbach resonances in ultracold gases. *Rev. Mod. Phys.*, 82(2):1225–1286, April 2010.
- [40] Panagiotis Christodoulou, Maciej Gałka, Nishant Dogra, Raphael Lopes, Julian Schmitt, and Zoran Hadzibabic. Observation of first and second sound in a BKT superfluid. *Nature*, 594(7862):191–194, June 2021.
- [41] A. M. Clogston. Upper Limit for the Critical Field in Hard Superconductors. *Phys. Rev. Lett.*, 9(6):266–267, September 1962.
- [42] Claude Cohen-Tannoudji, Jacques Dupont-Roc, and Gilbert Grynberg. *Atom-Photon Interactions: Basic Processes and Applications*. Wiley, March 1998.
- [43] Piers Coleman and Andrew J. Schofield. Quantum criticality. *Nature*, 433(7023):226–229, January 2005.
- [44] K. B. Davis, M. O. Mewes, M. R. Andrews, N. J. van Druten, D. S. Durfee, D. M. Kurn, and W. Ketterle. Bose-Einstein Condensation in a Gas of Sodium Atoms. *Phys. Rev. Lett.*, 75(22):3969–3973, November 1995.
- [45] B. DeMarco and D. S. Jin. Onset of Fermi Degeneracy in a Trapped Atomic Gas. *Science*, September 1999.
- [46] Russell J. Donnelly and Carlo F. Barenghi. The Observed Properties of Liquid Helium at the Saturated Vapor Pressure. *Journal of Physical and Chemical Reference Data*, 27(6):1217–1274, November 1998.
- [47] T. E. Drake, Y. Sagi, R. Paudel, J. T. Stewart, J. P. Gaebler, and D. S. Jin. Direct observation of the Fermi surface in an ultracold atomic gas. *Phys. Rev. A*, 86(3):031601, September 2012.
- [48] Christoph Eigen, Alexander L. Gaunt, Aziza Suleymanzade, Nir Navon, Zoran Hadzibabic, and Robert P. Smith. Observation of Weak Collapse in a Bose-Einstein Condensate. *Phys. Rev. X*, 6(4):041058, December 2016.
- [49] Christoph Eigen, Jake A. P. Glidden, Raphael Lopes, Nir Navon, Zoran Hadzibabic, and Robert P. Smith. Universal Scaling Laws in the Dynamics of a Homogeneous Unitary Bose Gas. *Phys. Rev. Lett.*, 119(25):250404, December 2017.
- [50] E. Elliott, J. A. Joseph, and J. E. Thomas. Anomalous Minimum in the Shear Viscosity of a Fermi Gas. *Phys. Rev. Lett.*, 113(2):020406, July 2014.
- [51] Tilman Enss. Quantum critical transport in the unitary Fermi gas. *Phys. Rev. A*, 86(1):013616, July 2012.

- [52] Tilman Enss, Rudolf Haussmann, and Wilhelm Zwerger. Viscosity and scale invariance in the unitary Fermi gas. *Annals of Physics*, 326(3):770–796, March 2011.
- [53] G. Eska, K. Neumaier, W. Schoepe, K. Uhlig, W. Wiedemann, and P. Wölfle. First-Sound Attenuation and Viscosity of Superfluid  $\hat{3}\backslash\mathrm{mathrm{He}}\$-\$B\$$ . *Phys. Rev. Lett.*, 44(20):1337–1340, May 1980.
- [54] Richard J. Fletcher, Airlia Shaffer, Cedric C. Wilson, Parth B. Patel, Zhenjie Yan, Valentin Crépel, Biswaroop Mukherjee, and Martin W. Zwierlein. Geometric squeezing into the lowest Landau level. *Science*, June 2021.
- [55] C. J. Foot and Department of Physics Christopher J. Foot. *Atomic Physics*. Oxford University Press, 2005.
- [56] Bernhard Frank, Wilhelm Zwerger, and Tilman Enss. Quantum critical thermal transport in the unitary Fermi gas. *Phys. Rev. Research*, 2(2):023301, June 2020.
- [57] Keisuke Fujii and Yusuke Nishida. Bulk viscosity of resonating fermions revisited: Kubo formula, sum rule, and the dimer and high-temperature limits. *Phys. Rev. A*, 102(2):023310, August 2020.
- [58] Peter Fulde and Richard A. Ferrell. Superconductivity in a Strong Spin-Exchange Field. *Phys. Rev.*, 135(3A):A550–A563, August 1964.
- [59] Victor Galitski, Gediminas Juzeliūnas, and Ian B. Spielman. Artificial gauge fields with ultracold atoms. *Physics Today*, 72(1):38–44, January 2019.
- [60] Arti Garg, Mohit Randeria, and Nandini Trivedi. Strong correlations make high-temperature superconductors robust against disorder. *Nature Phys*, 4(10):762–765, October 2008.
- [61] Samuel J. Garratt, Christoph Eigen, Jinyi Zhang, Patrik Turzák, Raphael Lopes, Robert P. Smith, Zoran Hadzibabic, and Nir Navon. From single-particle excitations to sound waves in a box-trapped atomic Bose-Einstein condensate. *Phys. Rev. A*, 99(2):021601, February 2019.
- [62] Alexander L. Gaunt. *Degenerate Bose Gases: Tuning Interactions & Geometry*. PhD thesis, University of Cambridge, 2014.
- [63] Alexander L. Gaunt, Tobias F. Schmidutz, Igor Gotlibovych, Robert P. Smith, and Zoran Hadzibabic. Bose-Einstein Condensation of Atoms in a Uniform Potential. *Phys. Rev. Lett.*, 110(20):200406, May 2013.
- [64] Fabrice Gerbier and Jean Dalibard. Gauge fields for ultracold atoms in optical superlattices. *New J. Phys.*, 12(3):033007, March 2010.
- [65] N. Goldman, G. Juzeliūnas, P. Öhberg, and I. B. Spielman. Light-induced gauge fields for ultracold atoms. *Rep. Prog. Phys.*, 77(12):126401, November 2014.

- [66] Igor Gotlibovych, Tobias F. Schmidutz, Alexander L. Gaunt, Nir Navon, Robert P. Smith, and Zoran Hadzibabic. Observing properties of an interacting homogeneous Bose-Einstein condensate: Heisenberg-limited momentum spread, interaction energy, and free-expansion dynamics. *Phys. Rev. A*, 89(6):061604, June 2014.
- [67] S. R. Granade, M. E. Gehm, K. M. O'Hara, and J. E. Thomas. All-Optical Production of a Degenerate Fermi Gas. *Phys. Rev. Lett.*, 88(12):120405, March 2002.
- [68] M. Greiner, C. A. Regal, J. T. Stewart, and D. S. Jin. Probing Pair-Correlated Fermionic Atoms through Correlations in Atom Shot Noise. *Phys. Rev. Lett.*, 94(11):110401, March 2005.
- [69] David J. Griffiths. *Introduction to Quantum Mechanics*. Cambridge University Press, 2017.
- [70] Rudolf Grimm, Matthias Weidmüller, and Yurii B. Ovchinnikov. Optical Dipole Traps for Neutral Atoms. In Benjamin Bederson and Herbert Walther, editors, *Advances In Atomic, Molecular, and Optical Physics*, volume 42, pages 95–170. Academic Press, January 2000.
- [71] Christian Gross and Immanuel Bloch. Quantum simulations with ultracold atoms in optical lattices. *Science*, September 2017.
- [72] Edmundo R. Sánchez Guajardo, Meng Khoon Tey, Leonid A. Sidorenkov, and Rudolf Grimm. Higher-nodal collective modes in a resonantly interacting Fermi gas. *Phys. Rev. A*, 87(6):063601, June 2013.
- [73] Elmer Guardado-Sánchez, Peter T. Brown, Debayan Mitra, Trithep Devakul, David A. Huse, Peter Schauß, and Waseem S. Bakr. Probing the Quench Dynamics of Antiferromagnetic Correlations in a 2D Quantum Ising Spin System. *Phys. Rev. X*, 8(2):021069, June 2018.
- [74] Z. Hadzibabic, C. A. Stan, K. Dieckmann, S. Gupta, M. W. Zwierlein, A. Gör-litz, and W. Ketterle. Two-Species Mixture of Quantum Degenerate Bose and Fermi Gases. *Phys. Rev. Lett.*, 88(16):160401, April 2002.
- [75] Zoran Hadzibabic. *Studies of a Quantum Degenerate Fermionic Lithium Gas*. PhD thesis, Massachusetts Institute of Technology, 2003.
- [76] H E Hall and K Thompson. The viscosity of liquid helium 3. page 15.
- [77] Sean A. Hartnoll. Theory of universal incoherent metallic transport. *Nature Phys*, 11(1):54–61, January 2015.
- [78] R. Haussmann and W. Zwerger. Thermodynamics of a trapped unitary Fermi gas. *Phys. Rev. A*, 78(6):063602, December 2008.

- [79] R. W. Hill, Cyril Proust, Louis Taillefer, P. Fournier, and R. L. Greene. Breakdown of Fermi-liquid theory in a copper-oxide superconductor. *Nature*, 414(6865):711–715, December 2001.
- [80] Tin-Lun Ho and Qi Zhou. Obtaining the phase diagram and thermodynamic quantities of bulk systems from the densities of trapped gases. *Nature Phys*, 6(2):131–134, February 2010.
- [81] P. C Hohenberg and P. C Martin. Microscopic theory of superfluid helium. *Annals of Physics*, 34(2):291–359, September 1965.
- [82] Sascha Hoinka, Paul Dyke, Marcus G. Lingham, Jami J. Kinnunen, Georg M. Bruun, and Chris J. Vale. Goldstone mode and pair-breaking excitations in atomic Fermi superfluids. *Nature Phys*, 13(10):943–946, October 2017.
- [83] Munekazu Horikoshi, Masato Koashi, Hiroyuki Tajima, Yoji Ohashi, and Makoto Kuwata-Gonokami. Ground-State Thermodynamic Quantities of Homogeneous Spin-\$1/2\\$ Fermions from the BCS Region to the Unitarity Limit. *Phys. Rev. X*, 7(4):041004, October 2017.
- [84] Kerson Huang and C. N. Yang. Quantum-Mechanical Many-Body Problem with Hard-Sphere Interaction. *Phys. Rev.*, 105(3):767–775, February 1957.
- [85] Klaus Hueck, Niclas Luick, Lennart Sobiery, Jonas Siegl, Thomas Lompe, and Henning Moritz. Two-Dimensional Homogeneous Fermi Gases. *Phys. Rev. Lett.*, 120(6):060402, February 2018.
- [86] Dominik Husmann, Martin Lebrat, Samuel Häusler, Jean-Philippe Brantut, Laura Corman, and Tilman Esslinger. Breakdown of the Wiedemann–Franz law in a unitary Fermi gas. *PNAS*, 115(34):8563–8568, August 2018.
- [87] Boldizsár Jankó, Jiri Maly, and K. Levin. Pseudogap effects induced by resonant pair scattering. *Phys. Rev. B*, 56(18):R11407–R11410, November 1997.
- [88] S. Jensen, C. N. Gilbreth, and Y. Alhassid. The pseudogap regime in the unitary Fermi gas. *Eur. Phys. J. Spec. Top.*, 227(15):2241–2261, March 2019.
- [89] S. Jochim, M. Bartenstein, G. Hendl, J. Hecker Denschlag, R. Grimm, A. Mosk, and M. Weidemüller. Magnetic Field Control of Elastic Scattering in a Cold Gas of Fermionic Lithium Atoms. *Phys. Rev. Lett.*, 89(27):273202, December 2002.
- [90] J. A. Joseph, E. Elliott, and J. E. Thomas. Shear Viscosity of a Unitary Fermi Gas Near the Superfluid Phase Transition. *Phys. Rev. Lett.*, 115(2):020401, July 2015.
- [91] Leo P Kadanoff and Paul C Martin. Hydrodynamic equations and correlation functions. *Annals of Physics*, 24:419–469, October 1963.

- [92] Mehran Kardar. *Statistical Physics of Particles*. Cambridge University Press, June 2007.
- [93] W. Ketterle, D. S. Durfee, and D. M. Stamper-Kurn. Making, probing and understanding Bose-Einstein condensates. April 1999.
- [94] W. Ketterle and M. W. Zwierlein. Making, probing and understanding ultracold Fermi gases. *Riv. Nuovo Cim.*, 31(5):247–422, May 2008.
- [95] Wolfgang Ketterle, Kendall B. Davis, Michael A. Joffe, Alex Martin, and David E. Pritchard. High densities of cold atoms in a dark spontaneous-force optical trap. *Phys. Rev. Lett.*, 70(15):2253–2256, April 1993.
- [96] Isaak Markovich Khalatnikov. *An Introduction to the Theory of Superfluidity*. W.A. Benjamin, 1965.
- [97] J. Kinast, S. L. Hemmer, M. E. Gehm, A. Turlapov, and J. E. Thomas. Evidence for Superfluidity in a Resonantly Interacting Fermi Gas. *Phys. Rev. Lett.*, 92(15):150402, April 2004.
- [98] J. Kinast, A. Turlapov, and J. E. Thomas. Damping of a Unitary Fermi Gas. *Phys. Rev. Lett.*, 94(17):170404, May 2005.
- [99] Kittel. *Introduction to Solid State Physics, 7th Edition*. Wiley India Pvt. Limited, 2007.
- [100] Marco Koschorreck, Daniel Pertot, Enrico Vogt, and Michael Köhl. Universal spin dynamics in two-dimensional Fermi gases. *Nature Phys*, 9(7):405–409, July 2013.
- [101] Sebastian Krinner, Martin Lebrat, Dominik Husmann, Charles Grenier, Jean-Philippe Brantut, and Tilman Esslinger. Mapping out spin and particle conductances in a quantum point contact. *PNAS*, 113(29):8144–8149, July 2016.
- [102] Mark Ku. *Thermodynamics and Solitonic Excitations of a Strongly-Interacting Fermi Gas*. PhD thesis, Massachusetts Institute of Technology, 2015.
- [103] Mark J. H. Ku, Ariel T. Sommer, Lawrence W. Cheuk, and Martin W. Zwierlein. Revealing the Superfluid Lambda Transition in the Universal Thermodynamics of a Unitary Fermi Gas. *Science*, 335(6068):563–567, February 2012.
- [104] C. C. N. Kuhn, S. Hoinka, I. Herrera, P. Dyke, J. J. Kinnunen, G. M. Bruun, and C. J. Vale. High-Frequency Sound in a Unitary Fermi Gas. *Phys. Rev. Lett.*, 124(15):150401, April 2020.
- [105] H. Kurkjian, Y. Castin, and A. Sinatra. Concavity of the collective excitation branch of a Fermi gas in the BEC-BCS crossover. *Phys. Rev. A*, 93(1):013623, January 2016.

- [106] H. Kurkjian, Y. Castin, and A. Sinatra. Three-Phonon and Four-Phonon Interaction Processes in a Pair-Condensed Fermi Gas: Three-Phonon and Four-Phonon Interaction Processes in a Pair-Condensed Fermi Gas. *ANNALEN DER PHYSIK*, 529(9):1600352, September 2017.
- [107] L. Landau. Theory of the Superfluidity of Helium II. *Phys. Rev.*, 60(4):356–358, August 1941.
- [108] L. D. Landau and E. M. Lifshitz. *Fluid Mechanics*. Pergamon, second edition, January 1987.
- [109] Martin Lebrat, Samuel Häusler, Philipp Fabritius, Dominik Husmann, Laura Corman, and Tilman Esslinger. Quantized Conductance through a Spin-Selective Atomic Point Contact. *Phys. Rev. Lett.*, 123(19):193605, November 2019.
- [110] Sangwook Lee, Kedar Hippalgaonkar, Fan Yang, Jiawang Hong, Changhyun Ko, Joonki Suh, Kai Liu, Kevin Wang, Jeffrey J. Urban, Xiang Zhang, Chris Dames, Sean A. Hartnoll, Olivier Delaire, and Junqiao Wu. Anomalously low electronic thermal conductivity in metallic vanadium dioxide. *Science*, January 2017.
- [111] A. Legros, S. Benhabib, W. Tabis, F. Laliberté, M. Dion, M. Lizaire, B. Vignolle, D. Vignolles, H. Raffy, Z. Z. Li, P. Auban-Senzier, N. Doiron-Leyraud, P. Fournier, D. Colson, L. Taillefer, and C. Proust. Universal T-linear resistivity and Planckian dissipation in overdoped cuprates. *Nature Phys*, 15(2):142–147, February 2019.
- [112] Y.-J. Lin, R. L. Compton, K. Jiménez-García, J. V. Porto, and I. B. Spielman. Synthetic magnetic fields for ultracold neutral atoms. *Nature*, 462(7273):628–632, December 2009.
- [113] Raphael Lopes, Christoph Eigen, Adam Barker, Konrad G. H. Viebahn, Martin Robert-de-Saint-Vincent, Nir Navon, Zoran Hadzibabic, and Robert P. Smith. Quasiparticle Energy in a Strongly Interacting Homogeneous Bose-Einstein Condensate. *Phys. Rev. Lett.*, 118(21):210401, May 2017.
- [114] Raphael Lopes, Christoph Eigen, Nir Navon, David Clément, Robert P. Smith, and Zoran Hadzibabic. Quantum Depletion of a Homogeneous Bose-Einstein Condensate. *Phys. Rev. Lett.*, 119(19):190404, November 2017.
- [115] Robert Löw, Hendrik Weimer, Johannes Nipper, Jonathan B. Balewski, Björn Butscher, Hans Peter Büchler, and Tilman Pfau. An experimental and theoretical guide to strongly interacting Rydberg gases. *J. Phys. B: At. Mol. Opt. Phys.*, 45(11):113001, May 2012.
- [116] Andrew Lucas. Conductivity of a strange metal: From holography to memory functions. *J. High Energ. Phys.*, 2015(3):1–17, March 2015.

- [117] C. Luciu, S. Smale, F. Böttcher, H. Sharum, B. A. Olsen, S. Trotzky, T. Enss, and J. H. Thywissen. Observation of Quantum-Limited Spin Transport in Strongly Interacting Two-Dimensional Fermi Gases. *Phys. Rev. Lett.*, 118(13):130405, March 2017.
- [118] Niclas Luick, Lennart Sobirey, Markus Bohlen, Vijay Pal Singh, Ludwig Mathey, Thomas Lompe, and Henning Moritz. An ideal Josephson junction in an ultracold two-dimensional Fermi gas. *Science*, July 2020.
- [119] Victor S. L’vov, Ladislav Skrbek, and Katepalli R. Sreenivasan. Viscosity of liquid  $4\text{He}$  and quantum of circulation: Are they related? *Physics of Fluids*, 26(4):041703, April 2014.
- [120] I Manek, Yu. B Ovchinnikov, and R Grimm. Generation of a hollow laser beam for atom trapping using an axicon. *Optics Communications*, 147(1):67–70, February 1998.
- [121] P. Massignan, G. M. Bruun, and H. Smith. Viscous relaxation and collective oscillations in a trapped Fermi gas near the unitarity limit. *Phys. Rev. A*, 71(3):033607, March 2005.
- [122] Anton Mazurenko, Christie S. Chiu, Geoffrey Ji, Maxwell F. Parsons, Márton Kanász-Nagy, Richard Schmidt, Fabian Grusdt, Eugene Demler, Daniel Greif, and Markus Greiner. A cold-atom Fermi–Hubbard antiferromagnet. *Nature*, 545(7655):462–466, May 2017.
- [123] John H. McLeod. The Axicon: A New Type of Optical Element. *J. Opt. Soc. Am., JOSA*, 44(8):592–597, August 1954.
- [124] C. Menotti, P. Pedri, and S. Stringari. Expansion of an Interacting Fermi Gas. *Phys. Rev. Lett.*, 89(25):250402, December 2002.
- [125] Harold J. Metcalf and Peter Van der Straten. *Laser Cooling and Trapping*. Springer Science & Business Media, 1999.
- [126] B. Michon, A. Ataei, P. Bourgeois-Hope, C. Collignon, S. Y. Li, S. Badoux, A. Gourgout, F. Laliberté, J.-S. Zhou, Nicolas Doiron-Leyraud, and Louis Taillefer. Wiedemann-Franz Law and Abrupt Change in Conductivity across the Pseudogap Critical Point of a Cuprate Superconductor. *Phys. Rev. X*, 8(4):041010, October 2018.
- [127] Biswaroop Mukherjee. *Homogeneous Quantum Gases: Strongly Interacting Fermions and Rotating Bosonic Condensates*. PhD thesis, Massachusetts Institute of Technology, 2022.
- [128] Biswaroop Mukherjee, Parth B. Patel, Zhenjie Yan, Richard J. Fletcher, Julian Struck, and Martin W. Zwierlein. Spectral Response and Contact of the Unitary Fermi Gas. *Phys. Rev. Lett.*, 122(20):203402, May 2019.

- [129] Biswaroop Mukherjee, Airlia Shaffer, Parth B. Patel, Zhenjie Yan, Cedric C. Wilson, Valentin Crépel, Richard J. Fletcher, and Martin Zwierlein. Crystallization of bosonic quantum Hall states in a rotating quantum gas. *Nature*, 601(7891):58–62, January 2022.
- [130] Biswaroop Mukherjee, Zhenjie Yan, Parth B. Patel, Zoran Hadzibabic, Tarik Yefsah, Julian Struck, and Martin W. Zwierlein. Homogeneous Atomic Fermi Gases. *Phys. Rev. Lett.*, 118(12):123401, March 2017.
- [131] S. Nascimbène, N. Navon, K. J. Jiang, F. Chevy, and C. Salomon. Exploring the thermodynamics of a universal Fermi gas. *Nature*, 463(7284):1057–1060, February 2010.
- [132] S. Nascimbène, N. Navon, S. Pilati, F. Chevy, S. Giorgini, A. Georges, and C. Salomon. Fermi-Liquid Behavior of the Normal Phase of a Strongly Interacting Gas of Cold Atoms. *Phys. Rev. Lett.*, 106(21):215303, May 2011.
- [133] N. Navon, S. Nascimbène, F. Chevy, and C. Salomon. The Equation of State of a Low-Temperature Fermi Gas with Tunable Interactions. *Science*, May 2010.
- [134] Nir Navon, Alexander L. Gaunt, Robert P. Smith, and Zoran Hadzibabic. Critical dynamics of spontaneous symmetry breaking in a homogeneous Bose gas. *Science*, January 2015.
- [135] Yusuke Nishida, Dam Thanh Son, and Shina Tan. Universal Fermi Gas with Two- and Three-Body Resonances. *Phys. Rev. Lett.*, 100(9):090405, March 2008.
- [136] K. M. O’Hara, S. L. Hemmer, M. E. Gehm, S. R. Granade, and J. E. Thomas. Observation of a Strongly Interacting Degenerate Fermi Gas of Atoms. *Science*, December 2002.
- [137] Yoshimasa A. Ono, Jun’ichiro Hara, and Katsuhiko Nagai. Shear viscosity of the B phase of superfluid<sup>3</sup>He. III. *J Low Temp Phys*, 48(3):167–188, August 1982.
- [138] Dany Page, Madappa Prakash, James M. Lattimer, and Andrew W. Steiner. Rapid Cooling of the Neutron Star in Cassiopeia A Triggered by Neutron Superfluidity in Dense Matter. *Phys. Rev. Lett.*, 106(8):081101, February 2011.
- [139] M. M. Parish, F. M. Marchetti, A. Lamacraft, and B. D. Simons. Finite-temperature phase diagram of a polarized Fermi condensate. *Nature Phys*, 3(2):124–128, February 2007.
- [140] Guthrie B. Partridge, Wenhui Li, Ramsey I. Kamar, Yean-an Liao, and Randall G. Hulet. Pairing and Phase Separation in a Polarized Fermi Gas. *Science*, January 2006.

- [141] Parth B. Patel, Zhenjie Yan, Biswaroop Mukherjee, Richard J. Fletcher, Julian Struck, and Martin W. Zwierlein. Universal sound diffusion in a strongly interacting Fermi gas. *Science*, 370(6521):1222–1226, December 2020.
- [142] W. Pauli. The Connection Between Spin and Statistics. *Phys. Rev.*, 58(8):716–722, October 1940.
- [143] David Pekker, Mehrtash Babadi, Rajdeep Sensarma, Nikolaj Zinner, Lode Pollet, Martin W. Zwierlein, and Eugene Demler. Competition between Pairing and Ferromagnetic Instabilities in Ultracold Fermi Gases near Feshbach Resonances. *Phys. Rev. Lett.*, 106(5):050402, February 2011.
- [144] C. J. Pethick and D. Ter Haar. On the attenuation of sound in liquid helium. *Physica*, 32(11):1905–1920, November 1966.
- [145] Wolfgang Petrich, Michael H. Anderson, Jason R. Ensher, and Eric A. Cornell. Stable, Tightly Confining Magnetic Trap for Evaporative Cooling of Neutral Atoms. *Phys. Rev. Lett.*, 74(17):3352–3355, April 1995.
- [146] William D. Phillips and Harold Metcalf. Laser Deceleration of an Atomic Beam. *Phys. Rev. Lett.*, 48(9):596–599, March 1982.
- [147] Lev Pitaevskii and Sandro Stringari. *Bose-Einstein Condensation and Superfluidity*. Oxford University Press, January 2016.
- [148] John V. Prodan and William D. Phillips. Chirping the light—fantastic? Recent NBS atom cooling experiments. *Progress in Quantum Electronics*, 8(3):231–235, January 1984.
- [149] Cyril Proust, Etienne Boaknin, R. W. Hill, Louis Taillefer, and A. P. Mackenzie. Heat Transport in a Strongly Overdoped Cuprate: Fermi Liquid and a Pure d-Wave BCS Superconductor. *Phys. Rev. Lett.*, 89(14):147003, September 2002.
- [150] Leo Radzhovsky and Daniel E. Sheehy. Imbalanced Feshbach-resonant Fermi gases. *Rep. Prog. Phys.*, 73(7):076501, June 2010.
- [151] Mohit Randeria and Edward Taylor. Crossover from Bardeen-Cooper-Schrieffer to Bose-Einstein Condensation and the Unitary Fermi Gas. *Annu. Rev. Condens. Matter Phys.*, 5(1):209–232, March 2014.
- [152] A. Recati, C. Lobo, and S. Stringari. Role of interactions in spin-polarized atomic Fermi gases at unitarity. *Phys. Rev. A*, 78(2):023633, August 2008.
- [153] G. Roati, F. Riboli, G. Modugno, and M. Inguscio. Fermi-Bose Quantum Degenerate  $\hat{\{40\}}\hat{\{K\}}\hat{\{R\}}$  Mixture with Attractive Interaction. *Phys. Rev. Lett.*, 89(15):150403, September 2002.

- [154] Ira Z. Rothstein and Prashant Shrivastava. Symmetry obstruction to Fermi liquid behavior in the unitary limit. *Phys. Rev. B*, 99(3):035101, January 2019.
- [155] Timur M. Rvachov, Hyungmok Son, Ariel T. Sommer, Sepehr Ebadi, Juliana J. Park, Martin W. Zwierlein, Wolfgang Ketterle, and Alan O. Jamison. Long-Lived Ultracold Molecules with Electric and Magnetic Dipole Moments. *Phys. Rev. Lett.*, 119(14):143001, October 2017.
- [156] Yoav Sagi, Tara E. Drake, Rabin Paudel, Roman Chapurin, and Deborah S. Jin. Breakdown of the Fermi Liquid Description for Strongly Interacting Fermions. *Phys. Rev. Lett.*, 114(7):075301, February 2015.
- [157] Yoav Sagi, Tara E. Drake, Rabin Paudel, and Deborah S. Jin. Measurement of the Homogeneous Contact of a Unitary Fermi Gas. *Phys. Rev. Lett.*, 109(22):220402, November 2012.
- [158] R. Saint-Jalm, P. C. M. Castilho, É. Le Cerf, B. Bakkali-Hassani, J.-L. Ville, S. Nascimbene, J. Beugnon, and J. Dalibard. Dynamical Symmetry and Breathers in a Two-Dimensional Bose Gas. *Phys. Rev. X*, 9(2):021035, May 2019.
- [159] J. J. Sakurai and Jim Napolitano. *Modern Quantum Mechanics*. Cambridge University Press, September 2017.
- [160] Florian Schäfer, Takeshi Fukuhara, Seiji Sugawa, Yosuke Takasu, and Yoshiro Takahashi. Tools for quantum simulation with ultracold atoms in optical lattices. *Nat Rev Phys*, 2(8):411–425, August 2020.
- [161] Thomas Schäfer. Fluid Dynamics and Viscosity in Strongly Correlated Fluids. *Annu. Rev. Nucl. Part. Sci.*, 64(1):125–148, October 2014.
- [162] Thomas Schäfer and Derek Teaney. Nearly perfect fluidity: From cold atomic gases to hot quark gluon plasmas. *Rep. Prog. Phys.*, 72(12):126001, November 2009.
- [163] André Schirotzek, Yong-il Shin, Christian H. Schunck, and Wolfgang Ketterle. Determination of the Superfluid Gap in Atomic Fermi Gases by Quasiparticle Spectroscopy. *Phys. Rev. Lett.*, 101(14):140403, October 2008.
- [164] Tobias F. Schmidutz, Igor Gotlibovich, Alexander L. Gaunt, Robert P. Smith, Nir Navon, and Zoran Hadzibabic. Quantum Joule-Thomson Effect in a Saturated Homogeneous Bose Gas. *Phys. Rev. Lett.*, 112(4):040403, January 2014.
- [165] F. Schreck, L. Khaykovich, K. L. Corwin, G. Ferrari, T. Bourdel, J. Cubizolles, and C. Salomon. Quasipure Bose-Einstein Condensate Immersed in a Fermi Sea. *Phys. Rev. Lett.*, 87(8):080403, August 2001.

- [166] C. H. Schunck, M. W. Zwierlein, C. A. Stan, S. M. F. Raupach, W. Ketterle, A. Simoni, E. Tiesinga, C. J. Williams, and P. S. Julienne. Feshbach resonances in fermionic Li 6. *Phys. Rev. A*, 71(4):045601, April 2005.
- [167] Stuart L. Shapiro and Saul A. Teukolsky. *Black Holes, White Dwarfs, and Neutron Stars: The Physics of Compact Objects*. John Wiley & Sons, November 2008.
- [168] Y. Shin, M. W. Zwierlein, C. H. Schunck, A. Schirotzek, and W. Ketterle. Observation of Phase Separation in a Strongly Interacting Imbalanced Fermi Gas. *Phys. Rev. Lett.*, 97(3):030401, July 2006.
- [169] Yong-il Shin, Christian H. Schunck, André Schirotzek, and Wolfgang Ketterle. Phase diagram of a two-component Fermi gas with resonant interactions. *Nature*, 451(7179):689–693, February 2008.
- [170] Henrik Smith, Henning Højgaard Jensen, and Physics Laboratory H. Højgaard Jensen. *Transport Phenomena*. Clarendon Press, 1989.
- [171] Robert P. Smith, Naaman Tammuz, Robert L. D. Campbell, Markus Holzmann, and Zoran Hadzibabic. Condensed Fraction of an Atomic Bose Gas Induced by Critical Correlations. *Phys. Rev. Lett.*, 107(19):190403, November 2011.
- [172] Lennart Söbirey, Niclas Luick, Markus Bohlen, Hauke Biss, Henning Moritz, and Thomas Lompe. Observation of superfluidity in a strongly correlated two-dimensional Fermi gas. *Science*, May 2021.
- [173] Ariel Sommer, Mark Ku, Giacomo Roati, and Martin W. Zwierlein. Universal spin transport in a strongly interacting Fermi gas. *Nature*, 472(7342):201–204, April 2011.
- [174] Ariel Sommer, Mark Ku, and Martin W. Zwierlein. Spin transport in polaronic and superfluid Fermi gases. *New J. Phys.*, 13(5):055009, May 2011.
- [175] D. T. Son. Vanishing Bulk Viscosities and Conformal Invariance of the Unitary Fermi Gas. *Phys. Rev. Lett.*, 98(2):020604, January 2007.
- [176] David Stadler, Sebastian Krinner, Jakob Meineke, Jean-Philippe Brantut, and Tilman Esslinger. Observing the drop of resistance in the flow of a superfluid Fermi gas. *Nature*, 491(7426):736–739, November 2012.
- [177] Dan Stamper-Kurn. *Peeking and Poking at a New Wauntum Fluid: Studies of Gaseous Bose-Einstein Condensates in Magnetic and Optical Trap*. PhD thesis, Massachusetts Institute of Technology, 2000.
- [178] Claudiu Andrei Stan. *Experiments with Interacting Bose and Fermi Gases*. PhD thesis, Massachusetts Institute of Technology, 2005.
- [179] Daniel Adam Steck. Sodium D Line Data. Review.

- [180] A. Tawfik, M. Wahba, H. Mansour, and T. Harko. Viscous quark-gluon plasma in the early universe. *Annalen der Physik*, 523(3):194–207, 2011.
- [181] Meng Khoon Tey, Leonid A. Sidorenkov, Edmundo R. Sánchez Guajardo, Rudolf Grimm, Mark J. H. Ku, Martin W. Zwierlein, Yan-Hua Hou, Lev Pitaevskii, and Sandro Stringari. Collective Modes in a Unitary Fermi Gas across the Superfluid Phase Transition. *Phys. Rev. Lett.*, 110(5):055303, January 2013.
- [182] David Tong. Lectures on the Quantum Hall Effect. June 2016.
- [183] G. Tonini, F. Werner, and Y. Castin. Formation of a vortex lattice in a rotating BCS Fermi gas. *Eur. Phys. J. D*, 39(2):283–294, August 2006.
- [184] Andrew G. Truscott, Kevin E. Strecker, William I. McAlexander, Guthrie B. Partridge, and Randall G. Hulet. Observation of Fermi Pressure in a Gas of Trapped Atoms. *Science*, March 2001.
- [185] Pieter van Wyk, Hiroyuki Tajima, Daisuke Inotani, Akira Ohnishi, and Yoji Ohashi. Superfluid Fermi atomic gas as a quantum simulator for the study of the neutron-star equation of state in the low-density region. *Phys. Rev. A*, 97(1):013601, January 2018.
- [186] L. Vichi and S. Stringari. Collective oscillations of an interacting trapped Fermi gas. *Phys. Rev. A*, 60(6):4734–4737, December 1999.
- [187] J. L. Ville, T. Bienaimé, R. Saint-Jalm, L. Corman, M. Aidelsburger, L. Chomaz, K. Kleinlein, D. Perconte, S. Nascimbène, J. Dalibard, and J. Beugnon. Loading and compression of a single two-dimensional Bose gas in an optical accordion. *Phys. Rev. A*, 95(1):013632, January 2017.
- [188] J. L. Ville, R. Saint-Jalm, É. Le Cerf, M. Aidelsburger, S. Nascimbène, J. Dalibard, and J. Beugnon. Sound Propagation in a Uniform Superfluid Two-Dimensional Bose Gas. *Phys. Rev. Lett.*, 121(14):145301, October 2018.
- [189] Dieter Vollhardt and Peter Wolfle. *The Superfluid Phases of Helium 3*. Courier Corporation, October 2013.
- [190] Nicholas Wakeham, Alimamy F. Bangura, Xiaofeng Xu, Jean-Francois Mercurie, Martha Greenblatt, and Nigel E. Hussey. Gross violation of the Wiedemann–Franz law in a quasi-one-dimensional conductor. *Nat Commun*, 2(1):396, September 2011.
- [191] Xin Wang, Xiang Li, Ilya Arakelyan, and J. E. Thomas. Hydrodynamic Relaxation in a Strongly Interacting Fermi Gas. *arXiv:2112.00549 [cond-mat]*, December 2021.
- [192] U.-J. Wiese. Ultracold quantum gases and lattice systems: Quantum simulation of lattice gauge theories. *Annalen der Physik*, 525(10-11):777–796, 2013.

- [193] Bo Yan, Steven A. Moses, Bryce Gadway, Jacob P. Covey, Kaden R. A. Hazard, Ana Maria Rey, Deborah S. Jin, and Jun Ye. Observation of dipolar spin-exchange interactions with lattice-confined polar molecules. *Nature*, 501(7468):521–525, September 2013.
- [194] Zhenjie Yan. *Quasi-Particle Breakdown and Heat Transport in a Homogeneous Strongly-interacting Fermi Gas*. PhD thesis, Massachusetts Institute of Technology, 2022.
- [195] Zhenjie Yan, Parth B. Patel, Biswaroop Mukherjee, Richard J. Fletcher, Julian Struck, and Martin W. Zwierlein. Boiling a Unitary Fermi Liquid. *Phys. Rev. Lett.*, 122(9):093401, March 2019.
- [196] Zoe Z. Yan, Jee Woo Park, Yiqi Ni, Huanqian Loh, Sebastian Will, Tijs Karman, and Martin Zwierlein. Resonant Dipolar Collisions of Ultracold Molecules Induced by Microwave Dressing. *Phys. Rev. Lett.*, 125(6):063401, August 2020.
- [197] Tarik Yefsah, Rémi Desbuquois, Lauriane Chomaz, Kenneth J. Günter, and Jean Dalibard. Exploring the Thermodynamics of a Two-Dimensional Bose Gas. *Phys. Rev. Lett.*, 107(13):130401, September 2011.
- [198] Jan Zaanen, Sudip Chakravarty, T Senthil, and Philip Anderson. Towards a complete theory of high Tc. *Nature Phys*, 2(3):138–143, March 2006.
- [199] Hang Zhou and Yongli Ma. Thermal conductivity of an ultracold Fermi gas in the BCS-BEC crossover. *Sci Rep*, 11(1):1228, December 2021.
- [200] G. Zürn, T. Lompe, A. N. Wenz, S. Jochim, P. S. Julienne, and J. M. Hutson. Precise Characterization of Li 6 Feshbach Resonances Using Trap-Sideband-Resolved RF Spectroscopy of Weakly Bound Molecules. *Phys. Rev. Lett.*, 110(13):135301, March 2013.
- [201] Wilhelm Zwerger. *The BCS-BEC Crossover and the Unitary Fermi Gas*. Springer Science & Business Media, October 2011.
- [202] M. W. Zwierlein, J. R. Abo-Shaeer, A. Schirotzek, C. H. Schunck, and W. Ketterle. Vortices and superfluidity in a strongly interacting Fermi gas. *Nature*, 435(7045):1047–1051, June 2005.
- [203] M. W. Zwierlein, C. A. Stan, C. H. Schunck, S. M. F. Raupach, A. J. Kerman, and W. Ketterle. Condensation of Pairs of Fermionic Atoms near a Feshbach Resonance. *Phys. Rev. Lett.*, 92(12):120403, March 2004.
- [204] Martin W. Zwierlein. *High-Temperature Superfluidity in an Ultracold Fermi Gas*. PhD thesis, Massachusetts Institute of Technology, 2006.
- [205] Martin W. Zwierlein, André Schirotzek, Christian H. Schunck, and Wolfgang Ketterle. Fermionic Superfluidity with Imbalanced Spin Populations. *Science*, January 2006.